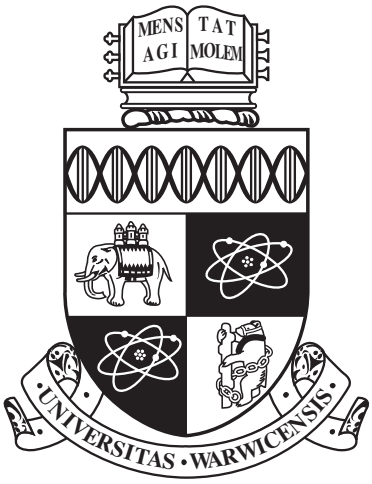

Exoplanet atmospheres at high spectral resolution in the near-infrared

by

Rebecca Karin Webb

Thesis

Submitted to the University of Warwick

for the degree of

Doctor of Philosophy in Physics

Department of Physics

September 2022

THE UNIVERSITY OF
WARWICK

Contents

List of Tables

List of Figures

Acknowledgments

Firstly, I thank my supervisor Dr Matteo Brogi who's knowledge and support these past 4 years has been invaluable and without which would have made this PhD impossible to complete. A special thanks also has to be given to Dr Siddharth Gandhi for his patience for providing me with what felt like at times to be an endless supply of high resolution atmospheric models which was crucial in completing this thesis.

I would also like to thank my fellow exoplanet atmospheres group members here at Warwick for sharing their expertise which has undoubtedly helped improve my own knowledge in this field. I also give my thanks to all of the international collaborators that have worked with me over the course of this PhD thesis, it has been an honour to have all of your guidance and encouragement through the tough field of high resolution spectroscopy!

Special thanks goes to the fellow PhD students at Warwick who have made the PhD a far more enjoyable experience, in particular to the back office crew; Patrick Cronin-Coltsmann, Tom Killestein, Catriona McDonald, Eva-Maria Ahrer, Ed Bryant, Sahl Rowther, Matthew Battley and Azib Norazman whom I will miss sharing an office with, and of course your friendship!

I cannot finish this section without mentioning the love and support I have received from parents and wider family during the PhD, even if they couldn't explain what it is I've actually been researching over the past 4 years.. And last but not least, many thanks goes to my enormously supportive and loving partner Rebecca Clark who has been by my side throughout (almost) the entire PhD process.

Declarations

I submit this thesis to the University of Warwick for the degree of Doctor of Philosophy in Physics. I declare that this thesis has been composed by myself and hasn't been submitted for a degree to another university.

The work presented in this thesis is largely based on work that has been published in peer reviewed journals. Namely, chapters 3 and 4 makes use of the work published in Webb et al. (2020) and Webb et al. (2022), respectively. The Introduction and Conclusions sections also make use of the work published in these papers. Chapter 5 is work that will be written for future publication.

All of the work presented in this thesis is my own work with the following exceptions:

- Chapter 3: Matteo Brogi was the PI of the original CRIRES observation proposal with Jayne L. Birkby and Ignas A. G. Snellen as further CO-I's. Matteo Brogi also helped to edit the main text in the published paper (Webb et al., 2020) which makes up this chapter. Siddharth Gandhi provided the calculations for the atmospheric models and helped to write the modelling section 3.5.3. Michael R. Line tested the data-set used in this chapter on their own HRCCS analysis framework. Katy L. Chubb and Sergey N. Yurchenko helped to supply the water line lists from the EXOMOL database.

- Chapter 4: Matteo Brogi was the PI of the CARMENES observation proposal which provided three nights of observations in this chapter, with Jayne L. Birkby, Ernst de Mooij and Ignas A. G. Snellen as further CO-I's. Matteo Brogi also helped to edit the main text of the published paper (Webb

et al., 2022) which makes up this chapter. Siddharth Gandhi provided the calculations for the atmospheric models used in this analysis and also tested this data-set on their analysis framework. Ignas A. G. Snellen and Yapeng Zhang provided a further two nights of observations that was used in this chapter. Stefan Pelletier and Björn Benneke used their analysis framework from Pelletier et al. (2021) to reproduce the results from this data-set in this chapter.

- Chapter 5: Matteo Brogi helped to edit the main text in this chapter which is as yet unpublished work. Siddharth Gandhi provided the transmission spectrum of an Earth-like atmosphere around the M-dwarf GJ 3470 and the calculations of the molecular cross-sections shown in Figure 5.2.

Abstract

The study of exoplanets planets as a field is only three decades old, however, it is now one of the biggest areas of research in astrophysics. This is because fundamentally all of the exoplanet research attempts to answer one of the biggest questions in humanity, are we alone in the Universe? One of the only ways for scientists to fully answer that question lies in the understanding of the gaseous envelope that surrounds these planets, known as the atmosphere. These atmospheres hold key information about their formation and migration histories through their primordial disks. The key to unlocking that information is through spectroscopic observations which can be used to determine the chemistry and physical processes within these atmospheres.

I present two separate analyses of high resolution observations of two non-transiting hot Jupiters, HD179949 b (chapter 3) and τ Boötis b (chapter 4), in the near-infrared. For HD179949 b, I present the detection of water vapour in the *L*-band using the CRIRES instrument. For τ Boötis b, I also present the detection of water vapour in the atmosphere using the CARMENES instrument. The latter detection is in disagreement with recent observations taken with the SPIRou instrument which is discussed in chapter 4.8.

In chapter 5, I present a simulated analysis of high resolution spectroscopic observations of an Earth-like planet from the ELT 39m telescope around M-dwarf stars. This study aimed to simulate the typical data analysis techniques on a time series data-set currently used on high resolution spectroscopic data typically used for faster orbiting planets. This analysis used principal component analysis (PCA) on these simulations to remove time varying flux variations. It was found that PCA removed most, if not all, of the planets signal due to the fact that a habitable planet, even around later type M-dwarfs move too slowly for this methodology to be feasible.

Abbreviations

1D, 2D, 3D one-, two-, three-dimensional

AO Adaptive optics

AU Astronomical units ($= 1.5 \times 10^{11}$ m)

CAHA Calar Alto Astronomical Observatory

CARMENES Calar Alto high-Resolution search for M dwarfs with Exoearths with Near-infrared and optical Echelle Spectrographs (on CAHA)

CC Cross-correlation

CCD Charge-coupled device

CCF Cross-correlation function

CC-to-log (L) Cross-correlation to log-likelihood mapping

C/O Carbon-to-Oxygen ratio

CoRoT Convection, ROtation and Transits

CRIRES/ CRIRES+ CRyogenic high-resolution InfraRed Echelle Spectrograph (on VLT)

ESO European Southern Observatory

ESPRESSO Échelle SPectrograph for Rocky Exoplanets and Stable Spectroscopic Observation (on VLT)

FWHM Full width half maximum

GCM General Circulation Model

HRS High resolution spectroscopy

HRCCS High resolution cross-correlation spectroscopy

HST Hubble Space Telescope

IR Infrared ($\lambda \sim 0.9$ - $200\,\mu$m)

JWST James Webb Space Telescope

LTE Local thermodynamic equilibrium

$\mathbf{M_\odot}$ Solar mass ($= 1.9884 \times 10^{30}$ kg)

$\mathbf{M_J}$ Jupiter mass ($= 1.8981 \times 10^{27}$kg)

MCMC Markov Chain Monte Carlo

Mid-IR Mid-infrared ($\lambda \sim 2.5$ - $10\,\mu$m)

NIR Near-infrared ($\lambda \sim 0.9$ - $2.5\,\mu$m)

OGLE The Optical Gravitational Lensing Experiment

PCA Principle Component Analysis

PWV Precipitable Water Vapour

$\mathbf{R_\oplus}$ Earth radius ($= 6.3781 \times 10^6$ m)

$\mathbf{R_J}$ Jupiter radius ($= 7.1492 \times 10^7$ m)

$\mathbf{R_\odot}$ Solar radius ($= 6.957 \times 10^8$ m)

S/N or SNR Signal-to-noise ratio

STIS Space Telescope Imaging Spectrograph (on HST)

SVD Singular Value Decomposition

T*-*p Temperature-pressure profile

TESS Transiting Exoplanet Survey Satellite

VLT Very Large Telescope

VMR Volume Mixing Ratio

WASP Wide Angle Search for Exoplanets

Chapter 1

Introduction

1.1 A brief history of exoplanet's

Planets orbiting around stars other than our own, known as extra-solar planet's or exoplanet's, had been theorised by philosophers centuries prior (Cenadelli and Bernagozzi, 2018) to their eventual detection. Early searches for these sub-stellar companions were limited by the precision of the high resolution spectrographs which looked for the elusive "Doppler-wobble" indicative of an orbiting body. This technique of using spectrographs to measure the motion of orbiting bodies around the centre of mass (see section 1.2.1) is not new and was used as early as 1880 (Batten, 1988) in stellar spectroscopic binary studies. However, it took another 100 years for the technology to improve enough to reach the $\sim 13\,\mathrm{m\,s^{-1}}$ radial velocity limit to measure a Jupiter analogue (i.e. Jupiter mass planet with an orbital period of roughly 11.2 years) around another Sun-like star.

First hints of sub-stellar companions around main-sequence stars came in the late 1980's with long period spectroscopic surveys of several nearby stars (Campbell et al., 1988; Latham et al., 1989; Hatzes and Cochran, 1993). The original analysis by Campbell et al. (1988) was not conclusively determined to be a planetary companion around the main-sequence star γ Cephei A, however, it was later confirmed that there is a planet in this system (Hatzes et al., 2003). These early surveys were primarily searching for planetary systems with similar architectures to that of our Solar system. Instead, the first discovery was the detection of two planetary mass objects around the post-main-sequence millisecond pulsar PSR 1257+12 (Wolszczan and Frail, 1992); a follow-up study (Bisnovatyi-Kogan, 1993) found a third planet in this system.

The breakthrough came in 1995 (Mayor and Queloz, 1995) with the discovery

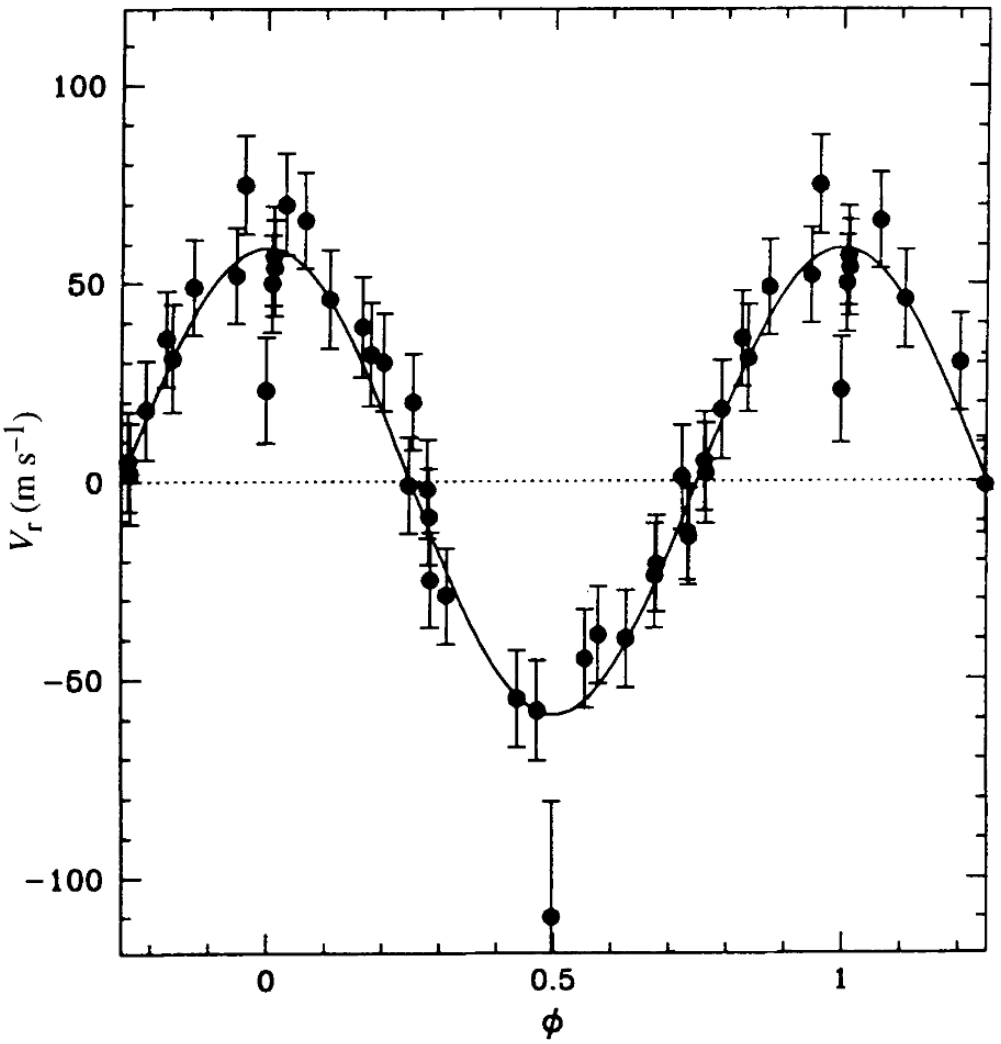

Figure 1.1: The first detection of a planetary mass companion around a main-sequence star. This planet was found to be a Jupiter mass planet on a much closer orbit than what was expected at the time. Figure taken from Mayor and Queloz (1995).

of a giant planet in a 4-day period orbit around the Sun-like star 51 Pegasi detected with the ELODIE high resolution spectrograph (Baranne et al., 1996). As this planet is large ($\sim 0.5\,\mathrm{M_J}$) and on a close-in orbit (0.052 AU), the radial velocity measurements were several times at $\sim 50\,\mathrm{m\,s^{-1}}$ from that of the anticipated $\sim 13\,\mathrm{m\,s^{-1}}$ for a Jupiter-like companion (see equation (1.2)). This detection is shown in Figure 1.1. This caused some initial scepticism (Gray, 1997) as it conflicted with planet formation theories at the time of this discovery as it was not thought possible that a gas-giant could form so close to its host star. Despite this, it was suggested that, at the time theoretical, giant planet's could exist on rapid orbital periods much earlier than their discovery (Struve, 1952) and may have even been observable with earlier spectrographs.

Subsequently, there were discoveries and confirmation of further Jupiter-mass planet's on close-in orbits (e.g. Butler et al., 1997) soon after the discovery of 51 Peg b, that removed any residual doubt that this exotic sub-class of exoplanet's do exist around other planetary systems. This sub-class of exoplanet's were later given the name the "hot Jupiters" due to their large mass, large gaseous envelope and extreme day-side temperatures ($T_{\mathrm{eq}} \geqslant 1000\,\mathrm{K}$). Some of these earliest discoveries include the non-transiting hot Jupiters HD 179949 b and τ Boötis b which are the subject of this thesis in chapters 3 and 4. Even in these early days of exoplanet discovery, it was noticed that exoplanet systems are indeed incredibly diverse (Marcy and Butler, 1996) and are often not in the relatively ordered system that we observe in our Solar system.

1.2 Exoplanet detection methods

From the early discoveries towards the turn of the century, there are now multiple methods used in the detection of new planetary systems. Some of the more prominent techniques used are described further below.

1.2.1 The radial velocity method

As eluded to in the opening section, the radial velocity method was the first exoplanet detection method, and is still highly successful today with several long term radial velocity surveys in operation. For example, the California Planet Survey (Howard et al., 2010) hunting for long period exoplanet's and the ESPRESSO blind exoplanet survey searching for Earth analogues (Hojjatpanah et al., 2019).

The radial velocity method uses the relatively simple, but powerful, idea of measuring the red- and blue-shifts of the resolved stellar emission spectral lines.

These periodic shifts from the rest frame wavelength, λ_0, can thus determine the orbital motion of the host star about its centre of mass with the Doppler radial velocity equation,

$$V(t) = \frac{c[\lambda(t) - \lambda_0]}{\lambda_0}, \tag{1.1}$$

where $\lambda(t)$ and c is the measured wavelength at time, t, and the speed of light, respectively. As only the radial velocity of the star can be easily measured as the planet's spectrum is orders of magnitude fainter than the stellar spectrum (see section 2.6.3), the observed spectra can only considered to be a single-line spectroscopic binary. As a result, the orbital inclination, i, along the observer's line of sight cannot be determined, thus this method usually only allows the minimum mass, $M_{\rm P} \sin i$, to be determined (if combined with transit observations, this degeneracy breaks). The orbital inclination of an exoplanet is defined as the angle between the normal to the orbital plane of the planet and the observer's line of sight, for example an $i = 0°$ and $i = 90°$ is for a face-on and edge-on (or transiting) orbit, respectively. With observations of the radial velocity curve, the radial velocity semi-amplitude ($K_\star$) along the line of sight can be determined which allows the minimum mass to be computed by Cumming et al. (1999),

$$K_\star = \left(\frac{2\pi G}{P}\right)^{\frac{1}{3}} \frac{M_{\rm P} \sin i}{(M_{\rm P} + M_\star)^{2/3}} \frac{1}{(1-e)^{1/2}}, \tag{1.2}$$

where G, P, $M_\star$ and e are the gravitational constant, orbital period, stellar mass and the orbital eccentricity, respectively. If the orbit is circular, i.e. $e = 0$, the final fraction drops from equation (1.2). It can be seen from this equation that this detection technique scales with planetary mass and inversely scales with the orbital period, hence, the radial velocity method is most sensitive to the most massive planet's on short orbital periods. This explains why the majority of the first planet's discovered were the hot Jupiters. Due to the need for ultra-high precision spectroscopy, these surveys will also suffer from observing biases towards the brightest stars in the sky.

Despite the ongoing success of this method, there are some important limitations of this technique that needed to be addressed. Such surveys require the observation of a single star at a time which is both time consuming and can be an ineffective use of telescope resources. Most importantly, as the orbital inclination is highly uncertain, the mass of the orbiting body can in some cases potentially range from planetary to over the deuterium burning mass limit at roughly $13\,{\rm M_J}$. For these reasons, transiting surveys quickly became a crucial tool for exoplanet studies.

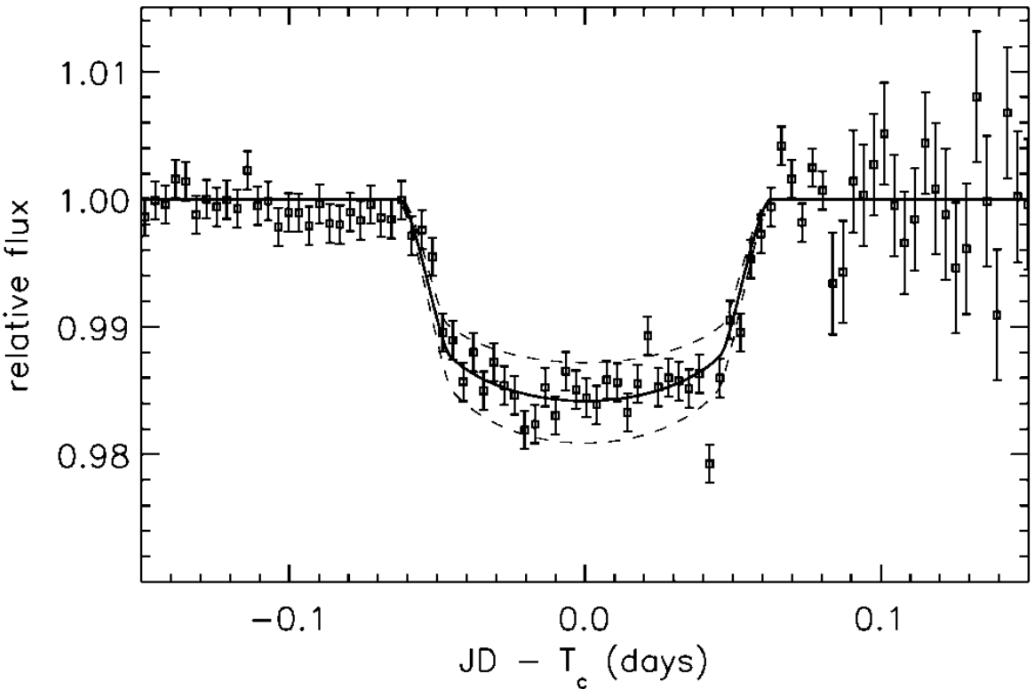

Figure 1.2: The first observed photometric transit of an exoplanet around a main sequence star, HD 209458 b. The data-points are binned in phase according to their best-fit orbital parameters. The best-fit transit model is shown as the solid black line. Figure taken from Charbonneau et al. (2000).

1.2.2 Transiting exoplanet's

The prediction for the potential to observe a transiting exoplanet again came in 1952 by Otto Struve (Struve, 1952). A transit of an exoplanet occurs when an object of planetary mass passes in front of its host star along the line of sight of observation resulting in a observable, periodic dimming of the light from the star. The first detection of a transiting exoplanet, HD 209458 b (Charbonneau et al., 2000), came only five years after the radial velocity detection of 51 Peg b. This transit is shown in Figure 1.2 which combines two photometric observations over two epochs, which acts to lower the uncertainty in the transit depth.

Measuring the depth of the transit gives an accurate value for the planetary radius if the stellar radius is well-known (Seager and Mallen-Ornelas, 2003),

$$\Delta = \frac{F_\star - F_{\star,\mathrm{transit}}}{F_\star} = \frac{R_\mathrm{P}^2}{R_\star^2}. \tag{1.3}$$

If one considers the geometric probability of viewing a transit from the observer's line of sight, this value scales with the radii and inversely scales with the orbital

separation, a, given by $p_{\rm transit} = \left(\frac{R_\star \pm R_{\rm P}}{a}\right)\left(\frac{1+e\sin\omega}{1-e^2}\right)$ (Winn, 2010), where the $\pm$ includes grazing transits (+) or not (-), and ω is the argument of periastron. The argument of periastron is defined as the orbital element describing the angle of an orbiting body's periapsis (the point of closest approach to the central body), relative to its ascending node (the point where the body crosses the plane of reference from south to north). The angle is measured in the orbital plane and in the direction of motion. Considering this probability and equation 1.3, the transit method is also biased towards planet's with large radii and on short orbital periods. For example, a 51 Peg b like planet has an orbital alignment probability of $\sim$ 10% and a transit depth of $\sim$ 1%, whereas, an Earth analogue around a Sun-like star has a transit probability of $\sim$ 0.5% and depth of $\sim$ 0.01%. Therefore, it was again the hot Jupiters that were typically being observed first with the earliest photometric transit searches such as the OGLE survey (Udalski et al., 1992).

One of the major advantages over radial velocity surveys, transiting surveys are able to observe a large patch of sky which can simultaneously measure the brightness of several stars per image. Also, radial velocity surveys rely on observing brighter targets whereas transit surveys can observe the transit of planetary objects for fainter targets. As such, many ground- and space-based photometric surveys, such as; WASP (Pollacco et al., 2006), CoRoT (Moutou et al., 2013), *Kepler* (Borucki et al., 2009) and TESS (Ricker et al., 2015), have been hugely successful in detecting a large number of exoplanet's to date, however, the majority of these detections are still to be confirmed. Follow-up radial velocity measurements are complementary to transit observations and are often used to confirm the dips in the light curve are transiting planetary bodies or some other astrophysical effect such as a blended eclipsing binary (e.g. Konacki et al., 2003b). The first such follow-up was the confirmation of the transiting planet OGLE-TR-56 b (Konacki et al., 2003a) which was the first planet to be discovered solely from a transit survey without previous radial velocity measurements suggesting its presence. With transit modelling, the orbital inclination can also be accurately determined which allows the mass and density of the planet to be calculated from follow-up radial velocity measurements. If the host stellar mass is known without any assumptions (e.g. from astroseismology measurements), then the absolute mass of the planet can be determined in this way. The bulk density measurement is particularly important to understand the nature of the planet, for instance, it can be used to infer whether there is a significant "puffy" outer atmosphere (large planetary radius attributed to the atmosphere, and low density, e.g. Masuda, 2014) or even the dense remnants of planetary cores (Armstrong et al., 2020).

1.2.3 Other methods

In addition to the radial velocity and transit methods, there are a few other less prolific techniques in the detection of exoplanet's. Such examples include direct imaging and microlensing which are discussed briefly below.

Direct imaging

To directly image an exoplanet, the light from the host star needs to be sufficiently suppressed by a coronagraph to observe the thermal emission from the exoplanet's. To date, this technique has only detected a handful of systems (see Figure 1.3) due to the difficulty in creating a coronagraph stable enough over a long enough period of time to detect the thermal emission from the exoplanet over the host stellar light. In addition, the systems need to be observed over many epochs to provide evidence that the emitting object is indeed a gravitationally bound planet rather than a faint background source (e.g. Zurlo et al., 2013). To be able to directly image exoplanet's, the exoplanet needs to be emitting a lot of thermal radiation and to be on a wide enough orbit to have enough angular separation to be imaged from the host star. For example, the HR 8799 system with three directly imaged planet's, have contrast ratios of $\sim 10^{-5}$ in the H-band (Marois et al., 2008). Therefore, all of the directly imaged planet's detected thus far have been on wide orbits, typically $> 9\,\mathrm{AU}$ (Lagrange et al., 2010), from very young exoplanet's that have a significant amount of residual thermal emission from formation.

Microlensing

Microlensing is also a very difficult method of detecting exoplanet's which requires the observation of a small amplification in the light of a background star caused by a gravitational lens from a foreground object, be it a star, planet or other compact object. This method is not only able to detect planet's bound to a host star (e.g. Bond et al., 2004), but also free floating planet's (e.g. Sajadian, 2021) (i.e. planet's that have been ejected from their system). However, large surveys of hundreds of stars (Udalski et al., 1992; Sako et al., 2008), typically in highly dense stellar regions such as the Galactic bulge need to be monitored in order to observe only a handful of events. This method does however has peak sensitivity for bound planetary mass systems at larger orbital separations, generally beyond the water snowline (Gould and Loeb, 1992) (see section 1.4.2 and Figure 1.7), and low mass planet's ($\sim M_{\oplus}$) around solar type stars (i.e. $R \sim R_{\odot}$) (Bennett and Rhie, 1996).

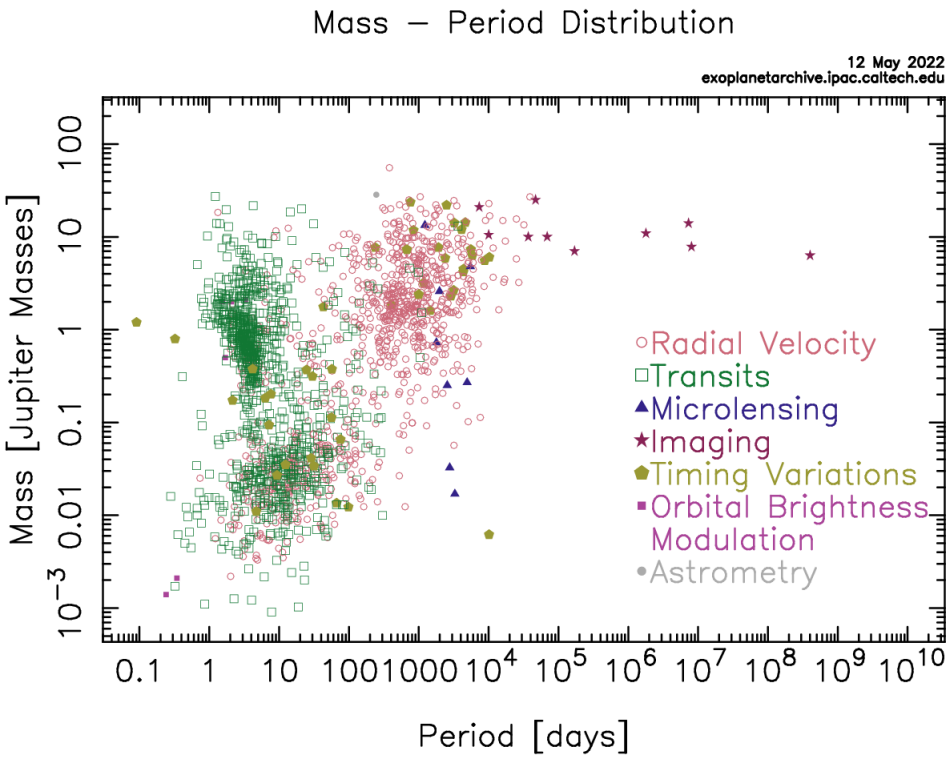

Figure 1.3: Mass-period exoplanet distribution of all the discoveries and their discovery methods to date (May 12, 2022). Figure accessed from the Nasa exoplanet archive (`https://exoplanetarchive.ipac.caltech.edu/`).

1.3 Population statistics

With the ever growing diversity of exoplanet discoveries, numerous population statistics studies have been done on the occurrence rates on different exoplanetary systems around their host stars. The occurrence rate (or planet frequency) is defined as the average number of planet's per star, i.e. $\frac{\text{Total number of planet's}}{\text{Total number of stars}}$, and is often reported as a percentage.

Figure 1.3 shows a mass-period distribution of the $\sim$ 5000 exoplanet discoveries made prior to May 12, 2022. This distribution also indicates the discovery method for each exoplanet of which shows some of the detection biases present for each method. For example, radial velocity and transiting planet's typically show a strong preference for higher mass, shorter period planet's. These biases need to be accounted for when calculating accurate population statistics of planetary systems.

Fulton et al. (2017) used the California-Kepler survey to show evidence for a deficit in the occurrence rates for planet's between 1.5-2.0 $R_\oplus$ for close-in systems (periods $<$ 100 days), this became well-known as the radius valley. This was the

first observational evidence that there is a physical distinction between bodies that are able to retain a thick gaseous H/He envelope (sub-Neptunes, $\gtrsim 2.4\,R_\oplus$) and a rocky world with a tenuous atmosphere (terrestrial, $\lesssim 1.3\,R_\oplus$). A more recent study from Hardegree-Ullman et al. (2020) with a higher sample of well-defined systems confirmed the existence of the radius valley at $\sim 1.9\,R_\oplus$.

Despite being some of the first observed systems and most amenable to detection which can be seen from the high density of points at $\sim 1\,M_J$ and $\lesssim 10$ days period in Figure 1.3, hot Jupiter occurrence rates, which are the topic of this thesis, are typically found to be below 1 per cent using either radial velocity (e.g. Sozzetti et al., 2009; Mayor et al., 2011; Wright et al., 2012; Mortier et al., 2012) or transiting surveys (e.g. Gould et al., 2006; Bayliss and Sackett, 2011; Petigura et al., 2018; Boley et al., 2021). Radial velocity surveys shows trends towards higher occurrence for hot Jupiters over transits, however, this may be due to observational biases as earlier type stars are not largely monitored in radial velocity surveys.

Using 316 well-constrained systems, Chen and Kipping (2017) were able to determine the transitions of exoplanet's into their different sub-groups by revealing the underlying mass-radius relationships. For instance, Terran (rocky), Neptunian, Jovian and stellar bodies can be classified with mass-radius relationships given by, $R \sim M^{0.28}, M^{0.59}, M^{-0.04}, M^{0.88}$, respectively. This study also makes the suggestion that the upper mass boundary for a terrestrial world is placed at $\sim 2.0\,M_\oplus$ (backed up with a study from Rogers, 2015). As the most commonly found exoplanet's around Sun-like stars are thought to be Neptunian (Foreman-Mackey et al., 2014), the Solar system is considered to be within the norm of the observed planetary systems as the majority of the Solar system planet's fall within this category.

1.4 Exoplanet atmospheres

1.4.1 Theoretical modelling of exoplanet atmospheres

In order to infer the presence of an exoplanet atmosphere from observations, the shape of the spectrum needs to be modelled accurately from theoretical predictions which will depend on the chemical content and various physical processes. Saumon et al. (1996) and Guillot et al. (1996) produced the first attempts of modelling the thermal emission of Jupiter-like exoplanet's around various stellar types with relatively few opacity sources. However, it was Seager and Sasselov (1998) that produced the first accurate atmospheric modelling in optical and IR wavelengths under the effects of strong irradiation from the host star, like those seen for the hot Jupiters. This part of the modelling is particularly important for close-in giant planet's as

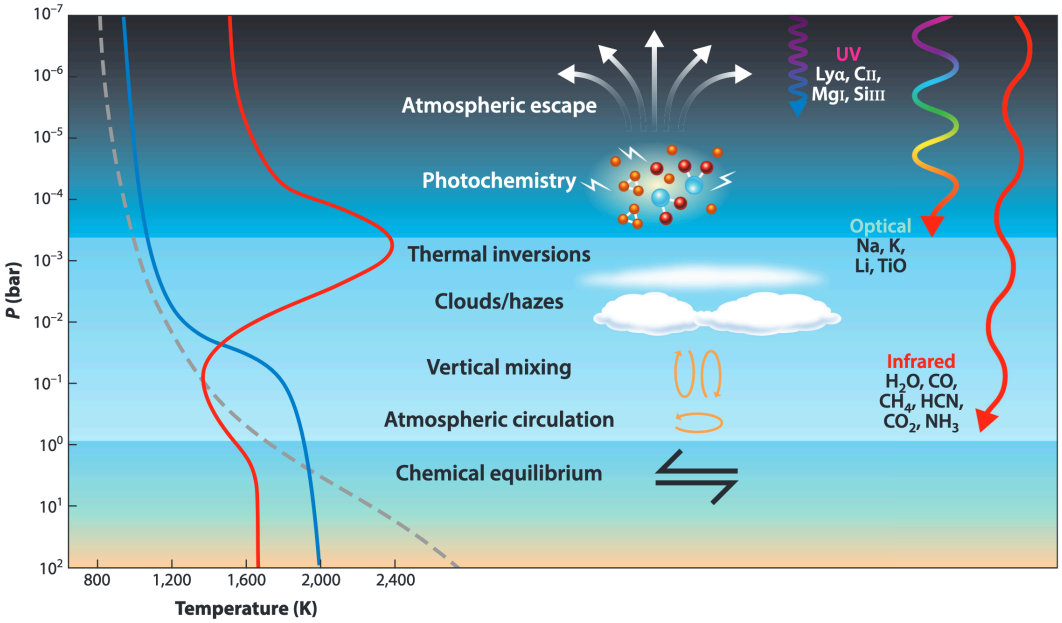

Figure 1.4: Schematic of the various processes that could occur in exoplanet atmospheres. On the left, the T-p profile can vary depending on the irradiation levels, red is a thermal inverted profile, blue is a non-inverted profile and the grey dashed line shows low levels of irradiation. On the right, there shows the typical depths at which different energies of light penetrate through the atmosphere. Figure taken from Madhusudhan (2019).

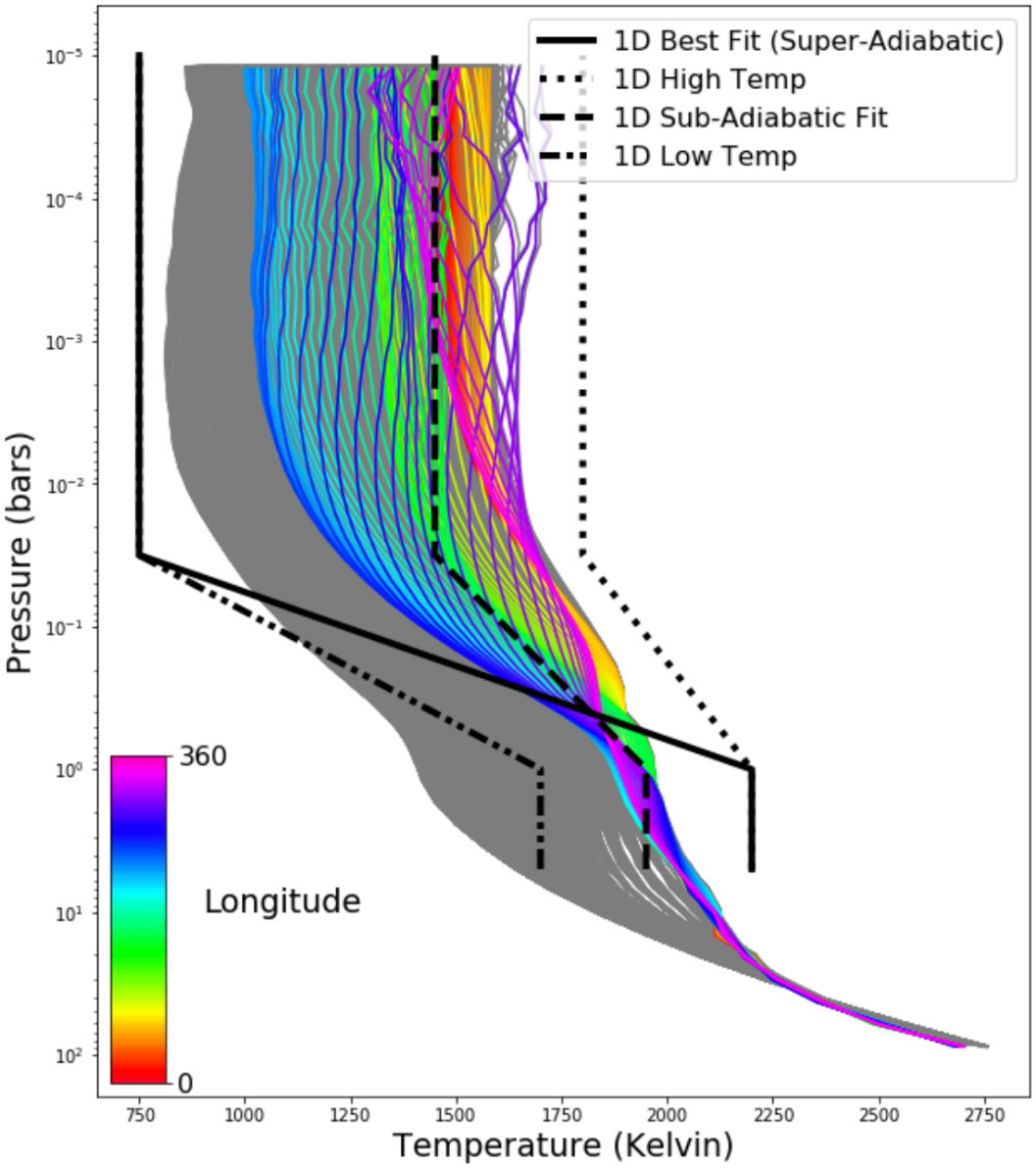

Figure 1.5: T-p profiles from a 3D model of the hot Jupiter HD209458 b. The grey profiles are from the whole planet, whereas, the coloured lines are from equatorial profiles (i.e. changing in longitude). The black and various dashed lines are typical 1D T-p profiles used to represent spectra without including any 3D effects. Figure taken from Beltz et al. (2021).

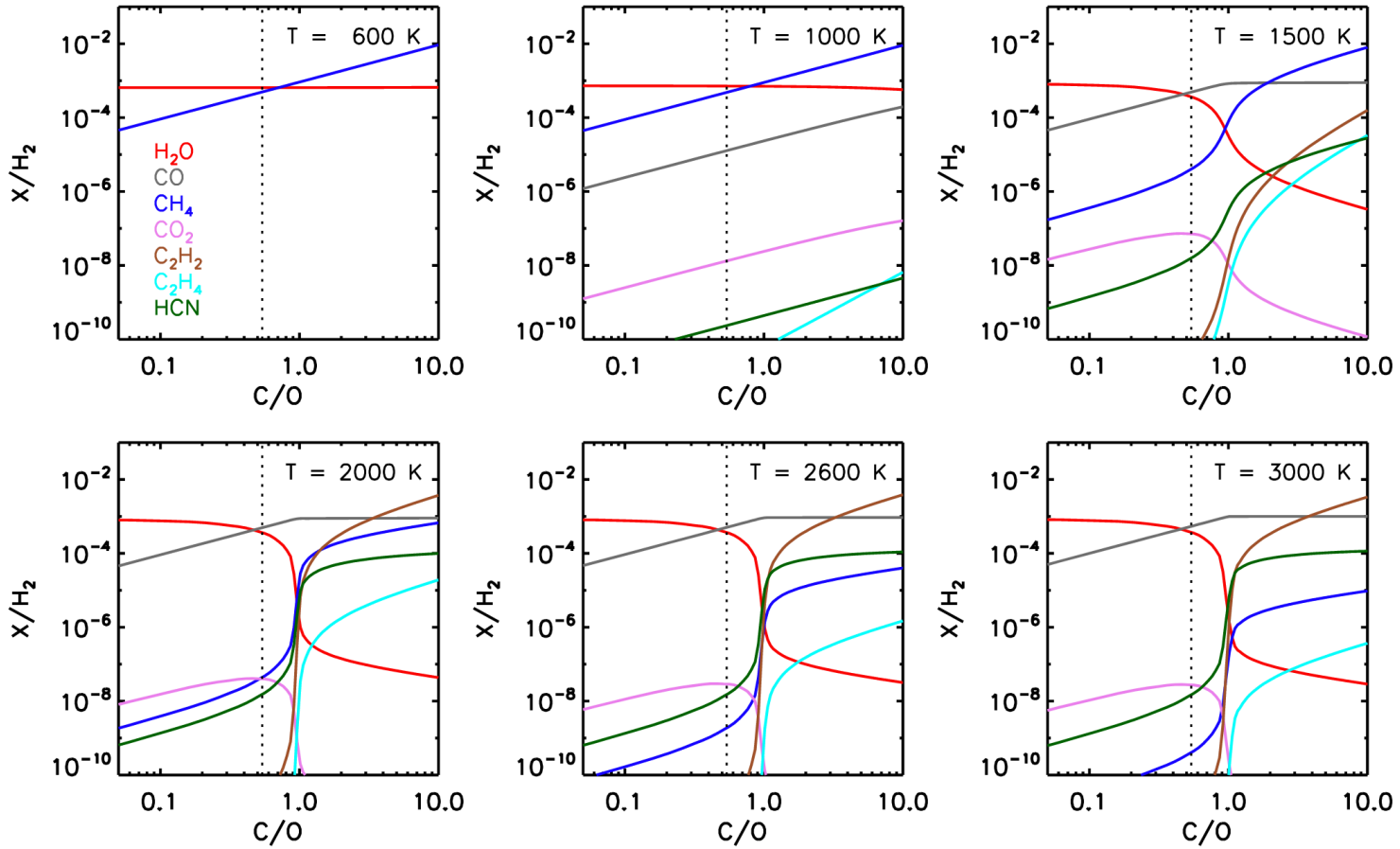

Figure 1.6: Molecular mixing ratios for the observable opacity sources in the IR at an atmospheric pressure of 1 bar as a function of temperature and the C/O ratio. The solar C/O value (0.55) is shown as the black dashed line. Figure taken from Madhusudhan (2012).

the stellar irradiation is the main source of heating within these atmospheres and thus will strongly influence the re-radiation and final spectrum. Figure 1.4 shows how the temperature structure is strongly dependent on the amount of stellar irradiation. For instance, the grey dashed T-p profile is for a typical isolated or weakly irradiated atmosphere, whereas, the blue and red profiles are for typical highly irradiated atmospheres such as for hot Jupiters. The red T-p profile shows a particular case which shows a thermally inverted layer ($\frac{dT}{dp} > 0$), similar to the stratospheric layer seen in the Earth's atmosphere. In the Earth's atmosphere, the stratospheric layer is caused by heating from ozone absorption of UV light, however, in ultra-hot Jupiters ($T_{\rm eq} \gtrsim 2000\,{\rm K}$), the cause of thermal invasions are still an open question with early theoretical studies suggesting that they may be caused by the strong optical absorbers TiO and VO (Hubeny et al., 2003; Fortney et al., 2008), but many other thermal inverting species candidates have since been put forward (Mollière et al., 2015; Lothringer et al., 2018; Gandhi and Madhusudhan, 2019). Observationally, thermal inversions have been measured in ultra-hot Jupiters both at low spectral resolutions (e.g. Mikal-Evans et al., 2020) and at high resolution (e.g. Nugroho et al., 2017) (see section 1.4.5 for a discussion on measuring thermal inversions at high resolutions). In depth reviews on atmospheric modelling techniques are given by Madhusudhan et al. (2014); Heng and Showman (2015); Madhusudhan et al. (2016); Madhusudhan (2019).

Typically, 1D models (see the black 1D T-p profiles in Figure 1.5) are used to model the spectrum of an exoplanet atmosphere, often in chemical and thermal equilibrium. The calculation of a 1D atmospheric model assumes several plane-parallel layers make up the atmosphere with each layer at a particular distance from the next layer. At each layer, a radiative transfer equation is computed to determine the balance of energy entering and leaving each layer in the vertical direction whilst assuming chemical and thermal equilibrium and the input opacity sources. This modelling technique can incorporate added complexities such as clouds and hazes (Mollière et al., 2017), disequilibrium processes (e.g. Drummond et al., 2016) and varying elemental chemical abundances (e.g. Mollière et al., 2015) that will each influence the final spectrum.

In general, longer wavelength observations such as those in the IR, compared to those in the optical and UV, are able to penetrate deeper into the atmosphere (or higher pressures, see Figure 1.4) as a result of the varying optical depths of the different species. For example, IR wavelengths are primarily absorbed by large molecular species (i.e. three or more atoms) excluding CO which strongly absorbs in the NIR at ~ 1.6 and $2.3\,\mu$m (e.g. Snellen et al., 2010; Brogi et al., 2012), which are

found deeper within the atmosphere at ~ 1 bar pressure. An exception to this has been the successful detections of the He triplet lines observable in the NIR, which if the spectral lines are deep enough can suggest an extended outflow escaping from the planet's atmosphere (Spake et al., 2018; Nortmann et al., 2018; Allart et al., 2019). Lighter species (such as metals with less than 3 atoms, TiO and VO) in general have greater opacity at optical wavelengths and are found higher up in the atmosphere at $\sim 10^{-3}$ bars of pressure (e.g. Charbonneau et al., 2002). As UV light can only penetrate at low pressures in the atmosphere, UV observations have become a useful tool to characterise the upper layers (Wakeford et al., 2020; Lothringer et al., 2022) where aerosols such as silicates could contribute in the formation of clouds and hazes.

Along with the temperature structure of the atmosphere, the opacity sources are equally important in matching the observations with the model spectrum as they will determine the absorption and/or emission features present. In gas giant atmospheres such as those in hot Jupiters, there will be additional collisionally induced absorption from H_2-H_2 and H_2-He (Richard et al., 2012a) that will have an imprint of the overall spectrum. Collisionally induced absorption is a result of inelastic collisions (i.e. kinetic energy is not conserved) between these molecules in the atmosphere that induces further quantum energy levels which imparts further spectral absorption or emission features. For giant gaseous atmospheres, H_2 is the dominant species, however, there will be additional observable minor species present. The abundance of these species are often measured as a volume mixing ratio (VMR) which is relative to the amount of hydrogen and the elemental abundances from the Sun (Asplund et al., 2009), i.e. $\mathrm{VMR} = \mathrm{X/H_2} = \log_{10}[(n_\mathrm{X}/n_\mathrm{H})/(n_\mathrm{X}/n_\mathrm{H})_\mathrm{Sun}]$, where X is some minor species and n is an elemental abundance. This allows species abundance measurements in different exoplanet atmospheres to be compared relative to a common reference frame. It is expected that the dominant minor molecular species at temperatures between $\sim$ 500 and 3000 K are H_2O, CH_4, CO, CO_2, HCN and C_2H_2 (e.g. Madhusudhan et al., 2011b), however, this is dependent on the temperature, C/O ratio (e.g. Madhusudhan, 2012) and metallicity (e.g. Moses et al., 2013). The C/O ratio is determined by the abundance ratio of the observed carbon and oxygen bearing species, for example, $\mathrm{C/O} = \frac{\mathrm{VMR(CO)+VMR(CH_4)}}{\mathrm{VMR(CO)+VMR(H_2O)}}$, if CO, CH_4 and H_2O have been observed in an atmosphere. Figure 1.6 shows the theoretical VMR of each of these species as a function of the planet temperature and the C/O ratio, the solar C/O ratio is shown for comparison as the black dashed line. As the species abundances are measured relative to that of the Sun, the elemental abundance ratios are also measured relative to that of the Sun, therefore, an atmospheric C/O ratio

is often compared to the solar C/O ratio of ~ 0.55 (Asplund et al., 2009). At solar C/O ratios, the primary species in planetary atmospheres are H_2O, CO and CH_4 which is governed by the reaction,

$$CH_4 + H_2O \leftrightharpoons CO + 3H_2. \tag{1.4}$$

At 1 bar of pressure, the reverse reaction is favoured at lower temperatures ($T \lesssim 1000\,\mathrm{K}$), therefore, H_2O and CH_4 is predicted to be highly abundant for more temperate planet's. Conversely, at higher temperatures, the forward reaction is favoured and thus the majority of the carbon will be locked up in CO rather than CH_4 for hot planet's such as hot Jupiters. Furthermore, for C/O $\lesssim 0.55$, water is expected to be the predominant minor species in exoplanet atmospheres for all temperatures (and CO for $T \geqslant 1500\,\mathrm{K}$), whereas at C/O$> 1$, there is a stark transition in which CH_4 becomes more abundant than water for hot Jupiters.

There are two different modelling approaches that are used to infer the observed spectra from exoplanet's. The first of which is known as forward modelling, which is a technique that uses a priori knowledge of the chemistry and physical structure of the atmosphere to statistically infer the shape of the observed spectrum. The other technique is to use atmospheric retrievals which are processes that compares models with the observed spectra through an iterative process which ultimately converges onto the most statistically favourable solution. These retrieval algorithms are coupled with various statistical frameworks. One of the earliest examples samples the prior distributions with a simple grid search approach (e.g. Madhusudhan and Seager, 2009) or, now more commonly, a suitable Bayesian approach such as an MCMC (e.g. Madhusudhan and Seager, 2010; Line et al., 2013) or a nested sampling algorithm (e.g. Benneke and Seager, 2013; Waldmann et al., 2015). While forward modelling can be computationally much less demanding, it is however limited in its ability to directly constrain observations.

To theoretically determine the opacity for a given species in a model for a given wavelength, two main approaches are used. The first, and most computationally efficient, is known as the correlated-k distribution method that estimates absorption coefficients for a given spectral bin for several overlapping opacity sources (e.g. see Lacis and Oinas, 1991). This has been used successfully for several different prescriptions of modelling hot Jupiter atmospheres (e.g. Drummond et al., 2016; Amundsen et al., 2017). This method is an accurate approximation for low resolution models with a large number of opacity sources, however, for high resolution spectroscopy (HRS, see section 1.4.5) a high level of precision and accuracy is

required in the modelling. Therefore, at high resolution, it is more appropriate to use the alternative line-by-line approach which uses highly accurate and complete line lists from numerous databases such as HITRAN (Gordon et al., 2017, 2022). High temperature line lists such HITMEP (Rothman et al., 2010a) and EXOMOL (Tennyson and Yurchenko, 2012; Polyansky et al., 2018) have also been developed specifically for hot exoplanet atmospheric observations. It is important that these line list databases are frequently kept up-to-date as inaccuracies can hinder detections (Hoeijmakers et al., 2015; de Regt et al., 2022). Tennyson and Yurchenko (2022) gives a recent review on the use of molecular line lists at high resolutions.

Modern techniques include 3D general circulation models (GCMs) (e.g. Showman et al., 2009; Rauscher and Menou, 2010) that allow for greater complexity in the modelling of exoplanet atmospheres that allow 3D observational effects to be constrained in the observations. These models compute the chemical, thermal and dynamical properties of the atmosphere as a function of latitude and longitude. This has been successfully used to explain 3D, phase-dependent effects in observations (e.g. Kataria et al., 2016). However, the amount of information incorporated into 3D modelling often leads to highly expensive computational times compared to 1D modelling, along with insufficient precision and resolution of observed spectra, has limited its use in interpreting observations thus far.

It is also expected that close-in planet's dominated with gaseous H/He atmospheres, particularly those close to the radius valley (see section 1.3), may undergo some evolutionary changes with time due to atmospheric mass loss (see Owen, 2019, for a recent review). This has been inferred with various observations of close-in systems, perhaps the most significant of which being the Kepler-36 system (Carter et al., 2012) which contains two planet's on similar orbits (b at 0.115 AU and c at 0.128 AU) but with significantly different densities (the inner planet having an increased density by a factor of 8). This is attributed to the inner planet being a solid rocky body whereas the outer planet has a significant gaseous outer H/He envelope making up $\sim$ 10 per cent of the planetary mass. Using thermal and photo-evaporative modelling techniques, Lopez and Fortney (2013) were able to show that both planet's in the Kepler-36 system could have been formed with significant gaseous H/He atmospheres but with the differences in the core masses between the two planet's, this can have an impact on the mass-loss evolutions of the two planet's. Thus, it is important to consider the evolutionary impact on the atmosphere of the planet in time.

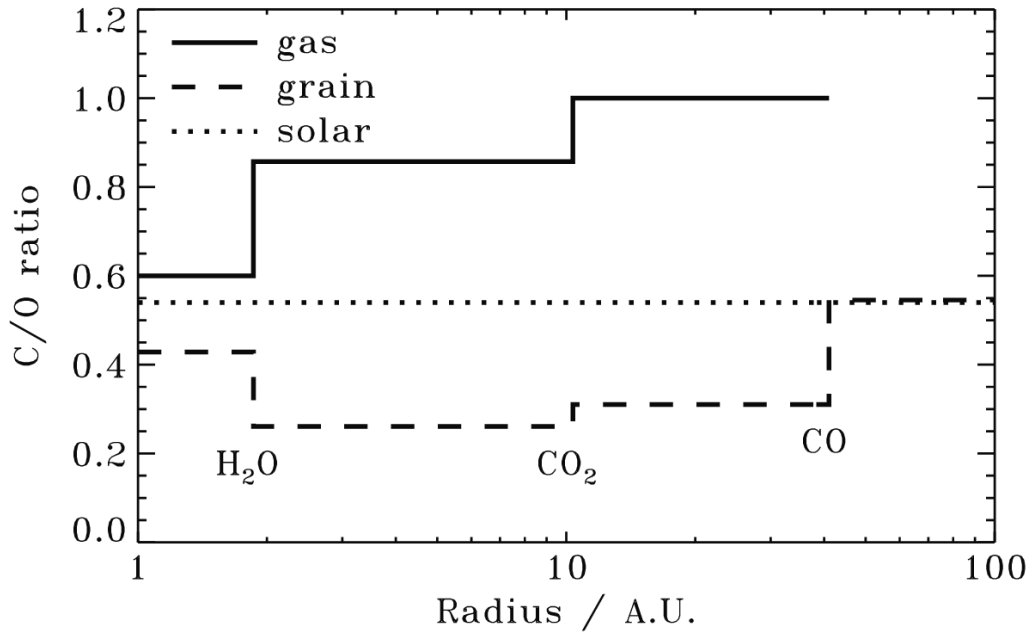

Figure 1.7: C/O ratio as a function of the distance from a solar type host star for a typical protoplanetary disk. The H_2O, CO_2 and CO snowlines are indicated at the locations of the step-functions at $\sim$ 2, 10 and 40 AU. These locations will vary depending on the temperature structure of a particular protoplanetary disk. Figure taken from Öberg et al. (2011).

1.4.2 Formation and migration processes on atmospheric spectra

Measuring elemental abundance ratios, such as C/O and C/H, of atmospheres can be key to unlocking the early formation of the exoplanet in the protoplanetary disk and subsequent migration pathways. Assuming a core-accretion scenario for a gas giant planet, the primordial atmosphere is thought to accrete the majority, if not all of the gaseous and grain material at the location of formation of the planetary core (D'Angelo and Lubow, 2008, show that the planet will migrate $\lesssim$ 20 per cent of its semi-major axis during the gaseous runaway accretion phase). However, the evolution of the primordial disk can alter the C/O ratio in time based on the accreting materials. The predominant molecular carbon and oxygen bearing species in protoplanetary disks are H_2O, CO_2 and CO (see review by Williams and Cieza, 2011) that each have different condensation temperatures which leads to the formation of theoretical "snowlines" which represent the minimum distance in the disk at which these volatile species condense into ices. The radii of these snowlines will differ depending on the particular temperature structure of the disk, i.e. how much the temperature drops as a function of distance. An example of a "typical" (i.e. a disk around a solar type star) set of snowlines are shown in Figure 1.7, for each

snowline there exists a step function in the C/O ratio as these species are no longer accreted into the atmosphere and thus the abundance of carbon and oxygen bearing species changes rapidly. For this typical disk set-up, the H_2O, CO_2 and CO snowlines are located at $\sim$ 2, 10 and 40 AU from the host star, respectively. Öberg et al. (2011) assume a static chemical composition in their protoplanetary disk simulations and find that a solar C/O ratio in atmospheres is expected for gas giant planet's formed through gravitational instabilities (i.e. formation through local isothermal or adiabatic disk dynamics) (Boss, 1997) or for core accreted planet's that form within the H_2O snowline. They also find that sub-solar C/O ratios (C/O$<$ 0.55) could indicate the pollution of a large amount of accreted icy solids following gas accretion through subsequent migration through the disk before dissipation and super-solar C/O ratios (C/O$\sim$ 1) could indicate the formation of the planet around the CO_2 and CO snowlines. Eistrup et al. (2018) follows on from this study showing that the expected chemical evolution of the protoplanetary disk through time, and thus the time evolution of the locations of the snowlines, is an important consideration when interpreting the chemical content and C/O ratios of exoplanet atmospheres.

Recent studies have started to determine these theoretical formation and migration scenarios with atmospheric observations. For example, Zhang et al. (2021) detected two isotopologues of CO in the atmosphere of the cool giant planet TYC 8998 b and constrained a relatively low $^{12}CO/^{13}CO$ abundance which is consistent with formation beyond the CO snow line in the protoplanetary disk. Line et al. (2021) were able to precisely constrain a solar C/O and a sub-solar (C+O)/H atmospheric ratios from the constraints on the abundances of water and CO in the atmosphere of the hot Jupiter WASP-77A b. This is suggestive of a planet that has not migrated through the protoplanetary disk and is depleted in carbon bearing species. Giacobbe et al. (2021) were able to simultaneously detect five species in the atmosphere of the hot Jupiter HD 209458 b and constrained a C/O ratio close to unity, thus suggesting that the planet may have formed between the H_2O and CO_2 snowlines and migrated inwards to its current 0.047 AU orbital separation. This shows the importance of detecting and constraining the abundances of the predominant minor species, H_2O, CO, CH_4 and CO_2 in the atmospheres of exoplanet's. For example, the absence of observable H_2O in a hot Jupiter atmosphere could be indicative of a planet with a super-solar C/O ratio (e.g. Pelletier et al., 2021) that has possibly formed beyond the water snowline and subsequently migrated inwards, however, this will depend on the presence of further species in the atmosphere as shown in Giacobbe et al. (2021).

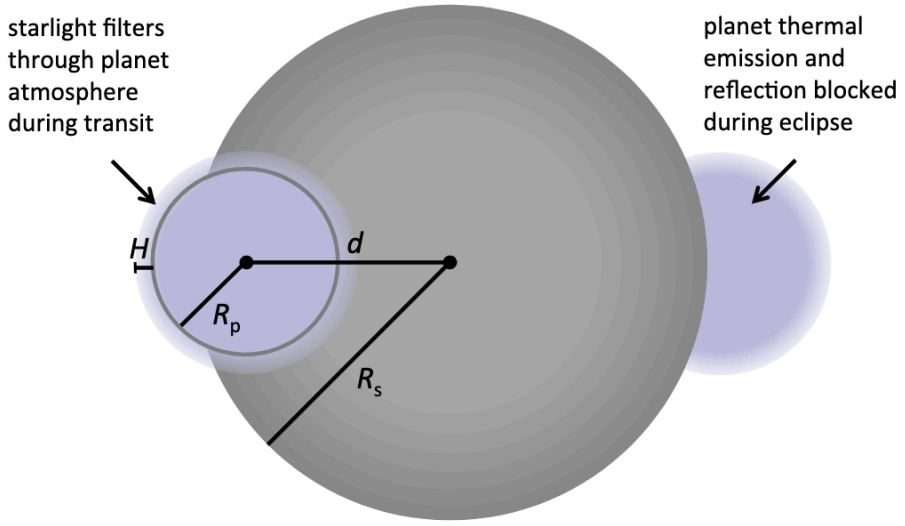

Figure 1.8: Schematic of the geometry of transmission, secondary eclipse and emission spectroscopy. During transmission the starlight is filtered through the atmosphere at a scale height dependent on the optical depth, emission is observed as the radiation being emitted directly from the planet before secondary eclipse (star eclipses the planet). Figure taken from Kreidberg (2018) which was adapted from Robinson (2017).

1.4.3 Transmission spectra

The first atmospheric detection from an exoplanet came soon after the first photometric transit detection, with the use of the STIS instrument ($R = \frac{\lambda}{\Delta\lambda} = 5540$) on the HST. Charbonneau et al. (2002) targeted the same transiting hot Jupiter, HD209458 b, to observe an additional dimming in the transit light curve as a function of wavelength, this is known as transmission spectroscopy. This occurs as the stellar light effectively filters through the planet's atmosphere, this stellar light may have some additional absorption and/or scattering depending to the chemical composition. Due to this geometric effect, transmission spectra primarily constrains the atmosphere at the day-to-night terminator regions (i.e. at the start and the end of the transit), see Figure 1.8 for an illustration of this effect.

The extra dimming effect from the exoplanet atmosphere takes the form (Brown, 2001);

$$\Delta_{\text{atmosphere}} = \frac{R_{\text{P}} H}{R_\star^2}. \tag{1.5}$$

H is the effective scale height of the atmosphere of which is determined by $k_b T/\mu g$

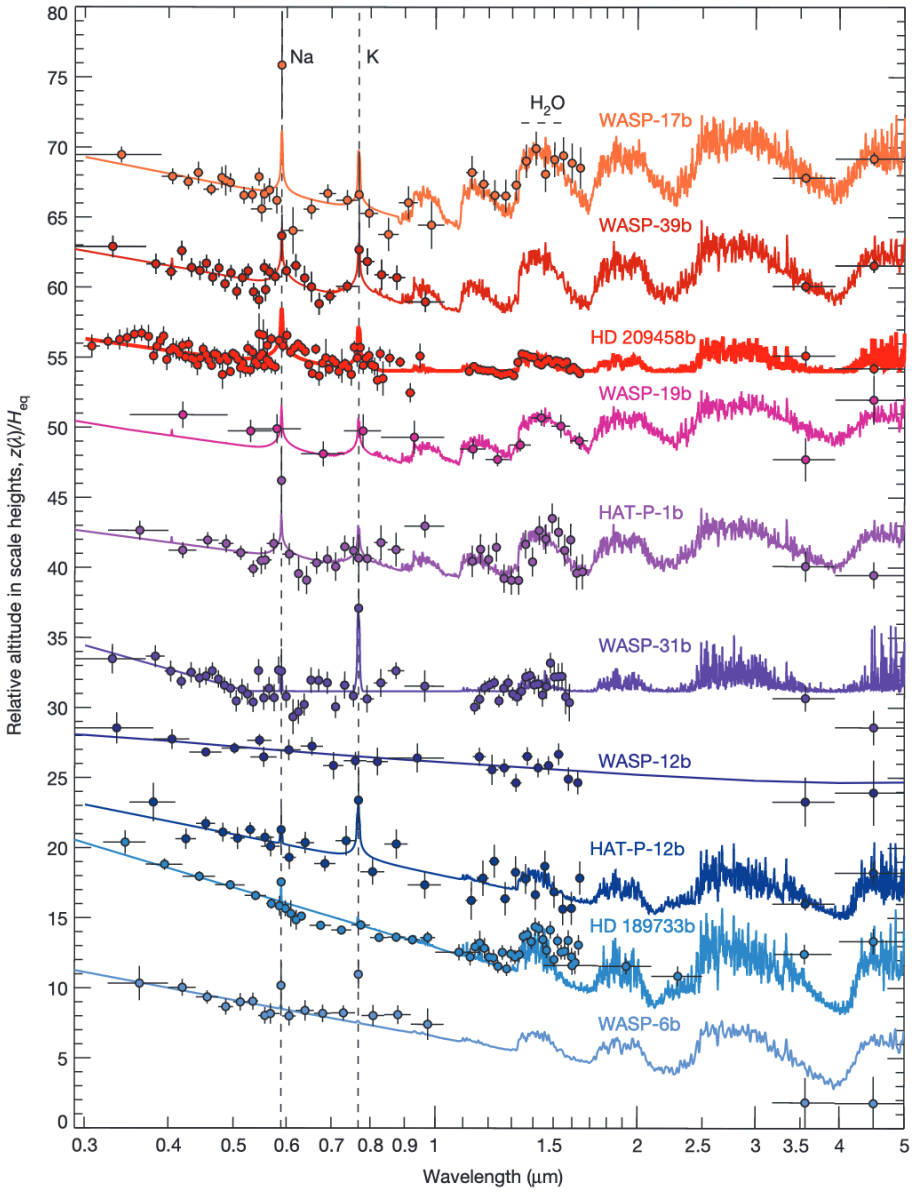

Figure 1.9: A survey of transmission spectra taken with HST of 10 hot Jupiters from the optical to the IR. The data-point show the binned spectral channels from the HST data and the solid lines show the best-fitting atmospheric model fit to the data. This indicates the variety of physical parameters and/or the chemical content for these atmospheres. Figure taken from Sing et al. (2016).

(Seager, 2010), where k_b, T, μ and g is the Boltzmann constant, temperature, the molecular weight of the atmosphere and the surface gravity, respectively. Therefore, to make the scale height larger, and thus more observable, the atmospheric temperature needs to be high with a low molecular weight, i.e. an atmosphere dominated by lighter species. This is true for the hot, gas giant planet's such as the hot or ultra-hot Jupiters ($T \geqslant 1000\,\mathrm{K}$) that have atmospheres predominantly made of H/He. This makes these planet's the most ideal laboratories for follow up studies on their atmospheres with current technology and thus have been the most studied exoplanet's to date.

At certain wavelengths, the atmosphere will appear more opaque or transparent dependent on the temperature, chemical composition and relative elemental abundance ratios such as the C/O ratio. Therefore, the altitude at which the atmosphere becomes optically thick will vary as a function of wavelength resulting in the characteristic peaks and troughs in a transmission spectrum (see Figure 1.9). As a result, a transmission spectrum allows for the temperature, the chemical composition and their abundances to be constrained. Figure 1.9 shows several examples of a typical transmission spectrum of an exoplanet. In this population study, Sing et al. (2016) analysed the transmission spectra of ten comparable hot Jupiters to show the variety of physical and chemical differences between their atmospheres. For example, some show strong water, Na and K features, whereas others appear to have muted or absent opacity features which could suggest the presence of an opacity deck such as clouds (e.g. Barstow et al., 2014) or hazes that scatter the light (e.g. Gao et al., 2021).

Despite hot Jupiters being the most amenable planet's for atmospheric characterisation, some cooler and smaller Neptune-sized planet's have been observed, typically through the detection of water in transmission (Fraine et al., 2014; Wakeford et al., 2017; Benneke et al., 2019; Tsiaras et al., 2019). However, smaller terrestrial planet's have thus far only reliably shown flat, or featureless, spectra (e.g. Kreidberg et al., 2014; Diamond-Lowe et al., 2018; Libby-Roberts et al., 2020), which could be due to clouds and/or have atmospheres with high mean molecular weights (i.e. dominated by chemistry other than hydrogen). For terrestrial planet's with higher mean molecular weight atmospheres, the scale heights will thus be much smaller than those of the hot Jupiters making these targets particularly difficult to characterise.

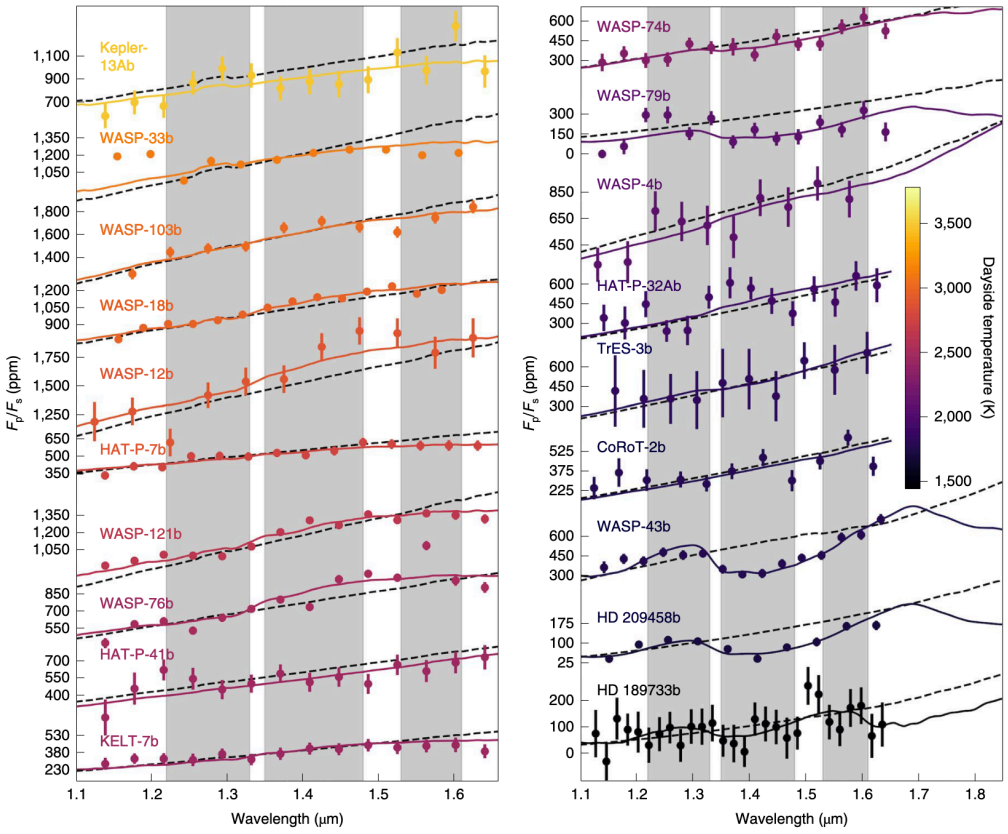

Figure 1.10: Thermal emission spectra from several hot Jupiters around the prominent water feature at 1.4 μm using the G141 grism on the HST. The spectra are ordered from the hottest day-side temperatures (top, left-hand plot) down to the coolest (bottom, right-hand plot). Figure taken from Mansfield et al. (2021).

1.4.4 Secondary eclipse and emission spectra

Observing the thermal emission is an alternative method of constraining the atmosphere of an exoplanet. Unlike transmission spectra, an emission spectrum (or emergent spectrum) is a direct observation of the emitted light from the atmosphere relative to the stellar flux, $F_{\rm P}/F_\star$. This is also illustrated in Figure 1.8. Typically, this emission is observed just before the planet passes behind it's host star (if transiting) known as the secondary eclipse, or when the day-side of the planet is facing the observer at $\phi \sim 0.5$ for non-transiting planet's (see section 1.4.5 and Figure 1.11). For transiting systems, the secondary eclipse depth is of the form,

$$\frac{F_{\rm P}}{F_\star} = \frac{R_{\rm P}^2 B(T_{\rm P}, \lambda)}{R_\star^2 B(T_\star, \lambda)}, \tag{1.6}$$

where B represents the blackbody functions for the star and planet which is a function of T and λ, which is the temperature of the planet and wavelength, respectively. Therefore, secondary eclipse photometric observations can give an accurate measurement of the temperature of the planet. For example, Deming et al. (2005b) measured a temperature of $\sim 1130\,\mathrm{K}$ for HD209458 b with the Spitzer space telescope at $24\,\mu$m, this provided the first evidence of irradiation heating from an exoplanet host star. Charbonneau et al. (2005) around the same time used the IRAC photometric instrument on the Spitzer space telescope to determine the day-side temperature of $\sim 1060\,\mathrm{K}$ for the hot Jupiter TrES-1b.

Observing the emission spectrum of an atmosphere allows for the temperature structure with pressure (e.g. Stevenson et al., 2014), i.e. the T-p profile, to be constrained as the emitting radiation forms in the deeper layers of the atmosphere ($p \sim 1\,\mathrm{bar}$) before filtering through the upper layers. This is in contrast to transmission spectroscopy which constrains only the upper atmospheric layers as it only probes the terminator regions of the planet. Typically, the emission is observed at IR wavelengths rather than optical wavelengths as the contrast ratio between the planet-to-stellar fluxes are at their highest levels. Hot and ultra-hot Jupiters are so strongly irradiated (Guillot et al., 1996; Seager and Sasselov, 1998) that they have typical IR contrast ratios of $F_{\rm P}/F_\star \geqslant 10^{-4}$ which is detectable with current instruments.

Figure 1.10 shows NIR emission spectra from nineteen hot Jupiters with a range of day-side temperatures (indicated by the colour scheme) from Mansfield et al. (2021). This study aimed to produce an emission population study similar to that of Sing et al. (2016) with transmission spectra. By studying the strength, or absence, of water opacity around $1.4\,\mu$m, they show a trend with the planet

temperature, typically water is seen in emission or absent at $T_{\rm P} > 2000\,{\rm K}$ and in absorption at $T_{\rm P} < 2000\,{\rm K}$. However, they do find some scatter around this general trend which again highlights the diversity in the C/O ratio and metallicity of hot Jupiter atmospheres.

Alongside these methods of atmospheric characterisation, there are a small number of direct molecular detections from directly imaged planet's. Similar to emission spectroscopy, direct imaging probes deeper into these atmospheres and enables higher SNR detections (Morley et al., 2015) as the host stellar light is effectively blocked out with a coronagraph. As such, there have been hints of chemistry in these atmospheres, e.g. H_2O (Barman et al., 2011), NH_3, C_2H_2 and CO_2 (Oppenheimer et al., 2013) in the HR 8799 system (Marois et al., 2008, 2010), that have been typically very difficult to detect with other methods. As this method relies on the observation of objects with substantial latent heat of formation rather than irradiation from the host star, much cooler objects have been characterised in this way. A mid-IR spectrum (Skemer et al., 2016) of the cold brown dwarf WISE 0855 ($\sim 250\,{\rm K}$) (Luhman, 2014) showed the presence of water vapour and clouds similar to the spectrum of Jupiter but without enhanced PH_3 as seen in Jupiter's atmosphere. As directly imaged planet's are typically at large orbital distances and are young systems, this method can provide unique insights into the composition of these planetary atmospheres soon after their formation. However, due to the complexities of the instrumentation and various analysis techniques (e.g. Marois et al., 2006) required to directly image sub-stellar objects, it is typically much more challenging to characterise planetary atmospheres and thus only a handful of systems have been directly observed in this way.

1.4.5 High resolution spectroscopy

With the first detection in 2010 using high resolution spectroscopy (HRS) by Snellen et al. (2010), HRS with the cross-correlation method (HRCCS) is one of the most recent techniques in the arsenal in the characterisation of exoplanet atmospheres. The earliest attempts to use high resolution ground-based spectrographs to observe exoplanet atmospheres were to find reflected optical light from the giant, non-transiting hot Jupiter τ Boötis b (Charbonneau et al., 1999; Collier Cameron et al., 1999). τ Boötis b was soon targeted again (Wiedemann et al., 2001) in observations with the high resolution CSHELL spectrograph ($R \approx 30,000$) (Greene et al., 1993) with the aim to detect the CH_4 opacity source at $\sim 3.3\,\mu$m, however, only an upper limit could be determined. Further searches were made for CO in HD209458 b (Brown et al., 2002; Deming et al., 2005a) with NIRSPEC/Keck ($R \approx 25,000$) (McLean

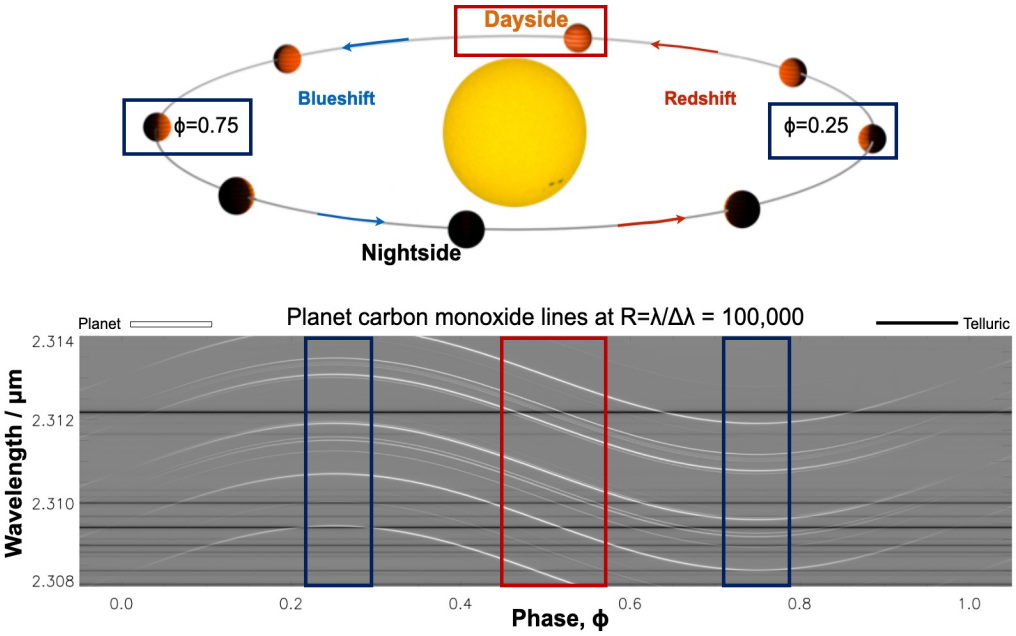

Figure 1.11: star-planet schematic showing how the spectral lines shift in wavelength as a function of phase. The red outlines the day-side emission and the maximally moving planet lines (in white) compared to the telluric lines (in black) at high resolution. The alternative method of observing the stationary but maximally separated planet lines from the telluric and stellar lines is outlined in blue. Figure adapted from Birkby (2018).

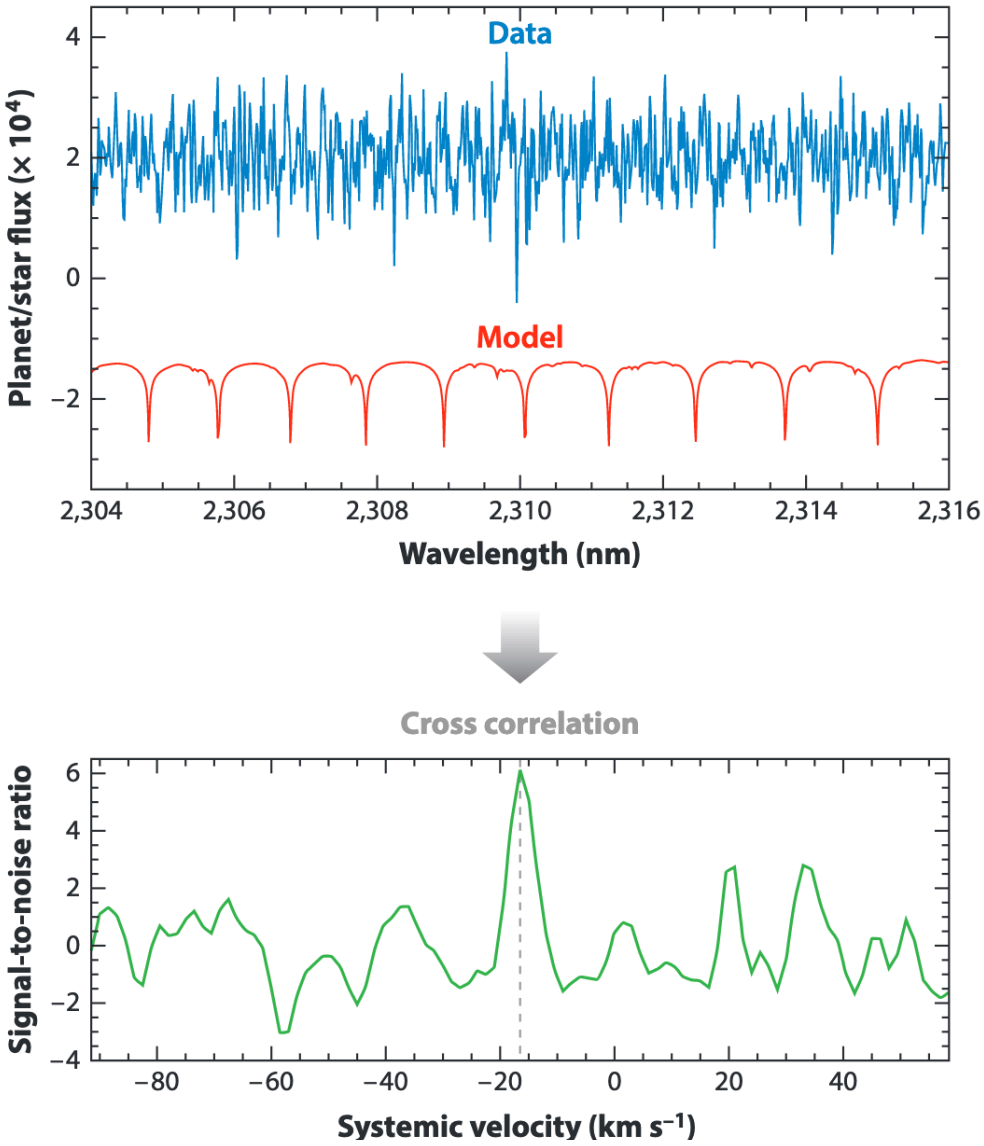

Figure 1.12: Typical cross-correlation function as a function of the systems systemic velocity (bottom in green). This is a result from the noisy telluric corrected observed spectrum in blue cross-correlated with a model spectrum in red. Figure taken from Heng and Showman (2015).

et al., 1995) and also in HD75289 b (Udry et al., 2000) with the Phoenix spectrograph ($R \approx 50,000$) (Hinkle et al., 2003) on Gemini South, again, with only upper limits were found for atmospheric CO (Barnes et al., 2007).

Similar to the radial velocity method of detecting exoplanet's (see section 1.2.1), HRCCS typically uses the Doppler shift of spectral lines from the planet's atmosphere to determine the orbital motion from that body from a time series of observations. This is usually done when the planet velocity is maximally changing compared to the Earths atmosphere (tellurics) and the star (i.e. $\frac{dV_P}{dt} \gg \frac{dV_\star}{dt}$). This occurs at phases $\phi \sim 0$ and 0.5 which can be seen in Figure 1.11 on the night-side and day-side positions of the planet on its orbit. For a transiting planet an orbital phase of $\phi = 0$ and 0.5 are positions of mid-transit and mid-secondary eclipse. For non-transiting planet's, orbital phases of $\phi = 0$ and 0.5 are instead considered the inferior and superior conjunctions (or the night-side and day-side) of the planet, respectively. Furthermore, the "quadrature" positions of the planet can be seen at phases $\phi = 0.25$ and 0.75 where the stellar (and telluric) lines are maximally shifted from the planet's spectral lines. Figure 1.11 highlights how the planet's spectral lines around the day-side of the planet are shifting across in wavelength from the quasi-stationary telluric features in the spectrum. This technique can also be used on transiting planet's during transit as the change in radial velocity will also be large around $\phi \sim 0$, however, stellar effects need to be carefully corrected for when searching for species that are in common between the planetary and stellar atmospheres (e.g. Chiavassa and Brogi, 2019). For planet's with NIR observations around hot stars at high resolutions, the stellar effects can often be neglected due to the stellar atmosphere containing relatively few/ weak molecular lines in their spectra and will thus be removed effectively in the telluric removal process. However, for observations in the optical, or NIR observations around M-dwarfs, the stellar effects need to be carefully removed from the observed spectra in order to prevent stellar contamination in the final analysis. This is particularly important when searching for elementary metals in ultra-hot Jupiters (e.g. Hoeijmakers et al., 2020) and CO in the NIR wavelengths (e.g. Brogi et al., 2016). From equation (1.2), for planetary masses, the radial velocity semi-amplitudes will typically be much greater than those of the host stars. This can reach hundreds of $\mathrm{km\,s^{-1}}$ for a typical hot Jupiter such as τ Boötis b or HD209458 b compared to the stellar radial velocity on the order of tens of $\mathrm{m\,s^{-1}}$. A comprehensive review of the methodology of HRCCS is given in chapter 2.

The most challenging aspect of using ground-based high resolution spectrographs to observe the atmospheres of exoplanet's is successfully isolating the planet's

spectral lines that are overwhelmed by the stellar and telluric lines. In the case of observing the maximum Doppler shift around transit or day-side emission, the telluric lines are typically removed using a custom pipeline that measures the depth variations in the telluric lines as a function of time that are stationary in wavelength (see Figure 1.11). However, the planet lines are shifting in time and wavelength and are thus largely unaffected by the telluric corrections. Section 2.5.2 gives a more detailed discussion on this method. Typically, the stellar effects are also removed with the telluric corrections, however in transmission, the Rossiter-McLaughlin effect (Rossiter, 1924; McLaughlin, 1924) will produce time-varying spurious signals in the planet's spectrum that need to be carefully corrected for (e.g. Brogi et al., 2016). For stable sites with typically low atmospheric precipitable water vapour (PWV) such as Paranal, the varying airmass of the observations will be the dominant driver of the telluric variations (Brogi et al., 2012; Brogi et al., 2013, 2014). There will be additional variations in the PWV and atmospheric seeing among other various observing and instrumental factors that are also corrected for. Other approaches to correct for tellurics include modelling the telluric spectrum (for example, the fitting code MOLECFIT (Smette et al., 2015; Kausch et al., 2015)) which can then be divided out of the spectra (e.g. Rodler et al., 2012; Allart et al., 2017), or using so-called blind algorithms such as Singular Value Decomposition (SVD) (Kalman, 1996), Principle Component Analysis (PCA) (Pearson, 1901; Hotelling, 1936) or the SYSREM algorithm (Tamuz et al., 2005; Mazeh et al., 2007). Each of these algorithms sorts the input matrix (in this case the spectra along the time axis) into their principle components, which can be thought of as the variables that contain the most variance within the data. As the planet's lines are moving significantly across the detector in time, these algorithms will avoid fitting the variance in the observed planet lines and instead on the stationary telluric and stellar lines. This is perhaps the most commonly used method with several successful detections, particularly in the NIR (e.g. de Kok et al., 2013; Birkby et al., 2013, 2017; Piskorz et al., 2017; Giacobbe et al., 2021; Line et al., 2021).

Despite the successful removal of the dominating telluric and stellar effects, the planet's spectrum is still well-hidden within the noise of the corrected spectrum. Therefore, in order to increase the SNR of the planet's Doppler shifted signal, all the resolved spectral lines need to be co-added in time and wavelength by cross-correlating with a model atmospheric spectrum. This is illustrated in Figure 1.12 as a function of the planet's velocity. Typically, a grid of 1D model spectra (see section 1.4.1 for details on how these are calculated) are used as a representation of the real underlying planet spectrum and the "best-fitting" spectrum is chosen by

maximising the CCF (e.g. Brogi et al., 2014). More recently, Flowers et al. (2019) and Beltz et al. (2021) were able to better constrain the planet's signal in the CCF with the use of 3D GCM modelling techniques that take into account the varying 3D dynamics from winds and line of sight effects which produce detectable differences in the line shapes with HRS (see the various T-p profiles assuming 3D effects in Figure 1.5).

There is an alternative technique with HRS that instead observes the planet's spectral lines when they are maximally separated from the stellar and telluric lines. This occurs then the planet is at quadrature ($\phi \sim 0.25$ and 0.75) and $\frac{dV_{\rm P}}{dt} \approx 0$ (see Figure 1.11). For this technique to work for fast moving planet's such as hot Jupiters, a lower resolution spectrograph (e.g. $R \approx$25,000) is used with only a few hours of observations per night to prevent smearing of the planet's signature across several pixels on the detector (Lockwood et al., 2014). This is in contrast, but complementary to the technique typically used in HRCCS (e.g. Snellen et al., 2010; Brogi et al., 2012; Birkby et al., 2013) as this could be used for example on slowly moving, non-transiting and potentially habitable terrestrial planet's. This alternative method has been particularly successful in detecting water vapour in the emission spectra of non-transiting hot Jupiters (Lockwood et al., 2014; Piskorz et al., 2016, 2017; Buzard et al., 2020). Piskorz et al. (2018) also used this technique of short multi-epoch HRS observations, combined with low resolution Spitzer observations to constrain the properties of the atmosphere of the transiting hot Jupiter KELT-2A b. However, this methodology is not the subject of this thesis but is discussed briefly in chapters 2.5.2 and 5.

HRS has been particularly successful in unambiguously detecting the chemical content of exoplanet atmospheres in the optical (e.g. Hoeijmakers et al., 2019; Kesseli et al., 2022) and NIR (e.g. Giacobbe et al., 2021). Using HRS, these species have been significantly detected (typically $> 4\,\sigma$); Na (e.g. Snellen et al., 2008), CO (e.g. Snellen et al., 2010), Hα (e.g. Jensen et al., 2012), H_2O (e.g. Birkby et al., 2013), TiO (e.g. Nugroho et al., 2017), He (e.g. Nortmann et al., 2018), HCN (e.g. Hawker et al., 2018), Fe/Fe+/FeII (e.g. Hoeijmakers et al., 2018a; Prinoth et al., 2022; Bello-Arufe et al., 2022), Ti/Ti+ (e.g. Hoeijmakers et al., 2018a; Prinoth et al., 2022), K (e.g. Keles et al., 2019), Ca II/Ca+ (e.g. Casasayas-Barris et al., 2021; Turner et al., 2020), Cr (e.g. Ben-Yami et al., 2020), V (e.g. Ben-Yami et al., 2020), Mg (e.g. Kesseli et al., 2022), OH (Landman et al., 2021), CH_4 (e.g. Guilluy et al., 2019), C_2H_2 (Giacobbe et al., 2021), NH_3 (Giacobbe et al., 2021), Li (e.g. Kesseli et al., 2022), Mn (e.g. Kesseli et al., 2022), Ni (e.g. Kesseli et al., 2022), Sr II (Kesseli et al., 2022), Co (Kesseli and Snellen, 2021), Si (Cont et al., 2022), O (Borsa et al.,

2021) and CO_2 (Carleo et al., 2022). This is not an exhaustive list of the detected species and references using HRS which is a quickly evolving field. Whereas, at low resolution, primarily using the HST and ground-based facilities, arguably, only Na (e.g. Charbonneau et al., 2002), K (Wilson et al., 2015), He (Spake et al., 2018) and H_2O (e.g. Wakeford et al., 2013) have been detected confidently ($> 4\,\sigma$) thus far. However, with the upcoming results from the JWST, this will likely change in the next few years (for example a recent detection of CO_2 from The JWST Transiting Exoplanet Community Early Release Science Team et al. (2022)). It should also be noted that only a handful of species detected using HRS have measured abundances thus far.

The reason for the large number of detections at high resolutions is because the forest of spectral lines are individually resolved and are unique to each species. This is in contrast with low resolution observations that are typically only able to resolve broad band features that could be attributed to different species, or even uncorrected instrumental errors (e.g. Gibson et al., 2011). Although the resolution needs to be high enough to resolve the individual spectral lines in HRS, there is a delicate trade-off with the SNR and resolution of the observations. This is because the SNR of the final combined CCF scales with the number of resolved spectral lines (which increases with increased resolution, see section 2.6.3). However, increasing the resolution will also decrease the SNR per resolution element which can make detecting species difficult if the noise of the observations cannot be corrected for at the appropriate level (see section 2.5.2). van Sluijs et al. (2022) proved that HRCCS could be done on spectra with measured resolutions as low as $R \approx 15,000$ with a strong phase resolved detection of CO in the atmosphere of the ultra-hot Jupiter WASP-33 b.

Beyond constraining the chemical content, HRS has been successful in constraining further chemical and physical properties of atmospheres such as; spatially resolved winds (Louden and Wheatley, 2015), line broadening due to winds (e.g. Seidel et al., 2020) and rotation (Snellen et al., 2014), chemical phase asymmetries (e.g. Ehrenreich et al., 2020; Kesseli and Snellen, 2021; Sánchez-López et al., 2022; Gandhi et al., 2022), constraints on the metallicity (e.g. Giacobbe et al., 2021), C/O ratio (e.g. Line et al., 2021) and non-local thermodynamic equilibrium (LTE) effects (e.g. Fossati et al., 2021; Borsa et al., 2021). Thermal inversions have also been measured using HRCCS by observing the emission lines from molecules in the NIR (e.g. Nugroho et al., 2017) or metal emission in the optical (e.g. Hoeijmakers et al., 2020) in ultra-hot Jupiter atmospheres.

From the direct detection of the spectral lines from the planet, the system can

now be considered a spectroscopic binary for which the mass and inclination can be determined via Kepler's third law (see chapters 3.9 and 4.8), assuming knowledge of the mass of the host star. This is a particularly powerful technique for non-transiting planet's (e.g. Brogi et al., 2012; Rodler et al., 2012) that have a degeneracy between the inclination and mass from the stellar radial velocities. However, it is crucial that the stellar mass, semimajor axis and systemic velocities have up-to-date, accurate and precise values otherwise the retrieved atmospheric properties could become inaccurate (see chapter 4.8).

More recently, new Bayesian techniques to analyse high resolution spectra (Brogi and Line, 2019; Gibson et al., 2020) can be used on the phase resolved data to retrieve statistically robust and precise orbital velocities, T-p profiles, chemical abundances, atmospheric scaling parameters (Pelletier et al., 2021; Nugroho et al., 2021; Gibson et al., 2022; Gandhi et al., 2022) among other parameters depending on the complexity of the modelling. Among this, HRCCS has also been combined with other complementary techniques such as high contrast imaging (Snellen et al., 2014, 2015) and low resolution spectra from HST (Brogi et al., 2017) and Spitzer (Piskorz et al., 2018) to place better constraints on the physical and chemical properties of the atmosphere.

1.5 Thesis outline

In this thesis, I analyse high resolution NIR observational and simulated data in the characterisation of exoplanet atmospheres. I cover the methodology and analysis techniques used throughout this thesis in chapter 2. In chapter 3, I present the work which has been published in Webb et al. (2020) that covers the detection of water vapour in absorption from the day-side thermal emission spectra of the non-transiting hot Jupiter HD 179949 b using the high resolution instrument CRIRES at 3.5 μm. In chapter 4, I present the published work from Webb et al. (2022) which covers the detection of water vapour in the day-side thermal emission spectra of the non-transiting hot Jupiter τ Boötis b using the NIR arm of high resolution spectrograph CARMENES. In chapter 5, I outline the unpublished work on the high resolution simulations of an Earth-twin around two late type M-dwarf systems. This final study analyses the detectability of an Earth-like atmosphere in these systems using a high resolution spectrograph with a simultaneous spectral coverage of 0.96-2.7 μm on the 3.9 m ELT. Finally, I summarise the results and conclusions from each of these studies in chapter 6.

Chapter 2

Methods and techniques

2.1 High resolution spectrographs

Spectroscopy is the study of absorption or emission lines from some object that contains some opacity source or sources. These spectral lines, depending on line shape and on the continuum flux, can then be used to study the chemical content, abundances, ionisation and temperatures among other physical effects. Spectroscopy involves splitting up the light into its constituent wavelength components. The measured changes in absorption/emission wavelengths can be used to determine the radial velocity of a moving object due to a shift from the rest-frame wavelength (as discussed in chapters 1.2.1 and 1.4.5).

In the following sections, I briefly describe how the light received from the telescope is split up using spectroscopy and how high resolutions are achieved.

2.1.1 Optical set-up

Firstly, the incoming light usually enters the spectrograph onto a slit or a set of fibres which is then collimated to produce a parallel wavefront ready to enter a diffraction grating. Figure 2.1 is a schematic for a typical blazed diffraction grating that is often used in spectroscopy.

The incoming light is split up into its component wavelengths with the use of a diffraction grating. The diffraction grating is a periodic structure of "grooves" on a reflective surface, this is a ruled grating, however, there are different types such as a transmission grating which instead has hollow slits on its surface. Assuming a plane wave of incident monochromatic light of wavelength λ, we can create the general grating equation of $m\lambda = d(\sin\theta' + \sin\theta)$, where θ and θ' describe the angle of the incident light to the grating normal and the angle of the diffracted light to the

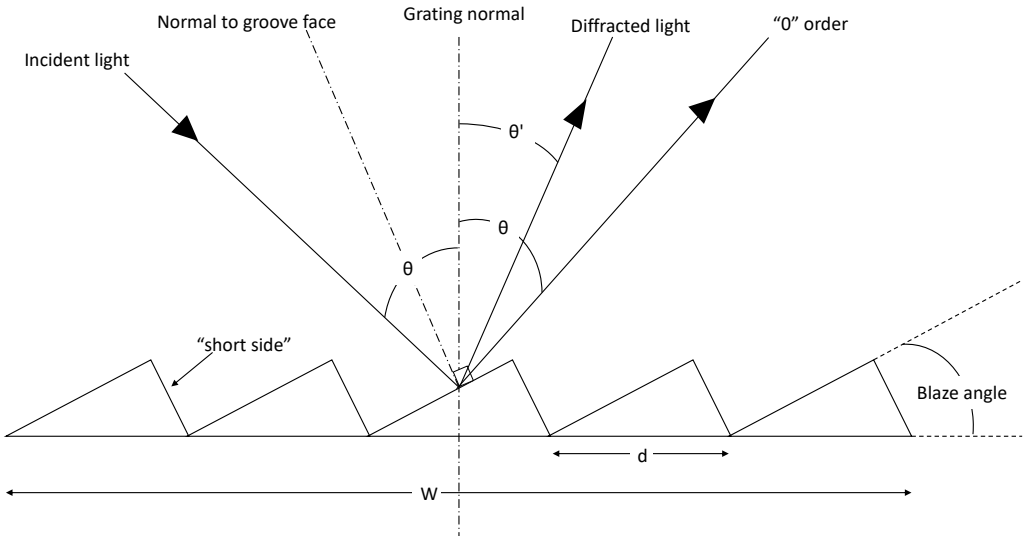

Figure 2.1: Schematic of a typical blazed plane diffraction grating used in spectroscopy. A type of blazed plane diffraction grating is an échelle spectrograph which is used in high resolution spectroscopy where the "short side" is used instead to achieve blaze angles greater than 45°.

grating normal, this is shown in Figure 2.1. m is just an integer which represents the "order" number. The spectral orders are separated out according to the angles at which the different wavelengths of light produce a constructive interference pattern.

In reality, the incoming wave of light from a ground-based telescope will not be an exact plane wave but will have been distorted due to the turbulence in the Earth's atmosphere. This effect reduces the throughput of the light into the spectrograph. To counteract this, adaptive optics (AO) systems will deform the mirror in real time to match the shape of the incoming light which decreases the seeing of the object (i.e. the size of the observed point source is reduced) and thus the SNR of the spectra increases as a result.

The "resolving power" of the grating is defined as the measure of its ability to spatially resolve two distinct wavelengths, by which itself is determined as the wavelength difference between the maxima and the minimum of the adjacent wavelength ($\Delta\lambda$, known as the Rayleigh criteria). This is calculated to be $R = \frac{\lambda}{\Delta\lambda} = \frac{2Nd\sin\theta'}{\lambda} = mN$ (Keliher and Wohlers, 1976), where $N = W/d$ and d refer to the number of grooves and the groove spacing, respectively. These variables are also shown in Figure 2.1.

Therefore, to achieve higher diffraction orders, an increased number of grooves,

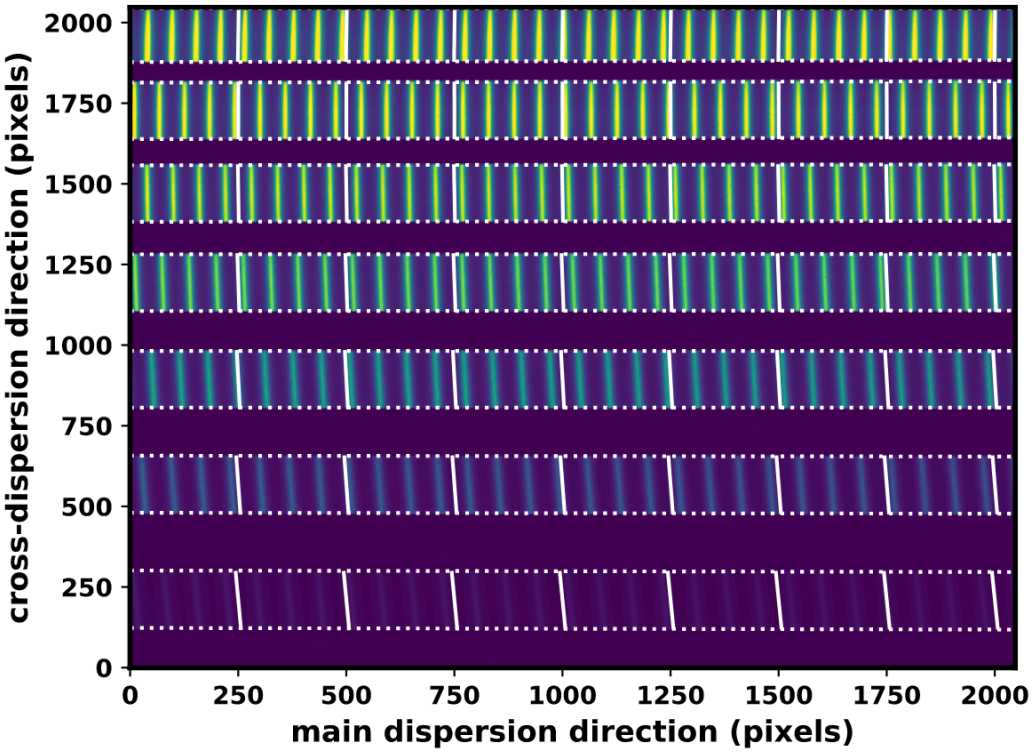

Figure 2.2: A raw cross-dispersed spectral image from a single CRIRES+ detector in the K-band. The x-axis shows the dispersion direction which contains the resolved wavelengths. The y-axis shows the cross-dispersed direction which images the individual spectral orders. The horizontal lines show the order tracing and the solid white lines represent the tilt of the slit image. Figure taken from Holmberg and Madhusudhan (2022).

or increased angle of incidence or diffraction can all produce greater spatial resolution in wavelength for use in high resolution spectroscopy. However, these methods all decrease the "free spectral range" which describes the upper and lower limits on the wavelength in the band of interest, leading to significant wavelength overlapping of these higher orders. The final instrument resolution is usually much lower than the grating resolving power as it also depends on various other optical properties of the full system.

2.1.2 Échelle spectrographs

Échelle spectrographs (Harrison, 1949; Harrison et al., 1952) have gratings designed for use in the higher spectral orders. They have a particular groove pattern, typically

in the shape of a saw-tooth (as shown in Figure 2.1), that allows for a high blaze angle (angle of the groove parallel to the surface) to achieve high resolutions without the need to increase the number of grooves. In order to separate the high orders due to the decrease in the free spectral range, an auxiliary dispersing element, which is usually a prism or a low dispersion grating, is placed at a right angle to the grating dispersion.

These multiple orders are then recorded onto a suitable detector. In spectroscopy, there are typically two dimensions that need to be imaged onto the detector. In long-slit spectroscopy, the image will contain a spatial direction along the slit and the dispersion direction which contains the resolved wavelength components of the light. In cross-dispersed spectrographs, the spatial direction becomes the cross-dispersion direction which separates out the individual orders. A typical 2D image from a cross-dispersed échelle spectrograph is shown in Figure 2.2 from the new CRIRES+ instrument on the VLT.

For optical spectra, the detectors are usually a silicon CCD which has a wavelength cut-off at 1.1 μm, whereas detectors with longer wavelength cut-offs are needed for the longer wavelengths in the NIR. A variety of materials can be used for IR detectors but some examples include Indium antimonide (InSb) which is used for the CRIRES detectors and Mercury cadmium telluride (HgCdTe) used on the CARMENES detectors. Due to the longer wavelength cut-offs with the NIR detectors, these detectors need to be cooled down to temperatures on the order of $\sim 100\,\mathrm{K}$ to prevent overwhelming thermal noise in the detector itself, whereas silicon CCDs can be operated at room temperature.

To prevent warping of the optical bench (i.e. expansion from heat where the optical components are placed onto), these high resolution spectrographs need to be housed in an ultra-stable vacuum chamber with a temperature stabilisation of $\sim \pm 0.01\,\mathrm{K}$ over a 24 hour period to prevent significant drifts in where the light falls onto the detector and thus the pixel-wavelength calibration will be inaccurate. For exoplanet atmospheric studies that rely on ultra-stable high resolution spectrographs to measure precise radial velocities, these detector drifts can indeed hamper or even prevent detections even on the sub-pixel level (Brogi et al., 2018).

In this thesis, spectra from two high resolution instruments were used in the two observational chapters 3 and 4. A brief description of each instrument is given in the following sections along with a description of the automated reduction and calibration pipelines.

2.2 CRIRES

The CRyogenic high resolution InfraRed Echelle Spectrograph (CRIRES) is an échelle high resolution instrument in the NIR at the VLT (8.2-m) in the Atacama desert at Cerro Paranal, Chile. The original CRIRES spectrograph ($0.92 - 5.2\,\mu$m) (Kaeufl et al., 2004), which has now since been decommissioned in 2014 and upgraded to CRIRES+ (Follert et al., 2014), was a single order, long slit ($40\,''$) spectrograph. Two entrance slit widths could have been chosen, $0.2\,''$ for the highest resolution of 100,000 or $0.4\,''$ for the lower 50,000 resolution setting.

The optical set-up for CRIRES only allowed for a narrow single spectral range of $\sim 1/70$ of the central wavelength (at $\sim 1\,\mu$m), the different wavelength settings could be chosen by tilting the échelle grating. The upgraded CRIRES+ now includes a cross-dispersing element and larger detectors to broaden the observed wavelength coverage, however, only spectra from the original CRIRES set-up was used in this thesis (see chapter 3). The upgraded CRIRES+ was only available at the start of 2022 and thus could not be used in the context of this thesis. Despite the lack of wavelength coverage, CRIRES led the way for high resolution exoplanet atmospheric studies from its inception in the last decade (Snellen et al., 2010) until its eventual decommissioning.

As with most large ground-based telescopes, the VLT has an in-house adaptive optics (AO) system which corrects for the incoming plane wave distortions. For the VLT, this system is called the MACAO or the Multi-Applications Curvature Adaptive Optics (Arsenault et al., 2003) and is essential for the use in all HRCCS studies so as to increase the light throughput from the telescope into the spectrograph slit thus increasing the SNR of the observations. The observed spectrum was then recorded onto four 1024×4096 pixels Aladdin III array detectors which had inter-detector separations of 283 pixels.

As CRIRES is a long slit spectrograph, for sky subtraction, typically the spectra are taken in an ABBA nodding pattern along the slit where the A and B positions are of the science object and the sky, respectively. Therefore, spectra are typically taken as follows: science frame (A) first, followed by a sky frame (B), and then to reduce nodding times, another sky frame is taken (B), then the telescope will slew back to take another science frame (A), finally another science frame is taken (A). This routine is then repeated throughout the observing night to take an equal amount of science and sky frame pairs. These frames are then filtered through the automated pipeline for CRIRES which is described further below.

2.2.1 The CRIRES pipeline

As with all raw telescope images, they need to be corrected from various detector effects such as dark current, hot/ dead pixels, non-linear effects and pixel-to-pixel sensitivity variations with dark and flat field frames.

For every scientific telescope observing run, there will contain a set of scientific frames (images containing the object of interest) and some calibration frames; bias, flat and dark frames, to correct for unavoidable noise features in the science images. Bias frames are images taken with zero exposure time to record the read-out noise of the detector when it reads the values of the pixels. Dark frames are images taken with no illumination on the detector to record the typical thermal noise produced by the detector for a particular exposure time. Therefore, the dark frames need to be taken with the same exposure time as the science frames. These frames also capture pixels whose sensitivity is too low (dead pixels) or too high (hot pixels). Finally, flat fields are taken by illuminating the spectrograph slit with a flat field lamp to correct for the wavelength dependent pixel-to-pixel sensitivities on the detector.

For CRIRES, the raw images are calibrated automatically using the calibration pipeline recipes[1] from `esorex`. At the VLT, usually the calibration frames are taken the morning after the observations were taken. Several calibration frames need to be taken and averaged in order to create a master calibration bias, dark and flat field. In the IR, detectors also need to be corrected for a non-linearity effect which is caused by a deviation from linearity conversion from charge to voltage in the detector. An additional so-called "odd-even effect" non-linearity effect which affects detectors 1 and 4[2] is also corrected for in the extraction of the final calibrated science frames. The correction is implemented automatically via a correction matrix provided by the CRIRES pipeline for the extracted frames. A flux calibration can also be done on the spectra, however, in HRCCS, the flux values are normalised in the analysis (see section 4.5) so a flux calibration is not necessary for these science frames.

A wavelength calibration is also done the morning after using a Th-Ar lamp, however, this calibration is not accurate enough for HRCCS work. Instead the wavelength calibration was calculated with the use of the measured telluric lines and the ESO skycalc telluric models (see section 3.5.1 for more details).

[1] `http://www.eso.org/sci/facilities/paranal/instruments/crires/doc/VLT-MAN-ESO-14200-4032_v93.pdf`

[2] `https://www.eso.org/sci/facilities/paranal/instruments/crires/doc/VLT-MAN-ESO-14500-3486_v93.pdf`

The final stage of calibrating the scientific spectra from CRIRES involves combining the A and B spectra using the CRIRES pipeline which removes the background emission from the spectra of the object of interest.

2.3 CARMENES

Unlike CRIRES, the Calar Alto high-Resolution search for M dwarfs with Exoearths with Near-infrared and optical Echelle Spectrographs (CARMENES) (Quirrenbach et al., 2014) is a fibre fed high resolution, cross-dispersed échelle spectrograph with a much wider simultaneous wavelength coverage at the 3.5-m Zeiss telescope at the Calar Alto observatory. The main science goal of CARMENES is to complete a radial velocity survey of M-dwarf stars that may host Earth-analogues, optimised for the mid-to-late type M-dwarfs (Quirrenbach et al., 2020). To this end, the optimal wavelength range for this work is in the optical to the NIR. As a result, the spectrograph is split into an optical ($0.520 - 0.960\,\mu$m) and a NIR ($0.96 - 1.71\,\mu$m) spectrograph due to the need to have separate detectors for each spectrograph. Each spectrograph have different resolutions of $R \sim 95,000$ and 80,000 in the optical and NIR, respectively. In this thesis, I only make use of the NIR spectrograph as described further in chapter 4.

As CARMENES is a cross-dispersed spectrograph, several spectral orders are imaged onto two 2048×2048 Hawaii-2RG detectors from the NIR arm. There are in total 28 orders that cover the $0.95 - 1.7\,\mu$m wavelength range which covers the Y-, J- and H-bands. These bands are particularly sensitive to opacity sources from H_2O, HCN, CH_4, NH_3 (e.g. Gandhi et al., 2020b) and the He triplet, which makes this instrument ideal for HRCCS atmospheric studies. This wavelength coverage does however exclude the prominent $2.3\,\mu$m CO feature which was one of the cornerstones for the first HRCCS observations with CRIRES (Snellen et al., 2010; Brogi et al., 2012).

There are 2 fibres that are fed into the spectrographs that can both be placed on sky, or alternatively one can be used for simultaneous wavelength calibration. However, this latter set-up is only necessary for $\sim \mathrm{m\,s^{-1}}$ precision radial velocity work. Instead for HRCCS, an accurate sky background subtraction is essential to remove any background contamination, therefore the second fibre is usually placed on the sky. As one of the two fibres is taking spectra of the sky background and the other is simultaneously taking spectra of the science target, there is no telescope nodding that takes place as with long slit spectrographs such as with CRIRES. This has the advantage of potentially taking more spectra of the science target over the

same time period on a typical observing night over long slit spectrographs.

2.3.1 The CARMENES pipeline

Similarly with CRIRES, the raw imaged spectra from CARMENES are first passed through an automated calibration and reduction pipeline called `caracal` (Caballero et al., 2016a).

After an observing block and spectral read-out, the science images are bias, dark, background subtracted and non-linearity corrected for similarly as in the CRIRES pipeline. However, for CARMENES spectra the 1D spectra are extracted from the 2D detector images using a flat-relative optimal extraction algorithm as described in Zechmeister et al. (2014). As the name suggests, this technique uses the flat field exposures as a measure of the instrumental profile and allows all the corrections of the spectra to be done in one step. This method significantly reduces computational time to model the instrumental profile. However, it is worth noting that this technique alters the units of the calibrated spectra thus making it impossible to determine the number of photon counts per pixel (or wavelength channel). This maybe an issue for certain astrophysical observations, however, in HRCCS the flux values are normalised in the data reduction process (see section 2.5.2) regardless so this is not an issue here. This extraction method requires that the instrumental profile does not change significantly over the course of the observations, i.e. the flat-fields are well-defined. Therefore, for a temporally stable instrument such as CARMENES, which was not the case for CRIRES, this algorithm is appropriate for use on these spectra.

The wavelength calibration in the NIR uses a U-Ne lamp and a Fabry-Pérot etalon which is accurate for use in HRCCS studies as there is no significant temporal shifts in the instrument over the course of the observations. The observed long term stability for data taken with the CARMENES instrument in the visible and NIR optics is stable to a radial velocity precision of $\sim 2\,\mathrm{m\,s^{-1}}$ (Quirrenbach et al., 2016; Bauer et al., 2020) over several months, including jitter from stellar variability.

2.4 Formatting the data for HRCCS work

Each calibrated spectrum comes in the form of a 2D array made up of the number of detectors by the number of pixels (i.e. $\mathrm{n_{detectors}} \times \mathrm{n_x}$). For pre-2014 CRIRES spectra, the 2D array is $\mathrm{n_{detectors}} \times \mathrm{n_x} = 4 \times 1024$. The number of pixels can also be thought of as the number of wavelength channels when the pixel to wavelength calibration is completed. For ease of use and reduced computational run times during the

analysis, at this stage the spectra are reformatted into a data cube that stacks all of the spectra into a time sequence from each observing night. Therefore, the final data cube will be of the form, $n_{detectors} \times n_{spectra} \times n_x$, the ordering of this data cube does not matter but needs to be consistent throughout the reduction and analysis pipeline. It should also be noted that if there are any significant time gaps in a observing night, it will be preferable to split the data cube up further into separate data cubes for each time interval to prevent discontinuities at the telluric removal stage of the analysis (see section 2.5.2). This would be the same as separating out the observing nights which are only combined after the data reduction stage (see section 2.5.2) and during the final cross-correlation analysis (see section 2.6.3).

The formatting of the NIR CARMENES scientific spectra were done in the same way as the formatting of the CRIRES spectra as described above, with the exception that $n_{detectors}$ is instead the number of spectral orders n_{orders} due to the fact CARMENES is a cross-dispersed spectrograph unlike the pre-2014 CRIRES spectrograph which only uses a single order. This will be the same when formatting the data cube for any high resolution spectrograph which is cross-dispersed. For CARMENES spectra in the NIR arm, the 2D data cube is $n_{orders} \times n_x = 28 \times 4080$.

2.5 Data reduction

2.5.1 Spectral alignment and wavelength calibration

Once the 1D spectra have been extracted and calibrated from the raw images through their respective pipelines, further cleaning needs to take place before they can be analysed. For spectra taken with less stable instruments such as the original CRIRES and GIANO (Oliva et al., 2006; Origlia et al., 2014), an alignment step is required to correct for temporal shifts in the observed spectral lines taken in the time sequence (Snellen et al., 2010; Brogi et al., 2012; Birkby et al., 2013; de Kok et al., 2013; Brogi et al., 2014; Birkby et al., 2017; Brogi et al., 2018; Guilluy et al., 2019; Giacobbe et al., 2021). There is also a description of this procedure that was required in chapter 3.5.1. For CRIRES, these temporal shifts from instrumental stability are on the order of a sub-pixel level (Birkby et al., 2013; Brogi et al., 2014) which are unlikely to cause large spurious radial velocity shifts in the analysis. However, if these are uncorrected for when calibrating the pixel-to-wavelength solution, then these temporal shifts may cause errors in the calibration at > 1 pixel and thus the planets signal will not co-add constructively due to large radial velocity shifts in the data. This was only required for the spectra taken with the pre-2014 CRIRES instrument and is described in section 3.5.1, however, a more general and in depth

explanation of the steps in this process is given below for spectra that need initial alignment.

1. A telluric model that with the same resolution and wavelength solution as the data is needed to cross-correlate or compare with the observed telluric spectra. This thesis made use of the online ESO sky calculator (Noll et al., 2012).

2. A "guess" wavelength solution to start with, i.e. this was taken to be the wavelength calibration produced in the pipeline. These calibrations should be calculated in vacuum, if they are not then the wavelength calibration needs to be converted from air to vacuum.

3. Decide on an appropriate wavelength solution for the instrument being used. For pre-2014 CRIRES and described in section 3.5.1, this was taken to be a second order polynomial.

4. Use a spline interpolation to fit the initial guess wavelength solution to the telluric model and correlate with the observed spectra per detector/order and spectrum. This will produce a data cube for the wavelength solution with the same dimensions as the spectral data cubes produced from section 2.4.

5. Find the optimal wavelength solutions by shifting the solution to maximise the above correlation per detector/order and spectrum, or alternatively convert the cross-correlation into a likelihood via (Zucker, 2003): $\log(L) = -\frac{N}{2}\log(1 - \mathrm{CCF}^2)$, where N and CCF are the number of pixels used in the cross-correlation and the cross correlation function, respectively.

6. Produce an average wavelength solution in time per detector/order and spline interpolate all the spectra to that solution, i.e. the wavelength solution should now be fixed in time and therefore has dimensions of $\mathrm{n}_{\mathrm{detectors/order}} \times \mathrm{n}_{\mathrm{x}}$.

7. As a final step, the now wavelength calibrated and aligned spectra and wavelength solution should be re-grid onto a constant $\Delta\lambda/\lambda$ grid.

By converting the cross-correlation in step 5 to the likelihood using the relationships from Zucker (2003) allows the use of Bayesian techniques to determine the wavelength solution. For example, in chapter 3.5.1, this likelihood function is used to drive MCMC chains that converge onto a new wavelength solution. This has the advantage of being able to determine the error in the new wavelength calibration for each set of observations.

For ultra-precise spectrographs such as CARMENES (and ESPRESSO, SPIRou etc.), an initial alignment and subsequent wavelength calibration is not required as the observed telluric lines will fall on the same pixel on the detector over a nights set of observations and thus the wavelength calibration for these instruments will be accurate enough for HRCCS analysis. It should be noted that if a high resolution instrument is not stable enough on the sub-pixel level over a nights set of observations, as is sometimes the case of slit-fed spectrographs such as CRIRES(+) and GIANO, then these temporal shifts in the data can ultimately lead to a non-detection of a planets spectrum. For example, Brogi et al. (2018) observed a water feature in the transmission spectrum of the hot Jupiter HD 189733b during a stable night with the GIANO spectrograph (drifts < 0.1 pixel), however during a less stable night with temporal drifts of > 0.1 pixel, this was attributed to the non-detection of the water feature during this night. Ideally for any HRCCS analysis to work effectively, the most stable instruments should be used in order to avoid any inaccuracies at the spectral alignment and wavelength calibration stage that may lead to non-detections of the planet spectrum.

The most crucial step in the processing of ground-based high resolution data is the extraction of the planetary lines from the host stellar and telluric spectra. For HRCCS, this is usually done in a non-standard way which is outlined below.

2.5.2 Removal of spectral contaminants

As these observations are taken with ground-based instruments, we need a way to accurately remove all spectral contaminants which include the host stellar and telluric lines. As the typical hot Jupiter atmospheric spectrum is at a planet-star contrast of $\sim 10^{-4}$, the planets spectral lines are well-hidden within the noise of the observed spectra, i.e. the SNR per line is $\ll 1$. The planet-star contrast is similar in magnitude to the planet-telluric contrast as the Earths atmospheric throughput in the IR is much greater than at optical wavelengths. Therefore, we need an accurate way of removing the contaminants close to the photon noise limit of the data (Brogi et al., 2014) without removing significant information from the underlying planet spectrum. In order to do this, we exploit the fact that the telluric and stellar lines are (quasi-)stationary ($\sim \mathrm{m\,s^{-1}}$, see section 1.2.1) in wavelength during an observing night, whereas a typical hot Jupiter can shift on the order of tens of $\mathrm{km\,s^{-1}}$, therefore shifting across several resolution elements of the spectrograph.

Typical telluric removal techniques observe an A-star during the observations which can be used as an accurate telluric template to correct the science frames. However, in the interests of gaining as much S/N from the planet and avoiding

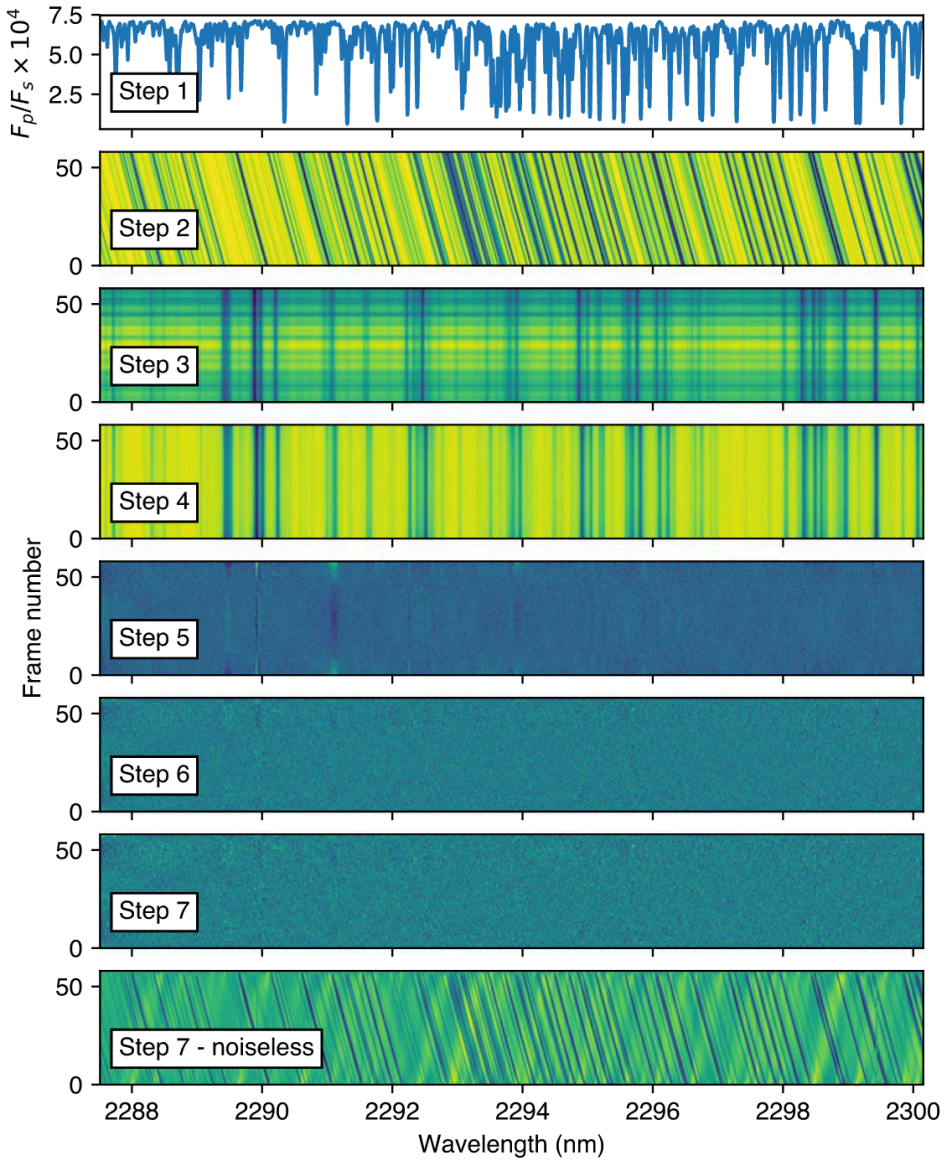

Figure 2.3: An example of typical steps (steps 3-7) taken to clean a time-series of high resolution ground-based spectra from the contaminating stellar and telluric features (dark vertical stripes). No matter the choice of technique, they all contain some form of corrections for telescope throughput variations (steps 3 to 4), telluric flux variations (steps 4 to 7) and correction for continuum modulations with high-pass filters. Step 1 shows a typical thermal emission spectrum from a hot Jupiter containing CO and H_2O. Step 2 shows how it is expected that the planet spectrum Doppler shifts across several pixels in time and wavelength in the time sequence without considering any contaminants. Step 7 shows how the planet spectrum can change when the data is passed through the telluric removal steps. Figure taken from Brogi and Line (2019).

discontinuities in the spectral sequence and/ or instrumental systematics, the exoplanet observations cannot be interrupted to take telluric frames. The sparsity of the telluric frames taken in this instance would not work for observations taken as a time series as telluric line depths can vary significantly over the course of an observing block which would leave significant telluric residuals left in the data. As these observations achieve typical SNRs on the order of hundreds per resolution element, a typical telluric correction of 1-5 per cent using telluric standards this way could result in residual correlated noise at least ten times higher than the photon limiting noise which will overwhelm the signal from planet by several orders of magnitude.

For these studies that have a time-series of high resolution spectra, different algorithms needed to be developed, each with their own advantages and limitations. Therefore, there is no one technique that is used by the whole of the community in the analysis of HRCCS in the NIR. All of these algorithms are however based on the same assumption that the planetary lines are Doppler shifting (on the order of several $\mathrm{km\,s^{-1}}$) across several pixels on the spectrograph whilst the telluric and stellar lines are essentially stationary (on the order of a few m/s) and thus fall onto the same pixel during the night. If some of these assumptions are not true, such as a slow orbiting planet (i.e. the $\frac{\mathrm{d}V_\mathrm{P}}{\mathrm{d}t}$ is smaller than the instrumental velocity sampling resolution), a lack of stability in the instrument or too low a resolution, then this methodology will start to fail and remove the planet spectrum as well as the contaminants.

Since the planet is shifting across the time-series spectra, the removal algorithms all use the same prescription which models the variations in the telluric lines as a function of time in some way, which can be subsequently removed from the spectra. As the planet spectral lines are instead shifting significantly in time and wavelength, it is thought that most of the planet lines will be missed in the modelling so are essentially ignored by the removal algorithm. It is not entirely true that the planet lines will be unaffected but this will be discussed further below (also see the bottom panel of Figure 2.3).

Normalising the spectra

As a first step, each observed spectrum needs to be continuum normalised (step 4 in Figure 2.3) to align all the spectra to the same continuum level (relative count levels). In 'typical' stellar observations, count levels are usually converted into absolute flux measurements by calibrating the spectra against standard stars (stars with well understood spectra). However, this approach cannot be done with HRCCS studies as the spectra are "self-calibrated" which means that the telluric lines are

modelled within the data itself and are subsequently removed without the need for standard star observations throughout the observing sequence.

The normalisation of the spectra in their respective data cubes with dimensions $n_{orders} \times n_{spectra} \times n_x$ is a simple division by the median value for each spectrum and detector/order (i.e. looping over the detectors/orders and spectra in the data cube and dividing by the median). The normalised spectra should resemble the step 4 panel in Figure 2.3. This normalisation of the spectra should be done before any telluric removal methodology is used. As discussed in chapter 1.4.5, there are a number of different methodologies that can be performed on these spectra to remove the time variability in the telluric lines. In this thesis, only the second order polynomial fitting of the telluric depths with time and the principle component analysis of the spectra are considered and thus only these methodologies will be discussed further below.

Second-order polynomial fitting in the time domain

The depth of the observed telluric lines primarily varies as a function of the airmass (amount of air the observed light has passed through) but the line depths can also vary with changing PWV and seeing. Modelling the telluric variation solely as a function of airmass has been successful in the past with some of the first studies of exoplanet atmospheres in the NIR with high resolution instruments (Snellen et al., 2010; Brogi et al., 2012; Brogi et al., 2014, 2016, 2018). However, this can usually only be done at highly stable sites such as at Paranal in Chile where the airmass is the dominating source of variation in the tellurics. A more general time modelling of the flux variations was developed by Brogi and Line (2019) for use in atmospheric retrievals. This takes the form of,

$$F_\lambda(t) = a_0 + a_1 T(t) + a_2 T^2(t), \tag{2.1}$$

where $T(t)$ is some time stamp such as the orbital phase or MJD at time t, etc. The coefficients a_0, a_1 and a_2 are not know and are thus fitted for in the removal process. This method was used in the observational analyses in this thesis (see chapters 3 and 4).

With this methodology, the spectra from chapters 3 and 4 were passed through these general telluric removal steps.

1. A time-averaged spectrum per detector/ order is created from the continuum normalised spectra, i.e. the normalised spectra correction described in chapter 2.5.2. Each observed spectrum is then modelled as a second order polyno-

mial with this time-averaged spectrum much like the form of equation (2.1), however in this instance, T and F_λ would represent the time-averaged spectrum and the observed spectrum (both as a function of wavelength), respectively. Finally, the fitted model, F_λ, is then divided throughout each spectrum. This step should result in the flux values in all spectra to be around 1. Step 5 in Figure 2.3 shows an example of what the time series spectra could look like after this step.

2. The next step requires the spectra to be detrended in time to remove the variation of the telluric lines in time per detector/ order. The variation in the depths of the telluric lines is modelled using the equation (2.1) where $T(t)$ can be any relevant time stamp of the observations. In this thesis as described in chapters 3 and 4, $T(t)$ is taken to be the orbital phase of the planet at the time of observation, i.e. $\phi(t)$. This second order fit with time, F_λ, for each order and wavelength channel is then divided throughout each spectrum. An example of the result of this process is shown in step 6 of Figure 2.3.

It should be noted here that step 2 can instead consider using airmass as the variable in equation (2.1) if the observing conditions are optimal, i.e. if airmass variation is the dominating variable in the depth of the telluric lines.

There is an alternative methodology used in chapter 5 that can be used to remove the stellar and telluric features in the spectra which uses principle component analysis (PCA). This technique can be used instead of the second order fitting described above, or it can be used in addition to the second order fitting as is done in the work from Pelletier et al. (2021) to provide some additional cleaning to the data.

PCA

In the simplest terms, PCA (Pearson, 1901; Hotelling, 1936) is a statistical technique that takes in a multi-variable data-set, reduces it into linear functions of those different variables of which those linear functions are ranked by maximal variance. Typically, this is a tool largely used to reduce the dimensionality of a large data-set by only using the main variances in the data. For the use of reducing HRS data, it is preferable to keep as much dimensionality as possible (i.e. preserving as much information as possible to prevent loss of the planet spectrum) and remove the maximum variances in the data that are likely to be attributable to the variance in telluric, instrumental and stellar features in the observed spectra. Theoretically,

for any matrix $\mathbf{X}$ with $n \times p$ dimensions, can be written in the form,

$$\mathbf{X} = \mathbf{U}\,\mathbf{L}\,\mathbf{A'}, \tag{2.2}$$

where $\mathbf{U}$ and $\mathbf{A}$ are $n \times r$ and $p \times r$ matrices with r is known as the rank (i.e. the order of variability). The matrix $\mathbf{L}$ is a $r \times r$ diagonal matrix which holds the singular values and the columns of the matrices $\mathbf{U}$ and $\mathbf{A}$ are called the left and right singular vectors of $\mathbf{X}$, respectively. As it is the columns of matrix $\mathbf{A}$ that define the right singular vectors of matrix $\mathbf{X}$, it is therefore necessary to use the transpose $\mathbf{A'}$ in equation (2.2) to define matrix $\mathbf{X}$. This is PCA in its simplest form which is known as singular value decomposition (SVD), however, there are various different forms of which PCA can take, some of which are discussed in a recent review by Jolliffe and Cadima (2016). Due to the geometric nature of SVD, matrix $\mathbf{X}$ can be reconstructed with the same size but with a new rank of k where $k < r$,

$$\mathbf{X}_k = \mathbf{U}_k\,\mathbf{L}_k\,\mathbf{A}'_k. \tag{2.3}$$

What is left is a data-set with the same shape but with a reduced set of eigenvalues and eigenvectors as described by equation (2.3). From this equation, matrix $\mathbf{X}$ represents the data cube of the spectra per detector/ order, therefore, in the use of HRS, matrix $\mathbf{X}$ will have dimensions of $\mathrm{n_{spectra}} \times \mathrm{n_x}$. This results in the left and right singular vectors, $\mathbf{U}$ and $\mathbf{A}$, having dimensions of $\mathrm{n_{spectra}} \times r$ and $\mathrm{n_x} \times r$, respectively. As is it still assumed that the planet's spectrum is shifting across several pixels in time, the PCA should be done in the time domain. As described above, typical PCA analyses are used to reduce the dimensionality of the data and thus only the highest variable eigenvectors are used to reconstruct the original matrix $\mathbf{X}$ using $\mathbf{X}_k$ in equation (2.3). For HRCCS analyses, the reverse methodology is used whereby the highest varying eigenvectors (or number of components) are removed by setting these vectors are set to zero or masked out.

In practice, the procedure to clean the spectra with PCA in the time domain will follow these main steps:

1. The normalised spectra from section 2.5.2 are standardised by setting the mean and standard deviation to zero and one, respectively. This is done by subtracting the mean in the time domain per detector/ order (i.e. the mean is calculated from the flux values per wavelength channel for each detector/ order and subtracted).

2. Each spectral cube with dimensions $\mathrm{n_{spectra}} \times \mathrm{n_x}$ is split up using SVD from the

standardised spectra in step 1, i.e. into matrices **U**, **L** and **A** in equation (2.2).

3. The highest varying eigenvectors are identified by selecting the desired number of components that is needed to sufficiently clean the spectra. The number of components (m) is thus removed from the **L** matrix by setting the first m singular values to be zero.

4. The spectral matrix can thus be reconstructed without the highest varying eigenvectors with the reduced singular matrix **L** on the original continuum normalised spectra, i.e. not on the standardised spectra that computed the SVD was computed from.

These steps were followed in the analysis from chapter 5. de Kok et al. (2013) use SVD in the analysis of CRIRES HRS data with an in depth analysis on how the highest ranking singular vectors correlate with various observing and instrumental variables. However, it should be noted that there is no automated procedure in the literature for HRCCS that uses this method on how many principle components should be removed from the data as it is likely to vary from data-set to data-set. Typically, the number of components is chosen based on visual inspection of the cleaned spectral sequence and/ or optimisation of an injected signal. However, the latter procedure has been shown to potentially bias the atmospheric model selection in the analysis and/ or optimise certain noise features rather than the planets signal (Cabot et al., 2019). For a derivation of equation (2.2), see Jolliffe and Cadima (2016).

Even after these telluric removal steps, it is highly likely that the spectra will require some further cleaning due to higher order variations in the depth of the telluric lines that were missed by these telluric fits from the data. The approaches used in chapters 3 and 4 is described further below.

2.5.3 Additional cleaning of the spectra

In the literature of HRCCS atmospheric studies, there are a number of different approaches to clean the spectra further, or to even weight the individual wavelength channels based on their variance in time (i.e. diving each wavelength channel by their variance in time) (e.g. Brogi et al., 2012; de Kok et al., 2013). It should be noted however that weighting the spectral channels in this way cannot be done if using the CC-to-log-likelihood mapping analyses from Brogi and Line (2019) and Gibson et al. (2020) as the variances are already considered in the log-likelihood calculations and thus should not be modified. It is crucial that the strong telluric

features in the spectra are removed down to the noise level of the data (Brogi et al., 2012), i.e. below the level of the planet's spectrum hidden within the noise, to prevent any residual telluric features overwhelming the planet's signal in the final cross-correlation analysis.

High-pass filtering

High-pass filtering should be used if there remains any wavelength dependent low frequency continuum fluctuations in the spectra post telluric removal. This was the case for the analysis of the CARMENES spectra in chapter 4. These continuum fluctuations can easily be seen in panels 3 and 4 in Figure 4.2. These fluctuations can be modelled using a number of different filtering techniques, in chapter 4 however, the continuum modulations were modelled using a 1D Gaussian kernel. An appropriate pixel bin size should be used whereby all the low frequency modulations are modelled without modelling the high frequency spectral lines. For chapter 4, a bin size with a width 80 pixels was chosen as the input of the Gaussian kernel high pass filtering. These smoothed spectral models can then be divided throughout each spectrum to correct for the continuum fluctuations. The high-passed spectra can be seen in panel 5 of Figure 4.2.

Masking

Post high-pass filtering, if there remains strong telluric residual at the end of the telluric removal stage, these highly deviant points in the spectra need to be masked out of the data before the cross-correlation analysis is performed. As with high-pass filtering, there are many different methods that have been used in the literature to mask out the telluric residuals.

It is at this stage of the analysis that is not easily generalised for every HRS data-set and will depend on the amount of residual tellurics and the observing conditions that the spectra were taken in. For example, only a standard standard deviation clipping may be needed, which is used in both analyses from chapters 3 and 4, however, a more involved masking process may be needed to ensure all the highly variant spectral channels are appropriately masked. One such example may be to mask the core of the telluric lines that fall below a certain transmission threshold (e.g. Pelletier et al., 2021; Gandhi et al., 2022), however, a more unique approach may be needed for certain data-sets. For the analysis in chapter 4, the highest variable spectral channels were determined by setting a certain threshold at which the standard deviation in time was raised significantly above the noise of

the data (see the bottom panel of Figure 4.2). If using the log-likelihood method, these masked channels can be set to zero as they will not feature in the likelihood calculations. However, one of the caveats of this method is that the threshold at which this variability is set is down to visual inspection of the resulting spectra and the noise matrix of the cross-correlation velocity map. It should be noted however that the same masking methodology should be used for all orders to avoid creating biases in the final cross-correlation map (Cabot et al., 2019), i.e. the variability threshold should be set the same over all orders.

2.6 Data analysis

Once the spectra have been sufficiently cleaned, the data can now been used a cross-correlation analysis. At such high resolutions and a planet-star contrast of $\ll 1$, the planet spectrum is still hidden within the noise of the data (see step 7 in Figure 2.3). Therefore, a CCF radial velocity mapping technique was developed by Brogi et al. (2012) which will be explained further in the following section.

2.6.1 The cross-correlation function

The CC function is a standard method to determine the degree of which two functions are correlated. This technique is widely used in signal processing applications to determine the time delay between 2 signals.

The definition for the CC of 2 functions $f(n)$ and $g(n-s)$, where s is some lag value is (Derrick, 2004),

$$C(s) = \frac{\sum_{n=0}^{N-1} [f(n) - \overline{f}(n)][g(n-s) - \overline{g}(n-s)]}{\sqrt{\sum_{n=0}^{N-1} [f(n) - \overline{f}(n)]^2 [g(n-s) - \overline{g}(n-s)]^2}}. \tag{2.4}$$

In HRCCS, $f(n)$, $g(n-s)$ and N, denotes the observed spectrum, the atmospheric model shifted by some radial velocity s, and the total number of spectral channels/ wavelength bins, respectively. $\overline{f}(n)$ and $\overline{g}(n-s)$ are the means of these functions. The denominator is a normalisation factor to ensure that the coefficients are limited between -1 and 1 with the former and latter values indicating perfect anti-correlation and perfect correlation between the two functions, respectively. Some definitions of the CCF misses the denominator in equation (2.4) (e.g. in the determinations of stellar radial velocities). In statistics, the numerator of equation (2.4) is known as the cross covariance which is often used in signal processing.

Equation (2.4) is a simple mathematical tool that is often used in HRS as a molecular "finger-printing" technique to match the hundreds or thousands of molecular features that is unique to the atmospheric spectrum of the planet that is hidden within the noise of the data. A full description of this HRCCS method is given below.

2.6.2 1D atmospheric modelling

As is it now understood that an atmospheric model is needed to create a CCF with the observed spectra, some prior assumptions are needed on what this spectrum might look like in the data. This is called forward modelling. As explained in section 1.4.1, a variety of complex techniques can be included into the radiative transfer code to model various chemical and physical parameters in the atmosphere. An atmospheric retrieval is becoming more commonly used in recent studies (e,g, Pelletier et al., 2021; Line et al., 2021; Gandhi et al., 2022) to directly infer the atmospheric parameters which are modelled as free parameters in this case. However, only forward modelling is used in this thesis the calculations of which have been performed by collaborators.

The atmospheric models used in this thesis are all modelled in 1D (see chapter 1.4.1 for details on 1D modelling) and are parameterised by two points in temperature and pressure [(T_1, p_1) and (T_2, p_2)] in the atmosphere with a constant lapse rate which is calculated as,

$$\frac{\mathrm{d}T}{\mathrm{d}\log_{10}(P)} = \frac{T_1 - T_2}{\log_{10}(p_1) - \log_{10}(p_2)}, \tag{2.5}$$

where the T-p profiles are assumed to be isothermal at pressures $p > p_1$ and $p < p_2$.

If the models have not been produced with a constant resolution, e.g. instead with a constant $\Delta\lambda$ wavelength step, then the model spectra need to be re-grid onto a new wavelength array. This can be done using $\lambda_{i=0}^{n} = \lambda_0(1 + \frac{1}{R})^i$, where λ_0, R is the minimum wavelength, the desired resolution, respectively, and i is an integer value in steps of 1 up to the value of n which is calculated by, $\frac{\log(\lambda_n/\lambda_0)}{\log(1+1/R)}$, where λ_n is the maximum wavelength. The spectra can then be convolved onto a constant resolution using a Gaussian kernel to match the resolution of the observed spectra.

2.6.3 Extracting the planet spectrum

Once a set of model spectra have been chosen to be a good estimate of the true atmospheric spectrum, these can now be cross-correlated with the data to create a CCF as a function of the planets radial velocity. This CCF boosts the signal from the planet by combining all the individual lines detected in the observed spectrum

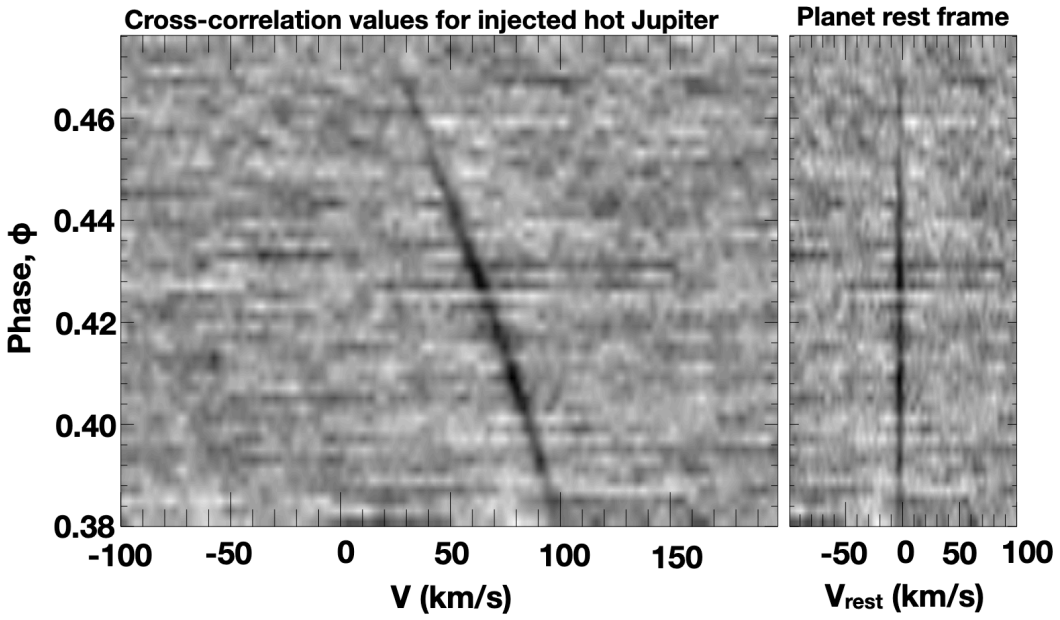

Figure 2.4: Left panel: Orbital phase resolved CCF as a function of the radial velocity. The darker and lighter hues show the positive and negative correlation coefficients. This is a CCF of a simulated sequence of model spectra injected into the data at 5× the nominal model strength. This was done to show how the signal from the planet shifts in the time sequence (i.e. the orbital trail) in the observers rest frame. This orbital trail is a combination of all the individual spectral lines in the spectra. For faster or slower orbiting planets, the gradient of this trail will become more horizontal or vertical, respectively. Right panel: The orbital trail shifted to the rest frame velocity of the planet. Figure taken from Birkby (2018).

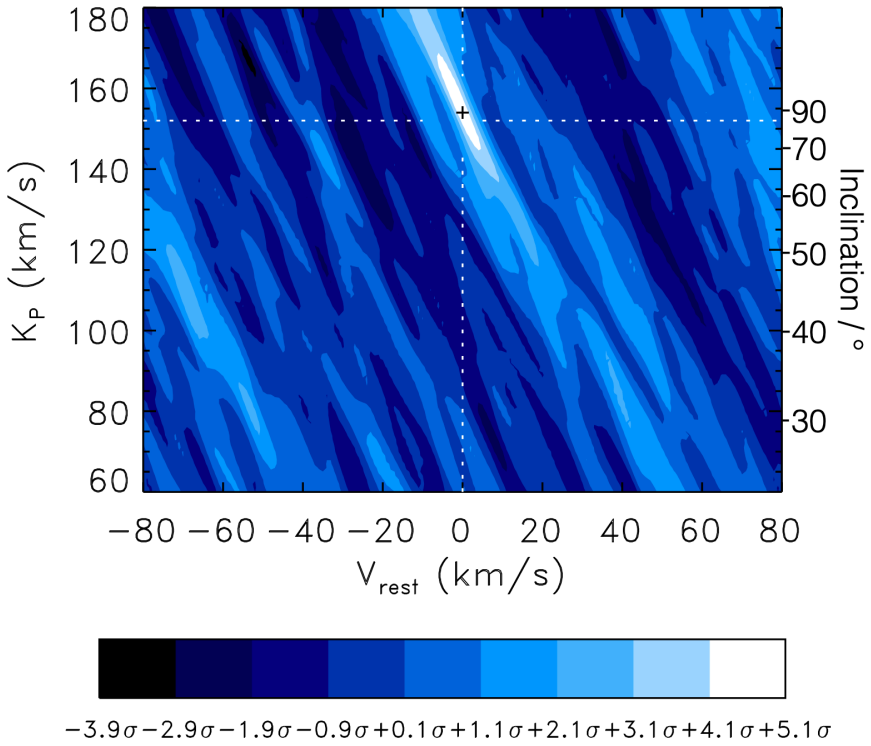

Figure 2.5: A K_{P}-V_{rest} map of the water signal from the atmosphere of the transiting hot Jupiter HD 189733 b. The orbital inclination is shown for reference in the right-hand y-axis. The coloured contours show the regions that contain the significance values indicated by the colour-bar. The peak in this map (black plus symbol) is nicely within the expected planetary velocity (white dashed lines). Figure taken from Birkby (2018), original analysis done in Birkby et al. (2013).

by $\sim \sqrt{N_{\rm lines}}$. "Detected" here means that the observed lines have been correlated with corresponding lines in the model spectrum that matches the expected radial velocity of the planet. To do this, a 2D model sequence can be produced at a range of estimated radial velocities of the planet calculated as,

$$V_{\rm P}(t) = V_{\rm sys} + V_{\rm bary}(t) + K_{\rm P} \sin[2\pi\phi(t)], \tag{2.6}$$

where $V_{\rm sys}$, $V_{\rm P}(t)$, $K_{\rm P}$ and $\phi(t)$ are the systemic velocity, the barycentric velocity of the Earth, the radial velocity semi-amplitude and the phases at the time t. It is crucial to get the sign of the barycentric radial velocity correction correct in equation (2.6). For instance, if the correction is calculated in the rest frame of the planet then the form of equation (2.6) is correct, if however, as is often the case, $V_{\rm bary}$ is calculated in the rest frame of the observer then the sign for $V_{\rm bary}$ needs to be reversed (see chapter 4.6.1 and equation (4.1)). Each phase is calculated using,

$$\phi = \frac{t - T_0}{P}, \tag{2.7}$$

where T_0 and P is the time of inferior conjunction (time at $\phi = 0$) and the period of the planet. Equation (2.6) assumes that the orbit is circular, if there is an eccentricity e, then the radial velocity will take the form,

$$V_{\rm P}(t) = V_{\rm sys} + V_{\rm bary}(t) + K_{\rm P}(\cos\left[f(t) + \omega\right] + e\cos\omega) \tag{2.8}$$

where $f(t)$ and ω are the true anomaly and longitude of periastron, respectively.

Now, the model spectrum can be spline interpolated and then shifted in wavelength at time t in the spectral sequence to,

$$\lambda(t) = \lambda_0(1 + \frac{V_{\rm P}(t)}{c}), \tag{2.9}$$

which is equivalent to equation (1.1), where c is the speed of light and λ_0 is the rest-frame wavelength. This will produce a 2D sequence with time (t) and the radial velocity ($V_{\rm P}$) along these two axes (see Figure 2.4 for an example), in which the model will be shifted to the 'guess' radial velocities of the planet ready to be correlated with the observed 2D spectral sequence. For transiting planets, the radial velocity of the planet is usually well understood from transit modelling with typical uncertainties of 1-3 $\mathrm{m\,s^{-1}}$ (e.g. Faria et al., 2020), however, for non-transiting systems, there is a large uncertainty in the orbital inclination i, and thus there is a degeneracy between the inclination and the orbital velocity: $\sin i = \frac{K_{\rm P}}{V_{\rm orb}}$, where

$V_{\rm orb} = \frac{2\pi a}{P}$, if the orbit is circular. Therefore, for non-transiting planets, a range of possible $K_{\rm P}$ values need to be tested in order to observe a peak in the CCF. Transiting planets are still mapped in this way as their could be a peak in the CCF which is slightly shifted from the expected radial velocity of the planet which is often the case due to observational/modelling effects and/or astrophysical effects such as telluric and stellar residuals and planetary winds.

In Figure 2.4, a phase resolved CCF is shown in the left-hand panel as a function of the radial velocity for an amplified planet signal injected into the data. Typically, it is often difficult to observe the velocity trail in the CCF unless the signal from the planet is prominent enough to be distinguished from the surrounding correlation coefficients (see e.g. van Sluijs et al. (2022)). In order to amplify the signal in the CCF further, the orbital trail needs to be shifted to the rest-frame of the planet (see right-hand panel in Figure 2.4) given some $K_{\rm P}$ using equation (2.6) or (2.8) and summed in time. If their are multiple observing nights, their individual CCFs can also summed together to amplify the signal even further.

For a distribution of $K_{\rm P}$ values tested, the above process needs to be repeated for all the possible orbital velocities. The retrieved $K_{\rm P}$ of the planet corresponds to the $K_{\rm P}$ that gives the strongest peak in the summed CCF. Brogi et al. (2012) developed a technique that shows the combined CCF as a function of $K_{\rm P}$ and the radial velocity. The radial velocity is usually shown in the frame of the systemic velocity $V_{\rm sys}$ or the rest-frame of the planet $V_{\rm rest}$, the resulting image is what is now called the "$K_{\rm P}$-$V_{\rm sys}$" velocity map, an example is shown in Figure 2.5.

An initial estimate of the strength of the signal in the final combined CCF map is usually determined in terms of the SNR which is estimated as the peak in the CCF divided by the standard deviation of the noise. The "noise" in the CCF map is somewhat difficult to define and therefore the peak SNR can often change quite significantly depending on which noise values are used, therefore, it is preferable to use one of the methods described in section 2.7 to determine the likelihood that the signal in the CCf matrix is attributable to the planet. These SNRs can be positive or negative depending if the data is positively correlated or anti-correlated with the chosen atmospheric model. If the model contains absorption features, a strong anti-correlation can potentially be interpreted as the data containing spectral emission features indicative of a thermally inverted lapse rate (i.e. $\mathrm{d}T/\mathrm{d}p > 0$).

Most HRCCS studies will now use these plots to show the strength of the peak in the CCF and where it lies within the velocity distribution. Usually, a 'detection' is claimed for some species in the atmosphere if the peak in the CCF is above some statistical level (see the following section 2.7) and at the expected

velocity of the planet. However, this can become complicated if there are complex physical processes occurring in the atmosphere, such as differing velocities in the trailing and leading limbs of the planet during transit, which can lead to multiple competing peaks in the K_{P}-V_{sys} map (Wardenier et al., 2021).

2.7 Statistical methods

It now needs to be determined how statistically significant a peak is in the CCF in the K_{P}-V_{sys} map. In general, statistical significance is a measure of the probability that a set of observations rejects the null hypothesis, given that the null hypothesis is true. This probability is called the p-value and is a measure of the evidence against this null hypothesis assuming the hypothesis is correct, i.e. the smaller the p-value, the more significant the alternate hypothesis is correct.

The most appropriate probability distribution this p-value is calculated from can depend on several factors but each test will have its own set of assumptions placed on the data. This most relevant for this work are the variance and the distribution that the data takes.

2.7.1 The Welch *t*-test

For HRCCS, there are a couple of statistical tests that can be done to properly define a detection significance. Brogi et al. (2012) developed a method to statistically compare a set of values thought to be within the radial velocity of the planet ("in-trail") and to the noise distribution ("out-of-trail"). This is done with a Welch t-test (Welch, 1947) which is a statistical measure of the difference between the mean values of two sets of data assuming that both distributions are Gaussian. As such, this method requires a definition on which values need to be included into the in-trail and out-of-trail distributions, thus, the significance value will depend on this definition (see chapter 3.8). The Welch t-test has been proven to be a robust method of determining a detection significance with many successful implementations in the community since then (e.g. Brogi et al., 2014; Birkby et al., 2017; Nugroho et al., 2017; Giacobbe et al., 2021), however, the significance value using this method will change depending on the width of the in-trail values (see section 3.8.1 and Figure 3.8). Therefore, like with the SNR CCF map, this method can be biased depending on the choice of values which are assumed to be noise.

In this methodology, the in-trail values are taken to be the CC values that fall on the radial velocity of the planet (or the derived velocity of the planet) within some range, for example, $V_{\mathrm{P}} \pm 1 - 2\,\mathrm{km\,s^{-1}}$. To visualise this, these values would include

the correlated value from the planets spectrum in Figure 2.4 (dark points) along the radial velocity of the planet. These values are then compared using the Welch t-test with the distribution of the CC values excluding those that follow the planets in-trail distribution, i.e. a noise distribution from the analysis. The comparison of the means of these two distributions will give a significance value of whether the in-trail distribution could have been drawn purely from the noise distribution.

2.7.2 A Bayesian likelihood approach

Typically for low resolution spectroscopy, a detection for some species in the atmosphere is most often done with a fairly simple goodness-of-fit chi-square test between an atmospheric model and the flux calibrated observed spectrum. This will often be expressed as a reduced chi-square test χ^2_ν, which will be calculated from a vector of residuals (i.e. the difference between the observed spectrum and the model). The ν in the chi-square is the degrees of freedom which is defined as the number of data points minus the number of parameters. For the reasons stated in section 2.6.3, this test cannot be done on HRCCS data as the spectra have been normalised due to the telluric removal process and as a consequence, the actual planet spectrum will be relative to the stellar spectrum.

Brogi and Line (2019) developed for the first time a likelihood function which encapsulates the nuances of the HRCCS method. This allows the correlation coefficients to be mapped into a Bayesian framework which is essential for determining posterior distributions of free parameters for a chosen prior distributions of these parameters. In Bayesian statistics, the "likelihood" is the conditional probability $p(x, \theta)$ of the observed data, x, given a set of parameters, θ, (van de Schoot et al., 2021), as such, the likelihood function for HRCCS needs to describe how the atmospheric model, $g(n)$, fits the observed spectra, $f(n)$. As the planet is expected to shift in wavelength in time, s, the data can be described as $f(n) = ag(n - s) + d_n$, where a and d_n are an atmospheric scaling factor and some noise at wavelength n, respectively. It should be noted here that the method described in Gibson et al. (2020) generalises this formulation further by introducing an additional scaling factor for the white noise of the spectra which allows a fit for the time and wavelength dependent noise in the data. However, in this thesis, only the Brogi and Line (2019) likelihood formulation is used and is thus derived below. The model spectrum, $g(n)$ will also be a function of the free parameters, θ, in the modelling and the orbital parameters, K_P and V_sys. Assuming the noise is Gaussian, the likelihood function

can hence be defined as (Brogi and Line, 2019),

$$L = \prod_n \frac{1}{\sqrt{2\pi\sigma^2}} \exp\left\{-\frac{[f(n) - ag(n-s)]^2}{2\sigma^2}\right\} \tag{2.10}$$

$$= \left(\frac{1}{\sqrt{2\pi\sigma^2}}\right)^N \exp\left\{-\sum_n \frac{[f(n) - ag(n-s)]^2}{2\sigma^2}\right\}, \tag{2.11}$$

where N is the total number of data points used and σ is the standard deviation at wavelength n. To remove the exponential, and to link it to the chi-square, $\chi^2 = \sum_n \frac{[f(n)-ag(n-s)]^2}{\sigma^2}$, the likelihood is converted into a $\log(L)$,

$$\ln(L) = -N \log \sigma - \frac{1}{2\sigma^2} \sum_n [f(n) - ag(n-s)]^2. \tag{2.12}$$

The maximum $\log(L)$ estimator is therefore of the form,

$$\ln(L) = -\frac{N}{2} \log[s_f^2 + s_g^2 - 2R(s)], \tag{2.13}$$

where s_f^2 and s_g^2 are the variances of the data and model, respectively. The term $R(s)$ is the cross-covariance matrix which is related to the CCF in equation 2.4 as,

$$C(s) = \frac{R(s)}{\sqrt{s_f^2 s_g^2}}. \tag{2.14}$$

For the full derivation details see Brogi and Line (2019).

As this $\log(L)$ is a function of $C(s)$, the $K_{\rm P}$-$V_{\rm sys}$ correlation maps can now be converted to a $\log(L)$ map. This allows statistically robust confidence levels around the maximum $\log(L)$ in the $K_{\rm P}$-$V_{\rm sys}$ map to be determined by calculated the p-value by taking the survival function of the chi-square distribution, i.e. $\chi^2 = -2\Delta \log(L)$ (Wilks, 1938), where $\Delta \log(L)$ is the difference of the $\log(L)$ from the maximum value. As the survival function will include both tails of the distribution, half of that value will be used as the p-value. Once the p-values has been obtained, the confidence levels in terms of σ are determined by taking the inverse survival function of the normal distribution. This can similarly be used to compare the how well different models fit with the data by calculating the $\Delta \log(L)$ as the difference the peak $\log(L)$ values for those models. With this likelihood function, a set of free parameters in the atmospheric modelling can now be explored with Bayesian inference techniques such as in MCMC and nested sampling algorithms. These algorithms allow the posterior probability distributions to be explored within the assumed prior distributions of

these free parameters.

The HRCCS algorithm steps

Here, I will describe the general steps to extract the planet spectrum from the observed/ simulated spectra used in chapters 3, 4 and 5.

1. The fully processed observed spectra from section 2.5.2 are passed into the CC algorithm. If noisy spectral channels were masked in the observed spectra, then the same mask was used on the model spectra at the start of this process by setting them to zero or "not a number" values depending on whether the log-likelihood orthe SNR CCF methods were used, respectively. This is important to ensure that both these values are not involved in the CC calculations from the observed or model spectra.

2. The model spectra wavelength grid are shifted by an amount given in equation (2.9) by assuming some range of lag radial velocities, $V_{\rm r}$, using spline interpolation. A large enough array of radial velocities was used when shifting the model spectra in order to encapsulate all of the possible radial velocities of the planet across the spectral sequence for the extremes of $K_{\rm P}$ and $V_{\rm sys}$ considered in the analysis.

3. For each spectrum in the data cube, the observed and shifted model spectra are correlated for each radial velocity which gives a CCF matrix with dimensions CCF($\rm n_{orders}, n_{spectra}, V_r$). This can be done by calculating the pure correlation coefficients using equation (2.14) or the log-likelihood values using equation (2.13). It is important to note at this stage that if the likelihood approach was used on emission observations, the atmospheric models ($F_{\rm P}$) were scaled to the stellar flux via,

$$F_{\rm scaled} = \left(\frac{F_{\rm P}}{F_\star}\right)\left(\frac{R_{\rm P}}{R_\star}\right)^2, \tag{2.15}$$

   where $R_{\rm P}$, $R_\star$ and $F_\star$ are the radii of the planet and star and the stellar flux.

4. The CCF matrix (containing either pure correlation coefficients or log-likelihood values) can now be summed along all detectors/ orders that have been used in the analysis per observing night giving a CCF matrix as a function of time and radial velocity, i.e. CCF($\rm n_{spectra}, V_r$).

5. Assuming a suitable range of $K_{\rm P}$ and $V_{\rm sys}$ (or $V_{\rm rest}$) values for the planet (i.e. values surrounding the expected velocities of the planet), the CCF($\rm n_{spectra}, V_r$)

matrix is shifted, per spectrum, to the radial velocity of the planet, $V_{\rm P}$, for each value of $K_{\rm P}$ using equation (2.6) via 1D interpolation. This step can be visualised in Figure 2.4 as the dark trail of the planets spectrum is shifted to the rest frame of the planet in time. This gives a CCF matrix of CCF($n_{\rm spectra}, V_{\rm P}$).

6. If the pure CC or the log-likelihood approach has been used, a time averaged CC values or the summed likelihood values are calculated along the time axis, respectively, for the all the collated CCF matrices for each observing night to leave a final CCF matrix with dimensions CCF($K_{\rm P}, V_{\rm sys}$) (or CCF($K_{\rm P}, V_{\rm rest}$) if $V_{\rm sys}$ is used in equation (2.6)).

7. The above step can be the final step for the log-likelihood approach (see Figure 4.4 for a CC-log(L) map), however, to convert the pure CC values into a SNR velocity map, the standard deviation of the matrix needs to be divided throughout the matrix. Figure 2.5 shows an example of SNR $K_{\rm P}$-$V_{\rm rest}$ map that highlights the peak in the CCF of HRS observations with a pure water atmospheric model.

As described in section 2.7.2, the CC-log(L) map can be converted to a significance map as a function of $K_{\rm P}$ and $V_{\rm sys}$ by calculating the chi-square distribution, $\chi^2 = -2\Delta \log(L)$, which can hence be converted into a p-value and subsequently significance values. As the chi-square is calculated from the peak in the CCF matrix, these significance values are defined as the number of σ away from the peak in the velocity map rather than a detection significance as is often quoted in the low-resolution atmospheric literature. See Figure 4.5 for significance CCF maps. However, a detection significance can be estimated by calculating the significance between the likelihood value from the peak in the CCF map with that of a likelihood value from a CCF map with a flat atmospheric model (i.e. correlating with a model with no spectral features).

2.7.3 Reproducing the telluric removal effects on the models

The analysis of Brogi and Line (2019) highlighted an important consequence of the effects of the telluric removal process on the underlying planet spectra. The step 7 panel in Figure 2.3 shows that the continuum and spectral lines have been distorted by scaling and stretching effects that is an unavoidable consequence of the removal procedure. If these effects are not accounted for the analysis steps, then it is highly likely that biases will be introduced into the retrieved molecular abundances and T-p structure of the atmosphere using the Bayesian approach described in section 2.7.2. Any methodology used to remove the telluric and stellar features using a

self-calibrated approach on the data (e.g. PCA, polynomial fitting and SYSREM) (Brogi and Line, 2019; Pelletier et al., 2021; Line et al., 2021) are ultimately likely to suffer from these same effects and thus needed to be accounted for in the data analysis. The models were only reprocessed in the analysis of chapter 4 as this applied the CC-log(L) method to the data. The process for how these atmospheric models were re-processed and correlated with the observed spectra is described below.

For each of the data reduction steps described in the steps of sections 2.5.2 and 2.5.3, the detrending matrices that are divided though by the observed data are stored. These detrending matrices will effectively store the transmission of the Earth, $T_{\oplus}(\lambda, t)$ and the stellar flux, $F_{\star}(\lambda)$, that has been modelled by the removal steps. For emission observations, the observed flux is assumed to be of the form,

$$F_{\rm obs}(\lambda, t) = F_{\star}(\lambda) T_{\oplus}(\lambda, t)(1 + F_{\rm scaled}), \tag{2.16}$$

where $F_{\rm scaled}$ is defined in equation (2.15). Thus, prior to the stage when the model spectra are correlated with the observed spectra (step 3 in section 2.7.2), the re-processed models can be created by injecting the detrending values for each spectrum and multiplying that with $(1 + F_{\rm scaled})$ factor to accurately reproduce the observed flux (in equation (2.16)) but with the inclusion of the model. Finally, the data cube containing $F_{\rm obs}(\lambda, t)$ can be passed through the same removal steps that the observed spectra to reproduce the effects on the observed spectra. Thus, the re-processed model, which is now a function of time, can be correlated with the observed spectra following the same steps 4-7 in section 2.7.2.

The analyses in the next chapters largely follow the broad outline for each of these methods described above. Due to the many nuances of HRCCS analyses, small differences in the reduction and data analysis are necessary for each individual data-set which will also be outlined in these following chapters.

Chapter 3

A weak spectral signature of water vapour in the atmosphere of HD 179949 b at high spectral resolution in the *L*-band

3.1 Notes

This chapter follows work published in Webb et al. (2020). Whilst most of this work is my own work there are however there have been some contributions from the other authors of the work. Matteo Brogi was the PI of the original CRIRES observation proposal with Jayne L. Birkby and Ignas A. G. Snellen as further CO-I's. Matteo Brogi also helped to edit the main text in the published paper (Webb et al., 2020) which makes up this chapter. Siddharth Gandhi provided the calculations for the atmospheric models and helped to write the modelling section 3.5.3. Michael R. Line tested the data-set used in this chapter on their analysis framework. Katy L. Chubb and Sergey N. Yurchenko helped to supply the water line lists from the EXOMOL database.

Corrigendum: the use of "absolute mass" of the planet was incorrectly used in the published version of this chapter Webb et al. (2020). Instead just the mass should have been used here as there are assumptions placed on the mass of the host star in this case. This will be corrected in a published corrigendum of this work.

3.2 Abstract

High resolution spectroscopy ($R \geqslant 20,000$) is currently the only known method to constrain the orbital solution and atmospheric properties of non-transiting hot Jupiters. It does so by resolving the spectral features of the planet into a forest of spectral lines and directly observing its Doppler shift while orbiting the host star. In this chapter, we analyse VLT/CRIRES ($R = 100,000$) L-band observations of the non-transiting giant planet HD 179949 b centred around 3.5 μm. We observe a weak (3.0 σ, or S/N = 4.8) spectral signature of H_2O in absorption contained within the radial velocity of the planet at superior-conjunction (i.e. the day-side of the planet, $\phi \approx 0.5$), with a mild dependence on the choice of line list used for the modelling. Combining this data with previous observations in the K-band (Brogi et al., 2014), we measure a detection significance of 8.4 σ for an atmosphere that is most consistent with a shallow lapse-rate, solar C/O ratio, and with CO and H_2O being the only major sources of opacity in this wavelength range. As the two sets of data were taken three years apart, this points to the absence of strong radial-velocity anomalies due, e.g., to variability in atmospheric circulation. We measure a projected orbital velocity for the planet of $K_P = (145.2 \pm 2.0)$ km s^{-1} (1 σ) and improve the error bars on this parameter by ∼70%. However, we only marginally tighten constraints on orbital inclination ($66.2^{+3.7}_{-3.1}$ degrees) and planet mass ($0.963^{+0.036}_{-0.031}$ Jupiter masses), due to the dominant uncertainties of stellar mass and semi-major axis. Follow ups of radial-velocity planets are thus crucial to fully enable their accurate characterisation via high resolution spectroscopy.

3.3 Introduction

The vast majority of atmospheric characterisations of exoplanets thus far have been for transiting systems of short-period hot Jupiters using photometry and low resolution spectra (e.g. Sing et al., 2016). Hot Jupiters are intrinsically more accessible for characterisation due to their extreme temperatures, $T_P > 1000$ K, giving a relatively large ($\sim 10^{-4}$) flux contrast between the planet and the parent star and larger size blocking out more of the stellar light. The molecular signatures of these hot atmospheres can be observed as extra absorption features in the transit light curve (Charbonneau et al., 2002) centred on specific wavelengths for different opacity sources. Further to this, it is known that this strong irradiation on the day-side will penetrate into the deep layers of the atmosphere producing observable emitted spectra in the near-infrared (NIR, Seager and Sasselov, 1998). With the continuing

improvement of spectrographs, atmospheric models and analytical techniques, exoplanetary atmosphere characterisation is now at the forefront of exoplanet research.

This past decade has seen the growth of ground based, high resolution spectroscopy (HRS) in the NIR in detecting the thermal emission from planet atmospheres (for a recent comprehensive review, see Birkby, 2018). Such observations have provided constraints on the chemical abundances and the physical structure of the atmosphere, the first of which coming from the detection of CO in the transiting hot Jupiter HD 209458 b by Snellen et al. (2010). The success of this technique results from isolating the hundreds of individually resolved molecular lines which shift by tens of $\mathrm{km\,s^{-1}}$ due to the large planetary velocity change over the orbit compared to quasi-stationary telluric and stellar absorption lines. There are now many methods to remove these dominating sources in the spectra, for example, through de-trending with geometric airmass (Brogi et al., 2013, 2014, 2016, 2018) or with blind algorithms (de Kok et al., 2013; Piskorz et al., 2016, 2017; Birkby et al., 2017). The cross-correlation technique with model atmospheric templates has now proved to be a robust technique in order to amplify the weak planet signal hidden within the noise of the spectra.

HRS has now lent itself to many detections of molecular species, most of which have come from absorption of the dominating opacity sources, CO (e.g. Brogi et al., 2012) and H_2O (e.g. Birkby et al., 2013). The resulting planet signal peak in the cross-correlation function has also allowed many physical parameters of the planet to be determined, such as, high-altitude winds (Snellen et al., 2010; Wyttenbach et al., 2015; Louden and Wheatley, 2015; Flowers et al., 2019), spin rotations (Snellen et al., 2014; Brogi et al., 2016; Schwarz et al., 2016) and mass loss rates (Nortmann et al., 2018; Allart et al., 2018). More recently, HRS has been used for the first time to infer the presence of a strong thermal inversion from the detection of the strong optical and UV absorber TiO (Nugroho et al., 2017) in the transmission spectrum of WASP-33 b. Also, HRS transmission observations of the ultra-hot Jupiter KELT-9 b has detected several ionised and neutral metal lines in this highly irradiated atmosphere (Hoeijmakers et al., 2018a; Cauley et al., 2019) with possible evidence for a large out-flowing, extended atmosphere (Hoeijmakers et al., 2019).

HRS is a particularly powerful tool when observing the thermal emission from non-transiting systems on short-period orbits. Currently, this is the only known method to directly detect the orbital motion of these planets as it passes through superior conjunction, breaking the inherent degeneracy with the orbital inclination of the system and, hence, providing an accurate determination of the

absolute mass[1] of the planet. Since the probability of having a transiting system in our local neighbourhood of main sequence stars is small, HRS could offer a means of characterising the majority of these systems, particularly for very close-by systems in the habitable zone, such as Proxima Cen b (Anglada-Escudé et al., 2016). However, only a handful of hot Jupiters have thus far have been characterised in this way, primarily in the K (Brogi et al., 2012; Rodler et al., 2012; Brogi et al., 2013, 2014; Guilluy et al., 2019) and L-bands (Birkby et al., 2013; Lockwood et al., 2014; Piskorz et al., 2016, 2017; Birkby et al., 2017).

In this chapter, we are revisiting the non-transiting system HD 179949 from previous HRS characterisation (Brogi et al., 2014, hereafter BR14) by observing the day-side of the planet at longer wavelengths (in the L-band centred around $3.5\,\mu$m) with the intention of potentially observing further C and O-bearing species. This is the first time a search for molecules at $3.5\,\mu$m is reported from HRS observations, and it tests the prediction made by de Kok et al. (2014) that further species should have stronger cross correlation signals than at $2.3\,\mu$m, in particular H_2O, CH_4 and CO_2. The detection of these species and measurement of their abundances can constrain the C/O ratio in the planetary atmospheres (Madhusudhan, 2012; Line et al., 2014; Brogi et al., 2014), which can in turn provide insights on the formation (Madhusudhan et al., 2011b) and evolution of the planetesimal in the protoplanetary disk (Öberg et al., 2011). The C/O ratio has also been used to predict whether thermal inversions are likely to be present in hot Jupiters (Madhusudhan et al., 2011a,b). Before outlining the rest of the paper, we will give an overview of the HD 179949 system.

3.3.1 Previous observations of the HD 179949 system

HD 179949 is an F8 V (Gray et al., 2006) spectral type star on the main sequence. It is slightly larger than the Sun with a mass and radius of $1.181^{+0.039}_{-0.026}\,M_\odot$ and $1.22^{+0.05}_{-0.04}\,R_\odot$ (Takeda et al., 2007) and roughly half its age. The system is in relatively close proximity to the solar system at 27.478 ± 0.057 pc (Gaia Collaboration, 2018) and is bright in the NIR with a magnitude of 4.936 ± 0.018 in the K-band (Cutri et al., 2003). Also, due to the relatively high effective temperature of the star ($T_{\rm eff} \approx 6260$ K, Wittenmyer et al., 2007), there are very few strong absorption lines observed (Carpenter et al., 2009) in the infrared stellar spectrum making it an ideal target for thermal emission HRS observations.

HD 179949 b was first discovered from a radial velocity survey (Tinney et al., 2001) of bright, near-by stars, with follow up photometric surveys finding

[1] see corrigendum in section 3.1

no evidence of a transit. The planet was determined to have a periodicity of P = (3.092514 ± 0.000032) days with a semi-major axis of a = (0.0443 ± 0.0026) au. Due to the initial uncertainty of the inclination of the system, only a minimum mass of $M_{\rm P} \sin i = (0.916 \pm 0.076)\,{\rm M_J}$ (Butler et al., 2006) could be determined. Subsequent analysis of mid-IR phase variations using the IRAC instrument on *Spitzer* by Cowan et al. (2007), indicated that the planet recirculates less than 21 per cent of the incident radiation to the night-side, this allows an estimate of the day-side equilibrium temperature to be $T_{\rm eq} \approx 1950\,{\rm K}$. Previous HRS analysis on this planet was done in the K-band by BR14, detecting CO (S/N = 5.8) and H_2O (S/N = 3.9) in absorption on the day-side of the atmosphere. As such, the amplitude of the orbital velocity of the planet was found to be $K_{\rm P} = (142.8 \pm 3.4)\,{\rm km\,s^{-1}}$, breaking the $\sin i$ degeneracy giving an orbital inclination of $i = (67 \pm 4.3)^\circ$ and an absolute mass of $M_{\rm P} = (0.98 \pm 0.04)\,{\rm M_J}$. That analysis also found no evidence for a thermally inverted $T - p$ profile and a weakly constrained oxygen-rich atmosphere (C/O = $0.5^{+0.6}_{-0.4}$) due to a non-detection of CH_4.

In the following sections we will give an overview of the observations in Section 3.4 and the data reduction in Section 3.5. We follow with the results obtained in the L-band in Section 3.6. We then revisit the K-band analysis by combining it with the K-band data in Section 3.7. Finally, we will produce a discussion and give conclusions on this analysis in Sections 3.9 and 3.10.

3.4 Observations

High resolution spectra (R ≈ 10^5) of HD 179949 b were taken with the Cryogenic Infrared Echelle Spectrograph (CRIRES, Kaeufl et al., 2004) on the Very Large Telescope (VLT) over two nights, 2014 April 26 and 2014 June 8. In order to achieve the highest resolving power of CRIRES, the instrument was set up using the 0.2″ slit and to maximise throughput, the MACAO (Arsenault et al., 2003) adaptive optics system was used. See chapter 2.2 for a more in depth description of the CRIRES instrument and MACAO optics system.

1-D spectra were imaged on the four CRIRES CCD detectors (1024×512 pixels) in the standard ABBA nodding pattern along the slit for accurate background subtraction (see chapter 2.2 for a description of this method). The spectra covered a wavelength range of 3.459-3.543 μm, giving a sampling precision of $\sim 1.5\,{\rm km\,s^{-1}\,pixel^{-1}}$. On the first night, forty spectra were taken from 2.4 h of observation (ϕ = 0.528 − 0.560). The second night was split into two separate observations taken 1 h apart, totalling 4.7 h of observation, with forty (ϕ = 0.397 - 0.428)

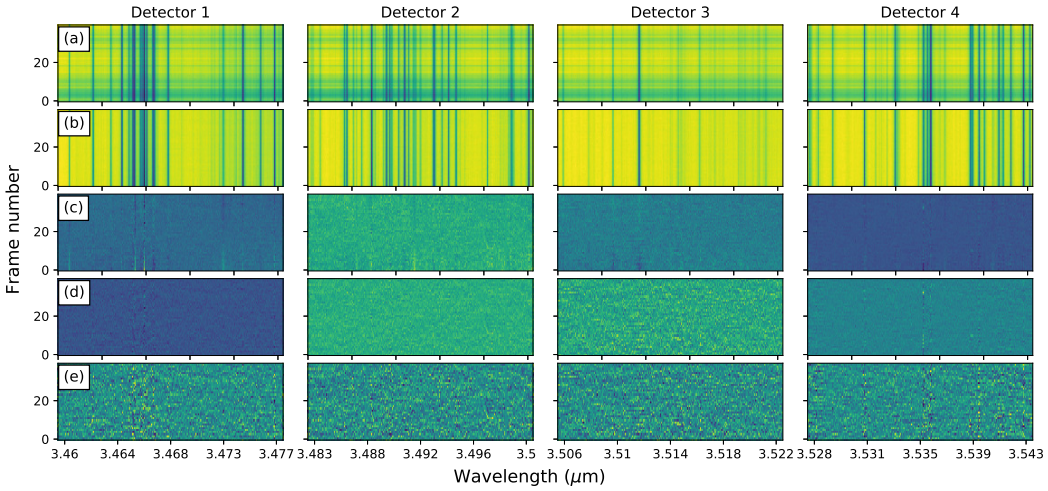

Figure 3.1: Example of the steps taken to remove telluric effects in the time-series of spectra taken during the first night of observations. Each column shows one of the four CRIRES detectors. Row (a): Time series of spectra extracted by the standard CRIRES pipeline, after removal of bad pixels and regions on the CCD. Row (b): Normalisation of the continuum of the spectra correcting for throughput variations. Row (c): Normalisation of the depth of the lines removing the main variability in the methane lines. Row (d): Normalisation of the time variability in the flux removing additional trends in water telluric lines. Row (e): Masking of noisy spectral channels. The same routine was applied to all of the nights observations.

and thirty-nine ($\phi = 0.440 - 0.471$) spectra taken, respectively. This gives a total of 119 spectra split into three sets of $4 \times n_{\rm frames} \times 1024$ spectral matrices, where $n_{\rm frames}$ is the number of exposures (couples of AB or BA spectra) taken. Each spectral image was extracted using the CRIRES pipeline v2.3.2 and calibrated from the calibration frames that are taken the morning after the set of observations. Master dark and flat fields were created, with the inclusion of the non-linearity coefficients on the latter, to correct for detector defects and the "odd-even" effect which is known to affect detectors one and four. Further detector effects, such as isolated bad pixels and bad regions on each detector, were viewed by eye and replaced by their spline interpolated and linear interpolated values, respectively.

3.5 Data reduction

3.5.1 Wavelength calibration and telluric removal

In order to extract the planet's signal from the spectra, the dominating telluric contributions need to be removed. In addition, an accurate wavelength solution

needs to be determined with respect to the pixel number for each detector on each set of observations. Each stage of the analysis was performed by writing our own custom-built pipeline in PYTHON 3.

The most delicate part of the data reduction for CRIRES high resolution spectra has always been the alignment of the time sequence of one-dimensional spectra to a common reference frame, and the wavelength calibration of the four detectors. In the past, this process has been done by finding the difference of the centroids of prominent telluric lines for each spectrum, shifting them through spline interpolation and comparing the spectra to a telluric spectrum with a known wavelength solution (Snellen et al., 2010; Brogi et al., 2012). This approach can be costly in time and may not be practically feasible for much larger data-sets, also. Here, we fully automate this process by running a simple MCMC routine, using the `python` package `emcee` from Foreman-Mackey et al. (2013), to determine a wavelength solution for each spectrum. This will also allow accurate error analysis on the wavelength solution. We remove detector 3 from further analysis due to the lack of prominent telluric features in these spectra which would result in an uncertain wavelength solution (see Figure 3.1). We initialised the MCMC with three 'guess' wavelengths for each spectrum which were taken to be three pixels across each detector, $x = 255$, 511, 767, and their associated calibrated wavelength values from the output of the CRIRES pipeline. As in Brogi et al. (2016), we use these three wavelengths to determine the parabolic wavelength solution of the CRIRES detectors. At each step of the MCMC, we allow the three wavelengths to randomly walk in the parameter space. Each step defines an updated wavelength solution, to which we spline-interpolate a telluric model spectrum computed via the ESO sky calculator (Noll et al., 2012). We compute the cross correlation between the telluric and the observed spectrum and convert it to a log-likelihood value using equation (1) from Zucker (2003). This log-likelihood is used to drive the evolution of the MCMC chains. We speed up the algorithm by running relatively short chains of a few hundreds steps multiple times and adopting their best-fit parameters as new 'guess' wavelengths. Typically after the second iteration the walkers settle around the best-fit solution and this allows us to run a last, relatively short chain (12 walkers with 250 steps each in our case) which converges after a few tens of steps. The resulting wavelength solutions were found to have an average error of 0.8 - $1.8 \times 10^{-6}\,\mu$m which translates to an error of 0.05 - 0.1 of a pixel and an error on the measured radial velocity of $\sim 150\,\mathrm{m\,s^{-1}}$ which was derived from the $1\,\sigma$ quantiles of the Markov chains. Finally, we re-grid the wavelength solution to have a constant $\Delta\lambda/\lambda$ value and re-grid the spectra by spline interpolating to the new wavelength

solution.

Recently, it has been suggested that de-trending the data with certain methods in order to remove telluric contamination can produce spurious signals in the data (Cabot et al., 2019) (some of these other methods are described in chapters 1.4.5 and 2.5.2). As a result, we implemented two slight variations in de-trending of the data, both of which rely on removing the time dependence on the variability in the strength of the absorption lines for each spectral channel. In doing so, all the dominating stationary absorption lines in the time-series spectra should be removed leaving the Doppler shifted planet signature largely unaltered. The first method used was to remove the linear relationship with the exponential of the airmass, directly following the de-trending method implemented by BR14. The second de-trending algorithm used here follows directly steps 3 - 7 from that used in Brogi and Line (2019) as shown in Figure 3.1. Panel (a) shows the data aligned on a constant $\Delta\lambda/\lambda$ grid, while in panel (b) we have normalised the data by dividing each spectrum by the median of the brightest 100 pixels to correct for throughput variations. In panel (c) we have divided each spectrum by a second order polynomial fit of these spectra as a function of the time averaged spectrum. While this removes most of the telluric lines, there are still residuals at the percent level, which are removed by dividing each wavelength channel through a second order polynomial fit of the measured flux as a function of time as shown in panel (d). Lastly, as in Brogi and Line (2019), we mask noisy channels (strong telluric residuals) with a standard deviation greater than $3.5\times$ of the total spectral matrix in order to use these data in a future analysis using the Bayesian atmospheric retrieval approach. We note that for future data processing through retrieval algorithms it is important to preserve the variance of each spectral channel because this enters the calculation of likelihood values directly (Brogi and Line, 2019). Therefore, the common practice of 'weighting' spectral channels by the variance cannot be applied, and masking is used instead. The application of two different versions of the telluric removal algorithm as outlined above was chosen to maintain consistency with BR14 while testing the performance of the more general algorithm proposed by Brogi and Line (2019). We found that there was no significant difference for either de-trending method on the final CCFs with the data in the following analysis and, therefore, we proceeded to only use the de-trending method used in Brogi and Line (2019). This choice will also enable us to retrieve the atmospheric properties of the system via Bayesian analysis in the future.

3.5.2 Cross-correlation analysis

As shown in the bottom panels of Figure 3.1, at the final stage of the analysis there remains very little residual artefacts from the spectral contaminants. However, any weak molecular signature from the planet is still hidden within the noise of the data. To observe this signal, we use a well established cross-correlation technique (see chapter 2.6.3 for further description) with several model atmospheric templates and look for any significant detection.

To match with the planet's orbital motion, the model wavelengths have to be shifted for all possible radial velocities of the planet;

$$V_{\rm P} = K_{\rm P} \sin[2\pi\phi(t)] + V_{\rm bary}(t) + V_{\rm sys}, \tag{3.1}$$

accounting for the barycentric velocity of the solar system compared to Earth ($V_{\rm bary}$) as function of time t, and the systemic velocity of the system ($\rm V_{sys}$). In equation 3.1, $K_{\rm P}$ is the maximum radial velocity of the planet and $\phi(t)$ are the orbital phases calculated from

$$\phi(t) = \frac{t - T_0}{P}, \tag{3.2}$$

where T_0 is the time of inferior conjunction and P is the orbital period. We shifted the wavelength solution for all possible radial velocities which was taken to be, $-249 < V_{\rm r} < 249$ $\rm km\,s^{-1}$ in steps of $1.5\,\rm km\,s^{-1}$. The model fluxes were then spline interpolated, mapped onto the shifted wavelengths and cross-correlated with the observed spectra. The correlation values were then summed for the three CRIRES detectors used on each night which gave three cross-correlation function (CCF) matrices in terms of time (or frame number) and radial velocity, $\rm CCF(\mathit{t}, \mathit{V}_r)$. Furthermore, we shifted these matrices to the rest frame of the planet, $V_{\rm rest}$. To do that, we needed to determine $V_{\rm p}$ from equation (3.1), for all orbital phases given by equation (3.2) observed, which were computed from the orbital parameters determined in Butler et al. (2006) and from the time of observation for each spectra. In the final CCF, we weight the spectra equally as a function of phase and wavelength. Due to the uncertainty in the inclination of the system, we map out all the possible projected orbital velocities of the planet; $K_{\rm P} = 0$ - $200\,\rm km\,s^{-1}$ in steps on $2\,\rm km\,s^{-1}$. The barycentric velocities were also computed from the observation times given in the fits files of each extracted spectrum. The final CCF matrix, $\rm CCF(\mathit{K}_P,\ \mathit{V}_{rest})$, was determined by co-adding the three matrices together along the time axis and dividing by the standard deviation of the total matrix, excluding values which may correspond to the planet signal, $|V_{\rm rest}| < 7.5\,\rm km\,s^{-1}$.

3.5.3 Model atmospheres

The high-resolution emergent spectra models were produced from the self-consistent, line-by-line exoplanetary modelling code GENESIS (Gandhi and Madhusudhan, 2017). The models are produced as described in Hawker et al. (2018) and Cabot et al. (2019) resulting in a spectral resolving power of $R = 300000$ in the observed spectral band. We tested against a grid of models with the vertical atmospheric temperature-pressure ($T - p$) profile constructed in the same way as in BR14 for consistency. Hence, we modelled the $T - p$ profile by parametrising two points in space where the temperature and pressure are varied by a constant lapse rate given by,

$$\frac{\mathrm{d}T}{\mathrm{d}\log_{10}(p)} = \frac{T_1 - T_2}{\log_{10}(p_1) - \log_{10}(p_2)}. \tag{3.3}$$

We set the region corresponding to the planet continuum to $(T_1, p_1) = (1950\,\mathrm{K}, 1\,\mathrm{bar})$, with the upper parameters, (T_2, p_2), varied depending on the model grid used (see Tables 3.1 and 3.2). Above and below these regions, the atmosphere is assumed to be isothermal. We note that because the CCFs of the spectra are not weighted in this analysis (see section 3.5.2), we approximate the day-side emission of the planet with a single $T - p$ profile and molecular abundance as an average atmospheric profile over several phases of the planet.

We included opacity from three molecular species, H_2O, CH_4 and CO_2, into the models for the 3.5 μm observations. The analysis by BR14 produced positive and negative detections of H_2O and CH_4, respectively, and since both species are predicted to produce more significant signals at 3.5 μm (de Kok et al., 2014), we wanted to analyse a broader range of abundances for the combined species consistent with what is expected at various atmospheric C/O ratios (Madhusudhan, 2012). Therefore, we generated a comprehensive grid of models (totalling 240) combining H_2O and CH_4 as described in Table 3.2. We also included a large under-abundance, $\log_{10}(\mathrm{VMR}) = -20$, for each species to simulate the absence of any opacity source from that species. We additionally also produced single molecular species models with H_2O and CO_2 as described in Table 3.1. The opacity of CO_2 is expected to be lower compared to that of the CH_4 and H_2O in chemical equilibrium. However, we include CO_2 as the single species models allow us to analyse the data for any disequilibrium chemical processes that could produce higher abundances of observable CO_2 in the atmosphere.

Some of the most up-to-date high resolution line list data were used for each species; CH_4 was taken from HITRAN 2016 (Gordon et al., 2017) and H_2O and CO_2 taken from the high temperature HITEMP 2010 (Rothman et al., 2010a) database.

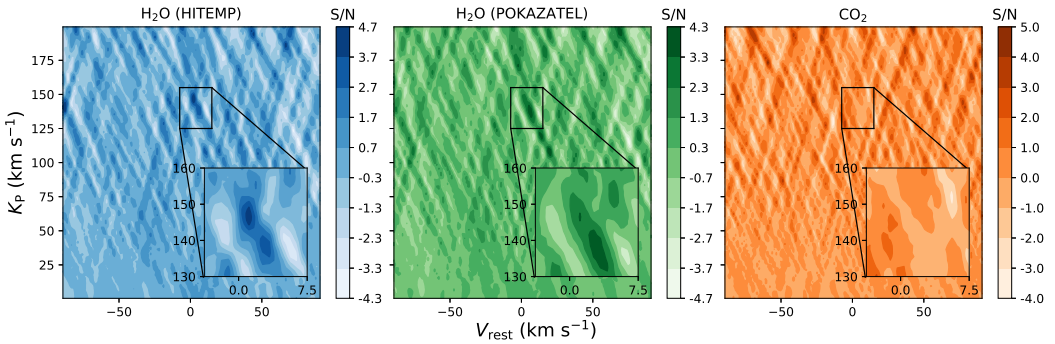

Figure 3.2: CCFs of all the various species analysed with the L-band data. The velocity map is given as the projected radial velocity, $K_{\rm P}$, and the planet rest frame, $V_{\rm rest}$. The colour-bar indicates the strength in S/N of the contours. Left: The best-fitting model for H_2O and CH_4 combined models, containing a high and negligible abundances of H_2O and CH_4, respectively, $\log_{10}(\mathrm{VMR}_{\mathrm{H_2O}}) = -3.5$ and $\log_{10}(\mathrm{VMR}_{\mathrm{CH_4}}) = -20$. A weak detection of H_2O can be seen in the zoomed image at $(K_{\rm P}, V_{\rm rest}) \approx (145,\, 1.5)\,\mathrm{km\,s^{-1}}$. Middle: CCF of H_2O with the POKAZATEL line list. There is also evidence for a weaker detection of water vapour in these models. Right: Same as the middle panel but for the models only containing CO_2. There is a non-detection for CO_2 for these models.

We also generated single molecular models of the new and more complete water line list, POKAZATEL (Polyansky et al., 2018), from the ExoMol database as a comparison to HITEMP regularly used in past HRS observations.

3.6 *L*-band analysis

As discussed in Section 3.5.3, we tested the L-data against a large grid of models with various opacity sources likely to be present in the L-band. Each model atmosphere in the grid was cross-correlated as a function of the projected radial velocity, $K_{\rm P}$, and the systemic velocity, $V_{\rm sys}$, from equation (3.1). The significance of any signal in the CCF was initially taken to be the S/N, which we estimated by dividing each cross correlation value through by the standard deviation of the total CCF matrix as described in Section 3.5.2.

In Figure 3.2 we show the best-fitting CCFs for all the models analysed. We find evidence for a weak and localised H_2O absorption signature on the day-side emission spectrum of the planet at a maximum S/N=4.8. This signal peaks in the CCF at a $K_{\rm P} \approx 145\,\mathrm{km\,s^{-1}}$ and slightly shifted from rest frame at a $V_{\rm rest} \approx 1.5\,\mathrm{km\,s^{-1}}$. It is obtained with models with a shallow atmospheric lapse rate of $\mathrm{d}T/\mathrm{d}\log_{10}(p) \approx 33\,\mathrm{K}$ per dex and a pure water spectrum, i.e. $\log_{10}(\mathrm{VMR}_{\mathrm{H_2O}}) = -3.5$ and $\log_{10}(\mathrm{VMR}_{\mathrm{CH_4}}) =$

Table 3.1: Single species grid of models analysed with the L-band data.

Trace species	$\log_{10}$(VMR)	T_2 (K)	$\log_{10}(p_2)$ (bars)	Line list database
CO_2	[−3.5, −4.5, −5.5]	[1450, 1800, 2150]	[−1.5, −2.5, −3.5, −4.5]	HITEMP 2010
H_2O	[−3.5, −4.5, −5.5]	[1450, 1800, 2150]	[−1.5, −2.5, −3.5, −4.5]	EXOMOL

Table 3.2: Multi-species grid of models analysed with both the L and K-band data. The exception with the K-band models being that they also included a third species of CO fixed at a $\log_{10}(\text{VMR}) = -4.5$.

Trace species 1	Trace species 2	$\log_{10}(\text{VMR}_1)$	$\log_{10}(\text{VMR}_2)$	T_2 (K)	$\log_{10}(p_2)$ (bars)
H_2O (HITEMP)	CH_4 (HITRAN)	[−3.5, −4.5, −5.5, −20]	[−4.5, −5.5, −6.5, −7.5, −20]	[1450, 1800, 2150]	[−1.5, −2.5, −3.5, −4.5]

−20. It should be noted that the significance of the peak in the CCF is only weakly dependent on the T-p profile, with a steeper profile only marginally decreasing the planet signal. Consequently, we find no evidence for CH_4 being a strong opacity source in the atmosphere, with an increasing abundance in CH_4 decreasing the strength of the planet signal from H_2O. There was also no positive correlation with the models including a inverted T-p profile, ruling out a temperature inversion in the atmosphere HD 179949 b in agreement with BR14.

When we analyse the data against the POKAZATEL line list grid of models in table 3.1, we find that the CCF peak is weaker (S/N = 3.5) than the planet signal seen in the analysis with the HITEMP line list. We also find no evidence for CO_2 in the atmosphere with no significant peak in the region of the planet signal in the CCF for the entire grid of models (see the middle and right-hand plots in Figure 3.2).

3.6.1 Expected signal retrieval with injected spectra

In order to give an estimation on the strength of the signal we would expect to be coming from the planet in the L-band data, we inject artificial atmospheric spectra at the expected planet radial velocity. This gives an estimation on how sensitive this data-set is to a detection for the various species used in the atmospheric models in Tables 3.1 and 3.2.

To extract an accurate artificial signal from the data, we first need to convert the model fluxes to the scale of observable flux values in thermal emission ($F_{\rm scaled}(\lambda)$). Here, we follow the approach from the literature (e.g. Brogi et al., 2014; Schwarz et al., 2015) whereby we scale each model spectrum with the host stellar black-body ($F_{\rm S}(\lambda)$), in the wavelength range of the observations, and the ratio between the radii of the planet and star, i.e.,

$$F_{\rm scaled}(\lambda) = \frac{F_{\rm model}(\lambda)}{F_{\rm S}(\lambda)} \left(\frac{R_{\rm P}}{R_{\rm S}}\right)^2 . \tag{3.4}$$

The host stellar and planet parameters were taken to be; $T_{\rm eff} = 6260\,{\rm K}$, $R_S = 1.22\,R_\odot$ and $R_{\rm P} = 1.35\,{\rm R_J}$, the latter of which was also taken from the estimate given in BR14. The scaled flux was convolved to the resolution of CRIRES, spline interpolated and shifted to the planet rest frame velocity using equation 3.1, with a fixed projected radial velocity at the position of the real planet signal observed in Figure 3.2, $K_{\rm P} = 145\,{\rm km\,s^{-1}}$. The artificial spectra was injected into the observed

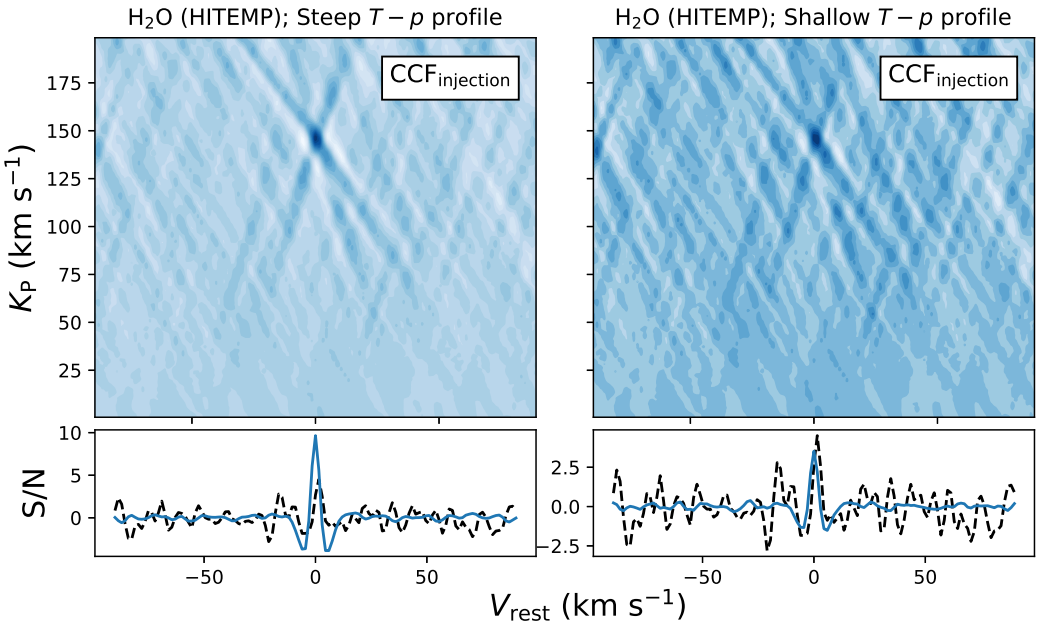

Figure 3.3: Injected CCFs into the L-band data as a function of the projected radial and rest-frame velocity of the planet, K_P and V_rest. Artificial spectra, pertaining to the models producing the strongest signals for the HITEMP H_2O models with no contribution from CH_4 (see Figure 3.2), were injected into the data (upper panels). The left and right-hand panels result from the differing steepness in $T-p$ profiles. The bottom panels show a slice of the expected ($\mathrm{CCF_{noiseless}}$, solid blue line) and observed CCFs ($\mathrm{CCF_{observed}}$, dashed black line) at the injected velocity, $K_\mathrm{P} = 145\,\mathrm{km\,s^{-1}}$. The shallower, more isothermal, $T-p$ profile gives us a better fit to the observed CCF.

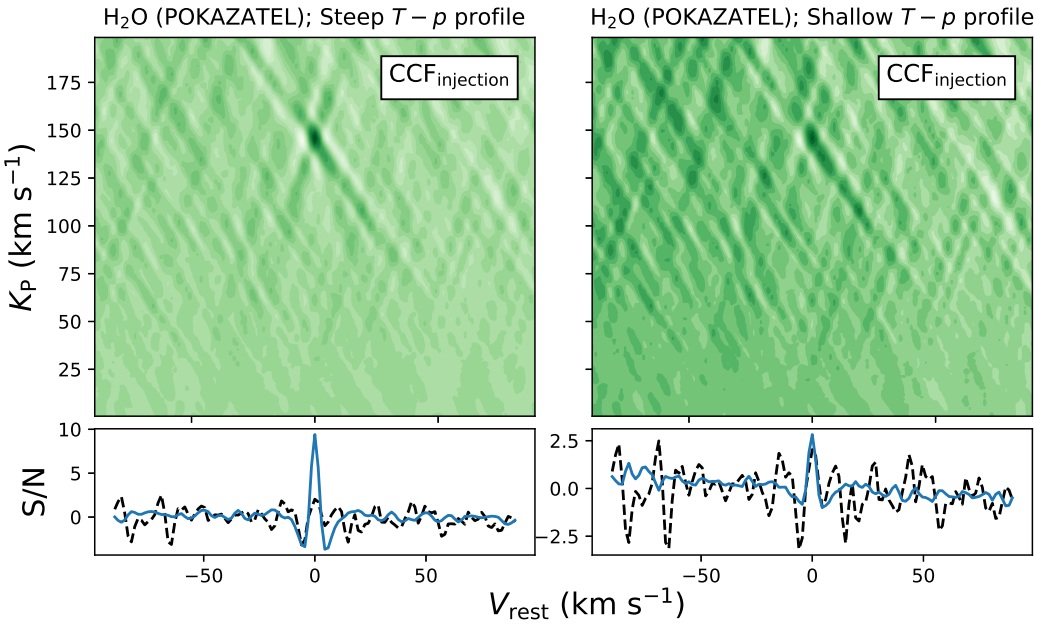

Figure 3.4: Same as Figure 3.3, but for the single species POKAZATEL H_2O line list. Again, the observed CCF is more consistent with a shallower $T - p$ profile.

spectra (F_{observed}) given by,

$$F_{\text{scaled+observed}}(\lambda) = F_{\text{observed}} \times (1 + F_{\text{scaled}}), \tag{3.5}$$

as a means to include the noise structure of the observations. As a final step, these spectra are passed through the telluric removal stage of the pipeline, as described in section 3.5, before they are cross-correlated with the model spectrum that correspond to their injected spectrum.

The final CCFs for the artificially injected signals will then contain a superposition of the actual observed spectra ($\text{CCF}_{observed}$) with that of the injected spectra ($\text{CCF}_{\text{injection}}$) due to the inclusion of the observed spectra as indicated in equation 3.5.

$$\text{CCF}_{\text{noiseless}} = \text{CCF}_{\text{injection}} - \text{CCF}_{\text{observed}}\,, \tag{3.6}$$

producing an almost noiseless CCF. We also note that because the artificial planet signal is injected into the observed spectra, we are still dividing through the cross-correlation values with the noise of the observed spectra, hence, the amplitudes of the CCFs are expressed in S/N units as in section 3.6.

In Figure 3.3, we show the injected CCFs from the combined H_2O and CH_4 model that produces the strongest signal (see Section 3.6) and compare the differ-

ence between the steep and shallow $T-p$ profiles, $\mathrm{d}T/\mathrm{d}\log_{10}(p) \approx 110$ and 33 K per dex, respectively. The weak planet signal seen in the CCF is more consistent with a shallower and therefore a more isothermal $T-p$ profile. The slight shift in V_{rest} from the observed signal can clearly be seen when compared to the injected CCF. The width of the observed signals is qualitatively consistent with the FWHM of CRIRES indicating that there is no rotational broadening of the planet. From the CCF with a steeper profile we would have expected a much higher S/N than that observed in Section 3.6. This is not surprising as a shallower temperature gradient would produce more muted absorption features in the emission spectrum. This differs from the results obtained in BR14, which find a steeper $T-p$ profile of $\mathrm{d}T/\mathrm{d}\log_{10}(p) \approx 330$ K per dex as their best-fitting atmospheric model. However, this result was also stated to be weakly dependant on the lapse rate. By inverting the molecular abundances in the combined models above (i.e. using a $\log_{10}(\mathrm{VMR}_{\mathrm{H_2O}}) = -20$ and $\log_{10}(\mathrm{VMR}_{\mathrm{CH_4}}) = -4.5$), we find very similar results as in Figure 3.3, hence, the data is highly and weakly sensitive to strong CH_4 spectral features in steep and shallow T-p profiles, respectively.

Similarly, in Figure 3.4 we show the injected CCFs for the H_2O POKAZATEL line list again for a shallow and steep T-p profile and show the expected significance of a planet signal from the data. The tentative detection in the observed CCF is again consistent with the atmosphere having a shallow temperature gradient with the steeper T-p profile clearly showing a strong signal. When the same procedure was repeated for the CO_2 models, however, even with the steep T-p profiles the expected signal strengths were not above the threshold of detection of $\mathrm{S/N} \geqslant 3$ suggesting this data-set is not sensitive enough to observe this species.

3.6.2 Constraints on the detectability of methane

We can also estimate the lowest abundance of CH_4 that we may be able to detect by modelling an atmosphere at the maximum possible atmospheric temperature gradient. We follow a similar analysis as in section 3.6.1 and model a spectrum of HD 179949 b at the adiabatic lapse rate for a diatomic gas, $(\mathrm{d}\ln T/\mathrm{d}\ln p)|_{\mathrm{ad}} = 2/7$. This lapse rate is the limit beyond which the atmosphere becomes unstable against convection. Injection and recovery of these adiabatic models with varying CH_4 abundances allows us to constrain the detectability.

In Figure 3.5, we show the CCFs for the varying abundances of CH_4 sliced at the injected planet velocity. For relatively high levels of CH_4 in the atmosphere, $\log_{10}(\mathrm{VMR}_{\mathrm{CH_4}}) \geqslant -6.5$, we find that these signals are detectable in the CCFs peaking above the noise of the data at $\mathrm{S/N} > 10$. However, we show in the bottom panel

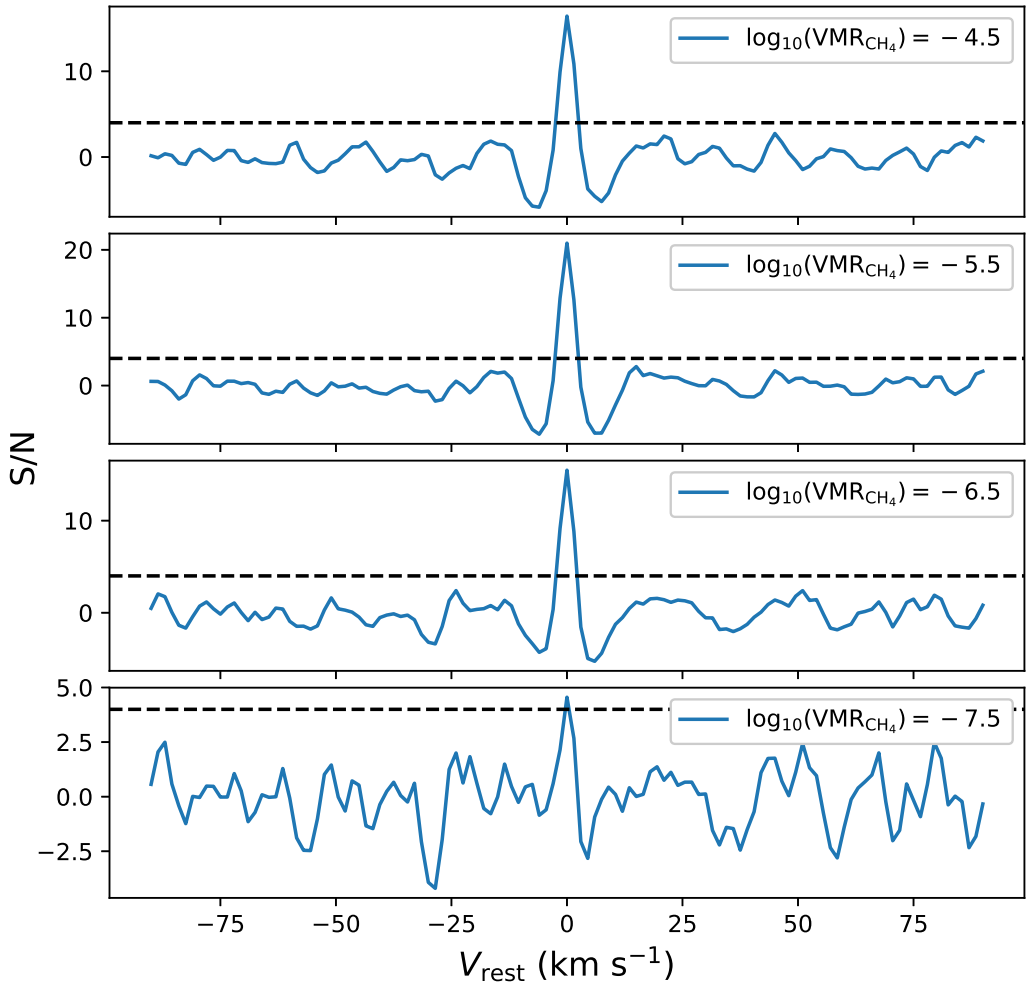

Figure 3.5: Injected CCFs ($\mathrm{CCF_{injection}}$) of pure CH_4 models at the atmospheric adiabatic limit, at varying abundances, into the L-band data. The CCFs have been sliced at the injected velocity of $K_\mathrm{P} = 146\,\mathrm{km\,s^{-1}}$. The black dashed lines indicate a detection level of $\mathrm{S/N} = 4$.

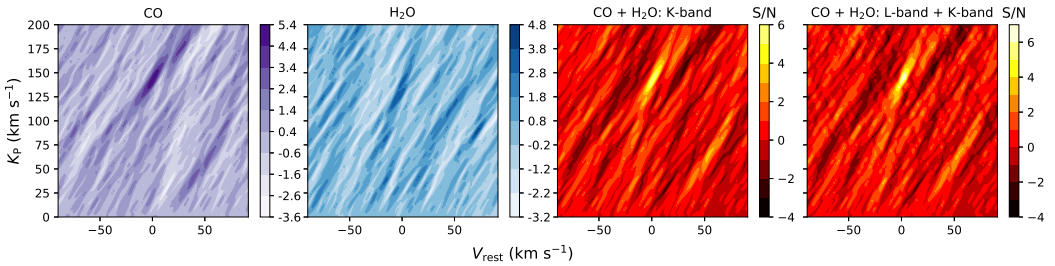

Figure 3.6: Best-fitting CCFs of single and combined species for the K-band and combined data-sets. Far-left: Pure CO model CCF with the K-band data. Centre-left: Pure H_2O model CCF with the k-band data. Centre-right: Combined CO and H_2O species model CCF for the K-band data. Far-right: Combined K- and L-band data-sets CCFs with their corresponding best-fitting combined species models (i.e. CO and H_2O and pure H_2O models for the K- and L-band, respectively).

of Figure 3.5 that for a CH_4 abundance of $\log_{10}(\mathrm{VMR}_{\mathrm{CH_4}}) = -7.5$, the CCF peaks at just above the detectable limit that we place at a $\mathrm{S/N} = 4$. This limit has been estimated as being $\Delta(|\mathrm{S/N}|) = 1$ above the approximate peak level of the noise of the data. At this level, we are roughly at the limit of what can be distinguished as a signal originating from the planet rather than a spurious peak in the CCF. Hence, regardless of the temperature gradient, we are unable to constrain CH_4 in the atmosphere of HD 179949 b at abundances below $\log_{10}(\mathrm{VMR}_{\mathrm{CH_4}}) = -7.5$. Chemical models of similar hot Jupiters indicate that the CH_4 VMR at solar abundance is $\log_{10}(\mathrm{VMR}_{\mathrm{CH_4}}) \sim -7.5$ (Moses et al., 2013). As the actual temperature gradient of the atmosphere of HD 179949 b is shallower than the adiabatic lapse rate, we would expect the limit of detectability to be at higher CH_4 abundances. Therefore, it is not unexpected that we are unable to detect CH_4 with these observations in the L-band.

3.7 *L* and *K*-band combined analysis

We expand on the analysis by combining this data at 3.5 μm with the previous data set observed at 2.3 μm in order to provide better constraints on the orbital parameters of the system. We do not re-process the 2.3 μm data here, we instead reuse the telluric-subtracted data already calculated by BR14. We also adopt their wavelength calibrations, while orbital phases are computed consistently with the previous analysis. As done in BR14, we remove detector 4 which showed residual behaviour from the known 'odd-even' effect. This data-set contained a total of 500 spectra taken over three separate nights, which combined with the data taken at

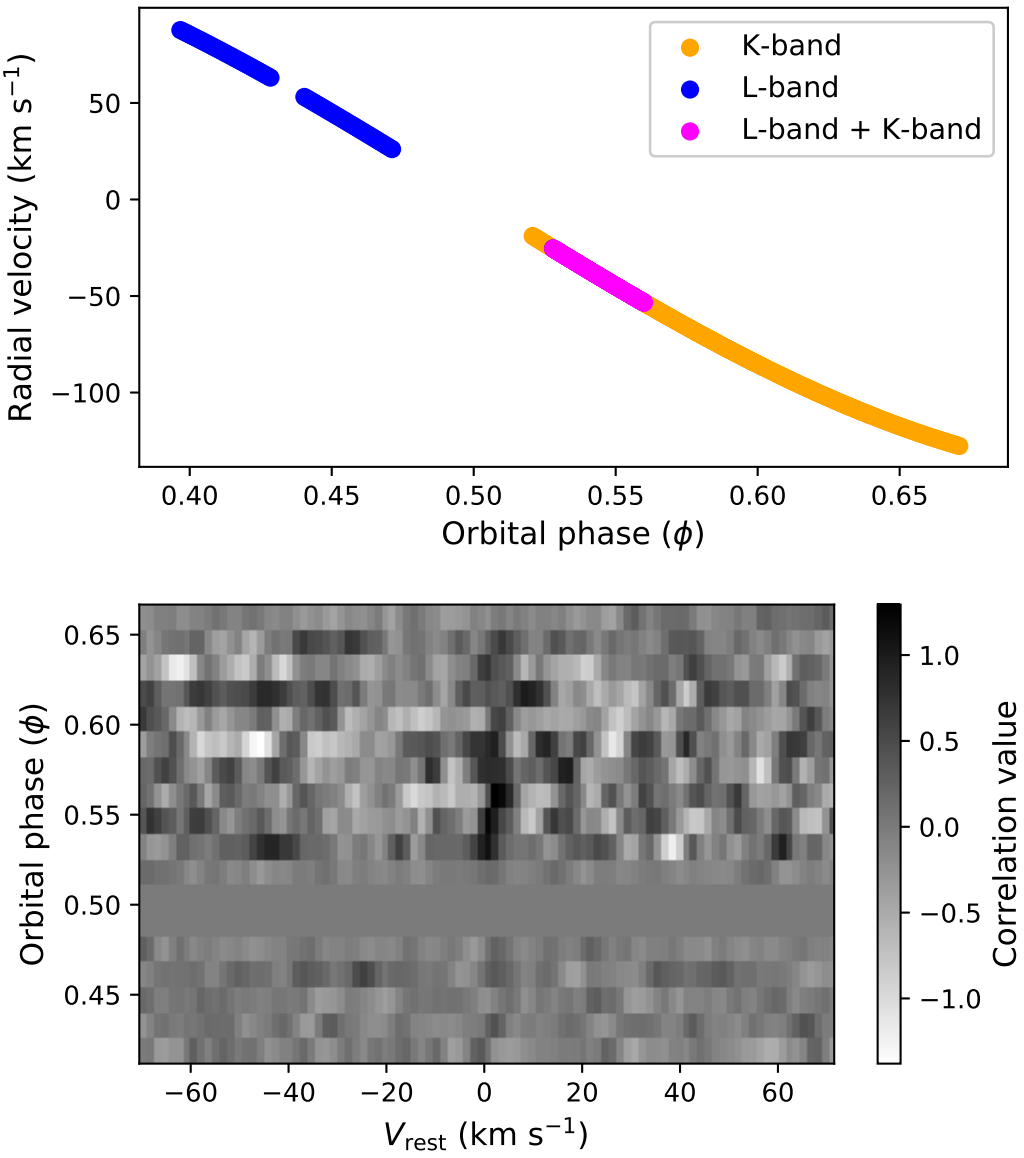

Figure 3.7: Top: Radial velocity of HD 179949 b as a function of the observed orbital phases in the L-band (blue circles), K-band (orange circles) and the phases observed with both data-sets (magenta circles). This planet radial velocity does not include the velocity corrections for an observer on earth. Bottom: Phase binned cross-correlation values of the combined data-set with both bands with their respective best-fitting model atmospheres, shifted to the planet rest-frame velocity. The gap in the right-hand panel corresponds to the large gap in the phase coverage shown in the top panel. There is a noticeable trail of positive correlation values at $V_{\rm rest} \approx 0\,{\rm km\,s^{-1}}$ indicating a detection of the atmosphere of HD 179949 b.

3.5 μm totals 619 spectra taken at high resolution of HD 179949 b, covering a phase range of $\phi \approx (0.397\text{-}0.671)$ (see the left-hand panel of Figure 3.7).

To remain as consistent with the analysis done here in the *L*-band and that done by BR14, we re-computed the cross correlation of the *K*-band data with the models listed in Table 3.2, and calculated with the addition of CO at a constant abundance of $\log_{10}(\mathrm{VMR_{CO}}) = -4.5$. As for the *L*-band data, we also estimate the S/N ratio by co-adding along the time-axis of all the spectra and dividing by the standard deviation of the total CCF matrix (see Section 3.5.2). This was to ensure that the both data-sets were weighted equally when co-adding their correlation values.

We are able to reproduce the results from BR14 with single species detections from CO and H_2O and a combined model of the two species as shown in the first three CCFs in Figure 3.6. We also find that the best-fitting atmospheric model for HD 179949 b in the *K*-band is a model containing both CO and H_2O which peaks at $\mathrm{S/N} = 5.6$, therefore, we include both species in the combined band analysis. We find that the best-fitting model for the *K*-band data to also have a shallow lapse rate of $\mathrm{d}T/\mathrm{d}\log_{10}(p) \approx 33\,\mathrm{K}$ per dex, with a H_2O abundance of $\log_{10}(\mathrm{VMR_{H_2O}}) = -4.5$ and with no contribution from CH_4. This is fully consistent with what was found in the *L*-band analysis as described in Section 3.6. We also find that the CCFs peak at $K_\mathrm{P} \approx 143\,\mathrm{km\,s^{-1}}$ and at $V_\mathrm{rest} \approx 0\,\mathrm{km\,s^{-1}}$, as found in BR14. The final panel in Figure 3.6 shows the CCF of the two best-fitting models, as described in Section 3.6 and above, with the combined band data-set. This CCF peaks at a $\mathrm{S/N} = 6.4$ in the expected region of the planet radial velocity, $K_\mathrm{P} \approx 145\,\mathrm{km\,s^{-1}}$ and $V_\mathrm{rest} \approx 0\,\mathrm{km\,s^{-1}}$. The combination of the two bands increase the significance in S/N and further constrain the orbital signature of the planet.

The phase resolved CCFs, binned by 0.015 in phase and spanning the orbital phase coverage for the combined data-set is shown in the bottom panel of Figure 3.7. These cross correlations have been shifted to the rest frame of the planet, and positive correlation should appear as a vertical line of darker hues at $V_\mathrm{rest} \approx 0$. Indeed for certain phase bins that contain more spectra (the overlapped phase coverage seen in the top panel of Figure 3.7), we see a noticeable positive correlation trail consistent with being contained within the planets radial velocity. This shows that the signal is present in both data-sets and co-adds constructively at the position of the planet, despite the difference of three years between the observations of BR14 and the *L*-band data.

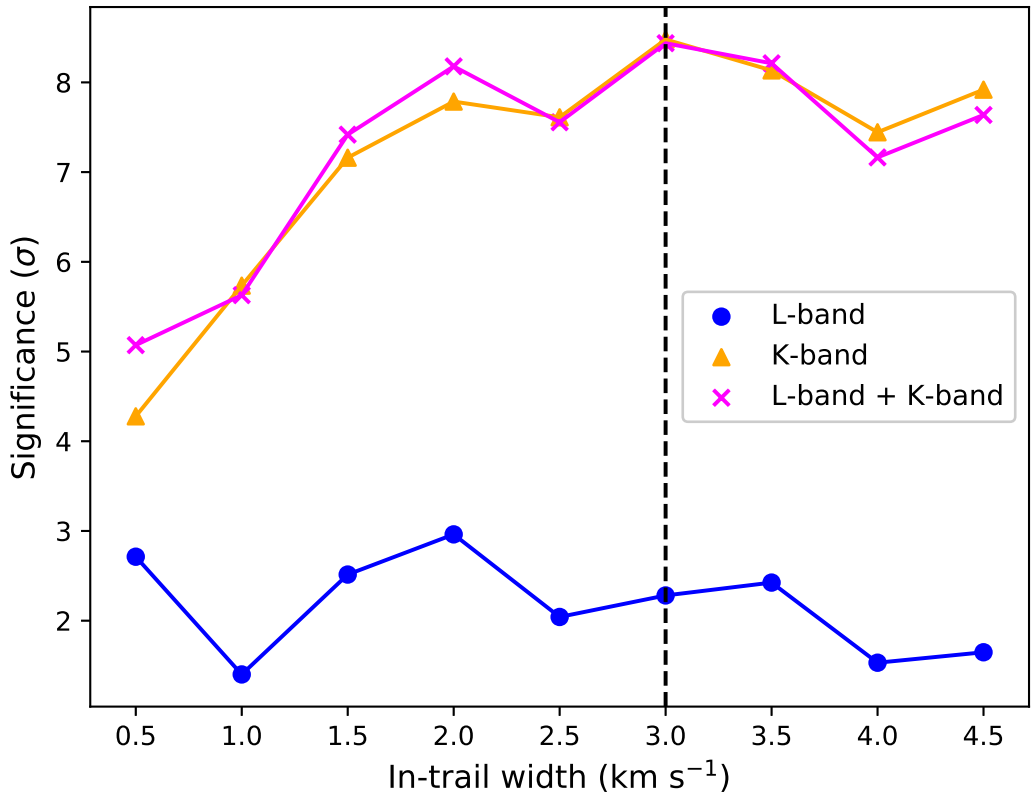

Figure 3.8: Welch T-test significance as a function of the radial velocity width included in the in-trail distributions for the best-fitting atmospheric model CCFs for each data-set. The dashed black line indicates the typical position of the FWHM of CRIRES detectors. The L-band data peaks in significance at an in-trail width of $2\,\mathrm{km\,s^{-1}}$. The K-band and combined bands peak in significance at the typical location of the FWHM for CRIRES, $3\,\mathrm{km\,s^{-1}}$.

3.8 Statistical analysis

3.8.1 Welch *T*-test

Thus far, we have only determined the significance of the CCFs by using the S/N analysis which has been shown to be a good proxy for the level of confidence for the detection of trace species in previous analyses (e.g. Brogi et al., 2012; Birkby et al., 2013; de Kok et al., 2013; Brogi et al., 2016; Hoeijmakers et al., 2018a; Cabot et al., 2019; Hoeijmakers et al., 2019). However, it is usually the case in the literature to perform further statistical tests on the significance of any peaks in the CCF resulting from the signature of the planet. Apart from the standard S/N analysis as explained in chapter 2.6.3, the most widely used test is the Welch T-test (Welch,

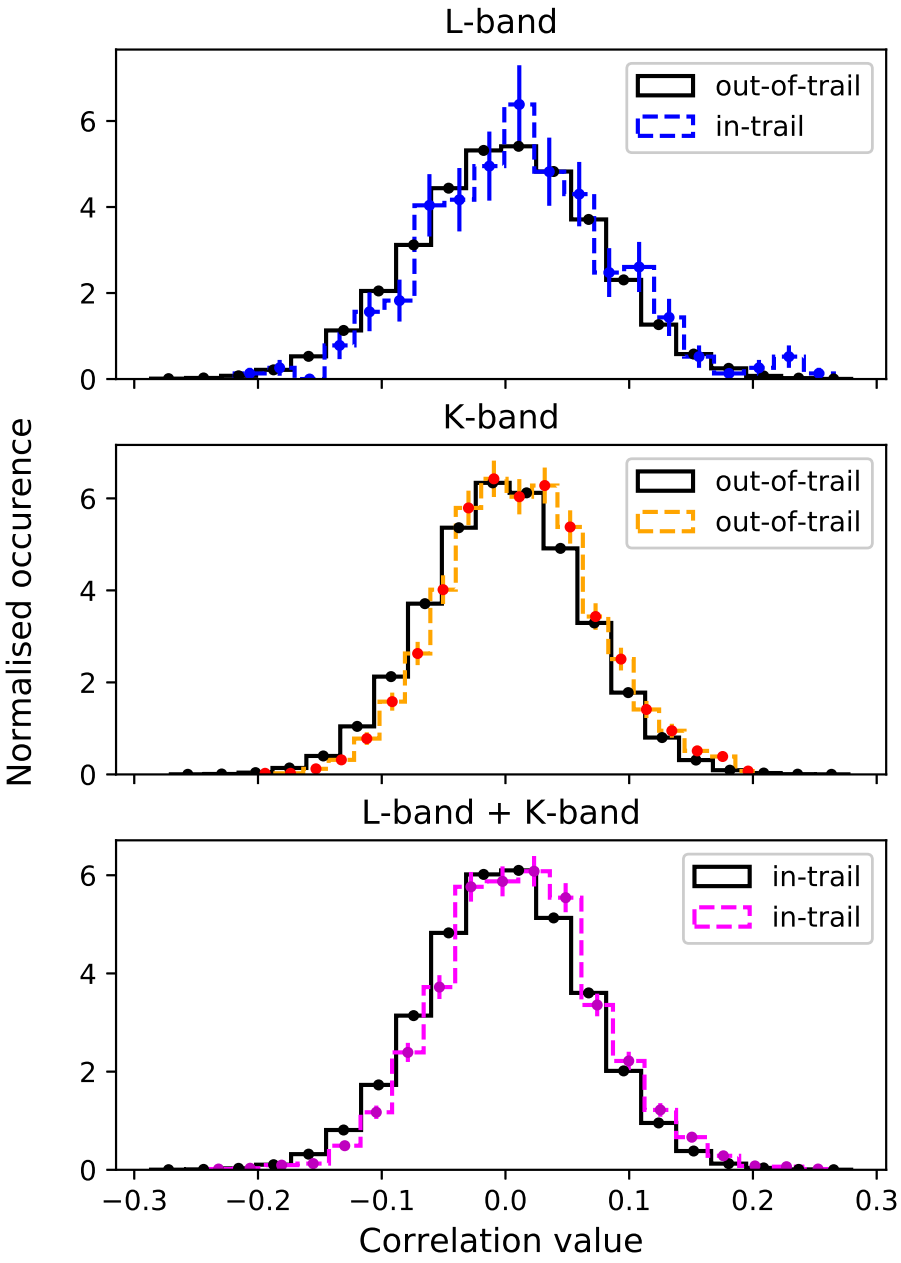

Figure 3.9: Normalised distributions of the correlation values within (in-trail) and outside (out-of-trail) the radial velocity of HD 179949 b for the L (upper panel), K (middle panel) and combined bands (lower panel). The Welch T-test rejects the null hypothesis for the L (blue circles), K (orange triangles) and combined bands (magenta crosses) by $3.0\,\sigma$, $8.4\,\sigma$ and $8.4\,\sigma$, respectively. There is a noticeable positive shift in the two distributions, particularly for the K and combined bands indicating stronger correlations for the atmospheric models within the radial velocity of the planet.

1947) (see section 2.7.1) which is used to measure the confidence from which you can reject the null hypothesis that two Gaussian distributions that have the same mean value. We follow similar methods in the literature (e.g. Brogi et al., 2012) where we sample two distributions which are correlation values that fall inside and outside the radial velocity of the planet (equation 3.1) and measure the significance that these two distributions are not drawn from the same parent distribution. We map out this significance as a function of $K_{\rm P}$ and $V_{\rm rest}$, as was done in the S/N analysis, and determine the $V_{\rm P}$ to be where the significance peaks in the T-test. We find for all bands, the detection significance peaks at the same projected radial velocity, $K_{\rm P} \approx 145\,{\rm km\,s^{-1}}$, therefore, we take the radial velocity to be at this value according to equation 3.1.

The significance of a detection that is stated by the T-test is strongly dependent on the chosen width of the in-trail distribution (Cabot et al., 2019) and can change depending on the specific data-set and instrument used (Brogi et al., 2018). We define the out-of-trail distribution to only include those correlation values more than $10\,{\rm km\,s^{-1}}$ away from the radial velocity of the planet. In Figure 3.8, we show the dependency of the significance on the chosen radial velocity width of the planet in-trail distribution (we note that a shift of $1.5\,{\rm km\,s^{-1}}$ corresponds to ~ 1 pixel on the map in Figure 3.7), for each band. These are obtained from the models which give the highest S/N, i.e. a pure H_2O model ($\log_{10}({\rm VMR_{H_2O}}) = -3.5$) and a combined model of CO and H_2O ($\log_{10}({\rm VMR_{CO}}) = -4.5$ and $\log_{10}({\rm VMR_{H_2O}}) = -4.5$) for the L and K-bands, respectively (see sections 3.6 and 3.7). Similarly to Cabot et al. (2019), we find that for the combined L- and K-band analysis the CCFs with the strongest signals (S/N $\gtrapprox 6$) result in a much higher detection significance (8.4σ) which varies by up to 1σ when changing the width by $\sim 0.5\,{\rm km\,s^{-1}}$. Vice versa, for a weak planet signal as that of the L-band analysis, the T-test returns a detection significance which is 1.8σ below the S/N level, peaking at $3.0\,\sigma$. Overall, we obtain a peak in significance at reasonable in-trail widths of roughly the FWHM of the CRIRES detectors ($\sim 3\,{\rm km\,s^{-1}}$). However, the exact width of the planet signal will likely differ between data-sets because of variations in the broadening of the CCF caused by the probing of different atmospheric pressures along the optical path which is a function of wavelength. Figure 3.8 also shows that the significance of each data-set shows a steady increase to $\sim 1.5\,{\rm km\,s^{-1}}$, as the in-trail distributions include more of the planet signal, where the significance plateaus before decreasing again as the in-trail distribution starts to include more noise. We note that the anomalous spike in the significance at $0.5\,{\rm km\,s^{-1}}$ ($\sim 3\,\sigma$) in the L-band data is probably due to low number statistics. Therefore, we quote to be the significance in the L-band

detection to be the peak of $3\,\sigma$ at an in-trail velocity of $2\,\mathrm{km\,s^{-1}}$.

In Figure 3.9, we show the in- and out-of trail distributions for the two bands separately and the combined data-set. We chose the in-trail widths that peaked in significance in Figure 3.8 for each data-set. For the K and combined bands, there is a clear shift towards higher correlation values in the in-trail compared to the out-of-trail distributions with a detection of $8.4\,\sigma$ for both data-sets for a model containing both CO and H_2O in absorption. Qualitatively it appears that the L-band distributions have more overlap and that is reflected in the reduced detection significance of $3.0\,\sigma$.

3.8.2 Constraining the orbital and physical parameters of HD 179949 b

Following the statistical testing above, we are now able to constrain the orbital and physical parameters as done in BR14. These parameters are derived from the analysis of the combined L and K-band data-set and their respective best-fitting atmospheric models (see Section 3.7).

We find that the cross correlation from the best-fitting models peaks at the projected radial velocity of $K_\mathrm{P} = (145.2 \pm 2.0)\,\mathrm{km\,s^{-1}}$ ($1\,\sigma$ error bars). The error bars on K_P were determined by measuring the width of the $1\,\sigma$ contour containing the peak in the T-test significance map. Since we have measured directly the orbital motion of HD 179949 b with a set of time-series spectra, we can combine the orbital motion of the host star and the planet and derive the planet mass and orbital inclination of the system. As in BR14, we take the most recent measurement of the radial velocity measurement of HD 179949, $K_\mathrm{S} = (0.1126 \pm 0.0018)\,\mathrm{km\,s^{-1}}$, and translate that to a mass and radial velocity ratio. Using the derived mass of HD 179949 in Takeda et al. (2007) (see Section 3.3.1), this translates to an absolute planet mass of

$$M_\mathrm{P} = \left(\frac{K_\mathrm{S}}{K_\mathrm{P}}\right) M_\mathrm{S} = \left(0.963^{+0.036}_{-0.031}\right) \mathrm{M_J}. \tag{3.7}$$

Using the derived value of the semi-major axis in Wittenmyer et al. (2007), $\mathrm{a} = (0.045 \pm 0.001)\,\mathrm{AU}$, and an orbital period of $P = (3.092514 \pm 0.000032)$ days (Butler et al., 2006), we were able to derive the orbital inclination as:

$$i = \arcsin\left(\frac{PK_\mathrm{P}}{2\pi \mathrm{a}}\right) = \left(66.2^{+3.7}_{-3.1}\right)^\circ \tag{3.8}$$

The error bars on both quantities were determined by drawing 10,000 random points from Gaussian distributions for the known parameters with the stan-

dard deviation equal to their quoted error bars and a mean value equal to their quoted best-fitting value. Unequal error-bars were reproduced by drawing from Gaussian distributions with unequal standard deviation for positive and negative values. Planet mass and orbital inclination were then computed as indicated above and the 15.85-84.15 per cent of the resulting empirical cumulative distribution taken as $1\,\sigma$ error bars.

Despite the revised error bars in $K_{\rm P}$ are 70 per cent smaller than in BR14, we were able to only slightly improve their constraints on planet mass and orbital inclination. The reason for this is that the determination of these parameters is dominated by the error on the stellar mass (for $M_{\rm P}$) and semi-major axis (for i). The parameters determined here are in full agreement within $1\,\sigma$ with those determined in BR14.

3.9 Discussion

In this chapter, we primarily wanted to explore the possibility that we could observe further molecular species with observations centred on $3.5\,\mu$m from the analysis done at $2.3\,\mu$m and, hence, improve the constraints on the C/O ratio of the planet. In de Kok et al. (2014), it is shown that at $3.5\,\mu$m, we should be able to observe H_2O, CH_4 and CO_2 with $\sim 2\times$ the relative correlation values than at $2.3\,\mu$m, if these opacity sources are present. Furthermore, we also wanted to test the new POKAZATEL H_2O line list with the cross-correlation technique in the L-band. Finally, we hoped to further constrain the orbital and, hence, the physical parameters of the non-transiting planet by combining the L and K-band data in BR14. Below, we discuss our results and the predictions made above with what we obtained in the L-band and the subsequent merging of this data and the one presented in BR14.

3.9.1 Weak detection of water vapour in the *L*-band: Astrophysical or line-list inaccuracies?

Here, we only detect a weak detection of H_2O in absorption in the thermal emission spectra of HD 179949 b at $3.5\,\mu$m with a steep $T-p$ profile. We find a peak detection of H_2O in the CCF at a $S/N = 4.8$ (see section 3.6) which translated into a Welch T-test significance of $3.0\,\sigma$ (see Section 3.8.1). This is perhaps on the boundary of detection significance, however, since the position of the planet signal in velocity space matches that of the strong detections in BR14, we are confident that this signal is produced by the planet and is not a spurious signal in the data.

The question that should now be asked is why we observe in the L-band a

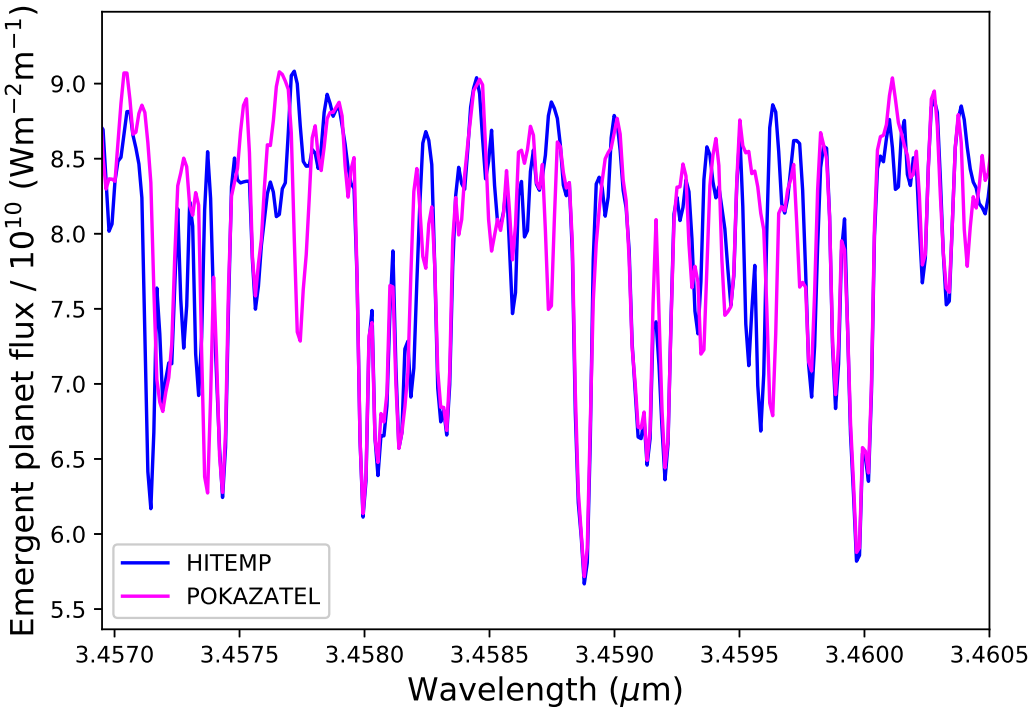

Figure 3.10: The model emergent planet flux in a small section of the spectral range covered in the L-band using the HITEMP (blue) and POKAZATEL (magenta) H_2O line lists.

weaker signal than expected from BR14. In their study, it was found that the best-fitting atmospheric T-p profile is rather steep, with a lapse rate of $\mathrm{d}T/\mathrm{d}\log_{10}(p) \approx 330\,\mathrm{K}$ per dex. Similar lapse rates were used to drive the predictions of de Kok et al. (2014), also resulting in correspondingly stronger spectral lines. In our re-analysis of the K-band data here, and consistently to the analysis of the L-band, the strongest signal is found for a shallower atmospheric profile. This is further corroborated by our injection tests that seem to produce a better match to the observed amplitude of the CCF with shallow $T-p$ profiles. It is also predicted that highly irradiated giant planets, such as HD 179949 b, would indeed produce weaker H_2O features in the emission spectrum due to a more isothermal temperature gradient in the upper atmosphere (Seager and Sasselov, 1998). However, as mentioned in Section 3.6, it should be noted that the cross-correlation technique is weakly dependent on the actual $T-p$ profile usually with only a marginal preference of the lapse rate used. By including all the models that produce a significant detection, which we chose to be within one $1\,\sigma$ of the maximum S/N, we find a slight preference of 54 per cent for the models with the shallower lapse rate. This dual behaviour is driven by a well known degeneracy between lapse rate and abundance, with steeper lapse rates that can be accommodated by less abundant water, and vice versa.

Previous studies have suggested that inaccuracies of line lists could hinder or even prevent detections at high spectral resolution (Hoeijmakers et al., 2015). In Figure 3.2 we show that for the L-band data of HD 179949 b a signal is seen with two of the most complete line lists currently available, i.e. HITEMP and POKAZATEL, but with the latter delivering a detection weaker by a $\Delta(\mathrm{S/N}) \sim 1$. This result is suggestive that minor differences between the line lists could play a role in this data-set too. In Figure 3.10, we show a small section of the emergent planet flux in the L-band comparing the two line lists used in this analysis at a resolution of $R = 300000$. There are some hints that these line lists show differences at such high resolving powers in the wavelength range of these observations. This is not completely unexpected, because the cross section of water vapour around 3.5 μm is relatively weaker, and this may result in more uncertain line positioning from experimental measurements particularly for the more numerous set of weaker lines in this wavelength range. However, we do expect to extract strong signals from either line list with higher S/N observations and at wavelength bands where water is at a higher opacity than in the L-band.

3.9.2 Non-detections of carbon-bearing species

We also analysed the L-band data against the carbon-bearing species, CH_4 and CO_2, that, if present, would be more observable at this wavelength range. Like in BR14, we also find no evidence of CH_4 producing an observable opacity source. Injection tests with atmospheric models at the adiabatic lapse rate allow us to place a lower limit on the detectability of CH_4 at a $\log_{10}(\mathrm{VMR}_{\mathrm{CH_4}}) = -7.5$, for a minimum S/N of 4 which is our threshold for claiming a detection (see Section 3.6.2). However, even for a large abundance of CO_2, the amount of spectra obtained in the L-band is not sensitive enough to observe this species at any physically realistic value of VMR.

Theoretically, if we expect that the atmosphere of HD 179949 b is oxygen rich with a solar C/O ratio at chemical equilibrium (as found in BR14), then we would expect the abundances of these carbon-bearing species to be several orders of magnitude lower than H_2O (e.g. Madhusudhan, 2012; Drummond et al., 2019). Hence, we would expect any spectral features from these additional species to be washed out by the strong opacity source of H_2O. Furthermore, this evidence of an atmospheric solar C/O ratio provides further evidence that the atmosphere does indeed have a shallow $T-p$ profile with the strong H_2O opacity potentially causing a strong greenhouse effect (Mollière et al., 2015) in the upper layers of the atmosphere. Therefore, we attribute the non-detection of CH_4 to be likely due to the atmosphere of HD 179949 b having a solar C/O composition in chemical equilibrium. As a result we qualitatively confirm the constraints of C/O< 1 provided by BR14.

3.9.3 Improving the orbital parameters of the non-transiting planet HD 179949 b

With the inclusion of the K-band data in this analysis, we were able to improve upon the significance in S/N of the molecular signature of the planet. More importantly, we were able to improve the constraint on the projected radial velocity of the planet, K_{P}, due to the combined observations being taken prior to and post superior conjunction. This acts to remove some of the smearing of the planet signal in the direction of whether the spectral lines are being blue or red-shifted, hence, further localising the signal in the CCF velocity map. This in turn allowed a determination on the mass and inclination of the system, however, due to the relatively large uncertainty in the stellar mass and semi-major axis, we were unable to constrain significantly better the mass of the giant planet, and we only provides a slight improvement on the inclination of the system. In line with this, all high resolution

analyses on non-transiting systems thus far have also only been able to constrain the mass to the same level of uncertainty of the host stellar mass ($\geqslant 4$ per cent) (Brogi et al., 2012; Lockwood et al., 2014; Birkby et al., 2017). Without further accurate characterisation of the stellar hosts (e.g. via asteroseismology) or follow up stellar radial velocity observations, improving the determination of planet orbital radial velocities alone using HRS with the cross-correlation technique is unlikely to significantly improve upon the determination of the mass and the inclination of the majority of non-transiting systems beyond a few percent uncertainty.

Remarkably, we find that the radial velocities of HD 179949 b taken three years apart (2011 for the K-band and 2014 for the L-band) agree well and add up coherently in the rest frame of the system. Given that atmospheric circulation patterns can produce shifts up to a few $\mathrm{km\,s^{-1}}$ in the emission spectrum of the planet (Zhang et al., 2017), this means that our observations do not support any strong variability of the circulation or vertical structure of the planet over a timescale of years. Furthermore, given that for a fixed water abundance the K-band spectrum emerges from deeper layers of the atmosphere (higher pressure) than the L-band spectrum, this also points to the absence of strong wind sheer between the lower and the upper portion of the day-side atmosphere. This can be seen from the lack of variability in the phase resolved CCFs (see the bottom panel of Figure 3.7) for the combined data-set for this planet.

3.10 Conclusions

In this chapter we have presented a follow up analysis of the non-transiting HD 179949 system using HRS in the L-band with the CRIRES instrument. We analysed 119 spectra taken as a time series of the day-side emission. We have also produced a combined analysis with high resolution K-band data from the previous analysis by BR14 giving a total of 619 high resolution time series spectra taken of the non-transiting planet HD 179949 b. We find a weak detection of H_2O in the L-band with a $\mathrm{S/N} = 4.8$ with a Welch T-test significance of $3.0\,\sigma$, the first such detection centred around $3.5\,\mu$m. We also find no evidence for any other major opacity sources in the atmosphere with this new data-set. On combining the two data-sets together, we find an improved detection significance of $8.4\,\sigma$ for an atmosphere with CO and H_2O as opacity sources. We state this combined detection significance as the best description of this atmosphere where shielding between the individual species is likely to occur due to the different pressure levels these species absorb in the atmosphere. However, we also independently verify that we also detect CO and H_2O individually

in the K-band data as in BR14. Our best-fitting atmospheric model corresponds to a shallow lapse rate of $\mathrm{d}T/\mathrm{d}\log_{10}(p) \approx 33\,\mathrm{K}$ per dex. This most likely explains the muted features of H_2O in the L-band. Therefore, we find that HD 179949 b is most likely a hot Jupiter with an atmosphere that is oxygen dominated with a solar C/O ratio in chemical equilibrium that is non-thermally inverted. We also determined slight improvements on the orbital and physical parameters of the planet; $K_\mathrm{P} = (145.2 \pm 2.0)\,\mathrm{km\,s^{-1}}$ (1σ error contour from the Welch T-test), $i = (66.2^{+3.7}_{-3.1})^\circ$ and $M_\mathrm{P} = (0.963^{+0.036}_{-0.031})\,\mathrm{M_J}$.

We have demonstrated in this chapter that multiple high resolution data-sets, taken several years apart, covering different bands can be used together to characterise exoplanet atmospheres. We have also shown that by combining these data-sets can be used to improve the orbital parameters of non-transiting systems, which are inherently difficult to constrain with radial velocity measurements alone due to the uncertainty in the inclination of the system. We also find hints that, at the high resolving power of these observations, H_2O line lists may suffer from inaccuracies in line position and strength, at least in the L-band. This is supported by the disagreement in the strength and shape of the CCFs obtained by cross correlating our data with models generated with different line lists. Although we measure a cross correlation signal from water with both line lists utilised for the modelling, we find that the strength of the signal is still dependent on the particular choice. These differences could still be relevant when the measured signals linger at the boundary of detectability, in these cases it may be necessary to use multiple line lists in order to extract the planet signal.

The recent advancements in high resolution spectrographs have and will likely provide significant improvements in HRS characterisation of exoplanet atmospheres in the future. For example, the CARMENES instrument at the Calar Alto Observatory Quirrenbach et al. (2014) (see chapter 2.3), which spans over several spectral orders optical ($\mathrm{R} \sim 94{,}000$) and NIR ($\mathrm{R} \sim 80{,}000$), has recently produced a number of robust detections of transiting systems (Salz et al., 2018; Allart et al., 2018; Alonso-Floriano et al., 2019b,a; Sánchez-López et al., 2019). The NIR high resolution instrument SPIRou (Artigau et al., 2014), which has an even larger simultaneous wavelength coverage with a resolving power of $\mathrm{R} \sim 73{,}000$, is currently in operation and should also produce detections at a S/N competitive with or superior to what was possible with CRIRES. And finally, CRIRES+ (Follert et al., 2014), which is expected to receive its first light in early 2020, will succeed the highly successful CRIRES instrument to provide improved stability and simultaneous NIR coverage by a factor of ten from its predecessor.

Chapter 4

Water observed in the atmosphere of τ Boötis Ab with CARMENES/CAHA

4.1 Notes

This chapter follows work published in Webb et al. (2022). Whilst most of this work is my own work there was however some contributions from the co-authors of the work. Matteo Brogi was the PI of the CARMENES observation proposal which provided three nights of observations in this chapter, with Jayne L. Birkby, Ernst de Mooij and Ignas A. G. Snellen as further CO-I's. Matteo Brogi also helped to edit the main text of the published paper (Webb et al., 2022) which makes up this chapter. Siddharth Gandhi provided the calculations for the atmospheric models used in this analysis and also tested this data-set on their analysis framework. Ignas A. G. Snellen and Yapeng Zhang provided a further two nights of observations that was used in this chapter. Stefan Pelletier and Björn Benneke used their analysis framework from Pelletier et al. (2021) to reproduce the results from this data-set in this chapter.

Corrigendum: the use of "absolute mass" of the planet was incorrectly used in the published version of this chapter Webb et al. (2022). Instead just the mass should have been used here as there are assumptions placed on the mass of the host star in this case. This will be corrected in a published corrigendum of this work.

4.2 Abstract

Characterising the atmospheres of hot Jupiters is important in understanding the formation and migration of these exotic planets. However, there are still many open questions about the chemical and physical properties of these atmospheres. Here, we confirm the detection of water vapour in thermal emission from the non-transiting hot Jupiter τ Boötis Ab with the high resolution NIR CARMENES spectrograph (see chapter 2.3 for more details on CARMENES). Combining over 17 h of observations (560 spectra) and using a Bayesian cross-correlation to log-likelihood approach, we measure a systemic velocity of $V_{\rm sys} = -11.51^{+0.59}_{-0.60}$ km s^{-1} and a radial velocity semi-amplitude of $K_{\rm P} = 106.21^{+1.76}_{-1.71}$ km s^{-1} for the planet, which results in an absolute[1] mass of $M_{\rm P} = 6.24^{+0.17}_{-0.18}\,M_{\rm J}$ and an orbital inclination of $41.6^{+1.0}_{-0.9}$ degrees. Our retrieved $V_{\rm sys}$ shows a significant shift (+5 km s^{-1}) from the literature value, which could be caused by an inaccurate time of periastron. Within the explored model grid, we measure a preference for solar water abundance (VMR = 10^{-3}) and no evidence for additional minor species in the atmosphere. Given the extensive orbital coverage of the data, we searched for a phase dependency in the water signal but found no strong evidence of variation with orbital phase. This detection is at odds with recent observations from SPIRou/CFHT and their tight upper limit on water abundance. We recommend further observations of the atmosphere τ Boötis Ab to try and resolve these discrepancies.

4.3 Introduction

Having been discovered by Butler et al. (1997), τ Boötis A b was one of the first exoplanets around a main-sequence star to be observed with precise ($\sim$ m s^{-1}) Doppler shift measurements of stellar absorption lines using high resolution echelle spectrographs. These first generation of exoplanet discoveries became known as hot Jupiters due to their large (Jupiter-like) masses and close-in orbits that are a fraction of the orbit of Mercury in the Solar system, which results in high day-side temperatures for these planets ($T_{\rm P} \geq 1000$ K). Due to these extreme conditions but favourable signals, these exoplanets are also the most ideal candidates for atmospheric characterisation despite accounting for $\lesssim 1$ per cent of sun-like stars (e.g. Wright et al., 2012; Petigura et al., 2018; Boley et al., 2021). τ Boötis b orbits a hot, bright F7 (Gray et al., 2001) star ($V = 4.49$, $H = 3.55$) (van Belle and von Braun, 2009; Cutri et al., 2003) that is part of a binary system with an M3 dwarf companion (τ Boötis B) (Joy and

[1] see section 4.1

Abt, 1974). Follow up photometric observations found that the planet was not to be transiting (Baliunas et al., 1997).

The close proximity of τ Boötis b to one of the brightest planetary host stars has made this system one of the most observed non-transiting planets over the last couple of decades. Searches for the reflected light from τ Boötis b using high resolution instruments commenced soon after its discovery (Charbonneau et al., 1999; Collier Cameron et al., 1999) to directly detect the atmospheric composition, geometric albedo, absolute mass and the orbital inclination. Successive observations (Leigh et al., 2003; Rodler et al., 2010) have also been unsuccessful in detecting the reflected light from the atmosphere of τ Boötis b. Hoeijmakers et al. (2018a) produced a meta-analysis of all the data determining an upper-limit on the planet-to-star contrast and the optical albedo of 1.5×10^{-5} and 0.12, respectively. Recent radial velocity measurements of τ Boötis A have constrained the orbital parameters of the M-dwarf companion and the planet (Justesen and Albrecht, 2019), the former of which is expected to reach periastron by $\sim$ 2026. By this time, the M-dwarf is likely to be within $1''$ of the A star which could cause significant contamination for spectroscopic measurements of the host star and the planet.

The first direct detections from an atmosphere of a non-transiting hot Jupiter was observed from τ Boötis b in the near-infrared (NIR) (Brogi et al., 2012; Rodler et al., 2012) with the high resolution CRIRES instrument (Kaeufl et al., 2004) at the VLT. At $\sim 2.3\,\mu$m, they were able to accurately constrain the radial velocity of the planet by tracing the thermal emission of CO around superior-conjunction where the hot day-side comes into view. Later, Lockwood et al. (2014) reported the first detection of water vapour in the atmosphere of τ Boötis b in the L-band with a $6\,\sigma$ detection from NIRSPEC/Keck (McLean et al., 1995). Over the past decade, the use of high resolution spectroscopy has been optimal for measuring the chemical composition (e.g. Giacobbe et al., 2021), wind speeds (e.g. Louden and Wheatley, 2015) and temperature-pressure ($T - p$) profiles (e.g. Brogi et al., 2014). More recently, developments have been made on a Bayesian framework to enable a full atmospheric retrieval from these high resolution spectra (Brogi et al., 2017; Brogi and Line, 2019; Gibson et al., 2020; Nugroho et al., 2020). This has allowed for the retrieval of precise absolute chemical abundances (Pelletier et al., 2021) and the C/O ratio (Line et al., 2021). The result from Pelletier et al. (2021) is particularly interesting in this context, as only carbon monoxide was measured in the atmosphere of τ Boötis Ab. In spite of the precise abundance derived for this species ($\log(\mathrm{CO}) = -2.46^{+0.25}_{-0.29}$), they reported a non-detection of water vapour and placed a tight upper limit of VMR $\log(\mathrm{H_2O}) \leq -5.66$ (3σ). Given the previous

detection of water by Lockwood et al. (2014) and the inconclusive evidence from Brogi et al. (2012), τ Boötis is an interesting planet to revisit with independent data, which is what we present in this paper.

The bulk of NIR observations of hot Jupiters thus far have been to measure the thermal emission brightness variation of the planet as a function of line of sight (i.e a phase curve). This gives a 3-dimensional picture of the temperature and cloud coverage across the longitude of the planet (e.g. Knutson et al., 2007; Kreidberg et al., 2018). These phase variations leave imprints in their chemical and $T - p$ structure as a function of the orbital phase (e.g. Stevenson et al., 2017). The variations are expected to become more prominent for the hotter class of hot Jupiters known as the ultra-hot Jupiters (> 2000 K) (Parmentier et al., 2018) because of the extreme temperature gradient between the hot day-side and cooler night-side. This variation in the temperature structure causes thermal dissociation to occur which plays an important role in the heat recirculation of the hottest planets (Bell and Cowan, 2018). Ehrenreich et al. (2020) and Kesseli and Snellen (2021) measured the phase resolved variation in the absorption of neutral iron in the transmission spectrum of the ultra-hot Jupiter WASP-76b, attributed to the rain-out of iron on the night-side, with high resolution spectroscopy. However, at high resolution, phase variations in the thermal emission spectrum have remained elusive.

In this analysis, we confirm the detection of water vapour in the thermal emission with day-side observations of the hot Jupiter τ Boötis b with high resolution spectroscopy. τ Boötis b is estimated to have day-side temperature limits between ~ 1980 and 1670 K assuming zero and perfect heat redistribution to the night-side, respectively (Cowan and Agol, 2011). We also split the spectra into pre- and post-superior conjunction to measure any variations in the water signal as a function of phase. We outline the observations in section 4.4, the data reduction and analysis in section 4.6, the results in sections 4.5 and 4.7. Finally, we discuss the results in section 4.8 with a summary of our conclusions in section 4.10.

4.4 Observations

The day-side emission from the τ Boötis Ab system was observed over five nights (see also Zhang et al. (2020)) with the high resolution spectrograph CARMENES mounted on the 3.5 - m telescope at the Calar Alto Observatory (Quirrenbach et al., 2014). We used two nights of spectra taken from the Calar Alto archive (PI: J.A.Caballero and F.J.Alonso-Floriano) which were taken on 2018 March 26 and 2018 May 11 (nights 1 and 2, hereafter). We also observed (PI: M.Brogi) τ Boötis b

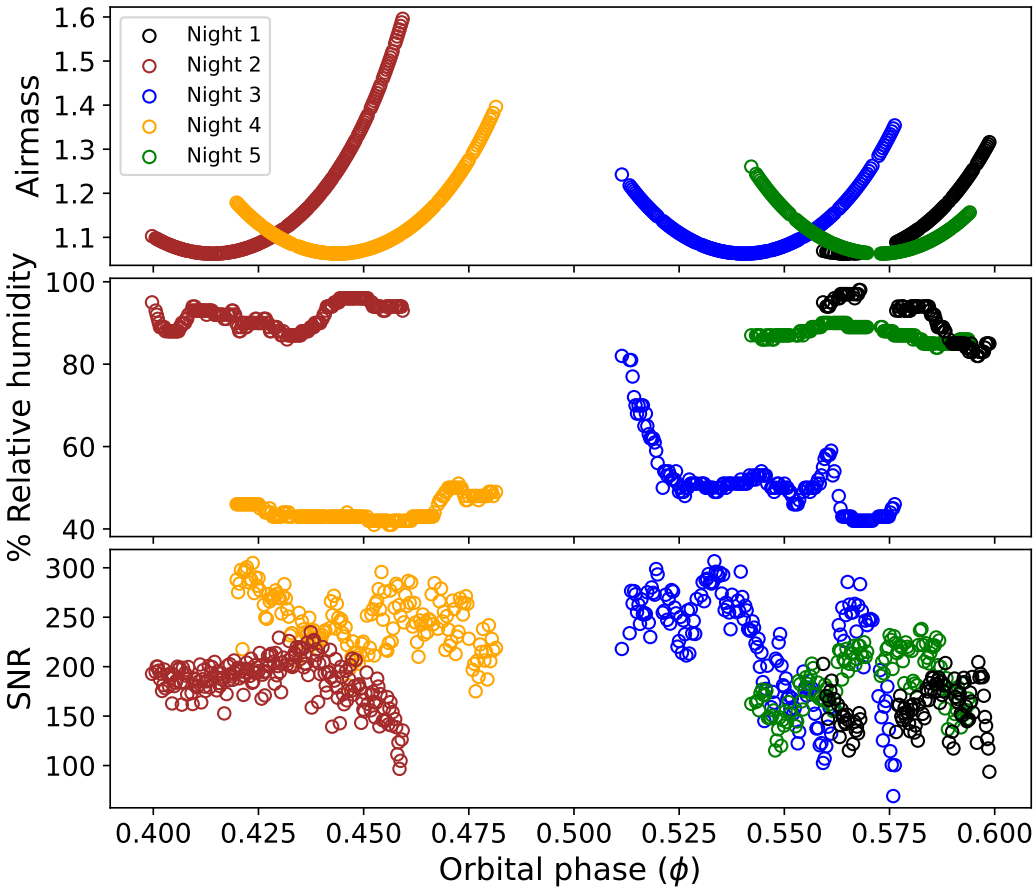

Figure 4.1: The airmass (top panel), relative humidity (middle panel) and the SNR of order 51 ($\lambda = 1.19 - 1.21\,\mu$m) as a function orbital phase for the observations of τ Boötis b of spectra taken with CARMENES.

Table 4.1: Observations of τ Boötis with CAMRNES. The SNR was calculated as the average SNR of order 51 ($\lambda = 1.19 - 1.21\,\mu$m) over the night. The average $V_{\rm P}$ is calculated from equation 4.1 assuming a planet $K_{\rm P}$ of 110 km s^{-1} and a $V_{\rm sys}$ of -16.9 km s^{-1} averaged over the entire night.

Night	**Date**	**Number of spectra**	**Exposure time (s)**	**Phase range**	**SNR**	**Average $V_{\rm P}$ (km s^{-1})**
1	2018-March-26	110	40	0.559-0.599	148	-76.6
2	2018-May-11	261	40	0.399-0.459	165	44.3
3	2019-March-12	161	70	0.511-0.576	222	-58.4
4	2019-March-15	165	65	0.420-0.481	246	5.74
5	2019-April-11	133	66	0.542-0.594	186	-61.4

for a further three nights on 2019 March 12, 2019 March 15 and 2019 April 11 (nights 3, 4 and 5, hereafter). CARMENES consists of separate optical and NIR spectrographs with spectral resolutions of $R = 94,600$ and 80400, respectively. In this analysis, we utilise the NIR spectra to probe the thermal emission from the planet with a wavelength coverage of $\lambda = 0.96 - 1.71\,\mu$m which spans the Y, J and H-bands with a sampling precision of $\sim 3.7\,\mathrm{km\,s^{-1}\,pixel^{-1}}$. The NIR spectra are dispersed into 28 echelle orders, orders 63 - 36, which are imaged on two 2k×2k Hawaii-2RG detectors.

A time series of spectra was taken pre- ($\phi < 0.5$, nights 2 and 4) and post superior-conjunction ($\phi > 0.5$, nights 1, 3 and 5). In table 4.1, we show the observations of τ Boötis taken with CARMENES with their respective average exposure times, number of spectra obtained and observed phase range. For nights 1 and 2, we removed the final 10 and 52 spectra, respectively, due to a rapidly decreasing SNR in the spectra likely due to increased cloud coverage. For each exposure, one fibre was held on the target and a second fibre was placed on the sky for accurate thermal background subtraction. Each spectrum was subsequently calibrated and reduced using the CARACAL v2.10 (Caballero et al., 2016b) pipeline which performs a dark/bias correction, order tracing, a flat-relative optimal extraction and an accurate wavelength calibration from a U-Ne lamp. We use this solution - which is known to be stable at the $\mathrm{m\,s^{-1}}$ level (Quirrenbach et al., 2016), for our analysis. Thus, we do not rebin the spectra onto a grid at constant resolving power, nor do we apply any correction for shifts at the sub-pixel level as was done in chapter 3.5 for CRIRES spectra.

From Figure 4.1, night 4 had the best observing conditions out of the five with the other nights suffering from large variability in atmospheric conditions and high humidity levels. This is reflected in the most stable signal-to-noise ratio (SNR) for all wavelengths (or orders) as shown in the bottom panel of Figure 4.1. We note that while the relative humidity at the level of the telescope is not an exact proxy for the precipitable water vapour over the entire atmospheric column density, it is at least an indicator of the overall quality of the night.

4.5 Telluric removal

Firstly, we need to remove the contaminating telluric and host stellar absorption that dominate the extracted spectra. For each order, the time resolved spectra are set-up in 2-D matrices with dimensions $\mathrm{n_f} \times \mathrm{n_x}$, where $\mathrm{n_f}$ is the frame number and $\mathrm{n_x}$ is the number of pixels or wavelength channel, for CARMENES detectors this

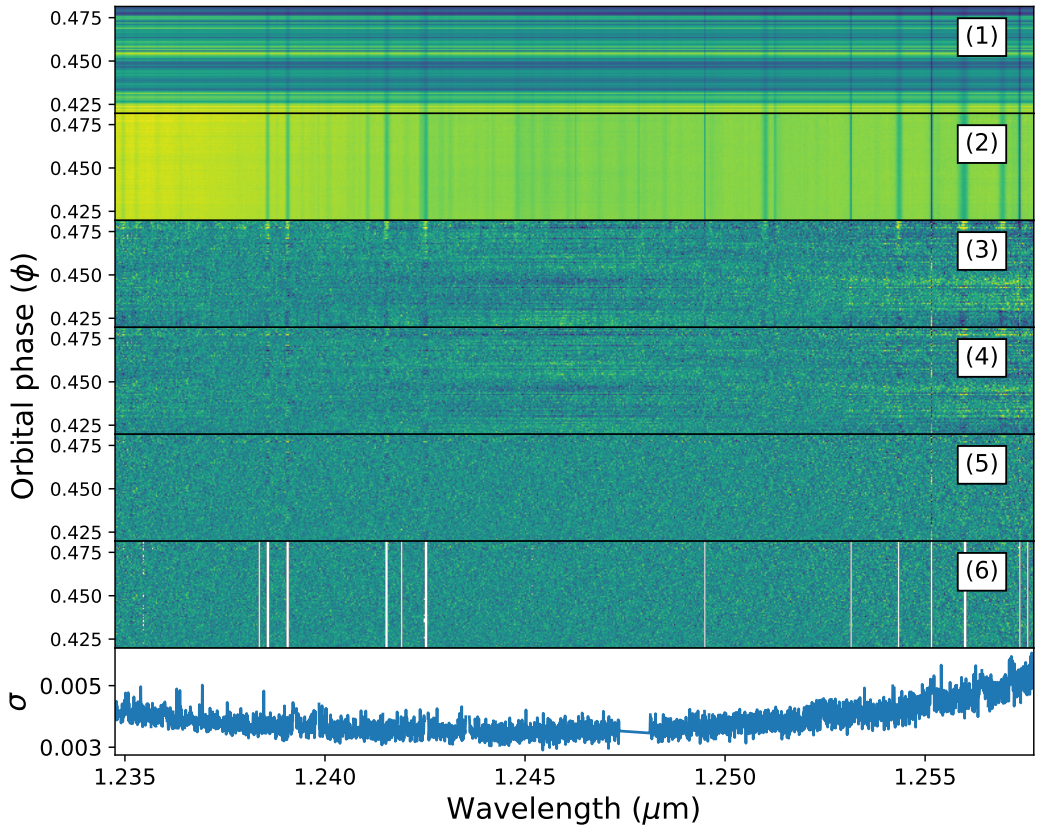

Figure 4.2: Example of the telluric removal sequence on order 49 of the NIR arm of CARMENES for night 4. The panel numbers indicate the telluric removal steps as described in the text. The bottom panel shows the final standard deviation in time for the spectra. The contrast is increased in panels 3-6 for better visualisation of the noise structure in the spectral sequence.

is 4080. Before passing the data through the telluric pipeline, we removed orders 41-46 ($\lambda = 1.32 - 1.50\,\mu$m), 52-55 ($\lambda = 1.10 - 1.19\,\mu$m) as these were saturated with telluric lines.

We remove the variation in the observed flux as a function of time. As the telluric features are stationary over a night's observations, we can effectively treat each wavelength channel as a light curve which can then be detrended from telluric depth variations. Since these spectra were taken at orbital phases close to superior conjunction, we are observing the maximum rate of change in the radial velocity shift of the planet ($\frac{\mathrm{d}V_P}{\mathrm{d}t}$) thereby minimising the losses of the planetary signature which will be Doppler shifted across several wavelength channels over the time series. Among the various techniques to remove telluric lines, in this analysis we primarily follow the algorithm used in Brogi and Line (2019) and Webb et al. (2020). Figure 4.2 shows an example of the 2-D time resolved spectra as a function of wavelength for the CARMENES echelle order 49 for night 4. Each panel shows each step in the reduction of the spectra, of which we outline below:

(1): Extracted spectra from the CARACAL calibration pipeline (see Section 4.4) stacked in time.

(2): The variations in the light throughput are removed by normalising each spectrum (each row in Figure 4.2) by the median of the spectrum.

(3): The time-averaged spectrum is fit with a second order polynomial to each observed spectrum. This fit is thus divided through each of the spectra to remove the telluric variability as a function of wavelength.

(4): The telluric lines are further detrended in time for each wavelength channel (each column in Figure 4.2). This is achieved by fitting the spectra in wavelength as a second order polynomial with time (we use the orbital phase as our time stamp here). This function is then divided through for each wavelength channel to remove the telluric variations as a function of time.

(5): At this stage, we pass each order through a Gaussian high-pass filter (bin-size of 80 pixels) to remove the wavelength dependent continuum fluctuations which are still present in the data.

(6): The strongest telluric residuals that remained were masked from the analysis. To determine these highly deviant channels, we calculated the ratio between the standard deviation and the relative errors output from the CARACAL pipeline and thus calculated a median value. A calculation of the difference

between this ratio and the median values was then used to determine the channels that rose above the average noise level of the data. Highly deviant pixels are also removed through a $5\,\sigma$ clipping.

As described above, in step (6) we had to mask telluric residuals that were not corrected for in the telluric removal algorithm and were seen as highly deviant channels in the time-series spectra. This is necessary so as to prevent strong time-correlated telluric noise appearing in the final cross-correlation analysis (see Figure 4 in Brogi et al. (2018)). The bottom panel in Figure 4.2 shows the final standard deviation in time as a function of wavelength, the lack of highly deviant wavelength channels indicates that the strongest residuals that were left in the data have now been removed. Over all orders, this resulted in a total of $\sim$9, 7, 7, 6 and 7 per cent of the pixels being masked for nights 1-5, respectively. In the case of night 2, we found particularly strong telluric residuals that still remained in the spectra despite this additional masking when correlated with a pure water model (see Figure 4.3). As a result, we remove night 2 from the remainder of the analysis in order to avoid any biases in our results. This is further explained in section 4.7.1. We do however repeat the analysis with the inclusion of night 2 in appendix 4.9.1 and 4.9.2.

4.6 Data analysis

4.6.1 Cross-correlation to log likelihood mapping

As seen in the residual spectral matrix in panel (5) in Figure 4.2, the planetary signal is still hidden within the noise of the data, i.e the SNR $\ll 1$ per line. To extract this signal, we cross-correlate the observed spectra with model spectra of opacity sources that may be present in the atmosphere. This amplifies the planet SNR by $\sim \sqrt{N_{\rm lines}}$, where $N_{\rm lines}$ is the number of strong spectral lines.

We Doppler shift the model spectra into the planet rest frame via spline interpolation, and by the radial velocity of the planet in the observer's frame,

$$V_{\rm P}(t) = K_{\rm P} \sin\{2\pi[\phi(t) + 0.5]\} - V_{\rm bary}(t) + V_{\rm sys}, \tag{4.1}$$

where $K_{\rm P}$ is the radial velocity semi-amplitude of the planet, $V_{\rm bary}$ and $V_{\rm sys}$ are the barycentric-earth radial velocity correction and the systemic velocity, respectively. The minus sign in $V_{\rm bary}$ corrects for the fact that barycentric velocities are the observer's velocity computed in the barycentre of the solar system, and not vice-

Table 4.2: Stellar and planetary parameters and their values that was used in the analysis.

τ **Boötis A**	**Symbol (units)**	**Value**	**Reference**
Spectral type		F7	Gray et al. (2001)
H-band infrared brightness	H (mag)	3.55	Cutri et al. (2003)
Effective temperature	$T_{\rm eff}$ (K)	6399 ± 45	Borsa et al. (2015)
Mass	$M_\star$ ($M_\odot$)	1.35 ± 0.03	Takeda et al. (2007)
Radius	$R_\star$ ($R_\odot$)	1.42 ± 0.08	Borsa et al. (2015)
Luminosity	$L_\star$ ($L_\odot$)	3.06 ± 0.16	Borsa et al. (2015)
Distance	d (pc)	15.66 ± 0.08	Gaia Collaboration (2018)
Radial velocity semi-amplitude	$K_\star$ ($\mathrm{m\,s^{-1}}$)	468.42 ± 2.09	Justesen and Albrecht (2019)
Systemic velocity	$V_{\rm sys}$ ($\mathrm{km\,s^{-1}}$)	-16.9 ± 0.3	Gaia Collaboration (2018)
τ **Boötis Ab**			
Orbital period	P (days)	$3.31245 \pm 3 \times 10^{-6}$	Justesen and Albrecht (2019)
Radius	$R_{\rm P}$ ($R_{\rm J}$)	1.2	(*estimated*)
Phase zero-point (in the rest frame of τ Boötis A)	T_0 (MJD)	56401.879 ± 0.004	Justesen and Albrecht (2019)
Orbital separation	a (au)	$0.04869^{+0.00039}_{-0.00040}$	Rosenthal et al. (2021)
Eccentricity	e	$0.0074^{+0.0059}_{-0.0048}$	Rosenthal et al. (2021)

versa as needed here. The orbital phases are defined as,

$$\phi(t) = \frac{t - T_0}{P}, \tag{4.2}$$

where t is the time of observations in HJD, T_0 and P is the phase zero-point in HJD and the orbital period in days, respectively. We note that the T_0 stated in Justesen and Albrecht (2019) is in MJD we needed to convert T_0 into HJD using the `astropy.time` module (Astropy Collaboration et al., 2013, 2018). The T_0 was also determined in the rest-frame of the host star, therefore, the orbital phases calculated with this solution will be in the rest-frame of the star. Thus, we need to correct the orbital phases by 0.5 to be in the rest-frame of τ Boötis b, as indicated in equation 4.1. Before cross-correlation, we must also scale the model spectra to the stellar flux of τ Boötis ,

$$F_{\rm scaled}(\lambda) = \frac{aF_{\rm P}}{\pi B(\lambda, T_{\rm eff})} \left(\frac{R_{\rm P}}{R_\star}\right)^2, \tag{4.3}$$

where $B(\lambda, T_{\rm eff})$ is the blackbody stellar flux calculated from the measured effective temperature ($T_{\rm eff}$), $F_{\rm P}$ is the modelled emergent flux from the planet in $\mathrm{W\,m^{-2}\,m^{-1}}$, $R_{\rm P}$ and $R_\star$ are the estimated planetary and measured stellar radii, respectively. The scaling factor a in equation 4.3 is assumed to be unity in sections 4.7.1 and 4.7.2, however, it is allowed to vary in the MCMC analysis as described in section 4.7.3. We assume a simple blackbody for the stellar flux as we do not expect any significant molecular absorption in the stellar atmosphere of τ Boötis , which has a temperature of $\sim 6400\,\mathrm{K}$. The parameter values that were used in the analysis are summarised in table 4.2. We adopt a radius of $1.2\,R_{\rm J}$, which is approximately the radius adopted in Pelletier et al. (2021) ($1.15\,R_{\rm J}$) corrected by their retrieved scaling factor of $\sim$ 1.04. Since τ Boötis b is a non-transiting planet, the $K_{\rm P}$ is uncertain, therefore, we must test a range of velocities of the planet around the expected value of $K_{\rm P} = 110\ \mathrm{km\,s^{-1}}$ from the literature (Brogi et al., 2012; Lockwood et al., 2014). We tested a range of velocities at $0 \geq K_{\rm P} \geq 200\ \mathrm{km\,s^{-1}}$ and $-60 \geq V_{\rm sys} \geq 60\ \mathrm{km\,s^{-1}}$ in steps of $2.0\ \mathrm{km\,s^{-1}}$ which is within the velocity resolution of CARMENES ($\sim 3.7\,\mathrm{km\,s^{-1}}$ in the NIR). The planet radius is also unknown for non-transiting systems; however, we can absorb any uncertainty in the radius into a scaling parameter $\log(a)$, which is then retrieved with the other atmospheric parameters (see section 4.7.3).

We now add an additional step into the analysis whereby we include a cross-correlation to log likelihood (CC-log(L)) mapping in order extract statistically robust atmospheric and orbital parameters at high resolution. Since we have time-

resolved spectra on a timescale where any planet signal will be Doppler shifted, we use the mapping from Brogi and Line (2019) as described by,

$$\log(L) = -\frac{N}{2}\log[s_f^2 - 2R(l) + s_g^2], \tag{4.4}$$

where the cross-covariance, $R(l)$, is related to the correlation coefficient by,

$$C(l) = \frac{R(l)}{\sqrt{s_f^2 s_g^2}}. \tag{4.5}$$

In equation 4.4, N is the number of wavelength channels used in the cross-correlation and s_f^2 and s_g^2 refer to the variance of the data and the model, respectively. In equations 4.4 and 4.5, l represents the cross-correlation lag, that is equal to the planet's Doppler shift at the time the $\log(L)$ is evaluated. Using this form of the $\log(L)$, we are assuming the case where an additional atmospheric scaling factor a is equal to unity. This is necessary because we treat the scaling factor as a model parameter, and therefore we apply it to the model spectrum *prior* to the likelihood computation (Equation 4.3), which is necessary to account for the effects of the analysis on the model. Using this method, we are able to directly convert the correlation values into a log likelihood velocity map.

The log-likelihood values from Equation 4.4 are calculated for each night, each order and each spectrum and subsequently summed to obtain a single log-likelihood value for each model and each set of parameters,

$$\log(L)_{\rm tot} = -\sum_{k=1}^{4}\sum_{i=1}^{N_{\rm o}}\sum_{j=1}^{N_{\rm s}}\frac{N_{kij}}{2}\log[s_{f,kij}^2 - 2R_{kij}(l) + s_{g,kij}^2], \tag{4.6}$$

where the index k denotes the observing night, i the spectral order, and j the frame number. We further note that the number of orders $N_{\rm o}$ and the number of spectra $N_{\rm s}$ vary from night to night.

4.6.2 Atmospheric models

To model the thermal emission from τ Boötis b, we use the line-by-line radiative transfer code GENESIS (Gandhi and Madhusudhan, 2017). These model spectra were produced using the same methods as described in Hawker et al. (2018), Cabot et al. (2019), Webb et al. (2020) and Gandhi et al. (2020a). The spectra were generated at a wavelength range of $\lambda = 0.96$ - $1.8\,\mu$m , with a wavenumber spacing of $0.01\,\mathrm{cm}^{-1}$ which corresponds to a resolution of $R(\lambda) = \frac{10^6}{\lambda}$, where λ is in μm . Before

Table 4.3: The grid of models that were used in the analysis. The range of abundances tested for each species are shown, these varied in steps of 1 dex. For each species, the abundance was also allowed to drop to zero in each opacity grid to model each species individually. The exceptions to this are the water abundances which were fixed to $10^{-3.3}$ and 10^{-3} for the water only models (top row) and the H_2O, HCN and C_2H_2 grid (bottom row), respectively.

Opacity source(s)	$\log_{10}$(VMR)	T_1 (K)	T_2 (K)	**Number of models**
H_2O	-3.3	[1400,1600,1800,2000]	[800,1200,1600,2000]	12
H_2O, CH_4, HCN	-3.0 to -5.0, -4.0 to -6.0, -5.0 to -7.0	1800	1200	64
H_2O, NH_3, C_2H_2	-3.0 to -5.0, -4.0 to -6.0, -5.0 to -7.0	1800	1200	64
H_2O, HCN, C_2H_2	-3.0, -2.0 to -7.0, -2.0 to -7.0	1800	1200	49

cross-correlation, these models were re-grid to a constant resolution (i.e. $\lambda/\Delta\lambda$) and then convolved with a Gaussian kernel with a FWHM equivalent to the instrumental resolution of CARMENES in the NIR ($R = 80400$). We also assume each model spectrum has a 1D $T-p$ profile that has been parameterised by upper (T_2, p_2) and lower (T_1, p_1) points in the atmosphere. Above ($p < p_2$) and below ($p > p_1$) these points the atmosphere is assumed to be isothermal.

Opacity sources were included from the following line list databases; HITEMP, for H_2O (Rothman et al., 2010b) and CH_4 (Hargreaves et al., 2020), ExoMol for HCN (Harris et al., 2006; Barber et al., 2014), NH_3 (Coles et al., 2019) and C_2H_2 (Chubb et al., 2020). We note that CARMENES has no sensitivity to CO in the Y, J and H-bands and therefore we do not include this molecule in the modelling. Even though there are CO lines at $\sim 1.6\,\mu$m , these are over two orders of magnitude weaker than in the K-band (e.g. Gandhi et al., 2020a). In addition, at $1.6\,\mu$m the water opacity is stronger than for CO, thus the weaker CO lines will be significantly shielded by water lines. These models also include collisionally induced absorption from H_2-H_2 and H_2-He (Richard et al., 2012b) and broadening from each opacity source (Gandhi et al., 2020b). In table 4.3 we show the grids of models that were used in our analysis tested against the observed spectra. We fix the pressure points to be $p_1 = 1$ and $p_2 = 10^{-3}$ bars for all the models in the grids. For pressures lower that 10^{-3} bars, the $T-p$ profile is predicted to be isothermal from GCM and 1D modelling (e.g. Beltz et al., 2021), therefore, most of the core of the lines will be formed at pressures of $> 10^{-3}$ bars. We generated a $T-p$ profile grid to explore various temperature gradients for the atmosphere with a single opacity source of water with a fixed chemical equilibrium and solar composition abundance of VMR$= 10^{-3.3}$. The choice of temperatures was guided by the range of equilibrium temperatures of the day-side of the planet, $T_{\rm eq} = 1600 - 2000\,$K, which depends on the efficiency of day-night heat redistribution. We also generated a large opacity grid with water combined with further minor species at varying abundances, including at zero abundance. We assume that the abundance for each opacity source in all of the models have a constant VMR with pressure. For these opacity grids, we fixed the temperature gradient to $T_1 = 1800$ and $T_2 = 1200\,$K. We note here that with a fixed grid of models, we are limited in our ability to constrain the atmospheric lapse rate and the molecular abundances individually due to the partial correlation between these parameters. A full atmospheric Bayesian retrieval with free parameters for the T-p profile and abundances will constrain these parameters individually for which we defer to a future study.

As with the data, we also pass these models through the telluric removal

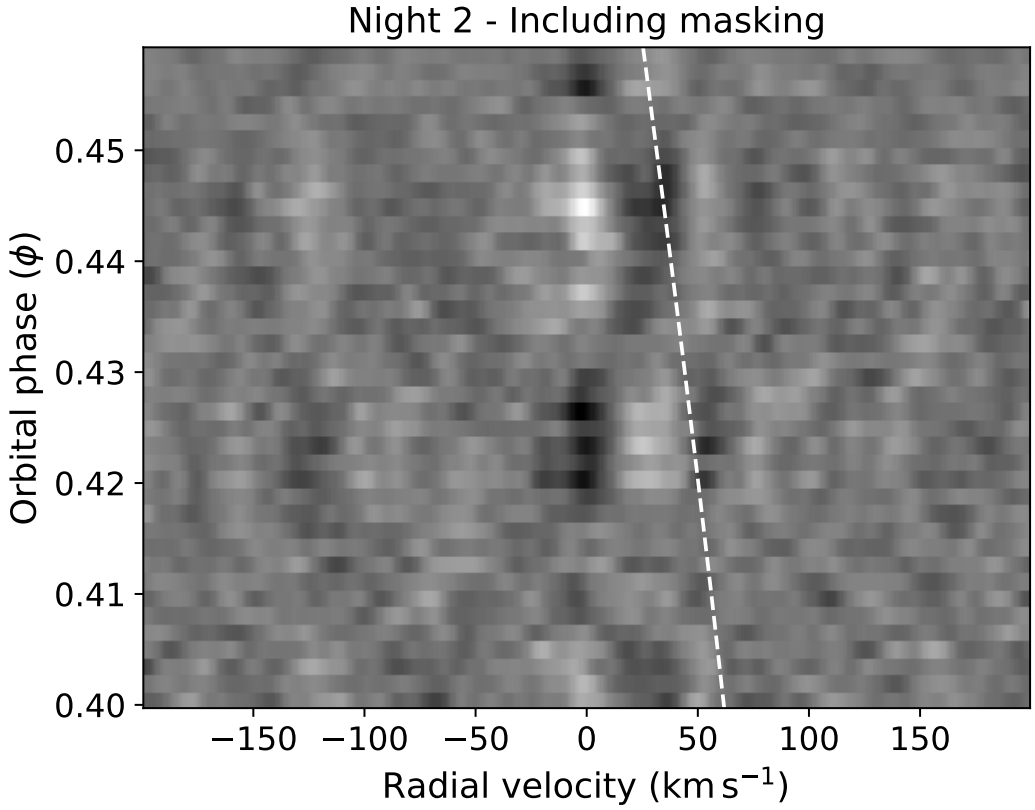

Figure 4.3: The relative CC-log(L) values binned in phase with a pure water model with a log(VMR) = −3.0 with the spectra from night 2. The spectra have been co-added in $\phi = 0.0015$ wide bins. Darker shades indicate anti-correlation whereas lighter shades indicate correlation with the water model. The white dashed line shows the expected radial velocity of τ Boötis b. The strong correlation and anti-correlation stripe in the telluric rest-frame (i.e. $\sim 0\,\mathrm{km\,s^{-1}}$) suggests strong telluric absorption in these spectra.

pipeline as described in section 4.5 prior to cross-correlation. This is to replicate the unavoidable scaling effects that occur to the atmospheric signal in the telluric removal sequence, thus avoiding potential biases in the cross-correlation analysis (see final panel in Figure 2 of Brogi and Line (2019).

4.7 Results

4.7.1 Single species analysis

We first analysed the data against five single species individually at abundances of $\log_{10}$VMR; H_2O = −3.0 to −5.0, CH_4 = −4.0 to −6.0, HCN = −5.0 to −7.0, NH_3

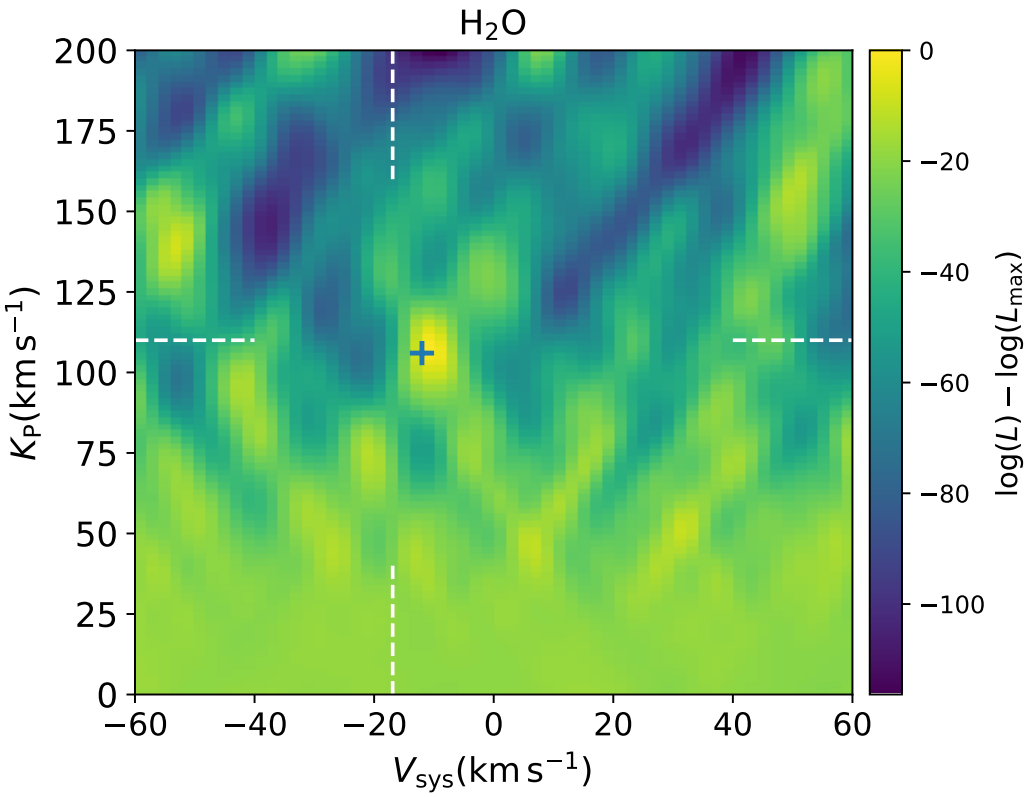

Figure 4.4: K_P-V_{sys} velocity map of the CC-log(L) mapping of the observed spectra with the best-fitting water model with a VMR= 10^{-3} in $\Delta \log(L) = \log(L) - \log(L)_{max}$. The white dashed lines indicate the expected position of the signal from τ Boötis b from the literature. The blue cross shows the location of the log(L_{max}).

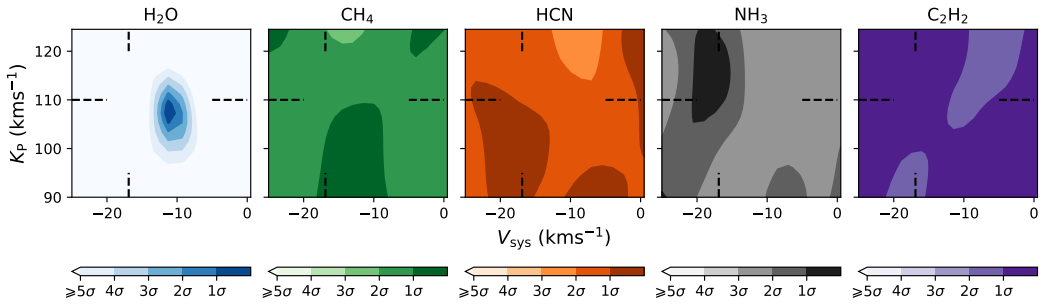

Figure 4.5: CC-log(L) significance $K_{\rm P}$ - $V_{\rm sys}$ maps of the five species at solar abundance co-added for the four nights of spectra. The filled contours indicate the areas of significance away from the peak in the log(L). From left to right, we show the maps of; H_2O, CH_4, HCN, NH_3 and C_2H_2. The H_2O map shows a zoomed in version of the signal seen in Figure 4.4. The black dashed lines indicate the location of the orbital solution given from the literature. There is a clear signal from water close to the velocity of the planet and no evidence for any other minor species.

= −4.0 to −6.0 and C_2H_2 = −5.0 to −7.0. These tests were done on the combined species models on rows 2 and 3 in table 4.3 with the additional species effectively removed by setting their abundances to zero. For H_2O, the range of abundances used corresponds to the expected solar abundance assuming a solar C/O ratio and metallicity at thermochemical equilibrium down to sub-solar values approaching the upper-limit determined in Pelletier et al. (2021) ($\log_{10}$(VMR) < -5.66). For the remaining species, the expected solar abundances are expected to be too low to be observable for a planet with a temperature of $\sim$ 1800 K at a solar C/O ratio and metallicity (e.g. Madhusudhan, 2012; Moses et al., 2013). However, we tested a range of enhanced abundances for CH_4, HCN, NH_3 and C_2H_2 to include potential scenarios where the atmospheric C/O ratio and metallicity are super-solar which has been observed in recent high resolution atmospheric studies (Giacobbe et al., 2021). For these modelling tests, we do not optimise the atmospheric scaling parameter, i.e. $a = 1$.

In Figure 4.3, we show the result of correlating the reduced spectra from night 2 with a pure water model for τ Boötis b, shifted in radial velocity. The prominent alternating pattern of correlation (lighter shades) and anti-correlation features (darker shades) at zero lag radial velocity shows that the tellurics are strongly correlating with the atmospheric water models. Even though the radial velocity trail of τ Boötis b is significantly shifted from the telluric rest frame, the correlated telluric noise is overwhelming any potential signal from the planet. Therefore, the inclusion of these spectra will cause spurious telluric noise in the CC-log(L) analysis and

have subsequently been removed from the rest of the analysis (see appendix 4.9.2 and Figure 4.12). We show the same phase resolved correlation with a water model with all nights combined in Figure 4.11 in appendix 4.9.2.

For the four nights of spectra, co-added in time and wavelength, we observe a signal for the presence of water vapour in the thermal emission of this atmosphere which is shown in Figure 4.4. We find that the water signal peaks at a planet velocity semi-amplitude of $K_{\rm P} = 106.0^{+2.8}_{-2.2}\,{\rm km\,s^{-1}}$ which is consistent within $1\,\sigma$ from the literature values (Brogi et al., 2012; Lockwood et al., 2014; Pelletier et al., 2021). However, we find a shift in the systemic velocity of τ Boötis with a $V_{\rm sys} = -12.0^{+1.0}_{-0.5}\,{\rm km\,s^{-1}}$ which is a $\sim$+5.4 $\rm km\,s^{-1}$ shift from the expected $V_{\rm sys} = -16.9\,{\rm km\,s^{-1}}$ (Gaia Collaboration, 2018; Justesen and Albrecht, 2019).

To test for the preference in the water abundance in the modelling, we set the abundances for the combined species in the second row of table 4.3 to zero, i.e. CH_4 and HCN are set to zero but H_2O is allowed to vary. We find that an abundance of $\rm VMR_{H_2O} = 10^{-3}$ is strongly preferred over the lower abundances of 10^{-4} and 10^{-5} by $3.8\,\sigma$ and $5.0\,\sigma$, respectively. In Figure 4.5, we show the confidence intervals in the $K_{\rm P} - V_{\rm sys}$ correlation maps for each individual species. This shows the tight confidence intervals from the water signal that we observe in the continuous CC-log(L) map in Figure 4.4 and no evidence for the presence of other minor species in this analysis. To calculate confidence intervals, we converted the CC-log(L) mapping to a chi-square distribution (with two degrees of freedom, $K_{\rm P}$ and $V_{\rm sys}$) from the peak in the log-likelihood, log($L_{\rm max}$), using Wilks' theorem (Wilks, 1938), $\chi^2 = -2\Delta\log(L) = -2\log(L/L_{\rm max})$. Hence, we can determine the p-values from log($L_{\rm max}$) by halving the two-tail survival function of the χ^2 distribution. Finally, we are able to convert these p-values into σ levels by calculating the normal distribution inverse survival function.

We also analysed the water signal against varying $T - p$ profiles (see section 4.6.2) with a fixed water abundance of $\rm VMR = 10^{-3.3}$. We find that a steeper temperature gradient is preferred for this atmosphere with $T_1 = 1800\,{\rm K}$ preferred over lower temperatures by $3.2\,\sigma$. With T_1 fixed to 1800 K, the upper temperature $T_2 = 800\,{\rm K}$ is marginally preferred over higher temperatures by $1.6\,\sigma$ (1200 K) and $2.9\,\sigma$ (1600 K). We do note however that these are only qualitative constraints on these parameters as the atmospheric lapse rate and chemical abundances partially correlate. Recent studies with high resolution spectroscopy observations (Pelletier et al., 2021; Line et al., 2021) have shown that by using a full Bayesian atmospheric retrieval, the lapse rate and the absolute abundances can be retrieved will little correlation between these parameters. Thus, constraining both parameters in these

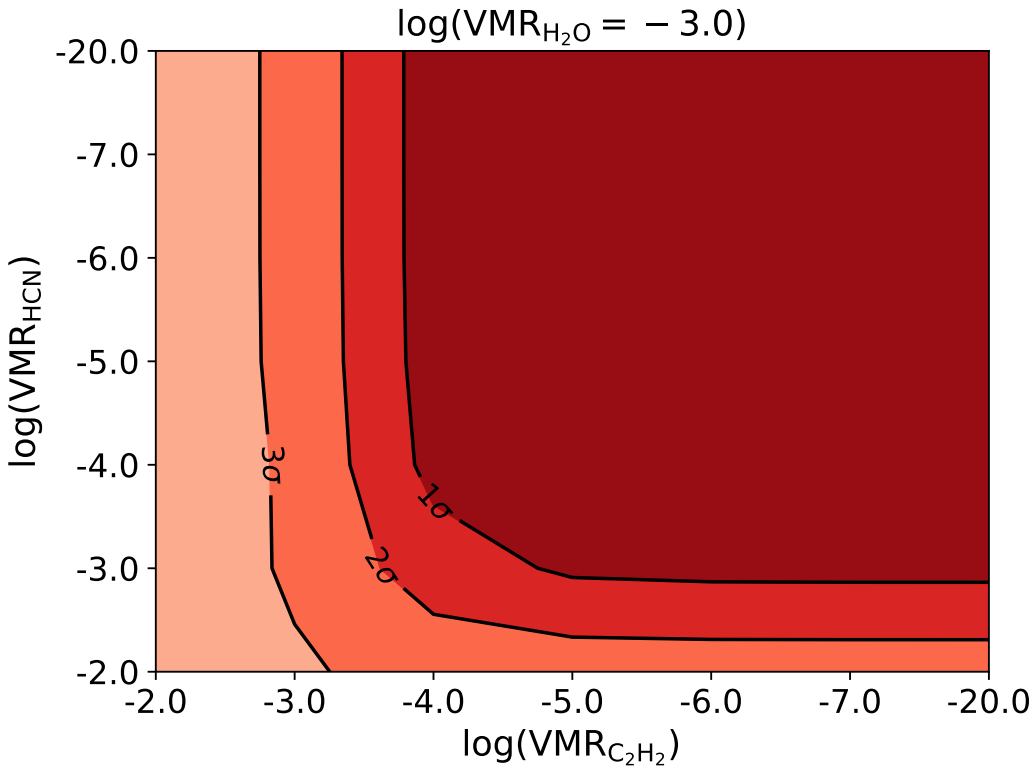

Figure 4.6: Abundance constraints on combining the best-fitting water abundance with additional HCN and C_2H_2 or without (abundance of -20.0). There is no preference for the addition of these additional species and we can only place upper limits on the abundances based on this analysis.

spectra will be possible with a full atmospheric retrieval analysis for which we defer to a future study.

4.7.2 Combined species analysis

In addition to the individual species, we also analysed a grid of models that combined the additional minor species to the best-fitting water model ($\log(\mathrm{VMR}) = -3.0$). Initial tests with models that have solar abundances in chemical equilibrium, we saw a marginal increase ($< 1\,\sigma$) in the $\log(L_{\max})$ with the addition of HCN and C_2H_2 in the modelling. Therefore, we expanded the abundance range of these species with water fixed at VMR$= 10^{-3}$ to super-solar values (see the bottom row in table 4.3) to explore whether these species significantly increase the detection significance from the pure water models. In Figure 4.6, we show the abundance constraints on the grid containing HCN and C_2H_2. We find no evidence $> 1\,\sigma$ that these additional

Table 4.4: Retrieved posterior values of τ Boötis b from a MCMC analysis with the best fitting atmospheric model.

Data-set	$V_{\rm sys}(\,\mathbf{km\,s^{-1}}\,)$	$K_{\rm P}(\,\mathbf{km\,s^{-1}}\,)$	$\log_{10}(a)$
$\phi < 0.5$	$-12.41^{+2.23}_{-2.60}$	$108.22^{+6.36}_{-7.81}$	$0.43^{+0.09}_{-0.15}$
$\phi > 0.5$	$-19.93^{+6.72}_{-12.28}$	$81.28^{+24.09}_{-76.31}$	$0.54^{+1.24}_{-0.27}$
Combined	$-11.51^{+0.59}_{-0.60}$	$106.21^{+1.76}_{-1.71}$	0.39 ± 0.07

species in the modelling improve the detection significantly from the pure water models in this analysis. However, we can place a $3\,\sigma$ and $2\,\sigma$ upper limits on the abundance of C_2H_2 and HCN at a VMR= 10^{-3} and VMR= $10^{-2.5}$, respectively. Again, we note that these limits in abundance are dependent on the choices for the change of temperature with pressure, i.e. the atmospheric lapse rate.

4.7.3 MCMC analysis

We performed an MCMC analysis on this data-set with the best-fitting model from the opacity model grid, i.e. a pure water model with a VMR=10^{-3} and a T-p profile of $(T_1, p_1) = (1800\,\mathrm{K},\ 1\,\mathrm{bar})$ and $(T_2, p_2) = (1200\,\mathrm{K},\ 10^{-3}\,\mathrm{bars})$. For the combined four nights data-set of 560 spectra, it was too computationally expensive ($\sim 82\,\mathrm{s}$ per step pooled over 40 processes) to viably explore all of the model grid and thus only the best-fitting model was used here. For this analysis, we used the `emcee` (Foreman-Mackey et al., 2013) package with 12 walkers and a chain-length of 1000, resulting in a total chain length of 12,000 points. We fit for a two parameter circular orbital solution ($K_{\rm P}$ and $V_{\rm sys}$) and an atmospheric scaling parameter ($\log_{10}(a)$) which allows the line strengths to vary. We allowed the MCMC to sample from uniform distributions of the prior parameters with ranges of, $-60 < V_{\rm sys}\,(\mathrm{km\,s^{-1}}) < 60$, $0 < K_{\rm P}\,(\mathrm{km\,s^{-1}}) < 200$ and $-2.0 < \log_{10}(a) < 2.0$. We initialise each Markov chain with the parameters set to the expected literature values, i.e. $K_{\rm P} = 110\,\mathrm{km\,s^{-1}}$, $V_{\rm sys} = -16\,\mathrm{km\,s^{-1}}$ and $\log_{10}(a) = 0$. The evolution of each chain is also driven by the CC-log(L) mapping as described in section 4.6.1.

In Figure 4.7, we show the retrieved posterior distributions from the combined set of spectra. It is clear that all of the spectra do co-add constructively to converge onto a single orbital solution from the water detection with $K_{\rm P} = 106.21^{+1.76}_{-1.71}$ and $V_{\rm sys} = -11.51^{+0.59}_{-0.60}$. The retrieved scaling factor of $\log_{10}(a) = 0.39$ suggests that the observed water lines are $\sim 2.5\times$ deeper compared to the best-fitting model. For these retrieved parameters, we determine a detection significance of $5.5\,\sigma$ when comparing the log(L) values of the best-fitting water model and a featureless spectrum

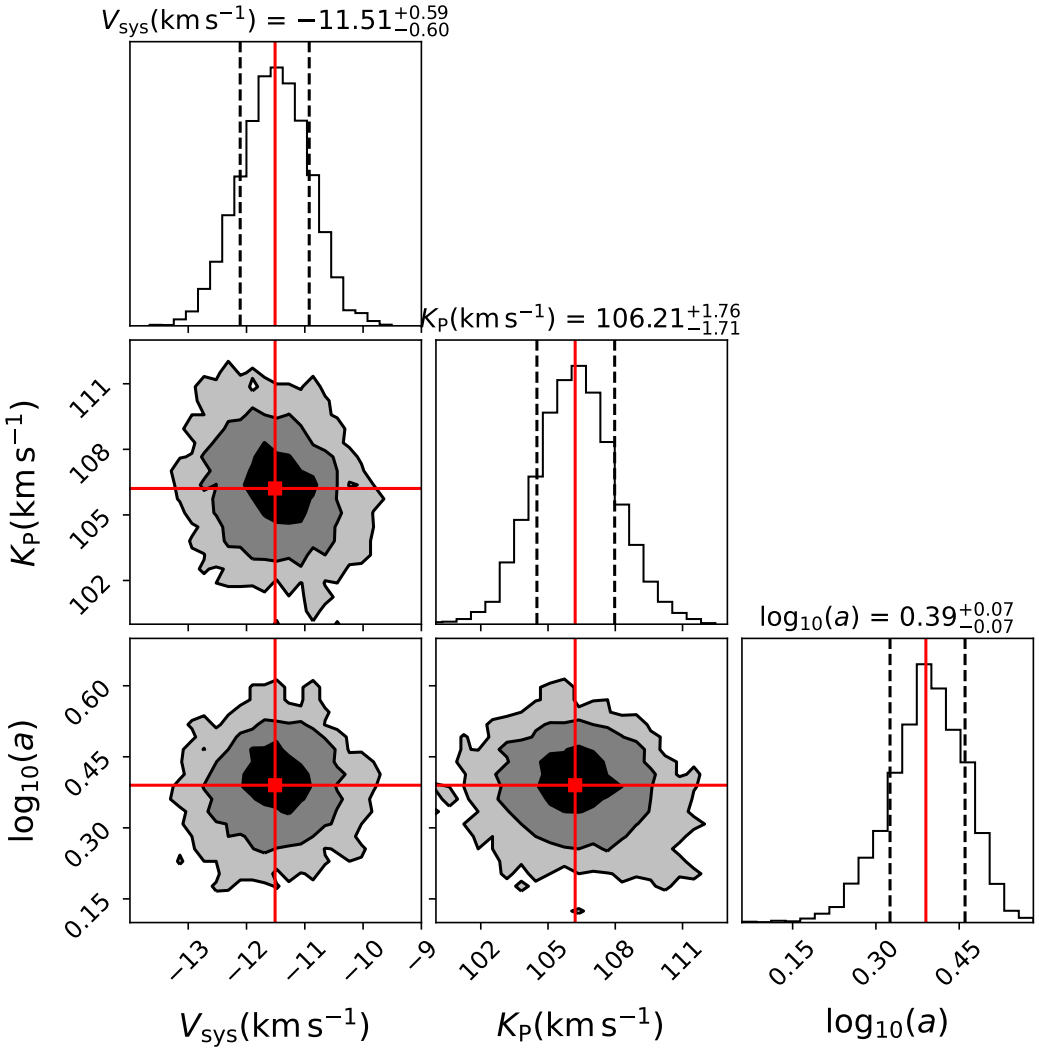

Figure 4.7: Posterior distributions of the orbital semi-amplitude (K_P), the systemic velocity (V_{sys}) and the logarithm of the atmospheric scaling parameter ($\log_{10}(a)$) retrieved from the best-fitting model. The median values for each parameter are given by the solid red lines on the corner plots and histograms. The black dashed lines on the histograms show the 0.16 and 0.84 quantiles. The filled in contours show the 1, 2 and 3 σ regions (darkest to lightest shades, respectively). The retrieved posteriors shows a constructive, co-added signal is retrieved from the best-fitting atmospheric model

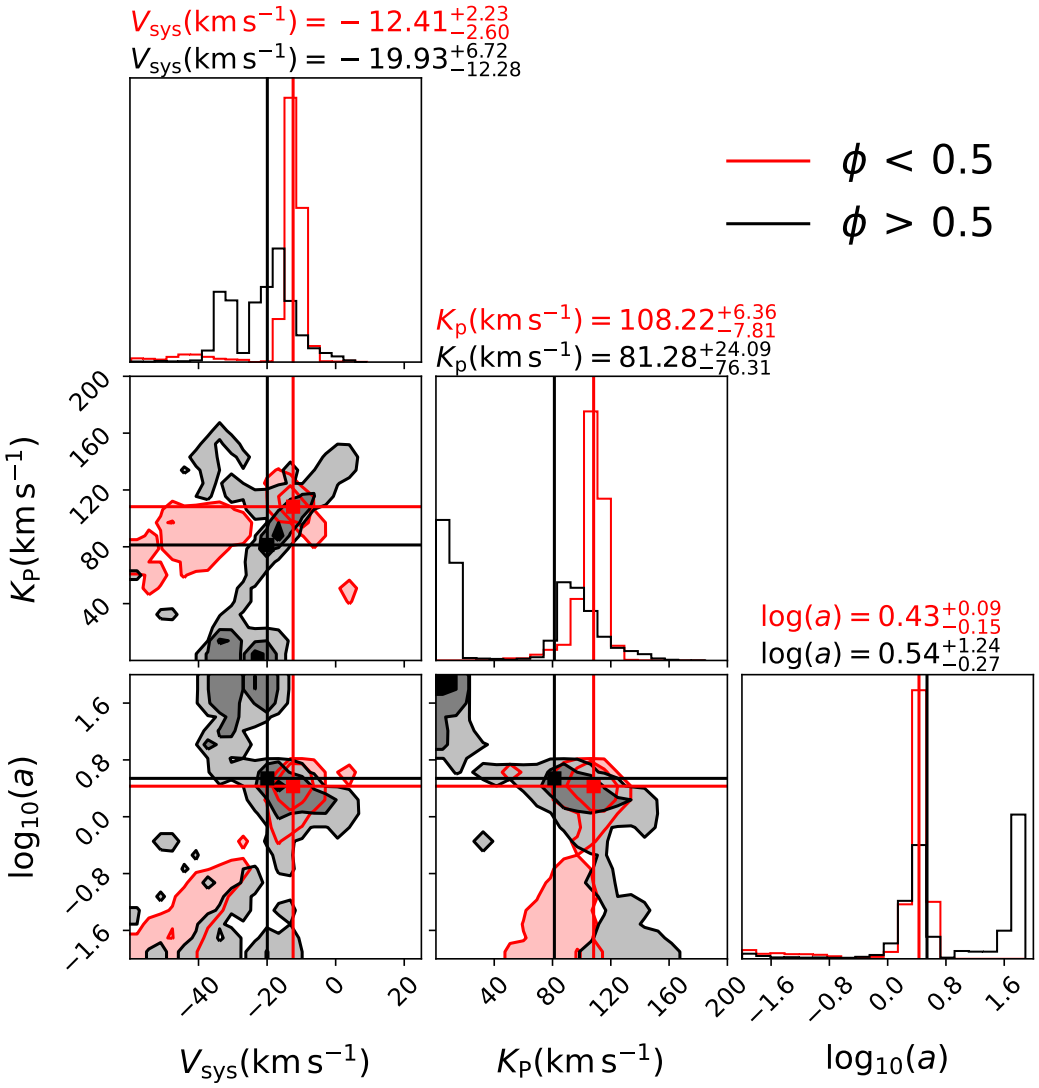

Figure 4.8: Same as Figure 4.7 but the data-set has been split into pre- (red) and post-superior (black) conjunction. The red and black solid lines show the median values of the pre- and post-superior conjunction data-set, respectively.

(i.e. a blackbody spectrum).

To test whether there is any phase dependence on the retrieved atmospheric parameters, we have split the data into pre- (i.e. all spectra $\phi < 0.5$, i.e. night 4 only) and post the superior conjunction (all spectra $\phi > 0.5$). For our data-set with only the four nights used, the pre- and post-superior conjunction spectra includes a phase coverage of $\phi = 0.420 - 0.481$ and 0.511-0.599, respectively. In Figure 4.8, we show a corner plot of the posteriors from the MCMC using only the pre-superior conjunction data in red, and the post-superior conjunction data in black. In table 4.4, we show the retrieved parameters from the two data-sets. It can be seen that the spectra at pre-superior conjunction provides a much more convincing detection of water with tighter constraints retrieved from the posterior distributions which gives a detection significance of water at $4.6\,\sigma$ for night 4 alone. The retrieved posteriors for the two data-sets do, however, show some overlap at the $2\,\sigma$ level at the expected radial velocity of τ Boötis b suggesting a weak agreement between the two data-sets. However, neither data-set converges to a single solution with the post-superior conjunction posteriors in particular showing a double peak in the distribution. This indicates that the detection of water is weak in the individual nights and that we need to co-add the full data-set of 560 spectra in order to converge onto a single solution from the water detection. The failure of convergence for both these data-sets means that we are unable to constrain the individual atmospheric scaling factors, therefore, we find no evidence for a phase dependence on the observed water signature from τ Boötis b.

4.8 Discussion

Using the CARMENES high resolution instrument, we detect a signature of water in absorption in the day-side spectrum from the non-transiting planet τ Boötis b. Co-adding all five nights of spectra, we determine an orbital solution with a $K_{\rm P} = 106.21^{+1.76}_{-1.71}\,{\rm km\,s^{-1}}$ and a $V_{\rm sys} = -11.51^{+0.59}_{-0.60}\,{\rm km\,s^{-1}}$. Using a stellar mass of $1.35 \pm 0.03\,{\rm M_\odot}$ (Takeda et al., 2007) and a radial velocity of $468.42 \pm 2.09\,{\rm m\,s^{-1}}$ (Justesen and Albrecht, 2019), we derive a planetary mass of $M_{\rm P} = 6.24^{+0.17}_{-0.18}\,{\rm M_J}$. Furthermore, we are able to derive an inclination of $i = 41.6^{+1.0}_{-0.9}$ degrees determined from a planet separation of $0.04869^{+0.00039}_{-0.00040}\,{\rm AU}$ (Rosenthal et al., 2021), which is consistent with those determined in Lockwood et al. (2014) and Pelletier et al. (2021). Despite having $\sim 3\times$ weaker constraints on $K_{\rm P}$, we are able to match the constraints on the inclination and the mass of the planet due to the recent improvement on the constraints on the measured semimajor axis (Rosenthal et al., 2021) than what was

used in Pelletier et al. (2021). This highlights the importance of regular improvements to the system parameters on planets with large monitoring radial velocity surveys such as in Rosenthal et al. (2021) which are essential for retrieving precise orbital parameters in high resolution atmospheric studies.

We find that the best fitting model requires a water abundance of VMR $= 10^{-3}$, which is consistent with solar, and a non-inverted $T - p$ profile of 1800-1200 K over a pressure range of 1-10^{-3} bars. We find no evidence for the presence of any further minor species from this analysis. We also split the spectra into a pre- and post-superior conjunction and we find that there is only weak evidence for a detection of water in the post-dayside spectra, this is likely due to the poorer observing conditions for those nights (see section 4.4) and perhaps an overall weak signal from the atmosphere. This may also hint at a phase dependence on the water signal from τ Boötis b, however, we find no evidence for this in these spectra. For this model, we also retrieve a scaling factor of $\log_{10}(a) = 0.39$ indicating that the water depths are $\sim 2.5\times$ deeper that the modelled spectral lines. As this planet is at an $\sim 41.6°$ inclination, we are viewing a mixture of the hot day-side and the cooler night-side of the atmosphere. Due to the absence of external irradiation from the host star on the night-side, it is expected that the lapse rate is steeper compared the day-side resulting in steeper spectral lines (e.g. de Kok et al., 2014). As water is expected to be formed on both sides (Madhusudhan, 2012), it is likely that our scaling factor is trying to compensate for the differences in line depths over the two temperature regions.

4.8.1 The orbital parameters of non-transiting planets

Assuming a circular orbit for τ Boötis b, we retrieve a systemic velocity of $-11.51^{+0.59}_{-0.60}$ km s^{-1} which is significantly shifted from the literature value of -16.9±0.3 km s^{-1} (Gaia Collaboration, 2018). However, these observations were taken a few years apart from those from the Gaia data release 2 survey, therefore, according to the radial velocity solution of τ Boötis A in Justesen and Albrecht (2019), it is likely that the systemic velocity has shifted further to over -17 km s^{-1}. This is due to the systems M-dwarf companion, τ Boötis B, approaching periastron which will impart an additional radial velocity shift of τ Boötis A from the planetary signal (see Figure 3 in Justesen and Albrecht (2019)). The analysis by Pelletier et al. (2021) also recovers a significantly shifted velocity of $V_{\rm sys} = -15.4 \pm 0.2$ km s^{-1}. This shift in our $V_{\rm sys}$ can be partially explained by assuming an eccentric solution from Borsa et al. (2015) ($e = 0.011 \pm 0.006$ and $\omega = 113.4° \pm 32.2°$), as used in Pelletier et al. (2021). If we used this eccentric solution on the phases calculated using the updated T_0 and

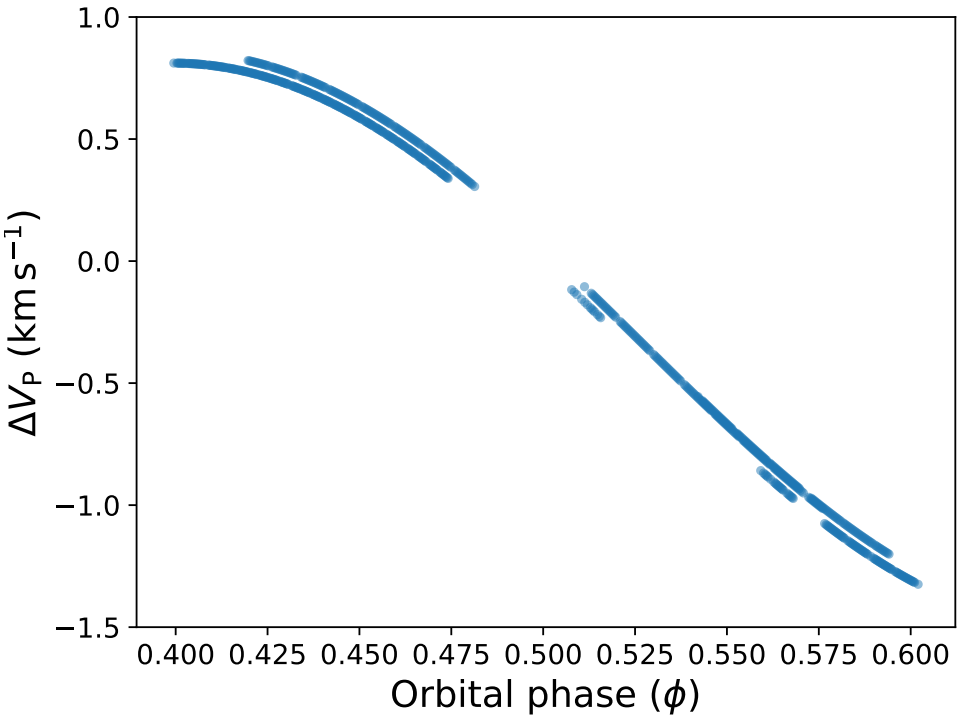

Figure 4.9: Difference in the radial velocity of τ Boötis b in $\mathrm{km\,s^{-1}}$ between the eccentric and circular orbital solutions. The magnitude of these velocity shifts do not explain the $\sim 7\,\mathrm{km\,s^{-1}}$ shift we retrieve from the systemic velocity.

the orbital period from Justesen and Albrecht (2019), this would result in a shift in the velocity by $\sim -3\,\mathrm{km\,s^{-1}}$. If we do adopt the full orbital solution from Borsa et al. (2015) (including their retrieved T_0 and orbital period), then we get at most a shift in the planetary velocity by $\pm 1.5\,\mathrm{km\,s^{-1}}$ as show in Figure 4.9 also does not resolve the discrepancy in the retrieved systemic velocity. However, the time of periastron (T_0) for the eccentric solution obtained in Borsa et al. (2015) is highly uncertain (± 0.3 in BJD) and could therefore result in an even greater shift of several $\mathrm{km\,s^{-1}}$ for the systemic velocity. Due to this uncertainty in time of periastron from the eccentric orbital solution, we do not implement this solution into our analysis and instead adopted the circular orbital solution from Justesen and Albrecht (2019). However, this does show that even a relatively small eccentricity can lead to significantly shifted planetary velocities of up to several $\mathrm{km\,s^{-1}}$ if the eccentric solution is highly uncertain. This was also true in the high resolution characterisation of the non-transiting planet 51 Pegasi b (Birkby et al., 2017) which needed to invoke a large shift in the time of periastron by $\Delta T_0 = 0.07$ in days for the circular orbital solution to match the observed water signal to that of the observed systemic velocity. This highlights the importance of retrieving and regularly updating precise orbital solutions with long period radial velocity surveys in order to accurately constrain the planetary velocities with follow-up high resolution atmospheric characterisation, particularly for non-transiting systems. Further observations of τ Boötis b are therefore necessary to try explain these apparent discrepancies in the characterisation of this system.

4.8.2 Comparison with previous analyses of the atmosphere of the planet

Our analysis confirms the detection of water in the L-band from Lockwood et al. (2014) who used the NIRSPEC instrument at the Keck Observatory. Curiously, our water detection is in stark contrast to the results in Pelletier et al. (2021) who find only a $3\,\sigma$ upper limit on the water abundance at a VMR$= 10^{-5.66}$ with a full atmospheric retrieval. This analysis detects the presence of water at a VMR$= 10^{-3}$ which is preferred over a VMR of 10^{-4} and 10^{-5} by $3.8\,\sigma$ and $5.0\,\sigma$, respectively, with a non-inverted $T - p$ profile of 1800-1200 K over $1 - 10^{-3}$ bars. However, we do emphasise that the molecular abundance and $T - p$ profile in our analysis will be partially correlated and therefore a full atmospheric retrieval is needed on these spectra to give an accurate comparison of the water abundance with Pelletier et al. (2021).

The analysis by Pelletier et al. (2021) observed the day-side thermal emission

of τ Boötis b with the SPIRou ($R = 70,000$) instrument over five nights of data spanning a similar phase coverage to this analysis. Due to the wider wavelength coverage of SPIRou ($\lambda = 0.95 - 2.50\ \mu$m) compared with CARMENES, it was expected that SPIRou should have observed the day-side emission of CO and H_2O simultaneously, however, only CO at was detected in these spectra. As CARMENES does not cover the strong 2-0 R-branch absorption feature at $\sim$2.3 μm, we cannot observe these two molecules simultaneously. Brogi et al. (2012) also only detected the absorption features from CO from τ Boötis b, however, their observations were taken with a narrow wavelength range to cover the 2.3 μm feature, therefore, it is likely that the strong CO lines obscured the H_2O lines to be observable. It could also be the case that Pelletier et al. (2021) suffer from the same sort of behaviour as the strong CO lines mask the weaker water absorption features in the atmosphere of τ Boötis b, although this explanation is perhaps unsatisfactory as they deduce that the spectra are sensitive to the presence of water from τ Boötis b with their injection and retrieval tests. We are only able to detect a convincing signal from water our fourth night which has a phase coverage of $\sim$0.42-0.48. The corresponding night in Pelletier et al. (2021) that covered the same phase range suffered from poorer seeing and a slightly lower SNR than the rest of their nights. If it is the case that there is some phase dependence and the signal is far stronger within this phase range, then this could explain the absence of water in their analysis. However, if there is a constant abundance of water across the orbit then it should be observable in the spectra from Pelletier et al. (2021). The final explanation for the discrepancies in the water detection could be due to differing line lists used in each analysis. In this analysis we use the HITEMP water opacities calculated using the BT2 line list (Barber et al., 2006) as also used in the analysis Pelletier et al. (2021), therefore, we rule out the possibility that line lists are the cause of the discrepancies between our two analyses.

4.9 Additional analysis with the inclusion of night 2

4.9.1 MCMC analysis on the individual nights

It is clear from Figure 4.8 that each nights set of spectra do not contribute equally to the overall water signal from τ Boötis b in Figure 4.10. Here, we repeat the analysis from section 4.7.3 but instead of combining the nights together, we run an MCMC on the individual nights to assess the contribution from each night. As the pre-superior conjunction data only included night 4, the retrieved parameters will be the same as shown in Figure 4.8.

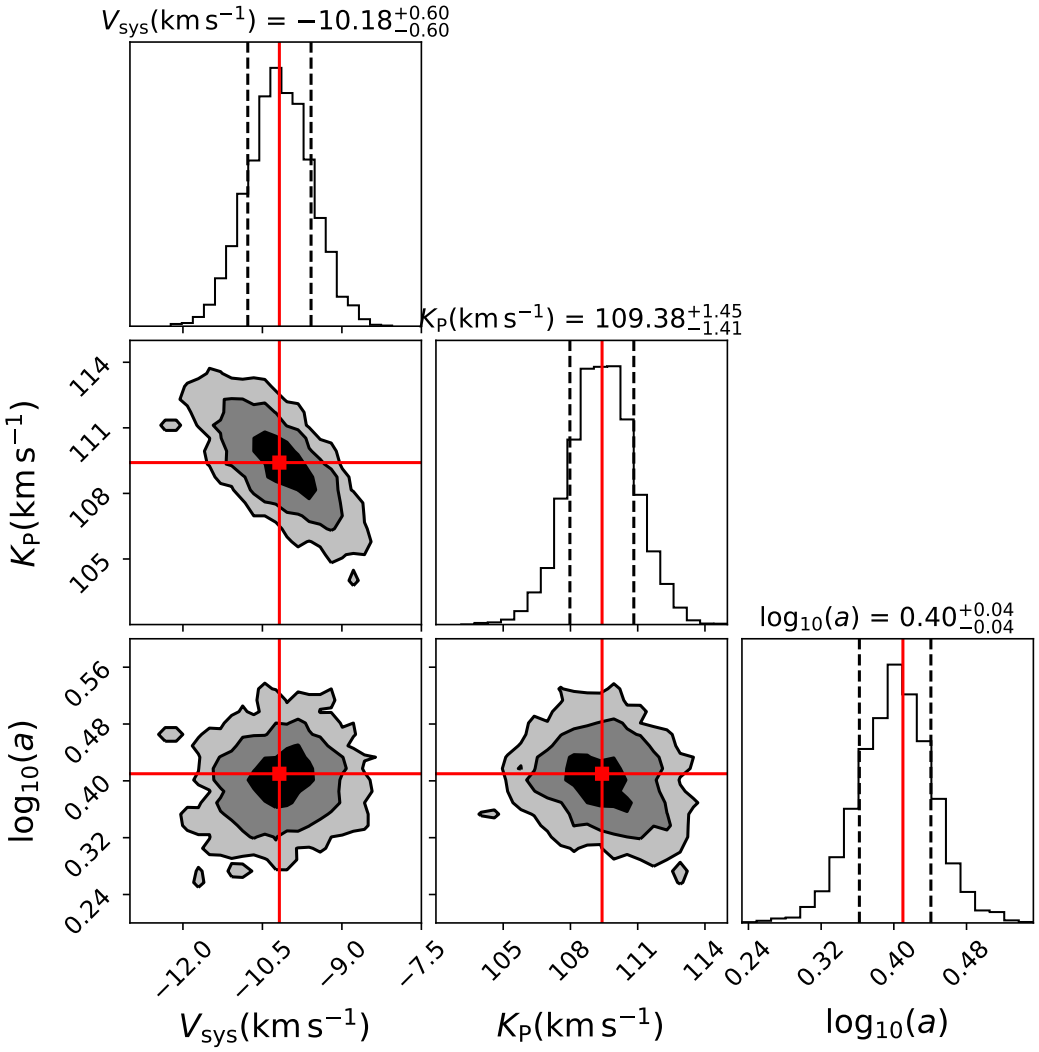

Figure 4.10: Same as Figure 4.7 and 4.8 but with only spectra from night 4 with the best-fitting combined water model. There is a clear signal from τ Boötis b with the retrieved parameters stated above each histogram.

Table 4.5: The median values retrieved from an MCMC analysis for the orbital solution and an atmospheric scaling parameter for each night in the analysis.

Night	**Retrieved parameters (median)**		
	$V_{\rm sys}$ ($\rm km\,s^{-1}$)	$K_{\rm P}$ ($\rm km\,s^{-1}$)	$\log(a)$
1	$-15.57^{+21.82}_{-2.70}$	$50.69^{+1.19}_{-0.55}$	$1.71^{+0.06}_{-0.08}$
2	21.44 ± 0.19	$50.03^{+0.05}_{-0.02}$	1.80 ± 0.01
3	$-10.56^{+10.86}_{-12.85}$	$102.25^{+37.92}_{-43.29}$	$0.27^{+0.26}_{-0.46}$
4	$-12.41^{+2.23}_{-2.60}$	$108.22^{+6.36}_{-7.81}$	$0.43^{+0.09}_{-0.15}$
5	$-15.56^{+5.67}_{-13.73}$	$110.78^{+8.00}_{-13.95}$	$1.36^{+0.60}_{-1.68}$

In table 4.5 we show the median values retrieved from an MCMC analysis on each night. As described in section 4.7.3, the MCMC is set-up with 12 individual walkers each with a chain length of 1000. All of the nights failed to converge to a single solution, however, night 4 performed the best with the main peak in the posterior distribution at the expected radial velocity of the planet. Nights 1 and 2 perform worse than the other nights as those chains settled onto the lower limit of the $K_{\rm P}$ prior. This is likely an indication that those spectra suffer from some residual tellurics despite the lack of visible highly deviant wavelength columns. Night 5 shows a potentially weak signal for water at the orbital solution of τ Boötis b, however, the MCMC did not converge to a single solution with a particularly wide posterior on the scaling factor $\log_{10}(a)$.

The lack of a water detection in every night except for night 4 is not one of surprise given the variable observing conditions between each night at the Calar Alto site. Given the variable SNR for nights 1, 2, 3 and 5 it is highly likely that these suffered from cloudy conditions intermittently throughout these nights. The variable SNR for nights 1 and 2 combined with the high humidity, which consistently exceeded > 85 per cent during the nights, is likely the reason why residual tellurics overpower the weak water signal in this MCMC analysis. Although we can only detect the water signal from the night 4 spectra, it is nevertheless the case that with the addition of nights together helps the water detection by tightening the confidence intervals on the retrieved parameters which is seen in Figure 4.8 and 4.10.

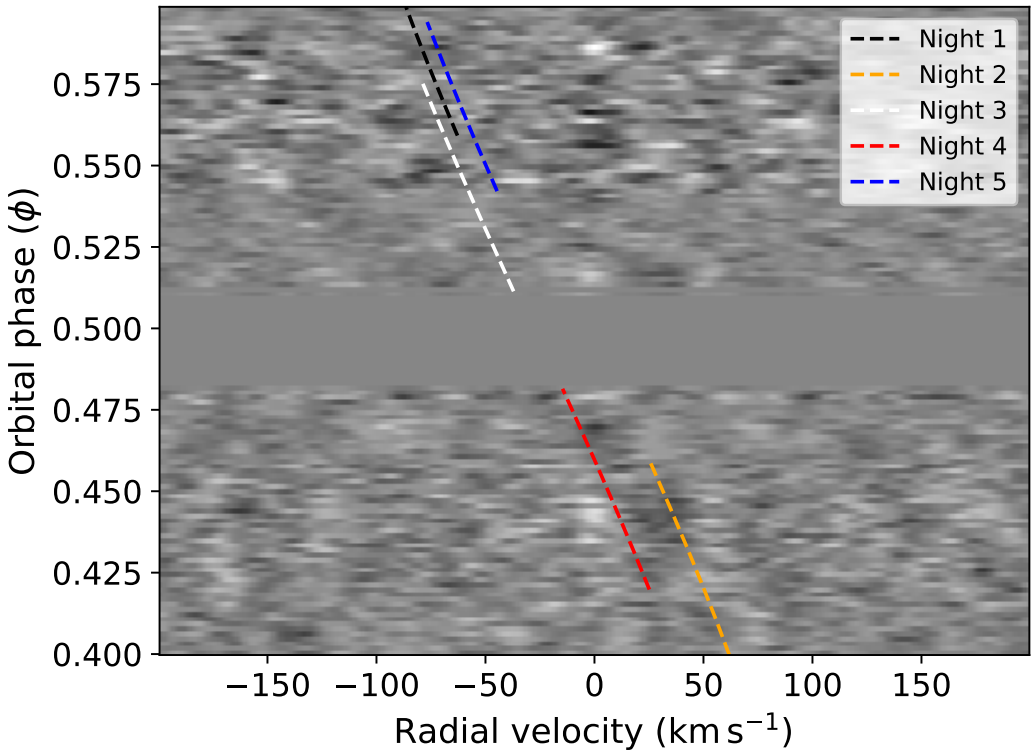

Figure 4.11: Same as Figure 4.3 but with all nights included binned in phase with a resolution of $\Delta\phi = 0.0015$. The black, orange, white, red and blue dashed lines show the expected radial velocity of τ Boötis b for nights 1-5, respectively.

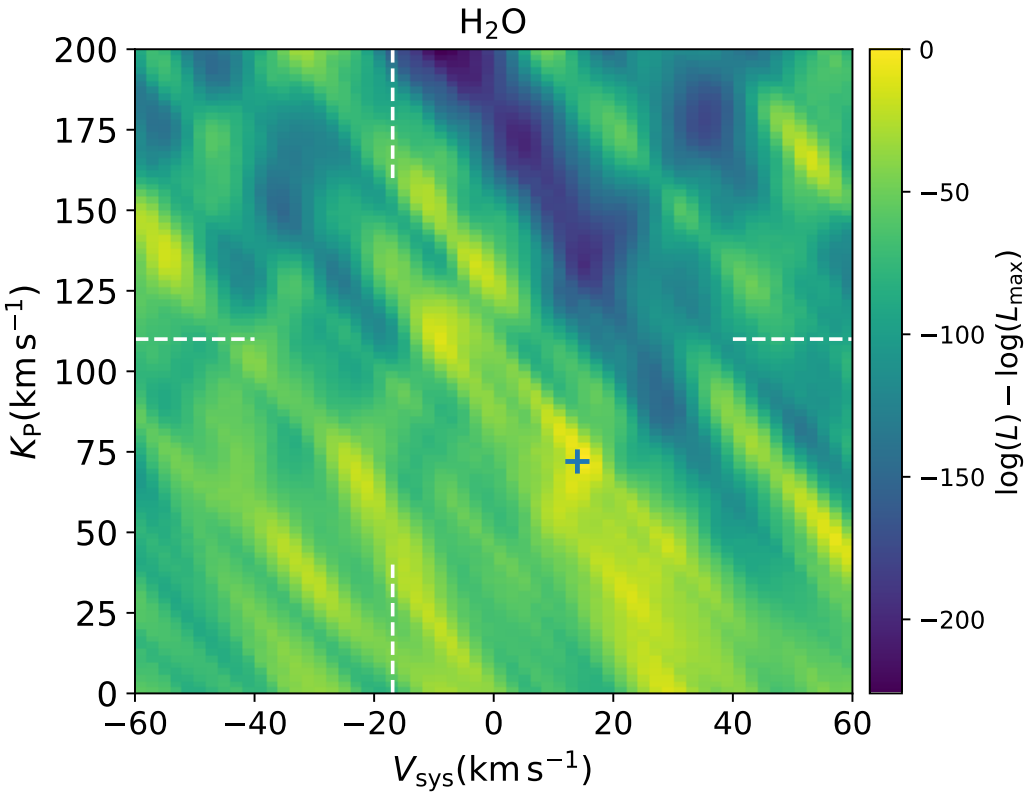

Figure 4.12: Same as Figure 4.4 but with the inclusion of night 2. The white dashed lines show the expected position of τ Boötis b. The blue cross shows the position of the maximum $\log(L)$ which no longer appears at the position of the detection in Figure 4.4.

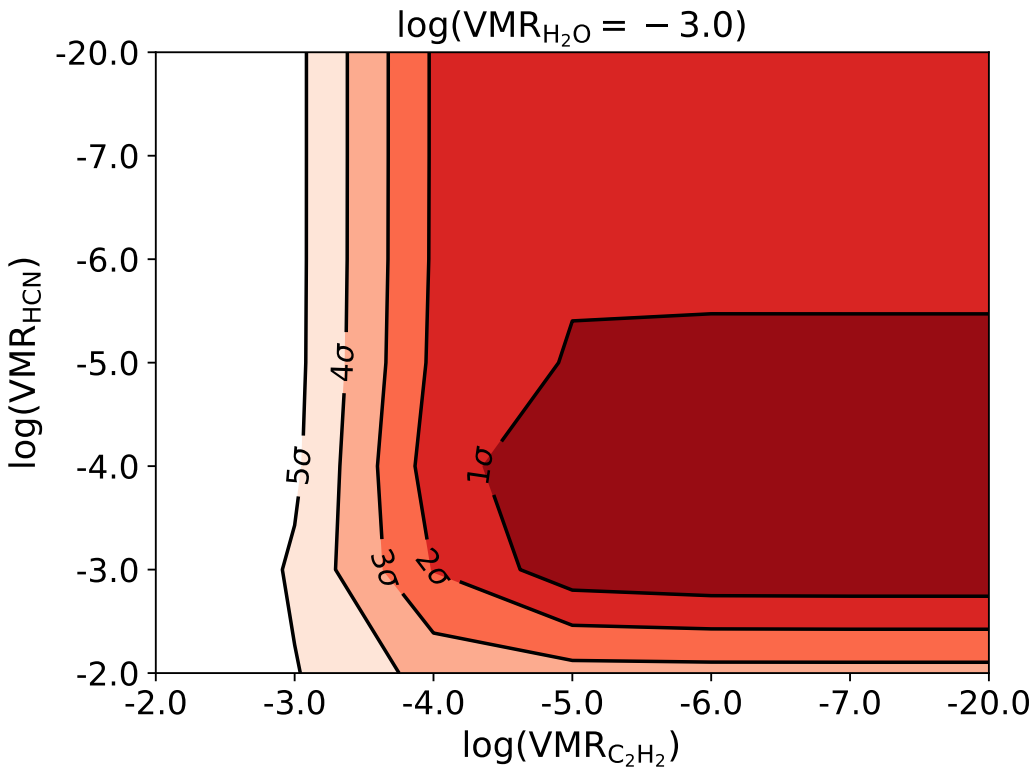

Figure 4.13: Same as Figure 4.6 but with the addition of night 2. With the inclusion of these spectra, we see a marginal preference for the addition of HCN at a VMR= 10^{-4} in the best-fitting atmospheric model.

4.9.2 Cross-correlation to log likelihood analysis including all nights

As shown in the main data analysis (see Figure 4.3), night 2 suffers from strong telluric residuals despite the telluric removal steps and the additional masking of highly deviant spectral channels. However, here, we show how the inclusion of the observations from night 2 (261 additional spectra) affect the results of the analysis from the four other nights.

Figure 4.11 shows all spectra correlated with a pure water spectrum as a function of phase and radial velocity shift from the telluric rest frame. The coloured dashed lines indicate the expected radial velocity trails of τ Boötis b during those observations. In Figure 4.12, we show the $K_{\rm P}-V_{\rm sys}$ velocity map with the inclusion of night 2. It is clear that the telluric noise from these spectra overwhelms the planet's water signal as seen in Figure 4.4 with the retrieved $\log(L_{\rm max})$ (shown as the blue cross) shifting beyond the expected orbital velocity of the planet. However, as shown in Figure 4.10, the MCMC still converges onto a local maximum at the expected orbital solution of the planet. Although this is a case of the MCMC algorithm converging onto a local maximum before exploring the wider parameter space, it is nevertheless showing that there is still a detectable signal of water from the atmosphere in the local vicinity of expected orbital solution. If we use the retrieved parameters from the MCMC analysis, we find a marginal preference of $1.1\,\sigma$ for the inclusion of HCN in the atmospheric models at an abundance of VMR$= 10^{-4}$. In Figure 4.13, we show the updated abundance constraints on HCN and C_2H_2 for the inclusion of night 2 spectra. With these results we can lower the $3\,\sigma$ upper limits on the these species at $\log(\mathrm{VMR}) \approx -2.0$ and ≈ -4.0 for HCN and C_2H_2, respectively.

4.10 Conclusions

With ~ 21 h of observations over five nights at high resolution with the CARMENES spectrograph, we unambiguously detect the presence of absorption features from water vapour through thermal emission from the atmosphere of τ Boötis b. We searched for, HCN, CH_4, NH_3 and C_2H_2 but found no evidence for these minor species. Using a grid of models, we found that these spectra prefer a high abundance of water (VMR $= 10^{-3}$) which is significantly preferred over models with lower abundances by $\leqslant 3.8\,\sigma$. However, a full atmospheric retrieval would be needed to provide confidence intervals on the retrieved abundance for water. On individual nights, we find that the predominant signal from water originates from night 4, in effect this means that we were able to detect the signature for water in only ~ 5 h of observation in a phase coverage of $\phi = 0.42 - 0.48$. We find no strong evidence for

any phase variability in the water signal over the phase coverage of our observations in our analysis when we split the data into pre- and post-dayside observations. We retrieve an atmospheric scaling factor of $\log(a) = 0.39$ which suggests the model is underestimating the depth of the water lines by $2.5\times$, however, this value could be dominated by the mixing of day and night-side emission from the atmosphere due to the $\sim 41^{\circ}$ inclination of the planet. This analysis is in agreement with the L-band detection from Lockwood et al. (2014) but is strongly in disagreement with the more recent analysis from Pelletier et al. (2021) which finds no evidence for water in the atmosphere of τ Boötis b.

Retrieving an accurate abundance is crucial if we are to understand the C/O ratio (e.g. Madhusudhan, 2012), metallicity (e.g. Moses et al., 2013) and the physical structure (e.g. Seager and Sasselov, 1998) of hot Jupiter atmospheres. It is likely that further analysis of the atmosphere of τ Boötis b is needed in order to resolve some of the discrepancies that remain over the detection of water. It is also likely that a full atmospheric retrieval is necessary in order to delve deeper into the water features that we have detected from the emergent spectra from τ Boötis b in the Y-, J- and H-bands.

Chapter 5

On the detectability of Earth-like atmospheres around M-dwarfs using high resolution spectroscopy with the ELT

5.1 Notes

This chapter follows unpublished work which is being prepared for future publication. Whilst most of this chapter is my own work, however, there were contributions to this work by the following people. Matteo Brogi helped to edit the main text in this chapter which is as yet unpublished work. Siddharth Gandhi provided the transmission spectrum of an Earth-like atmosphere around the M-dwarf GJ 3470 and the calculations of the molecular cross-sections shown in Figure 5.2.

5.2 Abstract

This study presents simulated observations of transiting Earth-like atmospheres on terrestrial planets in the habitable zone of an M5 and M7 host stars observed with the upcoming ELT at high resolution. Unlike with previous simulated observations focussing on molecular oxygen primarily in the optical, this study includes the full opacity set of molecules observable in the NIR with H_2O, O_2, O_3, N_2O, CH_4, CO_2 and N_2. These simulations assume a high resolution spectrograph with a resolution of $R = 100,000$ and a simultaneous wavelength coverage of 0.96-2.7 μm similar to spectrographs already in use such as SPIRou and GIANO. For uncorrelated noise,

perfect observing conditions and spectral contaminant removal from the spectra (similarly done to the previous literature), it is found that ~ 15 and 20 transits are needed on average to detect the atmosphere with HRCCS for the planets around the M5 and M7-dwarf at 10 pc, respectively. This study also simulates the typical data reduction and analysis used on HRCCS for a time series set of spectra with varying airmass. The use of PCA was tested here on the time variability on this data-set and find that planets orbit too slowly around either the M5 or M7 star to prevent the removal of the planetary spectral lines for this methodology to work. It is recommended that a future analysis explores the use of other data analysis techniques, such as the approach developed in the last decade to analyse Keck/NIRSPEC HRS data for habitable, Earth-like planets around M-dwarfs.

5.3 Introduction

The detection of an Earth-twin with observable biomarkers such as H_2O, O_2, O_3 and CH_4 (Lederberg, 1965; Lovelock, 1965) in its atmosphere is one of the main driving scientific cases for exoplanet atmospheric science both theoretically and observationally. Sagan et al. (1993) famously observed the Earth's spectrum in the optical and NIR with the Galileo spacecraft to indicate what observations could look like for a habitable exoplanet. The abundance measurements for the biomarkers in the spectrum were particularly important as this shows strong chemical disequilibrium within the atmosphere which is an indicator of life. One of the main science cases for the JWST and the upcoming ground-based 39 m ELT at Cerro Armazones in Chile is to revolutionise exoplanet atmospheric science by observing these smaller and cooler planets with unprecedented precision, provided they orbit late-type stars. Numerous simulation studies have been done on the detectability of the atmopsheres of habitable, terrestrial exoplanet atmospheres with JWST, in particular around M-dwarf host stars (e.g. Barstow and Irwin, 2016; Pidhorodetska et al., 2020; Komacek et al., 2020; Gialluca et al., 2021; Haqq-Misra et al., 2022). However, there have been fewer simulations of the detectability of biomarkers in the atmospheres of these cooler planets with HRS on the ELT.

HRCCS is now one of the most successful methods of detecting and determining the chemical and physical processes in exoplanet atmospheres. One of the key advantages of using high resolution spectrographs ($R \gtrsim 20,000$) is that each individual absorption or emission line will be unique to each species that is present according to each of their specific quantum energy states. However, at ever greater spectral resolutions, the SNR per resolved wavelength channel is reduced which

results in the need to cross-correlate with a model atmospheric spectrum either through forward modelling (e.g. Snellen et al., 2010; Brogi et al., 2012) (also applied in chapters 3 and 4) or with a Bayesian retrieval analysis (Gibson et al., 2020; Pelletier et al., 2021; Line et al., 2021; Gandhi et al., 2022; Gibson et al., 2022). This requires accurate modelling of each species with line lists of exquisite precision from large data-bases such as those from HITRAN (Gordon et al., 2017, 2022), HITEMP (Rothman et al., 2010a) and EXOMOL (Tennyson and Yurchenko, 2012; Polyansky et al., 2018). One of the most difficult aspects for high resolution ground-based observations, however, lies in the near perfect removal of the contaminating spectral features in the observed spectra. Typically, this has most often been done by assuming that the rate of change of the radial velocity of the planet is sufficiently high in order to disentangle these shifting planetary lines from the stationary tellurics and stellar lines. This has been hugely successful in the atmospheric studies of hot and ultra-hot Jupiters (e.g. Snellen et al., 2010; Brogi et al., 2012; Birkby et al., 2017; Hoeijmakers et al., 2018a; Line et al., 2021) that by their very nature produce the largest SNR observations both in transmission and emission HRS due to their large scale heights, planet-to-star contrast ratios and radial velocities. However, there haven't been any studies on the use of this technique for much slower moving, Earth-like planets for future observations on the ELT.

There have been a handful of studies on the detectability of transmission spectra of Earth-like atmospheres around M-dwarf host stars. As the transmission signal from the planet is inversely proportional to the square of the host stellar radius, $\Delta \propto \frac{1}{R_\star^2}$ (see equation (1.3)), habitable planet hosting M-dwarfs with their smaller size prove to be one of the best candidates for the first detections of biomarkers in their atmospheres. Therefore, the transit depth for the molecular lines in the NIR for a transiting Earth-like planet can be on the order of 10^{-5}-10^{-3} from early to late type M-dwarfs (e.g. from a M2-dwarf to an M7-dwarf, see section 5.5 and Figure 5.1) which is roughly on the order of that for CO around the hot Jupiter τ Boötis b (Snellen et al., 2013; Brogi et al., 2012). Moreover, M-dwarfs are the most common type of stellar objects within the 10 pc stellar neighbourhood[1] making up roughly 75 per cent of all stellar objects with an estimated 90 per cent completed sample (Henry et al., 2018). This is important as these stars are naturally faint objects and thus having a large sample of nearby M-dwarfs to have HRS observations with enough SNR to potentially detect an Earth-like atmosphere.

Snellen et al. (2013) and Rodler and López-Morales (2014) produced the first simulated HRCCS studies for an Earth-like atmosphere around nearby M-dwarfs

[1] `www.recons.org`

with the ELT. Both consider the prominent O_2 bands in the optical ($\sim 0.76\,\mu$m) and NIR ($\sim 1.27\,\mu$m), however, Snellen et al. (2013) only considers a fixed spectral resolution of 100,000, only white (uncorrelated) noise contributions and system distance of 12 pc. Whereas, Rodler and López-Morales (2014) (using the same O_2 bands as Snellen et al. (2013)) improves upon this analysis by considering the influence of red (correlated) noise on the data, varying spectral resolution ($R = 60,000$-$100,000$) depending on the spectral type and varying of the distance between 1-20 pc. Using S/N as a detection significance parameter (i.e. the peak in the CCF divided by the standard deviation of the noise), Snellen et al. (2013) finds that, in an idealistic observing scenario, combing roughly 30 transits is required to significantly detect the presence of O_2 on an Earth-like planet around an M5-dwarf. Rodler and López-Morales (2014) finds that in the most optimistic observing scenarios, a significant detection of O_2 is only realistically feasible (in < 60 transits) in the optical for host stars later than M3 at close distances ($d < 8$ pc).

Following on from this, Serindag and Snellen (2019) produced synthetic observations of the $0.76\,\mu$m O_2 features by injecting the transmission spectrum into three nights of real observations of Proxima Centauri, an M5-dwarf (Bessell, 1991), with the high resolution instrument UVES (Dekker et al., 2000) ($R \approx 42,000$). As these observations were taken with the 8 m VLT, the ELT is expected to have $\sim 25\times$ more light collecting power, however, M-dwarfs at $d \sim 10$ pc, the star will be $\sim 25\times$ fainter. Thus, the use of these observations allowed Serindag and Snellen (2019) to have more accurate noise distribution in the spectra for an observation of a late type M-dwarf with the ELT. They find a similar number of transits is required to detect the optical O_2 feature as Snellen et al. (2013) and Rodler and López-Morales (2014), indicating that real noise from instrumental and observational effects not simulated in the idealistic simulations did not affect the outcome of the detectability showing the power of HRCCS and the data reduction pipelines of high resolution spectrographs. López-Morales et al. (2019) perform a similar analysis as Rodler and López-Morales (2014), however, they study the effect of adding further O_2 bands in the NIR and varying the resolution from $R = 10^5$-10^6. They conclude that observations with a high resolution spectrograph with resolutions between $R = 3$-5×10^5 improve the detectability of an the O_2 bands around M-dwarfs with the ELT. At these resolutions it was found that the number of transits needed to detect the O_2 bands reduced by over 30 per cent.

This study aims to follow on from the work by Snellen et al. (2013), Rodler and López-Morales (2014), Serindag and Snellen (2019) and López-Morales et al. (2019) with the potential of observing the spectra of Earth-like spectra from ground-

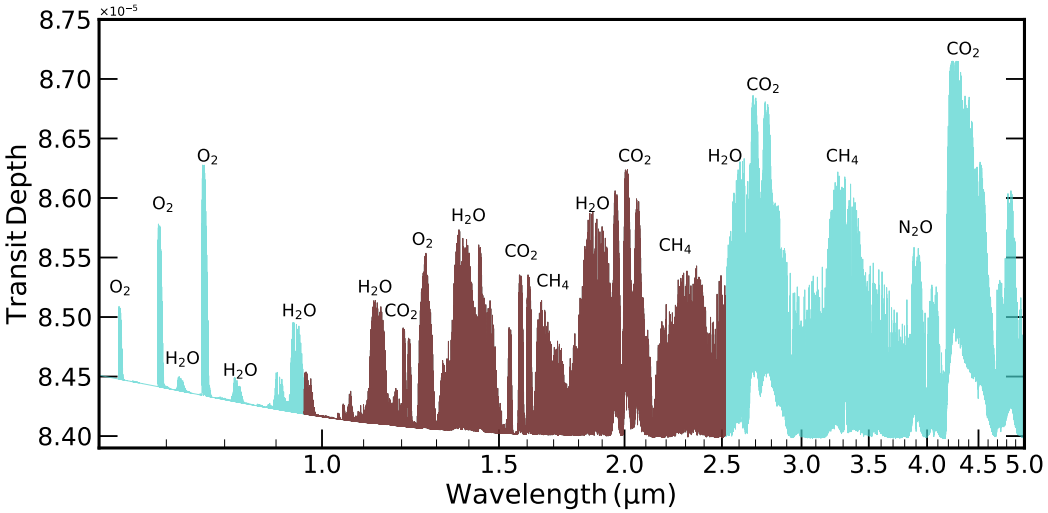

Figure 5.1: Transit depth as a function of wavelength for an Earth like spectrum around the early M2-dwarf GJ 3470 at 0.4-5.0 μm. This model is scaled to the stellar radii of the later type M-dwarfs considered in this work. The prominent molecular absorption bands are indicated above. The typical simultaneous wavelength coverage of high resolution spectrographs and thus only considered in this work is shown in maroon (0.96-2.5 μm).

based high resolution spectrographs. Our study however moves the focus away from solely observing the prominent O_2 bands in the optical and NIR (see Figures 5.2 and 5.1) but instead includes the additional spectral features from a wider range of molecular species in the NIR bands that the ELT (39 m) IR high resolution instruments will observe with HIRES (now ANDES) ($0.4 - 1.8\,\mu$m) (Marconi et al., 2021) and METIS ($3 - 13\,\mu$m) (Brandl et al., 2010). As explained in López-Morales et al. (2019), increasing the number of observed spectral lines (see Figure 5.1), N, will increase the strength of the final CCF by $\sim \sqrt{N}$, and therefore observing a full spectral composition from an Earth-twin here could be advantageous for which this study investigates in section 5.6.1. The second aim of this study is to simulate currently used data reduction and analysis techniques on a time sequence of spectra across the transit. For this, PCA is used here to remove the time varying components per wavelength channel as a function of time. This is discussed in section 5.6.2 with an outline of the results in section 5.6 and a final discussion and summary of the analysis in section 5.7.

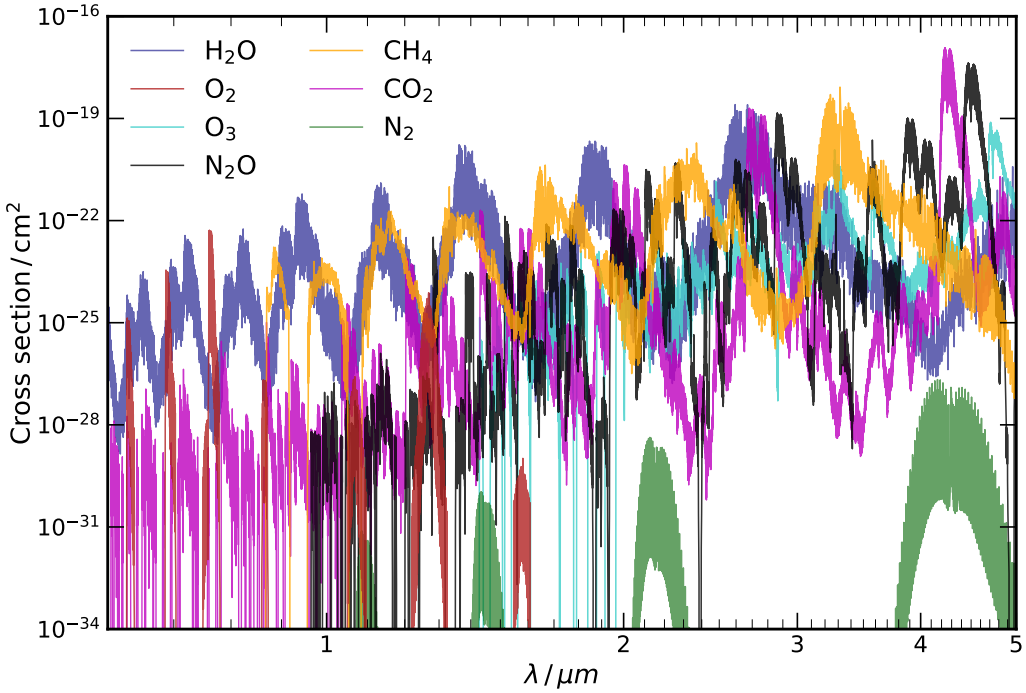

Figure 5.2: Cross-sections of the volatile species considered in the modelling as a function of wavelength. These are representative of an Earth like composition and temperature ($\sim 285\,\mathrm{K}$).

5.4 Earth-like model spectrum

The Earth's spectrum is calculated using the line-by-line radiative transfer code GENESIS by Gandhi and Madhusudhan (2017). The T-p profile was taken as the international standard atmosphere[2] (ISA) which provides the temperature and pressure value at altitudes from the bottom of the troposphere to the top of the mesosphere ($\sim 85\,\mathrm{km}$). The main opacity sources used here include; H_2, CH_4, O_2, CO_2, O_3, N_2 and N_2O. These are the main opacity sources in the optical and NIR and are thus included in the modelling of an Earth twin spectrum. The opacity cross-sections, given in cm^2, are shown in Figure 5.2 which were all calculated by the line lists given in the HITRAN database (Gordon et al., 2017, 2022). The cross-section in this case refers to a measure of probability that the species will get into an excited energy state and subsequently emit a photon at that wavelength. Typically, the largest opacity bands at these wavelengths are H_2O and CH_4 with other prominent features from CO_2 at $\sim 4.2\,\mu$m, O_2 at $\sim 0.76\,\mu$m and N_2O at $\sim 4.0\,\mu$m. The simulated wavelength coverage in this study is $\lambda = 0.96$-$2.5\,\mu$m and thus these prominent features from these species will be missed. However, these could be observable with coverage from the METIS or the GMTNIRS (2.9-5.3 μm) (Jaffe et al., 2006) high resolution instruments on the ELT and Giant Magellan Telescope, respectively.

The atmosphere is assumed to be a cloud free atmosphere in hydrostatic equilibrium, therefore, the following equation holds $\frac{dp}{dz} = -\rho g$, which describes that the gradient of the pressure with altitude is the negative density of the gas (ρ) multiplied by the gravitational acceleration (g). Rayleigh scattering is also modelled which is most efficient at bluer wavelengths owing to the scattering function being inversely proportional to the fourth power of wavelength, i.e. $S \propto \lambda^{-4}$. The chemistry is fixed with altitude with the following mixing ratios; $\mathrm{VMR}_{\mathrm{H_2O}} = 10^{-5.5}$, $\mathrm{VMR}_{\mathrm{O_2}} = 10^{-0.678}$, $\mathrm{VMR}_{\mathrm{O_3}} = 10^{-7.52}$, $\mathrm{VMR}_{\mathrm{N_2O}} = 10^{-6.52}$, $\mathrm{VMR}_{\mathrm{CH_4}} = 10^{-5.78}$, $\mathrm{VMR}_{\mathrm{CO_2}} = 10^{-3.44}$ and $\mathrm{VMR}_{\mathrm{N_2}} = 10^{-0.1025}$ which closely match the values found in the Earth's atmosphere (Farmer, 1987).

The resulting transit spectrum is shown in Figure 5.1 with the prominent opacity bands indicated above the features. The transit depth is calculated with respect to the planet hosting M2-dwarf (Lépine et al., 2013) star GJ 3470 which is not considered in this study and thus this transit depth with vary from these values, with a scaling factor that is described in further detail in the following section 5.5. The model shown in Figure 5.1 spans a wide wavelength from 0.4-5.0 μm in turquoise,

[2] `https://www.iso.org/standard/7472.html`

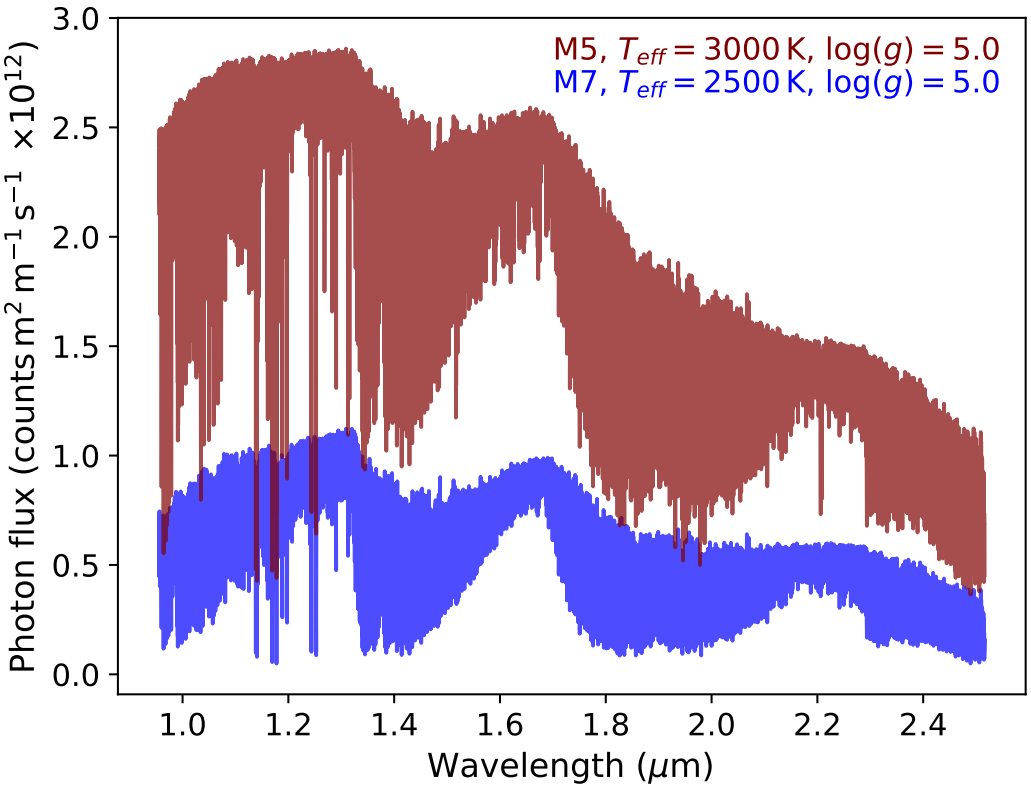

Figure 5.3: The photon flux from an M5 (in maroon) and M7 dwarf (in blue) at a distance of 10 pc with effective temperatures of 3000 and 2500 K, respectively. Both have been taken from the high resolution Phoenix BT-Settl grid of models with both having a log(g) = 5.0 and with zero metallicity. These spectra have been re-grid and convolved onto a constant resolution of 100,000 at a wavelength coverage of $0.96 - 2.7\,\mu$m.

however, the wavelength range considered here is shown in maroon. The sloping feature at the blue end of the spectrum is a result of the Rayleigh scattering which makes the planetary radius appear larger than at IR wavelengths.

5.5 Simulated observations

The observations of an Earth twin around late type M-dwarfs are simulated as follows. The Proxima Centauri (hereafter, Proxima) (Anglada-Escudé et al., 2016) and TRAPPIST-1 systems (Gillon et al., 2017) are used as proxies for the transiting planet with an Earth-like atmosphere. This is to say that the planets found in these systems are within the habitable zone and the host stars are mid-to-late M-dwarfs. However, it should be noted that these systems are being simulated at a

distance of 10 pc and not at the distances where the Proxima and TRAPPIST-1 systems are found. A distance of 10 pc was motivated by the findings of Dressing and Charbonneau (2015) that suggests this as a minimum distance for a potentially transiting Earth-sized planet within the habitable zone around an M-dwarf. The simulated observations are assumed to have an instrumental resolution of 100,000 on a 39 m telescope such as the ELT. This resolution was chosen as to match the resolutions of the old CRIRES (Kaeufl et al., 2004) and new CRIRES+ (Follert et al., 2014) instruments already operational on the VLT aswell as the resolution of the planned HIRES/ANDES (Marconi et al., 2021) and METIS (Brandl et al., 2010) instruments on the ELT.

Proxima is a mid-to-late M5 dwarf star and is modelled here with a temperature of 3000 K and $\log(g) = 5.0$ roughly matching that of Proxima (Anglada-Escudé et al., 2016). TRAPPIST-1 is a late type M7 dwarf star (Gizis et al., 2000) which is modelled here with a temperature of 2500 K and a $\log(g) = 5.0$ which roughly matches that of TRAPPIST-1 (Gillon et al., 2017). The metallicity is kept at zero for these models as a variability in metallicity is not considered in this study. These stellar spectra are obtained from the high resolution Phoenix BT-Settl models (Allard et al., 2012) and are shown in Figure 5.3. These spectra are subsequently re-grid onto a constant resolution and convolved to a resolution of 100,000 using a Gaussian kernel.

These models are output as an emitted stellar flux ($F_\star$) in $\mathrm{erg\,s^{-1}\,cm^{-2}\,\AA^{-1}}$ but are subsequently converted into SI units of $\mathrm{W\,m^{-2}\,m^{-1}}$. The steps of calculating the observed photon counts from the stellar models follows closely with that from Snellen et al. (2013) and Gandhi et al. (2020a). The stellar luminosity ($L_\star$) is thus calculated from the radii from the two stars, again Proxima and TRAPPIST-1 are taken to be an estimate here for these which is $0.1537\,\mathrm{R_\odot}$ (Stassun et al., 2019) and $0.1192\,\mathrm{R_\odot}$ (Agol et al., 2021), respectively. The observed flux from the systems are calculated at the top of the Earth's atmosphere via,

$$F_{\mathrm{obs}} = \frac{L_\star}{4\pi d^2}, \tag{5.1}$$

where d is the distance from the system which is taken to be 10 pc away. Furthermore, the photon flux (in $\mathrm{counts\,m^{-2}\,m^{-1}}$) at the top of the Earth's atmosphere is calculated by,

$$F_\gamma = \frac{F_{\mathrm{obs}}}{E_\gamma}, \tag{5.2}$$

where the photon energy is a function of the wavelength,

$$E_\gamma = \frac{hc}{\lambda}, \tag{5.3}$$

where h and c is the Planck's constant and the speed of light, respectively. The photon flux for the two stars are shown in Figure 5.3, the overall photon flux levels for the M5 are higher owing to the higher effective temperature over the M7 dwarf. The broad molecular features are also visible in these spectra as these temperatures are cool enough for several diatomic and triatomic species, such as CO, H_2O and metal hydrides, to be present in these stellar atmospheres (Rajpurohit et al., 2018). In real observations, the detectors on the telescope measure the total photon counts from a particular source. However, for ground based observations with the ELT, this photon flux must pass through the Earth's atmosphere which will ultimately incur some telluric absorption as a function of wavelength which is modelled from a transmission spectrum, $T_\oplus(\lambda)$, taken from the ESO sky model calculator (Noll et al., 2012) at a Paranal PWV median value of 2.5 mm. The telluric spectrum was created with a resolution of 200,000 which is convolved down to a resolution of 100,000 using a Gaussian kernel to simulate an observed spectrum at the Nyquist sampling rate. This is also consistent with the old CRIRES instrument on the VLT described further in chapter 2.2.

As the Earth-like transmission model, T_P, in Figure 5.1 is calculated from a larger star GJ 3470, the transit depth is scaled according to the simulated host stars being studied here. Therefore, the transit depth will be scaled by $\left(\frac{R_{\mathrm{GJ3470}}}{R_\star}\right)^2$, where R_{GJ3470} is the radius of GJ 3470 which is taken to be $0.5\,\mathrm{R}_\odot$ (Stassun et al., 2019) and $R_\star$ is the radius of the host stars being considered here. As this study is considering smaller, later type stars, the transit depth will increase by roughly three and four times that shown in Figure 5.1 for the Proxima-like and TRAPPIST-1 like stars, respectively.

An estimated wavelength coverage was taken to be that from the current SPIRou instrument which is likely to have a similar wavelength solution to the future high resolution instruments on the ELT. The wavelength solution of SPIRou covers the J, H and K-bands in the NIR at $\sim 0.96 - 2.5\,\mu$m and has an instrumental resolution of $\sim 70,000$. To match the simulated resolution of 100,000, the wavelength solution is interpolated onto new wavelength separations that has a sampling of 200,000 which is again at the Nyquist sampling frequency. We note that this interpolation is unlikely to be subject to errors because the pixel-wavelength solution varies smoothly and therefore it is optimally suited to be interpolated.

With real observations, a total photon count (N_γ) per spectral channel is measured from the detectors and thus the photon flux needs to be converted as such. This is computed via (Gandhi et al., 2020a),

$$N_\gamma(\lambda, t) \;=\; F_\gamma(\lambda)\; T_\oplus(\lambda, t)\; T_{\rm P}(\lambda)\; \epsilon\; \Delta\lambda\; A\; t_{\rm exp}, \tag{5.4}$$

where all the terms are multiplicative onto the stellar photon flux. In equation (5.4), ϵ, A and $\Delta\lambda$ are the instrumental efficiency, photon collecting area and the width of each resolved wavelength element, respectively. The errors for these simulations are assumed to be purely Poisson noise for photon counting and thus each wavelength channel has an associated error which is drawn from a Gaussian distribution with standard deviation of $\sqrt{N_\gamma(\lambda, t)}$ from equation (5.4). Each scenario was simulated 100 times by drawing 100 different random samples for photon count errors. This allows us to build an average detection significance to be determined in the simulations rather than relying on a single noise distribution.

The total collecting area of the telescope dish is computed to be $A = \pi \left(\frac{D}{2}\right)^2$, where D is taken to be the diameter if the ELT which is to be 39 m. As for a realistic observation, the time observing the system needs to be taken into account, for faint objects such as the M5 and M7 dwarfs at 10 pc considered here, a fairly long exposure time is assumed here at $t_{\rm exp} = 400$ s. A constant telescope and instrumental efficiency is assumed to be at 7 per cent which is a good approximation for high resolution spectrographs for orders with good transmission and relatively high throughput. Typically the efficiency is a function of wavelength, however this cannot be applied to this wavelength solution as it is only an estimation of a real spectrograph. The transit depth from the planet $T_{\rm P}$ will realistically vary due to variations in the chemical and physical properties of the planetary atmosphere, particularly at ingress and egress (e.g. Gandhi et al., 2022), however, for simplicity the transit model is kept constant throughout the transit duration.

Finally, the Earth's transmission $T_\oplus$ in the first stage of this analysis (section 5.6.1) is assumed to be constant in time and airmass at 1.0 as this section focuses primarily on the number of transits needed (and therefore the total SNR needed) to detect an Earth-like spectrum around the dwarf systems. However, in section 5.6.2, the airmass is varied as in a typical observational sequence to study whether the typical HRCCS time sequence telluric removal (as in Figure 2.3) can be utilised to detect the spectrum of slower moving Earth-twin planets around dwarf stars. For all the simulations, the spectral channels that have a telluric transmission below 20 per cent is masked to prevent strong telluric residuals influencing the final

Table 5.1: Orbital parameters used for the simulated Earth-twins around an M5 and M7 dwarf host star at a distance of 10 pc. The orbital values for Proxima b (Anglada-Escudé et al., 2016) and TRAPPIST-1 e (Agol et al., 2021) were used as proxies here for the M5 and M7 dwarfs, respectively, as these systems are already in their respective habitable zones.

Host star	Radius ($R_{\rm P}$)	Period (d)	Orbital separation (AU)
M5	$R_\oplus$	11.186	0.0485
M7	$R_\oplus$	6.101013	0.02925

analysis.

5.6 Results

5.6.1 Earth-like spectrum detectability

At this first stage of the analysis, the number of transits in order to detect the Earth-like spectrum is studied here. At this stage, the transmission of the Earth is assumed to be constant throughout the simulated observations with a constant airmass of 1.0 and a PWV of 2.5 mm. An ideal scenario is also considered here whereby the stellar photon count (F_γ), telluric ($T_\oplus$) and efficiency of the instrumentation (ϵ) is perfectly removed from the total photon count (N_γ). However, it should be noted that the errors are added onto the full photon count (i.e. with the inclusion of all the terms in equation (5.4)) prior to the division of the contaminating terms. These ideal scenarios will ultimately lead to an underestimation of the number of transits needed in order to detect an Earth-twin around an M-dwarf with a high resolution instrument with the ELT. However, this study nonetheless aids in the future potential of using such instruments on upcoming large telescopes in the study of terrestrial atmospheres that may contain observable biomarkers.

As equation (5.4) is only a photon count for one spectrum, i.e. for one exposure, the final total number of counts needs to include the final number of exposures taken from the number of transits considered. This is computed by considering the transit duration,

$$t_{\rm dur} = \frac{P}{\pi} \arcsin\left(\frac{\sqrt{(R_\star + R_{\rm P})^2 - (bR_\star)^2}}{a}\right), \tag{5.5}$$

for a terrestrial planet around the habitable zone for the M-dwarfs. Where in equation 5.5, P, b and a are the orbital period, impact parameter and orbital separation, respectively. For simplicity, the impact parameter is assumed to be zero and no

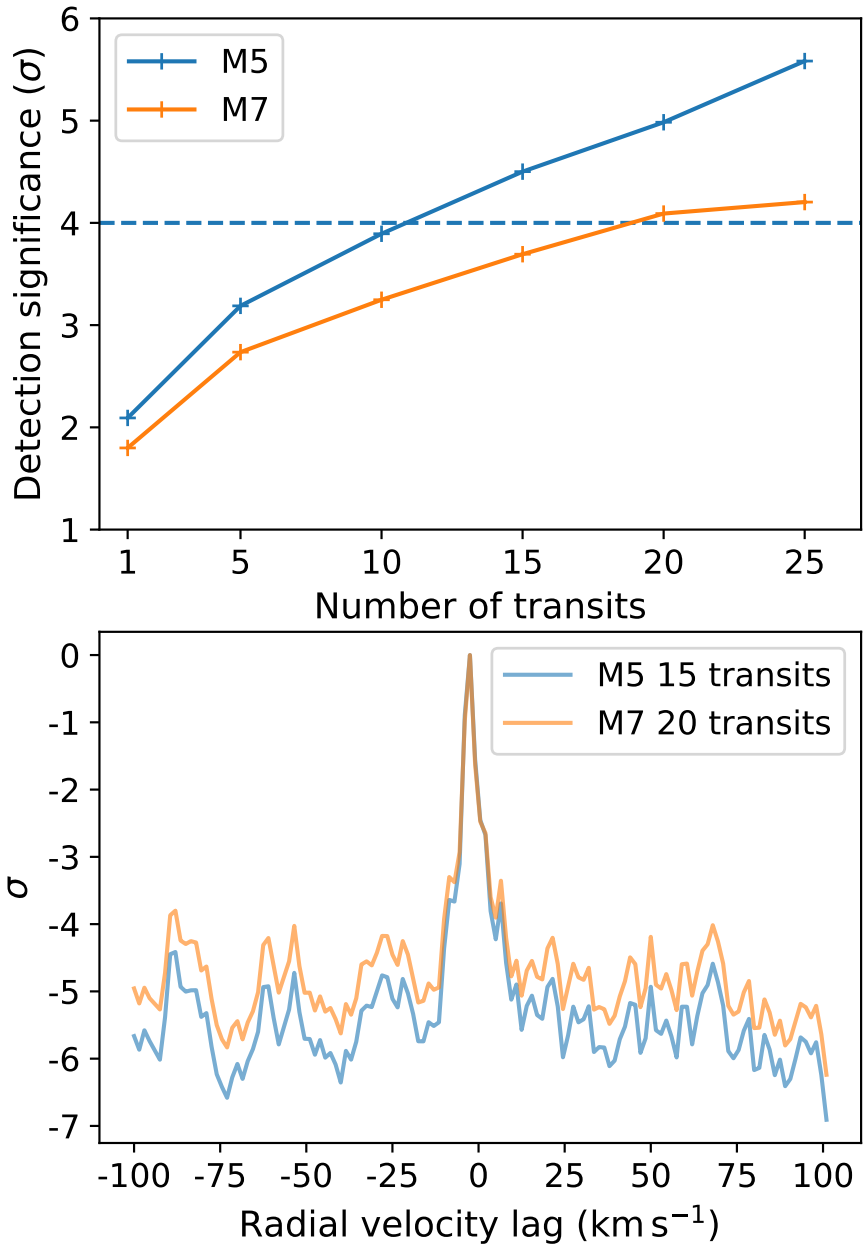

Figure 5.4: Top panel: Detection significance of the Earth-like spectrum around the M5 (in blue) and M7 (in orange) host stars at 10 pc as a function of the number of transits. The detection lower limit has been placed at 4 σ for which, on average, 15 and 20 transits are needed for these spectra to be detectable around the M5 and M7 dwarfs, respectively. Bottom panel: Example CCFs for the detectable number of transits deduced in the top panel. The σ here is computed from the $\Delta \log(L)$ from the peak in the CCF which is at zero radial velocity lag in this case.

effects from limb darkening from the stellar disk is considered here. As this study is considering the detectability of an Earth twin, the radius of the planet is assumed to be the same as the Earth's at a value of $R_{\rm P} \equiv R_{\oplus} = 6.3781 \times 10^6$ m. Table 5.1 gives the orbital parameters, P and a, used in these simulations. Again, the Proxima and TRAPPIST-1 systems are used here as proxies for these orbital parameters as these systems have planets in their respective habitable zones to potentially host an Earth-like spectrum. The innermost planet in the habitable zone of the TRAPPIST-1 system (i.e. TRAPPIST-1 e) is used as it has the largest radial velocity shift which is necessary for HRCCS (see section 2.5.2).

Finally, the total number of spectra can be calculated simply by dividing $t_{\rm dur}$ through by the total time to take a single exposure. As all observations contain some overheads which vary depending on several factors, a relatively short overhead time ($t_{\rm over}$) of 30 s per spectrum is used here. Thus, the total number of simulated spectra taken per transit here is $N_{\rm spec} = t_{\rm dur}/t_{\rm over} \approx 12$ and 8 for the Earth-twin around the M5 and M7 dwarf, respectively. As transmission spectroscopy is multiplicative, the final total photon count for each simulation is $N_{\gamma} \times N_{\rm spec} \times N_{\rm transits}$, where $N_{\rm transits}$ is the total number of transits observed.

The final spectral counts are hence cross-correlated with the CC-to-log(L) method from Brogi and Line (2019) (see equation (4.4)) with the planets transmission spectrum after being shifted on a radial velocity lag vector that ranges from -100 to 100 in steps of 1.5 km s^{-1}. A velocity step of 1.5 km s^{-1} is used here as it roughly corresponds to the velocity sampling per pixel for a 100,000 resolution spectrograph considered here. The top panel of Figure 5.4 shows the number of transits needed in order to detect the Earth-like spectrum at a conservative detection significance of $4\,\sigma$. Each detection significance is estimated by calculating a likelihood ration test of the peak in the CCF and the average likelihood of a flat line for the planet transmission spectrum via,

$$\log(L)_{\rm flat} = -\sum_{i} \frac{N}{2} \log(s^2_{f,i}). \tag{5.6}$$

This is the same as equation (2.13) but instead with only the contribution from the variance from the data, s^2_f, summed over each spectrum i. Typically for a cross-dispersed high resolution spectrograph, there is an additional summation over all spectral orders which would be included in equation (5.6), however, the simulated wavelength solution here is continuous which wouldn't be the case in realistic observations as is represented by equation (4.6). As stated in section 5.5, each simulated observation was repeated one hundred times to build a distribution of observations

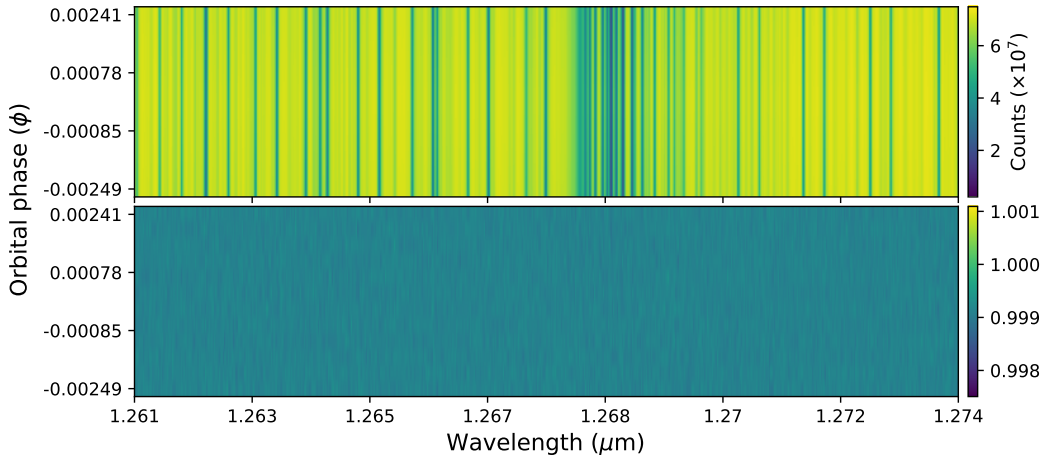

Figure 5.5: Top panel: The simulated time spectral sequence shown at a wavelength coverage of 1.261-1.274 μm for the M5 dwarf observations. This is a fraction of the full wavelength coverage, however, this region is shown for better visualisation of the contaminating lines seen as the dark vertical lines. Bottom panel: The perfect removal of the contaminating telluric and stellar features. The planet spectrum is still well-hidden within the noise of the data.

with varying noise structures in the data. Thus, an average detection significance was obtained from this distribution for each transit which is shown in the top panel of Figure 5.4. The bottom panel of Figure 5.4 shows example CCFs for a particular noise case for the M5 and M7 in terms of number of σ away from the peak in the CCF. This was calculated as a likelihood ratio test between each value and the peak in the CCF, therefore, the CCF peaks at $\sigma = 0$, and the noise far from the peak is several σ away.

From this analysis, it can be seen that on average 15 and 20 transits are needed to confidently detect ($> 4\,\sigma$) an Earth-like atmosphere around an M5 and M7 dwarf, respectively, at 10 pc. This equates to roughly 20 hours and 19 hours of on target observing, excluding any out-of-transit spectra being taken. However, it should again be noted that these are lower limits as ideal observing conditions have been considered here with perfect removal of the contaminating spectral features. It has also been assumed that the systemic velocity is sufficiently far ($\gtrsim 10\,\mathrm{km\,s^{-1}}$) from the telluric and stellar rest frame to prevent contamination of the spectral signature from the planet.

5.6.2 Time resolved HRCCS

In this section, a simulated time resolved spectral sequence analysis is performed to study whether the typical HRCCS analysis techniques can work with these cooler, slower moving objects around M-dwarfs. In particular, the frequently used methods of removing the contaminating telluric and stellar spectral features via the time dependent variations in the observed flux in each wavelength channel as described in section 2.5.2 work for these simulations will be investigated.

In the time sequence, the radial velocity of the planet is taken to be,

$$V_{\rm P}(t) = K_{\rm P} \sin\left[2\pi\phi(t)\right] + V_{\rm sys}, \tag{5.7}$$

which is the same as equation (2.6) but with the exclusion of the barycentric velocity correction term which is not simulated in this analysis. The simulated planet spectrum is hence shifted by this velocity across the transit in the spectral sequence. The $K_{\rm P}$ and $\phi(t)$ terms in equation (5.7) are calculated by,

$$\begin{aligned} K_{\rm P} &= \frac{2\pi a}{P}, \\ \phi(t) &= -\frac{t_{\rm dur}}{2P} + \left(\frac{t_{{\rm spec},i}}{P}\right)_{i=0}^{N_{\rm spec}}, \end{aligned} \tag{5.8}$$

where $\phi(t)$ is calculated as a sequence from the phase from beginning of the transit which is the $-\frac{t_{\rm dur}}{2P}$ term, with subsequent terms added on determined by the change in phase per spectrum up to the number of spectra per transit in the sequence, $N_{\rm spec}$. The $t_{\rm dur}$ in equation (5.8) is the transit duration as calculated in equation (5.5). For the M5 and M7 hosts, the transiting Earth twin orbital phase change over the transit is $\Delta\phi = 0.00496$ and 0.00648, respectively. The number of spectra in the time sequence here is the same as in the previous analysis with the exposure and overhead times at 400 and 30 s, respectively. Therefore, the simulated spectral matrices per transit are taken to be $N_{\rm spec} \times N_x$, where N_x is the number of wavelength channels used (i.e the length of the wavelength solution vector, excluding the masked values). The systemic velocity here is taken to be $V_{\rm sys} = -30\,{\rm km\,s^{-1}}$ which is far enough away from the telluric and stellar rest frame of $0\,{\rm km\,s^{-1}}$ so as to be able to distinguish a planetary or contaminated source for the signal in the final CCF velocity map. Therefore, it is expected that if the telluric and stellar contaminants haven't been sufficiently removed, the final CCF, which is in the rest frame of the planet ($V_{\rm rest}$), should peak around a $V_{\rm rest} = +30\,{\rm km\,s^{-1}}$. Using equation (5.7), the change in radial velocity for the Earth twin around the M5 and M7 from the start to the end

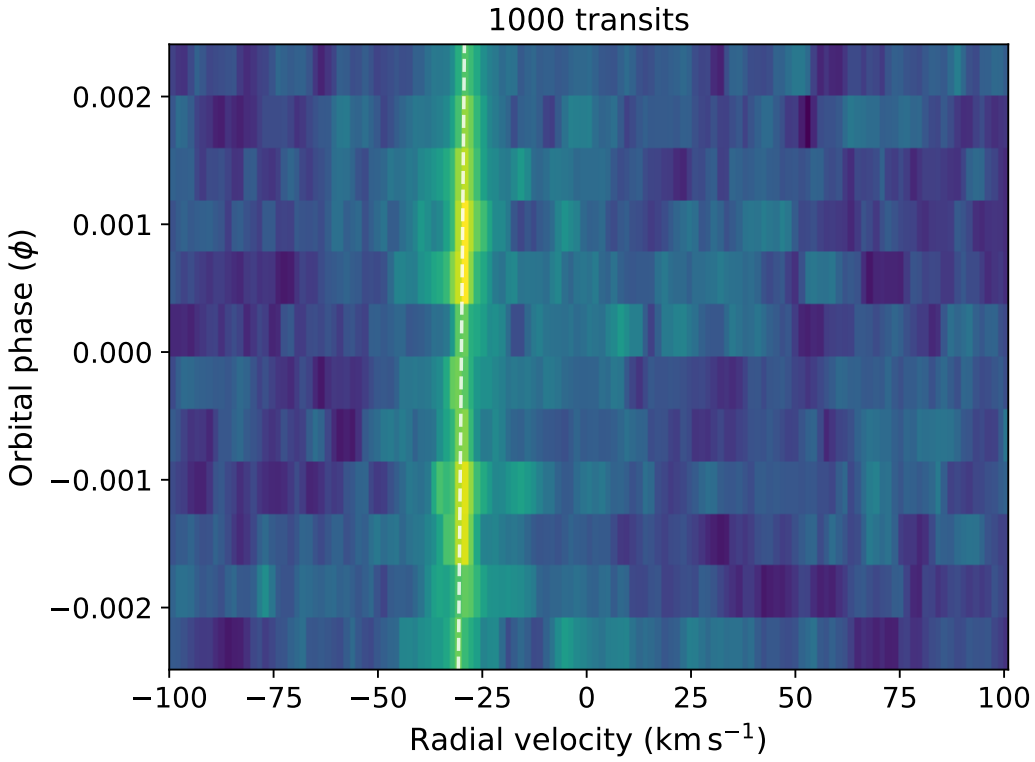

Figure 5.6: Phase resolved CCF of the M5 dwarf Earth twin co-added for 1000 transits for visual purposes of the CCF radial velocity trail. The white dashed line indicates the radial velocity trail of the simulated planet around the M-dwarf over the entire transit.

of transit is $\frac{dV_P}{dt} = 1.45$ and $1.60\,\mathrm{km\,s^{-1}}$, respectively.

Each spectrum in the simulated sequence of observations is calculated, as in the previous analysis, via equation (5.4). However, in this analysis, the telluric spectrum will vary in time ($T_\oplus(\lambda, t)$) to better simulate a real HRS observing sequence. The airmass is assumed to be at a minimum at mid-transit (i.e., airmass = 1.0 at $\phi = 0$) and changes by 0.025 per exposure. For realistic observations, there will be further time dependent variations in the telluric spectrum such as changes in the PWV, however, this analysis will not study these effects and leave it for a future analysis.

To begin this analysis, a perfect telluric removal is done on the spectral sequence whereby the stellar and time dependent telluric spectrum is divided out through each spectrum. This should lead to the same results as in section 5.6.1, however, the planet signal now comes from the sum of each CCF which have been shifted in velocity. Figure 5.5 shows a portion of the wavelength coverage to visualise

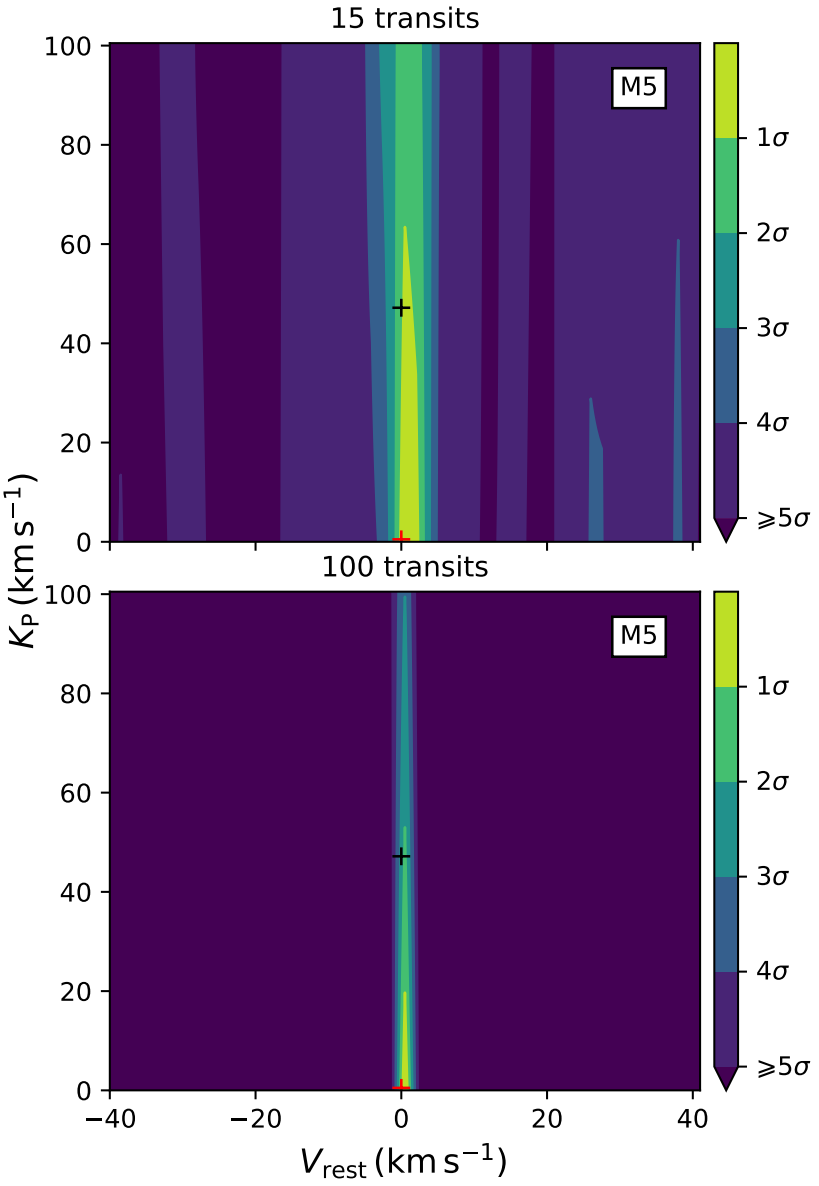

Figure 5.7: Confidence levels in the CCF K_P-V_{rest} velocity map for the M5 host star for 15 (top panel) and 100 transits (bottom panel). This is the case for perfect removal of telluric and stellar spectral features from the spectral sequence. The colourbar indicates the confidence levels in σ away from the peak in the CCF. The black and red plus symbols indicate the simulated and the retrieved position of the planets signal, with the latter taken as the peak in the likelihood CCF map.

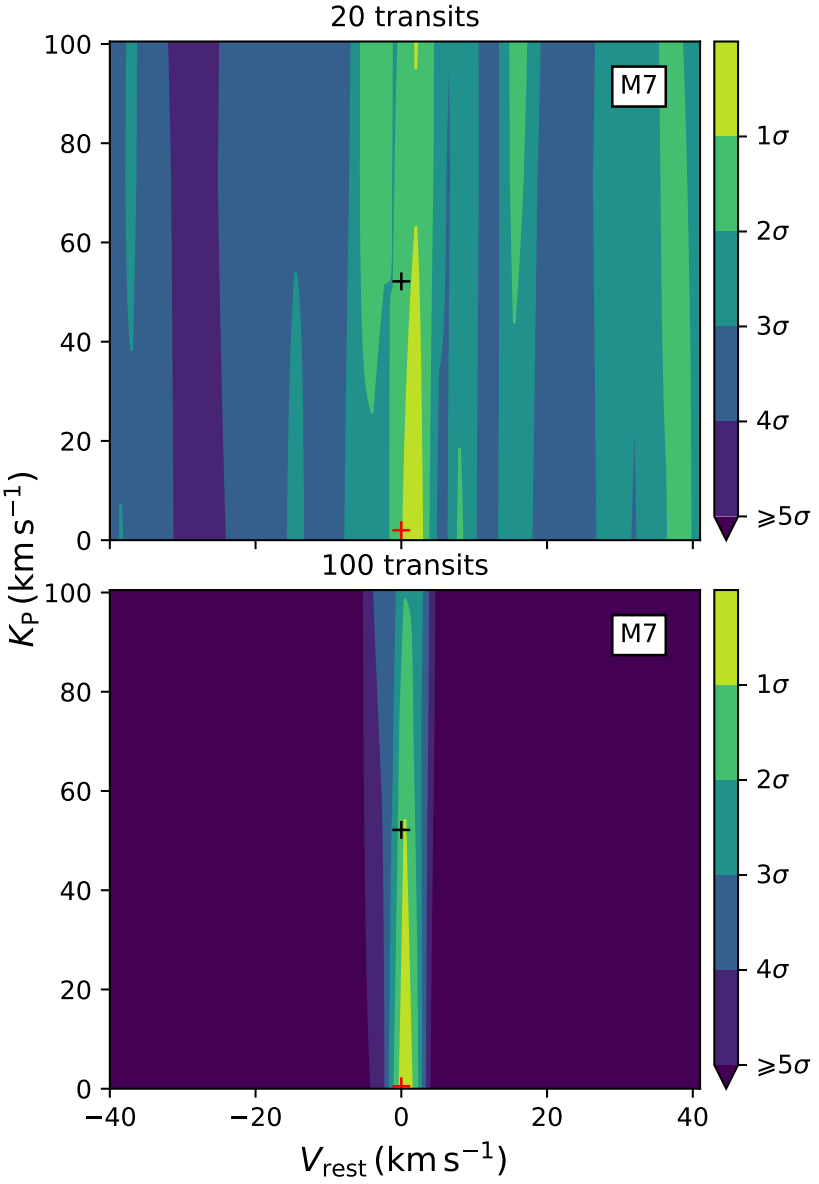

Figure 5.8: Same as Figure 5.7 but for the M7 host system.

how this removal cleans the spectral sequence, in the top panel, down to the noise of the data shown in the bottom panel. This sequence is then passed through the cross-correlation analysis pipeline as explained in detail in sections 2.6.1 and 2.6.3. Using equation (5.7), the planet spectrum is shifted onto a velocity grid where $K_{\rm P} = 0$ to $100\,{\rm km\,s^{-1}}$ and a $V_{\rm rest} = -40$ to $40\,{\rm km\,s^{-1}}$ in steps of $1.5\,{\rm km\,s^{-1}}$. Figure 5.6 shows an example of the phase, or time, resolved CCF as a function of the radial velocity. For visual purposes, the number of transits was set to a large number of a hundred in order to show the velocity trail of the planet around the M5-dwarf star which is guided by the white dashed line. If there were significant residual features left over from the removal stage from the tellurics or stallar spectrum, a strong CCF trail would show at $0\,{\rm km\,s^{-1}}$.

Figures 5.7 and 5.8 show the confidence intervals in the final $K_{\rm P}$-$V_{\rm rest}$ map for the M5 and M7 systems, respectively. In both of these figures, the black and red plus symbols indicate the positions of the simulated and retrieved radial velocity positions of the planet, respectively. Guided by the detectability of the planet around each system, the same number of transits have been used that corresponded to a greater detection significance of $4\,\sigma$ in section 5.6.1 in the top panels and a comparison map for a much larger number of transits of 100 in the bottom panels. It is the case for both the M5 and M7 systems that the retrieved radial velocity of the planet matches that of the planet at a $V_{\rm rest} = 0\,{\rm km\,s^{-1}}$, however, the retrieved semi-amplitudes of the velocity $K_{\rm P}$, are significantly lower than the simulated values of $K_{\rm P} = 47.2$ and $52.2\,{\rm km\,s^{-1}}$ for the M5 and M7 systems, respectively. By increasing the number of transits, the confidence intervals tighten, however, the retrieved $K_{\rm P}$ does not increase to the simulated value despite a perfect removal of the telluric and stellar features.

The next stage of this analysis moves further into a realistic HRCCS analysis scenario whereby the spectral sequence is cleaned with PCA from varying components. This reduction method is explained in further detail in section 2.5.2. Equation (2.2) is used to remove the time varying components in the spectral sequence shown in the top panel of Figure 5.5. As PCA is a blind algorithm, the spectra need to be visually inspected with increasing singular components removal. Figure 5.9 shows this process for the M5 system spectral sequence with an increasing number of PCA components removed with each panel down the figure. To prevent unwanted removal of the Doppler shifted planets spectral signature, the maximum number of components removed should be that at which the spectra no longer show any contaminant residuals (shown as the dark vertical lines in these figures). As shown in the bottom panel of Figure 5.9, six PCA components are needed to visually clean the

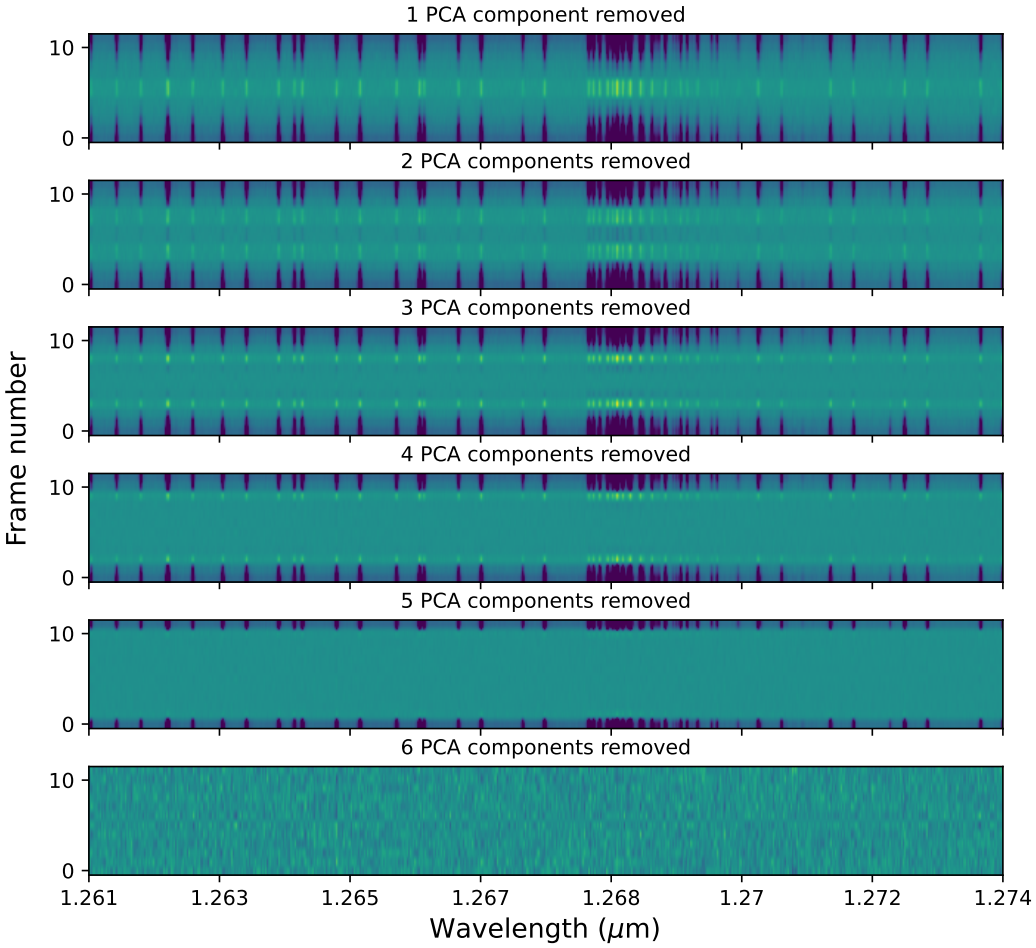

Figure 5.9: An example series of spectra showing how the number of PCA components removed cleans the simulated data sequence from the top panel in Figure 5.5. The final panel shows that the removal of six PCA components is the minimum required to clean the data of obvious visual telluric residuals.

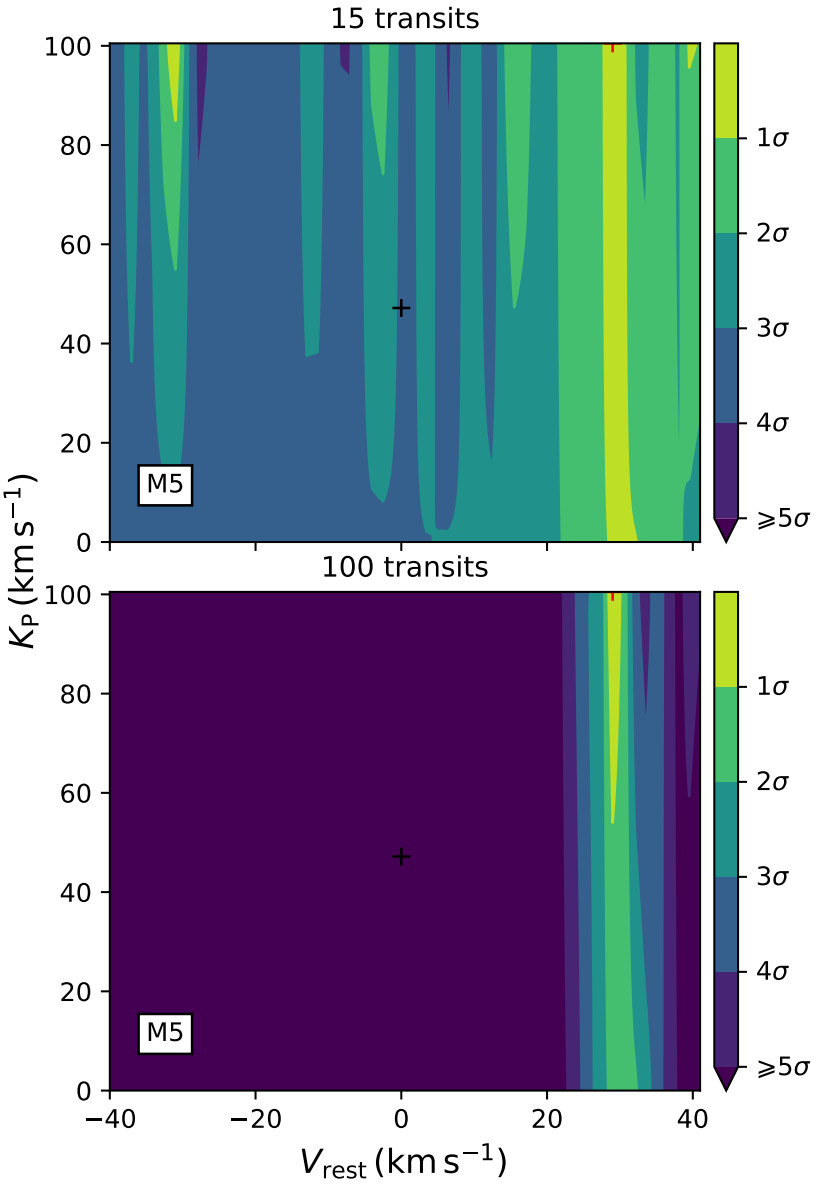

Figure 5.10: Same as Figure 5.7 but these are CCFs of the exoplanet spectrum with the spectral sequence cleaned with the removal of six PCA components shown in the bottom panel of Figure 5.9.

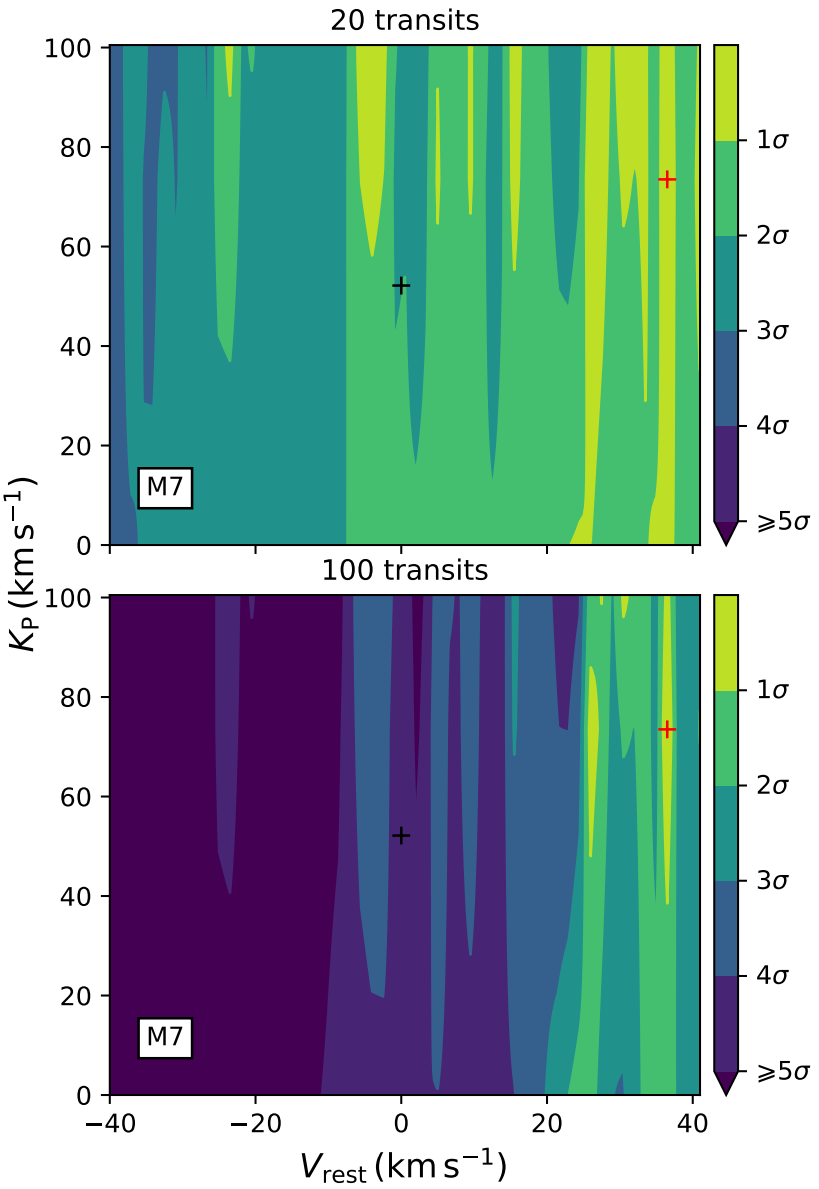

Figure 5.11: Same as Figure 5.10 but the M7 host system with the removal of three PCA components from the spectral sequence.

spectra for the M5 system to a similar noise level as with the perfect removal case shown in the bottom panel of Figure 5.5. Naively, there are only two variables that need to be removed from the data, namely the varying airmass and transit shape, however, as PCA is a blind algorithm, it is possible that these effects have been combined in unexpected ways resulting in the need to remove six components. For the M7 system, a fewer number of three were needed to visually clean the spectral sequence, which was expected for this system as there are fewer spectra in the time sequence (i.e. fewer frame numbers as stated in Figure 5.9) and thus has a lower dimensionaility than for the M5 system.

Figures 5.10 and 5.11 show the confidence intervals for the CCF as a function of radial velocity for the M5 and M7 host systems, respectively. Again, the black and red plus symbols indicate the simulated and retrieved radial velocity of the planet from the CCF. For both pf these systems, the retrieved radial velocity is not that from the planet but instead appears around the rest frame of the simulated observer, i.e. at a $V_{\rm rest} = +30\,{\rm km\,s^{-1}}$ as the systemic velocity was placed at $V_{\rm sys} = -30\,{\rm km\,s^{-1}}$. This suggests that the atmospheric model is correlating with low-level residual telluric or stellar features left in the data and the PCA algorithm has removed most of or all of the slowly moving planet's spectrum in the sequence.

5.7 Discussion and summary

Similarly to Snellen et al. (2013), Rodler and López-Morales (2014) and López-Morales et al. (2019), in the first stages of the analysis in section 5.6.1, the detectability of a terrestrial planet with an Earth-like atmosphere around M-dwarfs at 10 pc using HRS is studied. Here, a full atmospheric transmission spectrum of the Earth is modelled with the addition of six further molecular species with the O_2 bands focused on in the previous studies. A typical simultaneous wavelength coverage of 0.96-2.7μm for a high resolution spectrograph of resolution $R = 100,000$ is simulated here coupled to the upcoming 39 m ELT telescope. This analysis also assumes a M5 and M7 host stars with stellar parameters taken from the Proxima and TRAPPIST-1 systems, respectively, as proxies due to these systems hosting planets within their habitable zones. Using an ideal scenario where the contaminating telluric and stellar features are perfectly removed from the spectra, this analysis finds that on average, $\geqslant$ 15 and 20 transits which equates to $\geqslant$ 20 and 19 hours on-target observing time for the M5 and M7 systems, respectively. When compared to the simulations of Snellen et al. (2013), they find a lower limit of 30 transits required to observe the O_2 feature at 0.76 μm around an M4-dwarf at 10 pc. Due

to the similarities of these two studies, it is estimated that including a full opacity grid for an Earth-like atmosphere in the NIR reduces the necessary number of transits by roughly half. This highlights the power of HRCCS that covers a much larger wavelength coverage and thus more observable spectral lines, particularly in the NIR. The number of transits are stated as lower limits here because these simulations have used the most ideal observing conditions such as the telluric spectrum is constant in time and only white noise (i.e. random Poissonian noise) has been simulated for these observations. It is certain that there will be some red noise (i.e. time and/ or wavelength correlated noise) in realistic observations which is important to simulate as shown in Rodler and López-Morales (2014).

The following analysis in section 5.6.2 simulates a more typical HRS set of observations where the telluric spectrum is is time varying with airmass. With a perfect removal of the contaminants, the analysis is able to constrain the rest frame radial velocity of the planet, however, it is unable to correctly constrain the semi-amplitude (K_{P}) of the planet. This analysis is the first of its kind to study the use of standard HRS data reduction techniques on a simulated data-set for observations of an Earth-like atmosphere on a habitable terrestrial planet around M-dwarf hosts stars. The most regularly used method is followed by modelling the flux variations as a function of time for each wavelength channel and dividing through the spectra. This study focuses on the use of unweighted PCA for this purpose. With the several PCA components as shown in Figure 5.9, this reduction method is successful in cleaning the spectra down to the noise of the data. However, as described in the previous section, there should only be two physically motivated PCA components to be removed (airmass and transit shape) but six was required for the M5-dwarf system. This suggests that the PCA algorithm does not appear to choose these physically motivating factors in the removal process. Therefore, a different contaminant removal algorithm might be necessary in future simulation studies of this nature.

This analysis shows that the use of PCA on time detrending effects on HRS data to observe a slowly moving habitable planet fails to find or constrain the radial velocity of the planets in the K_{P}-V_{rest} maps in Figures 5.10 and 5.11. This is perhaps unsurprising due to the fact that the change of radial velocity of both planets roughly matches that of the velocity sampling rate of a 100,000 resolution spectrograph at the Nyquist frequency which has been simulated here. Therefore, the planets spectral lines will have effectively appeared stationary in the time series and thus have likely been mostly if not entirely removed by the data reduction.

It is unlikely that using the methodology as described in this analysis and

of which has used in past and current high resolution atmospheric studies of giant gaseous planets will be able to detect these slowly moving habitable planet with Earth-like atmospheres. However, it is possible that the reduction and analysis techniques as used in Lockwood et al. (2014); Piskorz et al. (2016, 2017); Buzard et al. (2020) could well work on time series simulations of slow moving planets. Other possibilities could include the use of an accurate telluric modelling such as MOLECFIT (Smette et al., 2015) or the removal of an average out-of-transit spectrum. The use of MOLECFIT could be preferential for HRS over the latter as this modelling tool takes into account the local weather conditions using meteorological data at the time of observations and fits the data through an iterative algorithm. The use of an out-of-transit fit might struggle to correct for the highly variable water vapour content over the full transit to the required precision needed for HRCCS. However, this is left for a future study to explore these other potential avenues in the detectability of an Earth-like atmosphere around nearby M-dwarfs using HRCCS.

Chapter 6

Conclusions

In this thesis, I have discussed and outlined the HRCCS analysis techniques of exoplanet atmospheres on both real observational and simulated data. Below, I will summarise the most important findings from this thesis and they mean in the wider context of exoplanet atmospheric science, and end with the future outlook of this field.

6.1 Summary of the thesis

6.1.1 Water vapour detection in the atmosphere of HD 179949 b

In chapter 3, I outline the discovery of a weak detection of water vapour in absorption on the day-side of the non-transiting hot Jupiter HD 179949 b ($T_{\rm eq} \approx 1950\,{\rm K}$) in the L-band ($\sim 3.5\,\mu{\rm m}$) with the CRIRES instrument ($R = 100,000$) on the VLT. These observations were taken over two nights in 2014 before the instrument was decommissioned to make way for the upgraded CRIRES+. Since this upgrade ended up lasting several years (until 2021/2022), it was therefore still relevant scientifically to complete the analysis of data from the old CRIRES, given that the VLT did not host a spectrograph with equivalent specs for roughly seven years. This analysis provided further evidence for the presence of water vapour at $3\,\sigma$ using a Welch t-test (see section 2.7.1) in the day-side thermal emission of this hot giant planet from a similar analysis done by Brogi et al. (2014) which showed an almost equally weak spectral signature from water but in the K-band ($\sim 2.3\,\mu{\rm m}$). With the addition of the K-band spectra (taken in 2011) to the L-band spectra, I show that both set of data co-add coherently to place tighter constraints on the orbital and physical parameters of the planet; $K_{\rm P} = 145.2 \pm 0.2\,{\rm km\,s^{-1}}$, $i = 66.2^{+3.7}_{-3.1}$ degrees and $M_{\rm P} = 0.963^{+0.036}_{-0.031}\,{\rm M_J}$. This result shows that the combination of spectra from

different bands for HRS can improve upon the system parameters which is particularly important for closely orbiting non-transiting planets where there exists a degeneracy between the planetary mass and inclination. Furthermore, as the K and L-band observations were taken several years apart, the coherent co-adding of the planet signal shows that HD 179949 b has a lack of atmospheric variability which is often not the case for ultra-hot Jupiters (e.g. Wardenier et al., 2021), and is on a stable orbit. At the relatively high day-side temperature of $\sim 1950\,\mathrm{K}$, it is perhaps not surprising that there is only a weak absorption feature from water with more recent evidence from Mansfield et al. (2021) showing observational and theoretical evidence for weak water features for systems like that of this HD 179949.

6.1.2 Water vapour detection in the atmosphere of τ Boötis b

In chapter 4, I outline the detection of water vapour absorption in the day-side thermal emission spectrum of the non-transiting hot Jupiter τ Boötis b with the CARMENES NIR spectrograph ($R = 80,400$) on the CAHA observatory 3.5 m telescope. This study made use of the Bayesian CC-to-log(L) analysis method on four nights of spectra to detect the presence of water vapour at an orbital semi-amplitude of $K_\mathrm{P} = 106.21^{+1.76}_{-1.71}\,\mathrm{km\,s^{-1}}$ and systemic velocity of $V_\mathrm{sys} = -11.52^{+0.59}_{-0.60}\,\mathrm{km\,s^{-1}}$ when assuming a circular orbital solution. The systemic velocity as measured by the Gaia Collaboration (2018) however is $V_\mathrm{sys} = -16.9 \pm 0.3\,\mathrm{km\,s^{-1}}$ which is significantly shifted from the solution found in this analysis which cannot be explained solely by adopted an eccentric orbital solution.

This detection confirms the detection from Lockwood et al. (2014) in the L-band, however, it is in diagreement with the recent analysis of SPIRou spectra from Pelletier et al. (2021). The observations from Pelletier et al. (2021) observe a strong detection from CO in the day-side emission spectra, however, they only find a $3\,\sigma$ upper limit of VMR $= 10^{-5.66}$ for water vapour in the atmosphere of τ Boötis b. This discrepancy between data-sets is somewhat of a mystery and a surprise as on of the key strengths of HRCCS is the consistency of species detections between different data-sets, e.g. H_2O in HD 189733 b by Birkby et al. (2013), Brogi et al. (2018), Alonso-Floriano et al. (2019b) and Boucher et al. (2021). Therefore, it is likely that further observations of this planets atmosphere is needed in the future to resolve the disputed claim of water vapour in the emission spectrum of τ Boötis b.

6.2 High resolution simulated observations of an Earth-like atmosphere with the ELT

In chapter 5, I outline simulations of HRS observations of two Earth-like planetary systems which orbit an M5 and an M7-dwarf. In these simulations, it is assumed that an exoplanet within their respective habitable zones with an Earth-like atmosphere at a distance of 10 pc away. The simulated spectrograph on the ELT is assumed to be similar to the high resolution SPIRou instrument ($R = 70,000$) on the Canada-France-Hawaii-Telescope which has a wavelength coverage of 0.96-2.7 μm in the NIR, simulated to have a resolution of $R = 100,000$. Like with the analysis of Snellen et al. (2013), this study also assumed only white noise contributions from the observations and instrument combined. Although the analysis from Rodler and López-Morales (2014) showed that this could be significantly underestimating the final number of transits needed to detect an Earth-like atmosphere with the ELT without considering red noise, however, Serindag and Snellen (2019) showed that only considering white noise in these simulations does not significantly differ from simulations which use real observational noise from the high resolution UVES spectrograph.

I show that, when considering the combined affect of all the opacity from numerous molecular species, a detection of an Earth-like atmosphere around the M5 and M7-dwarf is feasible in $\geqslant 15$ and $\geqslant 20$ transits, respectively. This is significantly lower than the ~ 60 transits needed which was predicted by Snellen et al. (2013),Rodler and López-Morales (2014),Serindag and Snellen (2019) and López-Morales et al. (2019). This is likely due to the fact that a much wider wavelength coverage is considered in this study, however, there could also be an additional factor of the use of the Bayesian CC-to-log(L) method which is a more accurate method of estimating a detection significance than the S/N methods used in the former studies. Finally, I show that these planets orbit these stars too slowly in the habitable zone for the use of typical use of HRCCS reduction techniques which rely on the assumption an object moving fast enough to Doppler shift across several pixels on the detector in time. Following this, it is recommended that further simulations of this nature test different approaches on the use of HRS observations for slowly moving habitable planets such as those used by Lockwood et al. (2014) and Piskorz et al. (2016) for example.

6.3 Future outlook

Looking to the future, the aims of HRCCS atmospheric science will lie in the continued development of the analysis techniques, some of which has already been shown in this thesis from the recently developed Bayesian techniques of Brogi and Line (2019) and Gibson et al. (2020). With these techniques, we are starting to see some of the first analyses with HRS which use the Bayesian likelihood framework in a full atmospheric retrieval (Pelletier et al., 2021; Line et al., 2021; Gandhi et al., 2022) to constrain accurate absolute chemical abundances, T-p profiles and various other physical system parameters. This had been one of the biggest drawbacks of HRCCS over low resolution spectroscopy from the analyses of HST and Spitzer data for many years.

In terms of future instrumentation, the newly upgraded CRIRES+ NIR cross-dispersed high resolution instrument on the VLT has recently shown promising performances with science verification HRCCS observations of the ultra-hot Jupiter MASCARA-1 b. Holmberg and Madhusudhan (2022) were able to detect strong emission lines from CO and water vapour from a thermally inverted atmosphere. With the lack of high resolution NIR instruments in the southern hemisphere, the CRIRES instrument is a welcome return for the characterisation of exoplanet atmospheres for more southern targets which have been missing since its decommissioning in 2014. Hopefully, within the next five years, the upcoming ESO ELT observatory should be built and received its first light with science verification observations. On the ELT there will be two different high resolution spectrographs, the more typical spectrograph for HRCCS will be the HIRES, or newly named, ArmazoNes high Dispersion Echelle Spectrograph (ANDES) (Marconi et al., 2021) which will have a resolution of $R \approx 100,000$ with a simultaneous spectral coverage of 0.4-1.8 μm as a baseline, with the goal of increasing that to 0.35-2.4 μm. This will cover the O_2 bands considered in Snellen et al. (2013), Rodler and López-Morales (2014) and López-Morales et al. (2019) which could provide an exciting prospect into the search for molecular oxygen for more temperate exoplanets in the near future. The second high resolution instrument planned for the ELT is an integral field unit (IFU) spectrograph METIS (Brandl et al., 2010) which can have a resolution of up to 100,000 in the L and M-bands. IFU's even down to medium resolutions of $R \approx 5000$, have proven to be effective at detecting exoplanet atmospheres in the NIR (e.g. Hoeijmakers et al., 2018b) for spatially resolvable systems using similar techniques used in HRCCS. ANDES will therefore help to characterise exoplanet atmospheres at mid IR wavelengths which could detect further molecular species not discussed in

this thesis.

Although there are no high resolution instruments on the JWST, the low-to-medium resolution NIR-to-mid IR spectrographs that will be used to observe a variety of exoplanet atmospheres will provide complementary analyses to those using ground-based high resolution spectrographs. Recent HRS analyses (Pelletier et al., 2021; Line et al., 2021) have constrained molecular abundances in the atmospheres of hot Jupiters down to uncertainties expected for the same type of planet and wavelength coverage with JWST (Greene et al., 2016). It would also be possible in future to combine low resolution spectra observations from JWST with those from HRS using frameworks such as those shown in Brogi et al. (2017) and Pino et al. (2018) to provide better constraints on the chemistry and physical processes of the atmosphere than by using just one or the other method.

With the unprecedented precision and accuracy of the observations from JWST in the near and mid IR and from the upcoming ELT both of these telescopes will help to revolutionise the field of exoplanet atmospheric science to beyond what we currently understand. These complementary observatories will be able to push the boundaries of what is currently possible with the HST and the VLT with observations of cooler, smaller and more Earth-like atmospheres. It is safe to say that the future of exoplanet atmospheric science in the next decade will be exciting with possibly a few unexpected results that are likely to push the theoretical understanding we currently have in this field.

Bibliography

Agol E. et al., 2021. *PSJ*, 2(1):1.

Allard F., Homeier D., and Freytag B., 2012. *Philosophical Transactions of the Royal Society of London Series A*, 370(1968):2765–2777.

Allart R. et al., 2017. *A&A*, 606:A144.

Allart R. et al., 2018. *Science*, 362(6421):1384–1387.

Allart R. et al., 2019. *A&A*, 623:A58.

Alonso-Floriano F.J. et al., 2019a. *A&A*, 629:A110.

Alonso-Floriano F.J. et al., 2019b. *A&A*, 621:A74.

Amundsen D.S. et al., 2017. *A&A*, 598:A97.

Anglada-Escudé G. et al., 2016. *Nature*, 536(7617):437–440.

Armstrong D.J. et al., 2020. *Nature*, 583(7814):39–42.

Arsenault R. et al., 2003. In P.L. Wizinowich and D. Bonaccini, editors, *Adaptive Optical System Technologies II*, volume 4839 of *Society of Photo-Optical Instrumentation Engineers (SPIE) Conference Series*, 174–185.

Artigau É. et al., 2014. In *procspie*, volume 9147 of *Society of Photo-Optical Instrumentation Engineers (SPIE) Conference Series*, 914715.

Asplund M. et al., 2009. *ARA&A*, 47(1):481–522.

Astropy Collaboration et al., 2013. *A&A*, 558:A33.

Astropy Collaboration et al., 2018. *AJ*, 156(3):123.

Baliunas S.L. et al., 1997. *ApJ*, 474(2):L119–L122.

Baranne A. et al., 1996. *A&AS*, 119:373–390.

Barber R.J. et al., 2006. *MNRAS*, 368(3):1087–1094.

Barber R.J. et al., 2014. *MNRAS*, 437(2):1828–1835.

Barman T.S. et al., 2011. *ApJ*, 733(1):65.

Barnes J.R. et al., 2007. *MNRAS*, 379(3):1097–1107.

Barstow J.K. and Irwin P.G.J., 2016. *MNRAS*, 461(1):L92–L96.

Barstow J.K. et al., 2014. *ApJ*, 786(2):154.

Batten A.H., 1988. *PASP*, 100:160.

Bauer F.F. et al., 2020. *A&A*, 640:A50.

Bayliss D.D.R. and Sackett P.D., 2011. *ApJ*, 743(2):103.

Bell T.J. and Cowan N.B., 2018. *ApJ*, 857(2):L20.

Bello-Arufe A. et al., 2022. *A&A*, 662:A51.

Beltz H. et al., 2021. *AJ*, 161(1):1.

Ben-Yami M. et al., 2020. *ApJL*, 897(1):L5.

Benneke B. and Seager S., 2013. *ApJ*, 778(2):153.

Benneke B. et al., 2019. *ApJL*, 887(1):L14.

Bennett D.P. and Rhie S.H., 1996. *ApJ*, 472:660.

Bessell M.S., 1991. *AJ*, 101:662.

Birkby J.L., 2018. In H.J. Deeg and J.A. Belmonte, editors, *Handbook of Exoplanets*, 16. Springer Cham.

Birkby J.L. et al., 2013. *MNRAS*, 436:L35–L39.

Birkby J.L. et al., 2017. *AJ*, 153:138.

Bisnovatyi-Kogan G.S., 1993. *A&A*, 275:161–162.

Boley K.M. et al., 2021. *AJ*, 162(3):85.

Bond I.A. et al., 2004. *ApJL*, 606(2):L155–L158.

Borsa F. et al., 2015. *A&A*, 578:A64.

Borsa F. et al., 2021. *Nature Astronomy*, 6:226–231.

Borucki W. et al., 2009. In F. Pont, D. Sasselov, and M.J. Holman, editors, *Transiting Planets*, volume 253, 289–299.

Boss A.P., 1997. *Science*, 276:1836–1839.

Boucher A. et al., 2021. *AJ*, 162(6):233.

Brandl B.R. et al., 2010. In I.S. McLean, S.K. Ramsay, and H. Takami, editors, *Ground-based and Airborne Instrumentation for Astronomy III*, volume 7735 of *Society of Photo-Optical Instrumentation Engineers (SPIE) Conference Series*, 77352G.

Brogi M. and Line M.R., 2019. *AJ*, 157(3):114.

Brogi M. et al., 2012. *Nature*, 486(7404):502.

Brogi M. et al., 2013. *ApJ*, 767:27.

Brogi M. et al., 2014. *A&A*, 565:A124.

Brogi M. et al., 2016. *ApJ*, 817:106.

Brogi M. et al., 2017. *ApJL*, 839(1):L2.

Brogi M. et al., 2018. *A&A*, 615:A16.

Brown T.M., 2001. *ApJ*, 553(2):1006–1026.

Brown T.M., Libbrecht K.G., and Charbonneau D., 2002. *PASP*, 114(798):826–832.

Butler R.P. et al., 1997. *ApJL*, 474(2):L115–L118.

Butler R.P. et al., 2006. *ApJ*, 646:505–522.

Buzard C. et al., 2020. *AJ*, 160(1):1.

Caballero J.A. et al., 2016a. In A.B. Peck, R.L. Seaman, and C.R. Benn, editors, *Observatory Operations: Strategies, Processes, and Systems VI*, volume 9910 of *Society of Photo-Optical Instrumentation Engineers (SPIE) Conference Series*, 99100E.

Caballero J.A. et al., 2016b. In *Society of Photo-Optical Instrumentation Engineers (SPIE) Conference Series*, volume 9910 of *Society of Photo-Optical Instrumentation Engineers (SPIE) Conference Series*, 99100E.

Cabot S.H.C. et al., 2019. *MNRAS*, 482(4):4422–4436.

Campbell B., Walker G.A.H., and Yang S., 1988. *ApJ*, 331:902.

Carleo I. et al., 2022. *AJ*, 164(3):101.

Carpenter J.M. et al., 2009. *The Astrophysical Journal Supplement Series*, 181:197–226.

Carter J.A. et al., 2012. *Science*, 337(6094):556.

Casasayas-Barris N. et al., 2021. *A&A*, 654:A163.

Cauley P.W. et al., 2019. *AJ*, 157(2):69.

Cenadelli D. and Bernagozzi A., 2018. *The Discovery of the First Exoplanets*, 3–20. Springer International Publishing, Cham. ISBN 978-3-319-55333-7.

Charbonneau D. et al., 1999. *ApJ*, 522(2):L145–L148.

Charbonneau D. et al., 2000. *ApJL*, 529(1):L45–L48.

Charbonneau D. et al., 2002. *ApJ*, 568:377–384.

Charbonneau D. et al., 2005. *ApJ*, 626(1):523–529.

Chen J. and Kipping D., 2017. *ApJ*, 834(1):17.

Chiavassa A. and Brogi M., 2019. *A&A*, 631:A100.

Chubb K.L., Tennyson J., and Yurchenko S.N., 2020. *MNRAS*, 493(2):1531–1545.

Coles P.A., Yurchenko S.N., and Tennyson J., 2019. *MNRAS*, 490(4):4638–4647.

Collier Cameron A. et al., 1999. *Nature*, 402(6763):751–755.

Cont D. et al., 2022. *A&A*, 657:L2.

Cowan N.B. and Agol E., 2011. *ApJ*, 729(1):54.

Cowan N.B., Agol E., and Charbonneau D., 2007. *MNRAS*, 379:641–646.

Cumming A., Marcy G.W., and Butler R.P., 1999. *ApJ*, 526(2):890–915.

Cutri R.M. et al., 2003. *VizieR Online Data Catalog*, II/246.

D'Angelo G. and Lubow S.H., 2008. *ApJ*, 685(1):560–583.

de Kok R.J. et al., 2013. *A&A*, 554:A82.

de Kok R.J. et al., 2014. *A&A*, 561:A150.

de Regt S. et al., 2022. *A&A*, 661:A109.

Dekker H. et al., 2000. In M. Iye and A.F. Moorwood, editors, *Optical and IR Telescope Instrumentation and Detectors*, volume 4008 of *Society of Photo-Optical Instrumentation Engineers (SPIE) Conference Series*, 534–545.

Deming D. et al., 2005a. *ApJ*, 622(2):1149–1159.

Deming D. et al., 2005b. *Nature*, 434(7034):740–743.

Derrick T., 2004. In N. Stergiou, editor, *Innovative Analyses of Human Movement*, 189–205. Human Kinetics Publishers.

Diamond-Lowe H. et al., 2018. *AJ*, 156(2):42.

Dressing C.D. and Charbonneau D., 2015. *ApJ*, 807(1):45.

Drummond B. et al., 2016. *A&A*, 594:A69.

Drummond B. et al., 2019. *MNRAS*, 486(1):1123–1137.

Ehrenreich D. et al., 2020. *Nature*, 580(7805):597–601.

Eistrup C., Walsh C., and van Dishoeck E.F., 2018. *A&A*, 613:A14.

Faria J.P. et al., 2020. *A&A*, 635:A13.

Farmer C.B., 1987. *Mikrochimica Acta*, 3:189–214.

Flowers E. et al., 2019. *AJ*, 157(5):209.

Follert R. et al., 2014. In *procspie*, volume 9147 of *Society of Photo-Optical Instrumentation Engineers (SPIE) Conference Series*, 914719.

Foreman-Mackey D., Hogg D.W., and Morton T.D., 2014. *ApJ*, 795(1):64.

Foreman-Mackey D. et al., 2013. *Publications of the ASP*, 125(925):306.

Fortney J.J. et al., 2008. *ApJ*, 678(2):1419–1435.

Fossati L. et al., 2021. *A&A*, 653:A52.

Fraine J. et al., 2014. *Nature*, 513(7519):526–529.

Fulton B.J. et al., 2017. *AJ*, 154(3):109.

Gaia Collaboration, 2018. *VizieR Online Data Catalog*, I/345.

Gandhi S., Brogi M., and Webb R.K., 2020a. *MNRAS*, 498(1):194–204.

Gandhi S. and Madhusudhan N., 2017. *MNRAS*, 472(2):2334–2355.

Gandhi S. and Madhusudhan N., 2019. *MNRAS*, 485(4):5817–5830.

Gandhi S. et al., 2020b. *MNRAS*, 495(1):224–237.

Gandhi S. et al., 2022. *MNRAS*, 515(1):749–766.

Gao P. et al., 2021. *Journal of Geophysical Research (Planets)*, 126(4):e06655.

Giacobbe P. et al., 2021. *Nature*, 592(7853):205–208.

Gialluca M.T. et al., 2021. *PASP*, 133(1023):054401.

Gibson N.P., Pont F., and Aigrain S., 2011. *MNRAS*, 411(4):2199–2213.

Gibson N.P. et al., 2020. *MNRAS*, 493(2):2215–2228.

Gibson N.P. et al., 2022. *MNRAS*, 512(3):4618–4638.

Gillon M. et al., 2017. *Nature*, 542(7642):456–460.

Gizis J.E. et al., 2000. *AJ*, 120(2):1085–1099.

Gordon I.E. et al., 2017. *Journal of Quantitiative Spectroscopy and Radiative Transfer*, 203:3–69.

Gordon I.E. et al., 2022. *Journal of Quantitative Spectroscopy and Radiative Transfer*, 277:107949.

Gould A. and Loeb A., 1992. *ApJ*, 396:104.

Gould A. et al., 2006. *Acta Astronomica*, 56:1–50.

Gray D.F., 1997. *Nature*, 385(6619):795–796.

Gray R.O., Napier M.G., and Winkler L.I., 2001. *AJ*, 121(4):2148–2158.

Gray R.O. et al., 2006. *AJ*, 132(1):161–170.

Greene T.P. et al., 1993. In A.M. Fowler, editor, *Infrared Detectors and Instrumentation*, volume 1946 of *Society of Photo-Optical Instrumentation Engineers (SPIE) Conference Series*, 313–324.

Greene T.P. et al., 2016. *ApJ*, 817(1):17.

Guillot T. et al., 1996. *ApJL*, 459:L35.

Guilluy G. et al., 2019. *A&A*, 625:A107.

Haqq-Misra J. et al., 2022. *Physical Science Journal*, 3(3):60.

Hardegree-Ullman K.K. et al., 2020. *ApJS*, 247(1):28.

Hargreaves R.J. et al., 2020. *ApJS*, 247(2):55.

Harris G.J. et al., 2006. *MNRAS*, 367(1):400–406.

Harrison G.R., 1949. *Journal of the Optical Society of America (1917-1983)*, 39(7):522.

Harrison G.R., Archer J.E., and Camus J., 1952. *Journal of the Optical Society of America (1917-1983)*, 42(10):706.

Hatzes A.P. and Cochran W.D., 1993. *ApJ*, 413:339.

Hatzes A.P. et al., 2003. *ApJ*, 599(2):1383–1394.

Hawker G.A. et al., 2018. *ApJL*, 863(1):L11.

Heng K. and Showman A.P., 2015. *Annual Review of Earth and Planetary Sciences*, 43:509–540.

Henry T.J. et al., 2018. *AJ*, 155(6):265.

Hinkle K.H. et al., 2003. In P. Guhathakurta, editor, *Discoveries and Research Prospects from 6- to 10-Meter-Class Telescopes II*, volume 4834 of *Society of Photo-Optical Instrumentation Engineers (SPIE) Conference Series*, 353–363.

Hoeijmakers H.J. et al., 2015. *A&A*, 575:A20.

Hoeijmakers H.J. et al., 2018a. *Nature*, 560(7719):453–455.

Hoeijmakers H.J. et al., 2018b. *A&A*, 617:A144.

Hoeijmakers H.J. et al., 2019. *A&A*, 627:A165.

Hoeijmakers H.J. et al., 2020. *A&A*, 641:A123.

Hojjatpanah S. et al., 2019. *A&A*, 629:A80.

Holmberg M. and Madhusudhan N., 2022. *AJ*, 164(3):79.

Hotelling H., 1936. *Biometrika*, 28(3/4):321–377. ISSN 00063444.

Howard A.W. et al., 2010. *ApJ*, 721(2):1467–1481.

Hubeny I., Burrows A., and Sudarsky D., 2003. *ApJ*, 594(2):1011–1018.

Jaffe D.T. et al., 2006. In I.S. McLean and M. Iye, editors, *Society of Photo-Optical Instrumentation Engineers (SPIE) Conference Series*, volume 6269 of *Society of Photo-Optical Instrumentation Engineers (SPIE) Conference Series*, 62694I.

Jensen A.G. et al., 2012. *ApJ*, 751(2):86.

Jolliffe I.T. and Cadima J., 2016. *Philosophical Transactions of the Royal Society A*, 374:20150202.

Joy A.H. and Abt H.A., 1974. *ApJS*, 28:1.

Justesen A.B. and Albrecht S., 2019. *A&A*, 625:A59.

Kaeufl H.U. et al., 2004. In A.F.M. Moorwood and M. Iye, editors, *Ground-based Instrumentation for Astronomy*, volume 5492 of *Society of Photo-Optical Instrumentation Engineers (SPIE) Conference Series*, 1218–1227.

Kalman D., 1996. *The College Mathematics Journal*, 27(1):2–23.

Kataria T. et al., 2016. *ApJ*, 821(1):9.

Kausch W. et al., 2015. *A&A*, 576:A78.

Keles E. et al., 2019. *MNRAS*, 489(1):L37–L41.

Keliher P.N. and Wohlers C.C., 1976. *Analytical Chemistry*, 48(3):333A–340a.

Kesseli A.Y. and Snellen I.A.G., 2021. *ApJL*, 908(1):L17.

Kesseli A.Y. et al., 2022. *AJ*, 163(3):107.

Knutson H.A. et al., 2007. *Nature*, 447(7141):183–186.

Komacek T.D. et al., 2020. *ApJL*, 888(2):L20.

Konacki M. et al., 2003a. *Nature*, 421(6922):507–509.

Konacki M. et al., 2003b. *ApJ*, 597(2):1076–1091.

Kreidberg L., 2018. In H.J. Deeg and J.A. Belmonte, editors, *Handbook of Exoplanets*, 100. Springer International Publishing.

Kreidberg L. et al., 2014. *Nature*, 505(7481):69–72.

Kreidberg L. et al., 2018. *AJ*, 156(1):17.

Lacis A.A. and Oinas V., 1991. *JGR*, 96:9027–9064.

Lagrange A.M. et al., 2010. *Science*, 329(5987):57.

Landman R. et al., 2021. *A&A*, 656:A119.

Latham D.W. et al., 1989. *Nature*, 339(6219):38–40.

Lederberg J., 1965. *Nature*, 207(4992):9–13.

Leigh C. et al., 2003. *MNRAS*, 344(4):1271–1282.

Lépine S. et al., 2013. *AJ*, 145(4):102.

Libby-Roberts J.E. et al., 2020. *AJ*, 159(2):57.

Line M.R. et al., 2013. *ApJ*, 775(2):137.

Line M.R. et al., 2014. *ApJ*, 783(2):70.

Line M.R. et al., 2021. *Nature*, 598(7882):580–584.

Lockwood A.C. et al., 2014. *ApJ*, 783:L29.

Lopez E.D. and Fortney J.J., 2013. *ApJ*, 776(1):2.

López-Morales M. et al., 2019. *AJ*, 158(1):24.

Lothringer J.D., Barman T., and Koskinen T., 2018. *ApJ*, 866(1):27.

Lothringer J.D. et al., 2022. *Nature*, 604(7904):49–52.

Louden T. and Wheatley P.J., 2015. *ApJL*, 814(2):L24.

Lovelock J.E., 1965. *Nature*, 207(4997):568–570.

Luhman K.L., 2014. *ApJL*, 786(2):L18.

Madhusudhan N., 2012. *ApJ*, 758(1):36.

Madhusudhan N., 2019. *ARA&A*, 57:617–663.

Madhusudhan N. and Seager S., 2009. *ApJ*, 707(1):24–39.

Madhusudhan N. and Seager S., 2010. *ApJ*, 725(1):261–274.

Madhusudhan N. et al., 2011a. *Nature*, 469(7328):64–67.

Madhusudhan N. et al., 2011b. *ApJ*, 743(2):191.

Madhusudhan N. et al., 2014. In H. Beuther, R.S. Klessen, C.P. Dullemond, and T. Henning, editors, *Protostars and Planets VI*, 739.

Madhusudhan N. et al., 2016. *SSR*, 205(1-4):285–348.

Mansfield M. et al., 2021. *Nature Astronomy*, 5:1224–1232.

Marconi A. et al., 2021. *The Messenger*, 182:27–32.

Marcy G.W. and Butler R.P., 1996. In S.A. Kingsley and G.A. Lemarchand, editors, *The Search for Extraterrestrial Intelligence (SETI) in the Optical Spectrum II*, volume 2704 of *Society of Photo-Optical Instrumentation Engineers (SPIE) Conference Series*, 46–49.

Marois C. et al., 2006. *ApJ*, 641(1):556–564.

Marois C. et al., 2008. *Science*, 322(5906):1348.

Marois C. et al., 2010. *Nature*, 468(7327):1080–1083.

Masuda K., 2014. *ApJ*, 783(1):53.

Mayor M. and Queloz D., 1995. *Nature*, 378(6555):355–359.

Mayor M. et al., 2011. *arXiv e-prints*, arXiv:1109.2497.

Mazeh T., Tamuz O., and Zucker S., 2007. In C. Afonso, D. Weldrake, and T. Henning, editors, *Transiting Extrapolar Planets Workshop*, volume 366 of *Astronomical Society of the Pacific Conference Series*, 119.

McLaughlin D.B., 1924. *ApJ*, 60:22–31.

McLean I.S. et al., 1995. In A.M. Fowler, editor, *Infrared Detectors and Instrumentation for Astronomy*, volume 2475 of *Society of Photo-Optical Instrumentation Engineers (SPIE) Conference Series*, 350–358.

Mikal-Evans T. et al., 2020. *MNRAS*, 496(2):1638–1644.

Mollière P. et al., 2015. *ApJ*, 813(1):47.

Mollière P. et al., 2017. *A&A*, 600:A10.

Morley C.V. et al., 2015. *ApJ*, 815(2):110.

Mortier A. et al., 2012. *A&A*, 543:A45.

Moses J.I. et al., 2013. *ApJ*, 777(1):34.

Moutou C. et al., 2013. *Icarus*, 226(2):1625–1634.

Noll S. et al., 2012. *A&A*, 543:A92.

Nortmann L. et al., 2018. *Science*, 362(6421):1388–1391.

Nugroho S.K. et al., 2017. *AJ*, 154(6):221.

Nugroho S.K. et al., 2020. *ApJ*, 898(2):L31.

Nugroho S.K. et al., 2021. *ApJL*, 910(1):L9.

Öberg K.I., Murray-Clay R., and Bergin E.A., 2011. *ApJL*, 743(1):L16.

Oliva E. et al., 2006. In I.S. McLean and M. Iye, editors, *Society of Photo-Optical Instrumentation Engineers (SPIE) Conference Series*, volume 6269 of *Society of Photo-Optical Instrumentation Engineers (SPIE) Conference Series*, 626919.

Oppenheimer B.R. et al., 2013. *ApJ*, 768(1):24.

Origlia L. et al., 2014. In S.K. Ramsay, I.S. McLean, and H. Takami, editors, *Ground-based and Airborne Instrumentation for Astronomy V*, volume 9147 of *Society of Photo-Optical Instrumentation Engineers (SPIE) Conference Series*, 91471E.

Owen J.E., 2019. *Annual Review of Earth and Planetary Sciences*, 47:67–90.

Parmentier V. et al., 2018. *A&A*, 617:A110.

Pearson K., 1901. *The London, Edinburgh, and Dublin Philosophical Magazine and Journal of Science*, 2(11):559–572.

Pelletier S. et al., 2021. *AJ*, 162(2):73.

Petigura E.A. et al., 2018. *AJ*, 155(2):89.

Pidhorodetska D. et al., 2020. *ApJL*, 898(2):L33.

Pino L. et al., 2018. *A&A*, 612:A53.

Piskorz D. et al., 2016. *ApJ*, 832:131.

Piskorz D. et al., 2017. *AJ*, 154:78.

Piskorz D. et al., 2018. *AJ*, 156(3):133.

Pollacco D. et al., 2006. *Ap&SS*, 304(1-4):253–255.

Polyansky O.L. et al., 2018. *MNRAS*, 480:2597–2608.

Prinoth B. et al., 2022. *Nature Astronomy*, 6:449–457.

Quirrenbach A. et al., 2014. In *procspie*, volume 9147 of *Society of Photo-Optical Instrumentation Engineers (SPIE) Conference Series*, 91471F.

Quirrenbach A. et al., 2016. In C.J. Evans, L. Simard, and H. Takami, editors, *Ground-based and Airborne Instrumentation for Astronomy VI*, volume 9908 of *Society of Photo-Optical Instrumentation Engineers (SPIE) Conference Series*, 990812.

Quirrenbach A. et al., 2020. In *Society of Photo-Optical Instrumentation Engineers (SPIE) Conference Series*, volume 11447 of *Society of Photo-Optical Instrumentation Engineers (SPIE) Conference Series*, 114473C.

Rajpurohit A.S. et al., 2018. *A&A*, 620:A180.

Rauscher E. and Menou K., 2010. *ApJ*, 714(2):1334–1342.

Richard C. et al., 2012a. *JQSRT*, 113(11):1276–1285.

Richard C. et al., 2012b. *Journal of Quantitative Spectroscopy and Radiative Transfer*, 113(11):1276–1285.

Ricker G.R. et al., 2015. *Journal of Astronomical Telescopes, Instruments, and Systems*, 1:014003.

Robinson T.D., 2017. *ApJ*, 836(2):236.

Rodler F., Kürster M., and Henning T., 2010. *A&A*, 514:A23.

Rodler F. and López-Morales M., 2014. *ApJ*, 781(1):54.

Rodler F., Lopez-Morales M., and Ribas I., 2012. *ApJ*, 753(1):L25.

Rogers L.A., 2015. *ApJ*, 801(1):41.

Rosenthal L.J. et al., 2021. *ApJS*, 255(1):8.

Rossiter R.A., 1924. *ApJ*, 60:15–21.

Rothman L.S. et al., 2010a. *Journal of Quantitiative Spectroscopy and Radiative Transfer*, 111:2139–2150.

Rothman L.S. et al., 2010b. *Journal of Quantitative Spectroscopy and Radiative Transfer*, 111:2139–2150.

Sagan C. et al., 1993. *Nature*, 365(6448):715–721.

Sajadian S., 2021. *MNRAS*, 506(3):3615–3628.

Sako T. et al., 2008. *Experimental Astronomy*, 22(1-2):51–66.

Salz M. et al., 2018. *A&A*, 620:A97.

Sánchez-López A. et al., 2019. *A&A*, 630:A53.

Sánchez-López A. et al., 2022. *A&A*, 661:A78.

Saumon D. et al., 1996. *ApJ*, 460:993.

Schwarz H. et al., 2015. *A&A*, 576:A111.

Schwarz H. et al., 2016. *A&A*, 593:A74.

Seager S., 2010. *Exoplanet Atmospheres: Physical Processes*. Princeton University Press.

Seager S. and Mallen-Ornelas G., 2003. *ApJ*, 585(2):1038–1055.

Seager S. and Sasselov D.D., 1998. *ApJ*, 502:L157–L161.

Seidel J.V. et al., 2020. *A&A*, 633:A86.

Serindag D.B. and Snellen I.A.G., 2019. *ApJL*, 871(1):L7.

Showman A.P. et al., 2009. *ApJ*, 699(1):564–584.

Sing D.K. et al., 2016. *Nature*, 529:59–62.

Skemer A.J. et al., 2016. *ApJL*, 826(2):L17.

Smette A. et al., 2015. *A&A*, 576:A77.

Snellen I. et al., 2015. *A&A*, 576:A59.

Snellen I.A. et al., 2010. *Nature*, 465(7301):1049.

Snellen I.A.G. et al., 2008. *A&A*, 487(1):357–362.

Snellen I.A.G. et al., 2013. *ApJ*, 764(2):182.

Snellen I.A.G. et al., 2014. *Nature*, 509:63–65.

Sozzetti A. et al., 2009. *ApJ*, 697(1):544–556.

Spake J.J. et al., 2018. *Nature*, 557(7703):68–70.

Stassun K.G. et al., 2019. *AJ*, 158(4):138.

Stevenson K.B. et al., 2014. *Science*, 346(6211):838–841.

Stevenson K.B. et al., 2017. *AJ*, 153(2):68.

Struve O., 1952. *The Observatory*, 72:199–200.

Takeda G. et al., 2007. *ApJS*, 168:297–318.

Tamuz O., Mazeh T., and Zucker S., 2005. *MNRAS*, 356(4):1466–1470.

Tennyson J. and Yurchenko S.N., 2012. *MNRAS*, 425(1):21–33.

Tennyson J. and Yurchenko S.N., 2022. *Frontiers in Astronomy and Space Sciences*, 8:218.

The JWST Transiting Exoplanet Community Early Release Science Team et al., 2022. *arXiv e-prints*, arXiv:2208.11692.

Tinney C.G. et al., 2001. *ApJ*, 551:507–511.

Tsiaras A. et al., 2019. *Nature Astronomy*, 3:1086–1091.

Turner J.D. et al., 2020. *ApJL*, 888(1):L13.

Udalski A. et al., 1992. *AcA*, 42:253–284.

Udry S. et al., 2000. *A&A*, 356:590–598.

van Belle G.T. and von Braun K., 2009. *ApJ*, 694(2):1085–1098.

van de Schoot R. et al., 2021. *Nature Reviews Methods Primers*, 1(1):1–26.

van Sluijs L. et al., 2022. *arXiv e-prints*, arXiv:2203.13234.

Wakeford H.R. et al., 2013. *MNRAS*, 435(4):3481–3493.

Wakeford H.R. et al., 2017. *Science*, 356(6338):628–631.

Wakeford H.R. et al., 2020. *AJ*, 159(5):204.

Waldmann I.P. et al., 2015. *ApJ*, 802(2):107.

Wardenier J.P. et al., 2021. *MNRAS*, 506(1):1258–1283.

Webb R.K. et al., 2020. *MNRAS*, 494(1):108–119.

Webb R.K. et al., 2022. *MNRAS*, 514(3):4160–4172.

Welch B.L., 1947. *Biometrika*, 34(1/2):28–35. ISSN 00063444.

Wiedemann G., Deming D., and Bjoraker G., 2001. *ApJ*, 546(2):1068–1074.

Wilks S.S., 1938. *Annals of Mathematical Statistics*, 9(1):60–62.

Williams J.P. and Cieza L.A., 2011. *ARA&A*, 49(1):67–117.

Wilson P.A. et al., 2015. *MNRAS*, 450(1):192–200.

Winn J.N., 2010. In S. Seager, editor, *Exoplanets*, 55–77. University of Arizona Press.

Wittenmyer R.A., Endl M., and Cochran W.D., 2007. *ApJ*, 654(1):625–632.

Wolszczan A. and Frail D.A., 1992. *Nature*, 355(6356):145–147.

Wright J.T. et al., 2012. *ApJ*, 753(2):160.

Wyttenbach A. et al., 2015. *A&A*, 577:A62.

Zechmeister M., Anglada-Escudé G., and Reiners A., 2014. *A&A*, 561:A59.

Zhang J., Kempton E.M.R., and Rauscher E., 2017. *ApJ*, 851(2):84.

Zhang Y. et al., 2020. *A&A*, 641:A161.

Zhang Y. et al., 2021. *Nature*, 595(7867):370–372.

Zucker S., 2003. *MNRAS*, 342(4):1291–1298.

Zurlo A. et al., 2013. *A&A*, 554:A21.